MECHANISM DESIGN OF VENTRICULAR ASSIST DEVICE

Jeerasit Bumrungpetch
Bachelor of Mechanical Engineering

Submitted in fulfilment of the requirements for the degree of
Doctor of Philosophy

School of Chemistry, Physics and Mechanical Engineering
Faculty of Science and Engineering
Queensland University of Technology
2016

Keywords

BiVAD, CFD, Computational Fluid Dynamics, Heart Pump, VAD, Ventricular Assist Device

Abstract

Heart disease is a serious health problem that affects numerous patients worldwide. The reliable methods for the severe cases are mainly limited to the heart transplantation which is restricted by very limited number of available donor heart. The Ventricular assist device (VAD) have been a promising option to support a patient, for its versatility to be used in both short and long term, while also possible to be removed if the heart is recovered. However, it still suffer from many device complications in both term of mechanical failure and damaging of red blood cell especially in long term support. The situation is worse in the patients who developed bi-ventricular failure in which normally two VADs are required for supporting each ventricle that leads to more difficulty for device managements and more limited available device.

This thesis is aimed to solve both the reliability problem and the lack of the device for supporting biventricular failure. This was done by proposing the concept design of an innovative BiVAD and the use of the computational fluid dynamics (CFD) to the development of this new device. CFD was used as a main development tool to analyse the flow and pump performance and predict the risk of hemodynamic related issue from the early stage of development. The new VAD is a high efficiency pump that offer long term support to both ventricle with a single module.

In this thesis the new design of BiVAD was split for individual analysis on LVAD and RVAD functions and was extensively analysed by CFD for its efficiency under different low condition of the CHF patients. The hydraulic performance was predicted, and the blood damage was estimated from the shear stress information obtained from the simulation results. Flow visualisation was used to identify the area that have risk of forming thrombosis and possible design correction. Combining these information, the pump design was optimised and a prototype was created for the experimental evaluation.

The human mock circulation loop which capable of simulating the pulse flow environment and the heart failure condition was specifically designed for this pump

testing. The pump was tested in both steady flow to identify the pump characteristic and the pulse flow to observe its performance in its real working condition.

The successful development of this pump and CFD analysis method will provide useful techniques in the heart pump development that improve the pump performance and reduce the risk of device complications, while also reduce the lead time and cost of development. The newly designed heart pump can be developed further through later phase of development on animal and clinical trials. Then it will able to use for long term support of bi-ventricular failure patient so they no longer rely to the limited donor heart supply.

Table of Contents

List of Figures

List of Tables

Nomenclature

AoP	Aortic Pressure
AP	Atrial Pressure
BEP	Best Efficiency Point
Bpm	Beats per minute
BTR	Bridge to Recovery
BTT	Bridge to transplantation
C	Compliance
CFD	Computational Fluid Dynamics
CHF	Congestive Heart Failure
CO	Cardiac Output
DT	Destination Therapy
H	Head
HF	Heart Failure
HR	Heart Rate
LAP	Left Atrial Pressure
LHF	Left Heart Failure
LVP	Left Ventricular Pressure
MAP	Mean Arterial Pressure
MIH	Modified Index of hemolysis
MPAP	Mean Arterial Pressure
NIH	Normalised Index of Hemolysis
P	Pressure
P_h	Hydraulic Power
PAC	Pulmonary Arterial Compliance
PAP	Pulmonary Arterial Pressure
PP	Pulse Pressure
P_{dias}	Diastolic Pressure
P_{sys}	Systolic Pressure
Q	Flow Rate
R	Resistance

RAP	Right Atrial Pressure
Re	Reynolds Number
RVP	Right Venous Pressure
SV	Stroke Volume
η_h	Hydraulic Efficiency
ρ	Fluid Density
μ	Fluid viscosity

Statement of Original Authorship

The work contained in this thesis has not been previously submitted to meet requirements for an award at this or any other higher education institution. To the best of my knowledge and belief, the thesis contains no material previously published or written by another person except where due reference is made.

Signature:

Date: 16/03/2016

Acknowledgements

I would like to thank you everyone around me that provide help and support throughout my candidature. I would not be able to complete this project without continuous support from my family. Words cannot convey the extent of support I received during my study, I'm very grateful to have all of you with me throughout all the difficult time.

I would also like to express my deepest gratitude to my supervisor Professor Andy Tan in introducing me to this field of PhD research in CFD Analysis of Heart Pump. For his endless support in every possible way to get me going throughout the entire program. I'm very thankful for your dedication in guiding me in the right direction for my study.

Professor Jason Yuan for providing the original pump design and information about the centrifugal pump, which helped me to get a proper start at the beginning of my study.

Peter Wilson for sharing a lot of knowledge about CFD program in my early study which made it easier for me to gather all the necessity information and helped me stay on the right track throughout my study.

A special thanks to all QUT DMC Workshop and Lab staffs for providing support throughout my research.

William Gordon for many advices about machining process so I could successfully crate a model of the pump that is suitable for manufacturing. Thank you for your dedicated assistant and continuous supports in producing the pump prototype including optimization of the design several times until it can work perfectly.

Jose Chakkamkunnel for creating the mock circulation loop components and solving several problems of my design.

Lincoln Hudson for providing the data logging system and his assistant in setting up the measuring equipment

Gregory Paterson for helped space allocating for my test apparatus

Len Wilcox for your help in managing the test rig layout.

Antho Tofoni for your help with wiring the electrical equipment.

Thank you for my fellow PhD students and every person involve with this research project. This thesis will never be completed without the support from all of you.

Chapter 1: Introduction

Heart failure is one of the cardiovascular diseases and is a major global health concern because of its fatality and the rapidly growing number of diagnosed patients. Although there are many treatments available for different degrees of heart failure, the only reliable approach for severe cases is heart transplantation. However, the availability of this treatment is restricted mainly by the very limited number of heart donors, hence only a handful of patients receive transplantations each year.

A Ventricular Assist Device (VAD) has been developed to address this heart shortage problem by providing support to sustain patients while they are waiting for donor hearts to become available, or even to use as a permanent support if transplantation is not possible. The results for VADs in clinical studies have confirmed the viability of the devices for long term support in improving the quality of life and in increasing the survival rate compared with the optimal medical treatment (Rose, Gelijns, & Moskowitz, 2001). Despite the better performances of VADs over optimal medical therapies in many long terms trials, there are two main problems related to the devices'performance and structure that are still a major concern and limit the use of these devices.

The first problem involves biventricular support which is used to provide support when both ventricles of a patient have failed. Most pump designs are aimed for the left ventricle support function as it is the most common case of heart failure. Consequently, there are fewer choices of pumps available for patients with biventricular failure as it requires pumps that can function in the left and right flow environments. Two pumps need to be implanted, one for each ventricle, and operated at the same time. Transplanting two pumps into a patient leads to a complex control system and additional drivelines, and more space is needed for the implantation. Therefore, the development of a bi-ventricular assist device (BiVAD or BVAD) within a single module could be the solution for reducing the complications of an additional device being needed for biventricular failure patients.

The second problem is related to the durability and hemodynamic performance of the pump. There are reports of a significant number of adverse cases arising from device complications that cause serious issues such as blood damage, blood clots and mechanical failure. These problems are major concerns for pump development and need to be addressed during the pump design phase. However, to develop a heart pump that could achieve the performance requirements with the minimum mechanical and hemodynamics complications, several design selections, optimizations and an experimental analysis need to be conducted. These processes are generally costly and time consuming, which results in a long development time for the pump before it could become available for clinical use and it makes the device too expensive to be widely accessible for patients.

To solve these two problems, an innovative BiVAD was designed with a unique structure that incorporates two identical sets of rotors and stators for the left and right ventricles in a single pump unit. The rotors were designed to operate independently from each other and operate at different speed to deliver flow rates and pressures to meet the different required perfusion of systemic and pulmonary circulation. Computational Fluid Dynamics (CFD) was used as the main design tool in the development of this pump to predict the flow and performance of the design and conduct the optimization before making a prototype for experiments.

This study is based on the preliminary design of a BiVAD with five different rotor designs to support the left and right heart. The pump design in this study still lacks the driving and suspension mechanism for the whole BiVAD unit, hence, the confirmation of BiVAD is separated into LVAD and RVAD for individual analysis. CFD was used to identify performance of both the hydrodynamics and hemodynamics aspects of the design selection to obtain the best performance. In terms of the hydrodynamic properties, the simulation was able to predict the pressure raised under the average flow rate of the ventricles, the related pump speed could be determined, and the efficiency of the pump at each operating condition was calculated. In addition to these hydraulic performance parameters, the hydraulic force on the rotor was also calculated and can be later used for the suspension and actuator design. The hemodynamic analysis focused on the prediction of blood clots or thrombosis that is caused by recirculation flow and hemolysis from the excessive

shear stress on the red blood cells. This information was used to select the best impeller design that would provide the best performance under the designed operational range of the pump.

The pump prototype designed on the individual pump to work on the available driving mechanism. It could operate in both LVAD and RVAD functions. The detailed simulation was conducted and additional transient simulations were used for further analysis on the unbalanced structure of a rotor. The information gathered from the simulations were used as a final confirmation before the creation of the pump prototype for the experimental evaluation.

In order to test the pump's performance, a mock human circulation loop was designed and constructed. The loop was capable of replicating the pulse flow environment of the left and right ventricles using a piston pump with adjustable speed and stroke volume. The compliance effect from the elastance of the arteries was simulated by an air-trapped compliance tank, and the vascular resistance was replicated by an adjustable valve.

The information and prototype from this study can be later used in the development of the driving and controlling systems in the final stage of the pump mechanism design process.

1.1 SIGNIFICANCE AND SCOPE

The significance of this study is it attempts to solve the problem in the shortage of hearts for transplantation to heart failure patients, the lack of an efficient device to support bi-ventricular failure cases, and the expense and limited lifetime of current heart pumps for long term support.

This study uses CFD for the development process of a new BiVAD. It provides a computational simulation methodology that can be used to significantly shorten the development time and reduce the development cost which should result in a lower cost BiVADs. This would make BiVADs more accessible for patients and the new pump would be available on the market faster. With this approach, it will also allow the pump's hydraulic performance to be investigated before making a prototype, so the design selection and optimization can be done more efficiently. The hemolysis information gathered from the simulation results will allow the pump to be optimised to reduce the occurance of thrombosis and blood damage which is one of the major issues of the long term use of VADs reported from clinical trials.

With the information from the CFD simulation and the structural design of the pump, a newly developed BiVAD from this study will be a highly efficient pump that is durable enough for long term support. The device's complications involving mechanical failure, blood damage and coagulation, which are the major issues in a long term blood pump should be minimised. Therefore, this new heart pump would be able to provide support for a heart failure patient waiting for heart transplantation until a suitable heart become available or until a patient's physical condition is stable enough to receive a heart transplantation. Furthermore, it will also provide an alternative treatment for permanent support to ease a requirement arising from an increasing number of heart failure cases, as well as improve the quality of life for the patients with VAD support.

The limitation of this thesis is mainly dictated by the lack of driving rotor suspension mechanism for the BiVAD which need to be done separately in later stage of development. To solve this problem, the LVAD and RVAD were analysed separately and the prototype was created as a single sided pump that can operated on both left and right functions.

1.2 AIMS

This thesis focuses on two important aspects: (i) the development of an innovative BiVAD, and (ii) the implementation of CFD analysis to optimize the development of a heart pump. The development of a new BiVAD is to create an innovative device that will be able to provide long term support for bi-ventricle heart failure patients, and limit device complications from mechanical failure and hemolytic issues. The implementation of CFD will provide simulation and analysis methods that can be used to reduce the development cost and emphasis the processes necessary to achieve the requirements of the newly developed BiVAD.

The specific aims are described as follows:

I. Literature Review

- To conduct an extensive review of the VAD designs and requirements for the development of a new BiVAD.
- To review and research the CFD background and techniques used for performance prediction of the VAD in both hydraulic and hemodynamic terms.

II. VAD design and simulations

- To review the design and structure of a BiVAD and create a fluid model for computational simulation.
- To conduct the computational simulation for design selection and optimisation to achieve the BiVAD requirements.
- To optimise the design by incorporating the driving mechanism and refine the pump structure to be suitable for the manufacturing process to produce a working prototype.

III. Mock Circulation Loop

- To design and construct a mock circulation loop that is capable of simulating the human circulation system for the experimentations of the VAD prototype under different physiological conditions.

IV. Experimental Evaluation

- To identify the hydraulic performance of the pump and verify the accuracy of the simulation.

- To obtain additional information for further design optimization.

1.3 THESIS OUTLINE

This thesis is divided into six chapters that detail the basic knowledge of the VAD and CFD, the basic structure and simulation process of the pump, the design and construction of the test rig, and the testing procedure with the results summary. Figure 1-1 outlined the structure of this thesis.

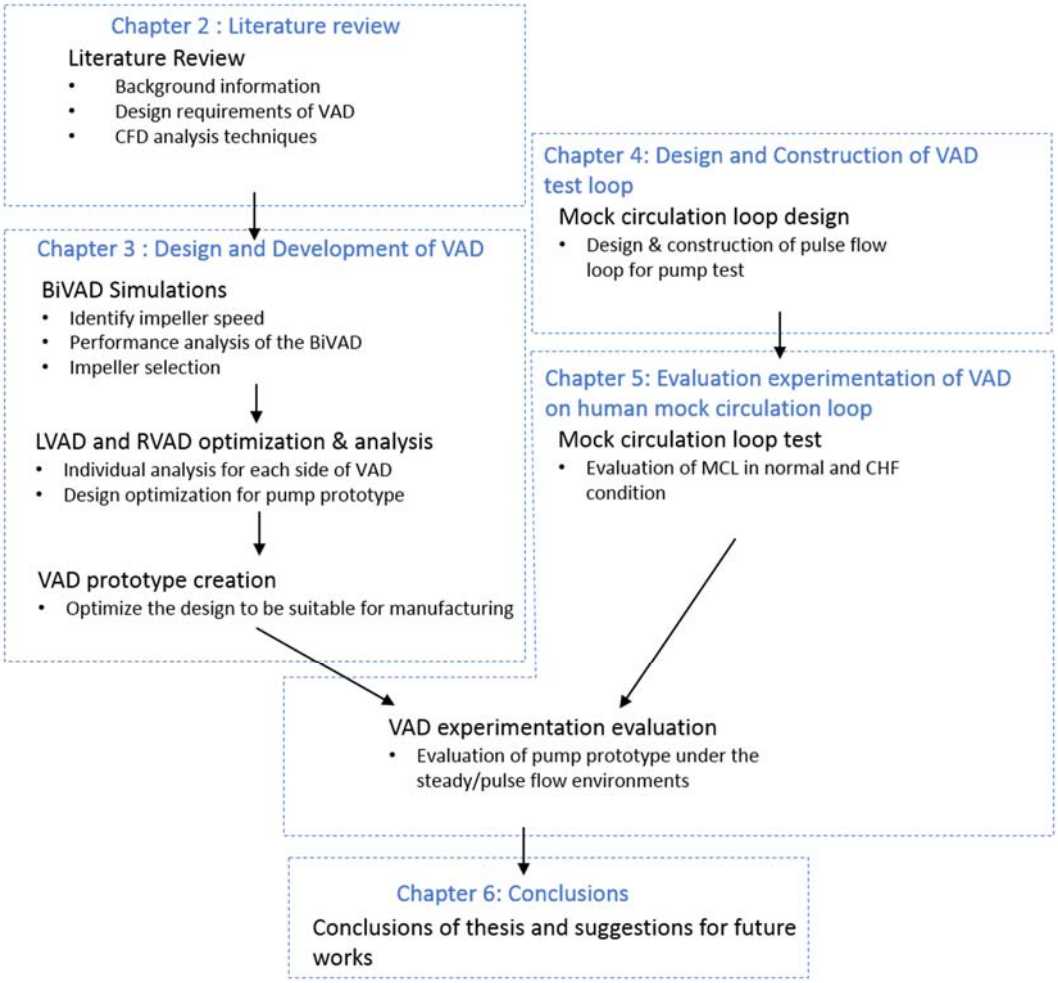

Figure 1-1: Outline of this thesis

Chapter 2

This is a literature review to provide background information about the global heart failure situation and the significance of the VAD as an alternative therapy. This

chapter allows the reader to understand the current development situation, the design requirements, limitations and expectations of the VADs.

The review of CFD simulation is included in this chapter as an effective tool for fluid dynamics analysis that could be implemented for the design of the VAD. The review covers the strengths of CFD and the information that it could provide, along with the background theories for the simulation configurations and analysis of the results.

Chapter 3

This chapter discusses the structural design of the BiVAD and the simulation process for performance prediction and design selection, design modification, and optimization to create a working prototype for the in-vitro evaluation.

Chapter 4

The design and construction of human mock circulation loops are reviewed and discussed in this chapter. It includes an analysis of the parameters, structures and equipment that are required to establish a test rig that could simulate the human circulation system and flow variations to reflect the flow conditions of a heart failure patient.

Chapter 5

This chapter outlines the experimental evaluation procedure of the pump prototype in the mock circulation loop with the results and performance analysis of the pump in comparison to the CFD simulation results.

Chapter 6

This is the conclusion of the thesis with a summary of the outcomes from this study, including a suggestion for further development of this pump.

1.4 THESIS OUTCOMES AND CONTRIBUTIONS

The work presented in this thesis describes the development of the BiVAD with an implementation of CFD for the analysis of hydrodynamics and hemodynamics. The completion of this study has led to the following outcomes:

1. The computational analysis method for an analysis of the VADs which includes:

a. The procedure for the computational model creation, mesh generation and boundary conditions for the simulation of VADs.

b. The analysis method and results interpreting the hydraulic performance of the pump that allows the prediction of pump efficiency and optimum speed to deliver the required pressure, including the hydraulic force exerted on the rotor.

c. The prediction and analysis method for hemolysis and thrombosis that are generated within the pump.

2. The verification and analysis of an innovative design concept of BiVAD with the following features:

a. The pump designed as a centrifugal pump which has high durability and is suitable for long term usage. The design of the rotors to support LVAD and RVAD was selected based on the CFD analysis to ensure the high pump efficiency with a low risk of thrombosis and hemolysis.

b. The proposed design of BiVAD in this thesis has identical structure between the left and right side. This allows two pump module that developed in this study to be combined as a single BiVAD after the driving mechanism is completely designed. The LVAD and RVAD side can be operate at different rotation speed to deliver the required perfusion for systemic and pulmonary circulation.

3. According to the outcomes from (1) and (2), a working prototype of a VAD was produced and tested. The pump has been optimized to be able to operate in both LVAD and RVAD functions at high efficiency with a low risk of thrombus formation and hemolysis. This new pump can function on its own as an individual pump, and the information from evaluation in this thesis will be used to combine two pump module to a working BiVAD in future study.

Chapter 2: Literature Review of Ventricular Assist Devices

This section critically evaluates the literature according to the current situation relating to heart failure, the use of mechanical devices for circulatory support on heart failure patients, and their impact on heart failure treatment. The review also examines and emphasizes the mechanism development process of the Ventricular Assist Devices (VADs) including the design tools and technique that could be implemented in the development process of a new heart pump, in order to identify a gap in heart pump research and development.

In the first section, the review focuses on the current status of the incidence of heart failure, the application and implementation of VADs, and explains how VADs could be used instead of donor hearts to treat heart failure. The limitations and expectations of a heart pump are examined based on experiments and clinical results in order to understand the current issues of heart pumps and the possibility of future developments.

The second section highlights the evolution of the heart pump mechanism. The development process and design concerns are listed and analyzed to ensure that the newly developed VAD mentioned in this research could meet the performance requirements and achieve the objectives of the heart pump development.

The last section of this literature review focuses on the main development tool, the computational simulation. Computational Fluid Dynamics (CFD) is investigated for its strengths and the information that it can provide. The details of each simulation stage with configuration options and the background theories are also covered.

2.1 HEART FAILURE

Congestive Heart Failure (CHF) or chronic heart failure is when the heart muscle is weakened and loses its contraction resulting in inadequate systemic blood pressure or venous blood return. This event leads to an inadequate perfusion to meet the body's needs, resulting in fatigue and breathlessness. The lack of pressure of the circulation also causes the blood to back up in the veins returning to the heart and the blood becomes congested in the tissues. This buildup fluid could cause weight gain as well as swelling in the ankles, legs, and feet which is called "edema". In addition, the fluid can also build up in the lungs and cause congestion in the pulmonary system (Braunwald, 2013).

The common causes of CHF are coronary artery disease, hypertension, and diabetes. Statistically, elderly people are more at risk of having this disease, and it is the most common cause of hospitalization for the elderly. More than 70 % of CHF patients hospitalized in the United States are 65 years and older (Braunwald, 2013; M. J. Hall, Levant, & DeFrances, 2015).

2.1.1 Heart failure incidence

CHF has become a worldwide health concern, as it has been one of the leading causes of death in the past decade with an estimated 38 million patients worldwide (Braunwald, 2015), and the number is still rising. According to the World Health Organization, the total number of deaths from all the cardiovascular diseases could rise to 23.3 million by 2030. In the past, CHF was more of a problem to those in the high income levels due to the lifestyle that risked causing CHF-related health problems such as obesity, hypertension, and diabetes. However, the change in the lifestyles of medium and low income countries leads to an increase in CHF becoming a global problem in the near future (Braunwald, 2015; Mendis, Puska, & Norrving, 2011).

In the US alone it was reported that there were almost 300,000 deaths each year while there are new cases being diagnosed bringing the total to approximately 870,000 cases annually (Mozaffarian et al., 2015). The long-term survival rate from CHF is relatively low. An estimated 50% of the patients die in the first year of the disease and about 70% of patients die by the fifth year (Michael E DeBakey, 2000).

2.1.2 Treatment options

There are several treatment options available for patients with different degrees of CHF, from lifestyle adjustments, taking optimum medication, and transcatheter interventions to transplantation in the severest cases (Katharine H. Fraser, Taskin, Griffith, & Wu, 2011; Harris & Thompson, 2012). Heart transplantation is the most reliable way of treating CHF; however, the major problem is the limited number of donor hearts as there are only around 2,100 to 2,500 hearts available annually in the US (Mozaffarian et al., 2015) compared to the estimated 35,000 US patients who would benefit from heart transplantation (Katharine H. Fraser et al., 2011). The number of patients is growing each year while the number of available hearts tends to be steady. Therefore, there have been attempts to develop mechanical circulatory support devices to relieve the need for short and long-term circulatory support for patients (Kirklin & Naftel, 2008). The devices that have mainly been developed to improve the pumping function of the failing heart are the Total Artificial Heart (TAH) and the Ventricular Assist Device (VAD). The TAH function is like its name implies, as it completely replaces the function of the native heart and requires removal of the ventricles in order to effect the transplant, while the VAD operates in parallel with the weakened heart by pumping blood from the ventricle to the aorta (Gregory, Timms, Gaddum, Mason, & Fraser, 2011) (Figure 2-2). Currently, both devices appear to be a promising alternative to heart transplantation, but the use of the VAD has some advantages over the TAH because of its flexibility in use as it could be used for both short and long-term support, while leaving the native heart in place. This provides some chance for the ventricles to recuperate to the stage where the device could be removed.

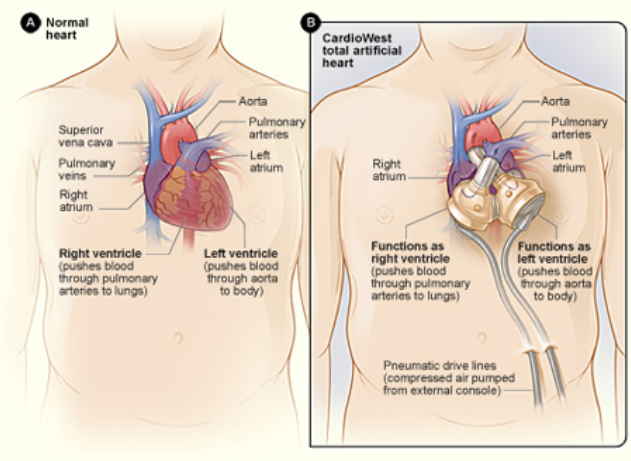

Figure 2-1: A transplantation with the CardioWest TAH that requires removal of the ventricles (NIH, 2012).

2.1.3 Applications and implantation of VAD

Heart failure can occur on both the left and right side of the ventricles but failure on the left side is much more common, so the majority of VAD developments aim to primarily function as a left ventricular assist device (LVAD). However, there have been reports of the development of right heart failure following the long-term support from the LVAD at a significant rate from 10 to 50% (Gregory et al., 2011). This development of the failure of both ventricles is called "bi-ventricular failure" and is considered to be serious as it is associated with more than 90% of deaths if not treated (Daniel Timms et al., 2008). Patients with bi-ventricular failure will require an additional VAD to function as the right ventricular assist device (RVAD) to support the failing right ventricle, or the alternative approach is to totally replace the native heart with a TAH (S. R. Wilson, Givertz, Stewart, & Mudge Jr, 2009).

Currently, an implantation of the VAD can be done either externally for short-term support after a cardiac operation, or implanted internally for patients who require long-term support (Nishimura, 2014; Teuteberg & Chou, 2014). If the device is to be implanted internally, it can be placed sub-diaphragmatically in pre-peritoneal or intra-abdominal positions and connected to the control unit and batteries outside the body with the driveline tunneled through the skin of the abdominal wall as shown in Figure 2-2 (S. R. Wilson et al., 2009).

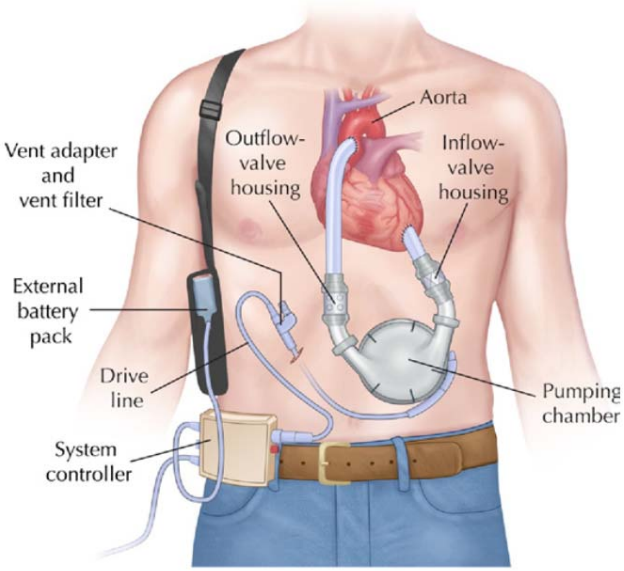

Figure 2-2: Ventricular Assist System (VAS) of the HeartMate XVE surgically implanted to the abdomen for left ventricle support (S. R. Wilson et al., 2009).

The pump is typically connected to the circulatory system by the inflow and outflow cannula. In the LVAD support, this inflow cannula or inlet of the device is normally attached to an apex of the left ventricle and the outflow cannula is connected to the aorta for additional blood pumping in parallel with the native flow from the heart. For the RVAD, the device works in a similar manner to the LVAD by pumping blood from the right ventricle to the pulmonary artery (Stone, 2007), but under a lower flow rate and pressure than the left ventricle support function. With the differences in the flow conditions, many of the pumps that are specifically designed as an LVAD cannot be operated for the RVAD function. However, some of the VADs could be used for either the LVAD or RVAD support; or two independent modules can be used to support both ventricles at the same time, which is called a bi-ventricular assist device (BiVAD or BVAD). Some examples are the Abiomed AB5000, Thoratec IVAD, Berlin heart EXCOR, Levitronix Centrimag, Jarvik 2000 and HeartWare HVAD (Gregory et al., 2011).

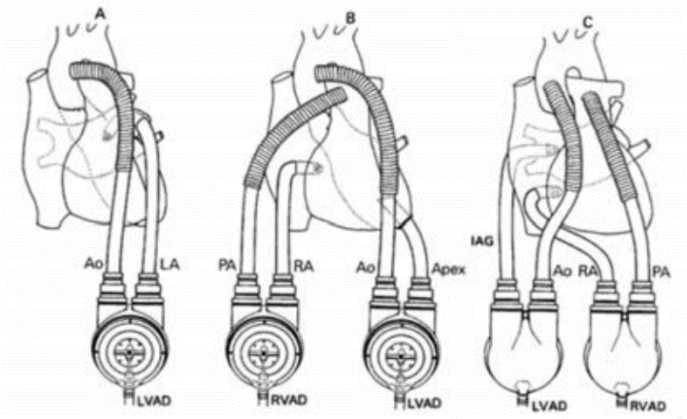

Figure 2-3: Implantation of a VAD for a left ventricle support (left) and both sides support at the same time (middle and right) (Stone, 2007).

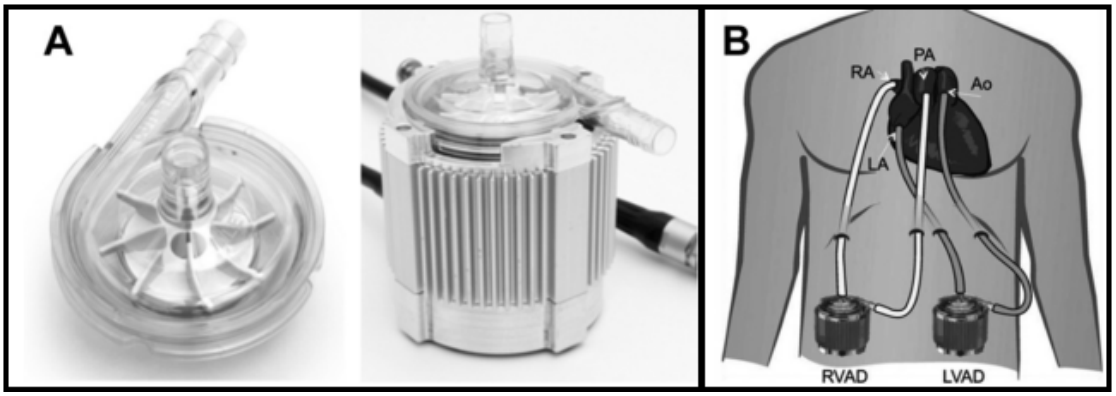

Figure 2-4: (A) The Centrimag pump and the pump as it is installed on a motor. (B) The Centrimag as a BiVAD application with the extracorporeal device placement (Teuteberg & Chou, 2014).

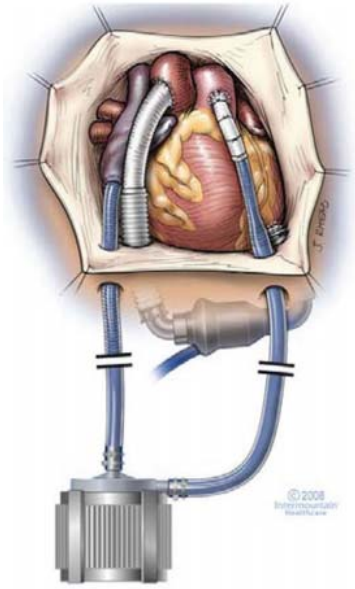

Figure 2-5: The combination of HeartMate II for LV support and Centrimag for RV support in a bi-ventricular failure patient (Eric A Rose et al., 2001).

The current pumps available that could be used for the BiVAD function have separate modules for each ventricle, as shown in Figure 2-3 and Figure 2-4 . Having two separate pumps makes a transplantation more complicated because it would require a more complex control system, additional drive lines and, if the devices are to be implanted, more space would be required in the patient's body. Currently, the only pump that aims to perform a BiVAD support with a single unit is the BiVACOR BV Assist which contains two stator sets on a shared rotating hub for the left and right ventricles. This pump was designed to be able to serve as both a BiVAD and TAH, however it is still being developed (M. Ferrari, Kruzliak, & Spiliopoulos, 2015; Daniel Timms et al., 2008; D Timms, Fraser, Thompson, McNeil, & Steinseifer, 2009) and there is still no report of the long-term clinical trial results.

Figure 2-6: BiVACOR BiVAD/TAH (Teh, 2015).

2.2 CLINICAL IMPACT OF VADS

2.2.1 VAD support indication

As discussed in the above section, a heart transplant is currently the most preferable destination therapy for severe heart disease patients. However, in order for the patients to receive the transplantation, they have to pass diagnostic tests in the screening process to ensure that they would be able to undertake the operation and recovery from the transplantation before they can be placed on the transplant list to wait for a suitable donated heart to be available. These processes usually take up to several months due to the limited number of heart donations.

The uncertainty during these long screening and waiting periods has always been a very difficult and stressful period for both the patients and their families. Therefore the VAD can be used as a Bridge to Transplantation (BTT) to support patients as they wait for the available heart. At present, the advancement in VAD technology allows the new generation of devices to generate low hemolysis and requires low maintenance. Consequently, the use of a VAD is no longer limited to temporary support but it can also be used for long-term support until the patient's heart recovers its function which is known as the Bridge to Recovery (BTR), or even permanent support, known as a Destination Therapy (DT), in some cases (Capdeville & Smedira, 2013; Tang, Oyer, & Mallidi, 2009; Yamane et al., 2010).

2.2.1.1) Bridge to transplantation (BTT)

The BTT is currently the majority application in the usage of VADs being involved in up to 54.1% of cases, according to the report from the Interagency Registry for Mechanically Assisted Circulatory Support (INTERMACS) in 2012 (Kirklin et al.). There are 2 main scenarios for patients to receive this method of treatment; the first is as an emergency measure in the event of acute carcinogenic shock, for which it has been reported to have a better outcome than emergency transplantation. For the second case, VADs are used on patients to stabilize their condition while they are waiting for heart transplantations or other proper treatment. Additionally, the implementation of a VAD to a CHF patient can also sometimes help to improve the organ's functions and make it possible for a patient who is critically ill and ineligible for a heart transplantation to become listable. This is referred as a Bridge to Candidacy (BTC) (Attisani et al., 2012; Gaudino et al., 2014; Miller et al., 2007).

With regard to the design and evaluation of heart pumps for the BTT application, the devices are generally expected to be able to support patients for at least 180 days (Jorde et al., 2014).

2.2.1.2) Bridge to recovery (BTR)

There are a small number of cases where the prolonged support of VADs combined with drugs for severe heart failure patients has led to myocardial recovery over a varying time period from 320±186 days (Birks et al., 2006). Some patients could recover to the stage where they no longer require a mechanical support device and

thus could have a normal quality of life. Therefore, the use of VADs is usually the preferable option over the TAH which requires removal of the native heart. Currently there are an estimated 1% of patients who receive this means of therapy each year (Kirklin et al., 2013; Nosé, Yoshikawa, Murabayashi, & Takano, 2000).

2.2.1.3) Destination therapy (DT)

It is estimated that 44% of the total VAD implantations are used as a means of DT for CHF patients and the number is continuing to grow (Porepa & Starling, 2014). The patients who require this means of therapy are those who are ineligible for heart transplantation due to the limitations of their physical condition, mainly as a result of advanced age. The average age of patients for DT is 61.7 years, which is considerably higher than that for other applications of VAD usage which is estimated at 52.7 years (Flint, Matlock, Lindenfeld, & Allen, 2012).

The VAD is one of the most suitable support options for a patient as it could suit every role from the BTT, BTR, to DT, as stated above, while still giving a chance for the native heart of the patient to recover and become device independent again. In addition, the heart itself may also serve as a safety measure for the patient to survive in the case of a device malfunction (Gregory et al., 2011).

2.2.2 Clinical Trials of VADs

Many clinical trials have been conducted in the past decade to collect and assess the data of patients using VADs for long-term support. This data is used for several researches and developments and also for the approval of the pump for clinical usage. The trial programs that have had a notable clinical impact are the REMATCH and INTERMACS programs:

2.2.2.1) REMATCH

The Randomized Evaluation of Mechanical Assistance for the Treatment of Congestive Heart Failure (REMATCH) was a long-term clinical trial program of LVADs in collaboration with Columbia University, the National Institute of Health (NIH) and Thoratec Corporation. The main objective of the program was to evaluate the reliability and effectiveness of the devices in chronic end-stage heart failure

patients. This program was run for three years from May 1998 to July 2001. The criterion for the patients who participated in the program was that they were required to have had New York Heart Association (NYHA) class IV heart failure which is the highest severity in the classification. In addition to this requirement, the participants must not have had one of the following conditions: aged more than 65 years old, insulin-dependent diabetes, chronic renal failure, or other clinically significant conditions. A total of 129 patients enrolled during the course of the program, and were then divided into 2 groups. The first group consisted of 68 patients who were assigned to receive the Thoratec HeartMate VE LVAD implant, while the second group which had 61 patients was a control group and was assigned for optimal medical therapy (Eric A. Rose et al., 2001).

The study outcomes showed a significant reduction in death from heart failure for the patients with LVAD support, with 52% of the patients in the device group and 25% of the medical therapy group having survived after one year of the program. After 2 years of the treatment, the survival rate for the device group declined to 23 % and only 8 % for the optimal medical group. This result indicated that a VAD is a promising alternative long-term treatment for the CHF patients. However, there was a high number of device failures; up to 35% of all the devices had failure problems during the second year of the program, which caused up to 17% of all the deaths in the device group (Oz et al., 2003; Eric A. Rose et al., 2001; Rose et al., 1999; Smart & Palanichamy, 2005) that is still considered to be a relatively high risk in terms of pump reliability for the DT. Some discussions also suggested that the cost and morbidity associated with the device when compared to the survival rate after 2 years may not provide the benefits that are favourable enough for most of the patients who required DT (J. Timothy Baldwin, Robbins, & National Heart, 2005; Dembitsky, 2006).

The results from the REMATCH program were widely accepted in the VAD development field by both the device companies and government agencies and so then influenced the development direction of the later generation devices. The outcome of this study also provided crucial information for the US Food and Drug Administration (FDA) to grant premarket approval for the Tharatec HeartMate XVE

to be used in DT which made it the first VAD approved for this indication (Raman & Jeevanadam, 2004).

2.2.2.2) INTERMACS

The Interagency Registry for Mechanically Assisted Circulatory Support (INTERMACS) is an ongoing program started in June 2006 under the collaboration of the National Heart, Lung, and Blood Institute (NHLBI), FDA, Centre of Medical and Medicare Services (CMS), 15 device manufacturers and the professional community. This program began with the decision by the NHLBI, after the completion of the REMATCH program, to create a long-term follow up program on the patients who received VADs (Kirklin et al., 2008). Unlike the REMATCH program, this program is not limited to LVADs but included the whole range of VAD support, including the TAH, in the program; thus, the database contains a large variety of devices in real clinical practices. Currently, this program has collected the largest database on the clinical outcomes of the mechanical circulatory system (MCS) from more than 12,000 patients (Kirklin et al., 2014).

All the long-term heart pumps implanted in the patients as long-term support in the US are mandated to participate in the INTERMACS program, and hospitals are required to submit reports directly to the FDA for any serious events relating to the devices. Therefore, the clinical results of all the FDA approved devices are recorded regardless of type and structure. The major limitation of this program is that information on investigative devices under evaluation could not be included in the registry, so the results of new pump technologies may not be recorded (Holman, 2012; Mann, Zipes, Libby, & Bonow, 2014).

The INTERMACS program has published a series of annual reports that accumulates and summarizes the information about the devices and patients in the program since 2008 (Kirklin et al., 2008). This series of reports has been used as a reference for the many device improvements and publications and also addresses several MCS questions such as the influence of the sex of the patient on the transplantation outcome, the causes of device malfunctions, and other crucial information to increase the effectiveness and safe use and development of the MCS.

This information benefits the device companies and researchers, as well as the government agencies, by providing a standard guideline for future device approvals.

The information from 2 different time periods 2006 - 2007 and 2011 - 2013 in the latest annual report shows a major increase in the number of patients receiving devices as DT from 14.7 % to 41.6 %, which indicates a growing trend of long-term permanent support, while currently 8.5% of patients have received pump replacements during the first three years of the program (Kirklin et al., 2014).

2.3 MECHANISM AND STRUCTURE OF VENTRICULAR ASSIST DEVICE

A mechanical device to support blood circulation was first used in cardiac surgery in 1952 by Dr. Dodrill to perform a left heart bypass operation; the machine used in that operation was named the Dodrill–GMR machine and it was a large machine with estimated dimensions of 10 x 12 x 17 inches for the external and temporary support and used a vacuum pump to circulate the blood through the patient's body. That operation was regarded as the beginning of the open heart surgery advancement with the help of a mechanical circulatory device (Stephenson, Arbulu, Bassett, Silbergleit, & Hughes, 2002; Stoney, 2009).

With the establishment of the NHLBI artificial heart program in 1964, a large amount of funds was invested in the development of short and long-term circulatory devices as well as in the total heart replacement pump. Many smaller versions of mechanical heart supports were then developed for uses outside circulation support during an operation. The DeBakey VAD was developed in this period and became the first VAD successfully implanted for post cardiac surgery in 1966, where it was used to support a 37-year-old woman for a total of 10 days (Kirklin & Naftel, 2008; Naughton & Bashour, 2002; Olsen, 2000; Tang et al., 2009).

The direction of mechanical circulatory support development became more focussed on VADs in the 1970s due to the unsuccessful results of the first TAHs and the increasing need for long-term support devices for patients waiting for donor hearts (Kirklin & Naftel, 2008; Mancini & Colombo, 2015). The direction of this

development became clearer when the NIH invited proposals for the development of a more mobile heart assist system. With the support of this NIH program, several clinical trials were conducted and large amounts of data were collected, which later led to the approval by the FDA of many long-term support VADs. In turn, this led to many developments to improve the pumps' reliability and durability so as to increase their lifetimes in the expectation of providing permanent support for patients.

2.3.1 VAD structure

The improvements in the VAD design over the course of time have resulted in several changes to its mechanism. With these changes, the VAD can be generally categorized into 3 generations based on the output characteristics and the mechanism that generates the output flow.

2.3.1.1) 1st Generation

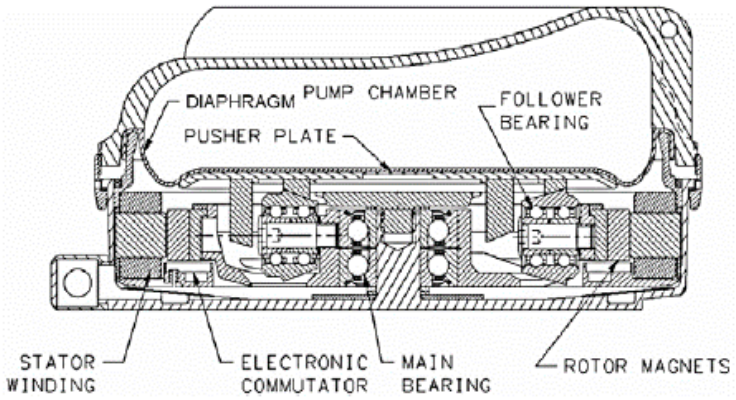

Figure 2-7: Cross-sectional view of the HeartMate XVE (Thoratec Corp., 2009) (ThoratecCorporation, 2006).

At the dawn of the VAD's development, the pump designers attempted to replicate the pulse flow characteristic of the native heart resulting in positive displacement pump designs which usually had a moving diaphragm that could be moved to increase the internal pump volume during the filling or diastolic phase and which compressed to eject blood during the systolic phase. This type of VAD has a major drawback in its reliability and life span as a result of a complicated drive mechanism and wear on repeatedly moving parts like the valve, membrane and

bearings; moreover, it also had a high risk of causing thrombosis, hemolysis and post-operative bleeding while the non-return valves, which are an important component that are used to regulate the flow direction, also had a risk of causing blood cell trauma (Frazier et al., 1992; Stone, 2007). With the risks of these device complications, this pulsatile pump required changing frequently and was not a preferable option for long-term support (Greenwood & Herr, 2014). Examples of the first generation pumps are the HeartMate XVE, Abiomed AB5000, Medos HIA-VAD, Berlin Heart EXCOR and Thoratec PVAD.

2.3.1.2) 2nd Generation

The development of the second generation VADs was in response to a request issued by the NHLBI in 1994 for an implantable VAD that has better durability and wider applicability (Tang et al., 2009). The continuous flow pump then became an interesting option for many developers and researchers with its advantage of a smaller design, better reliability and lower power consumption, despite the remaining concern over the long-term effect of the lack of pulsatility (Sciolino, 2012; Zareba, 2002). Therefore, rotary devices such as centrifugal and axial flow pumps which provide a continuous flow were evaluated to replace the displacement type of VADs. These rotary pumps operate using an impeller rotating at high speed to build up the pressure within the pump's volute and push the blood through the outlet port. With this new structure, the components that are exposed to repeating forces, like the diaphragm and pump valve, were no longer needed, so that the lifetime of the pumps was greatly improved (Kirklin et al., 2013). However, the drawback of the pumps in this generation is that the rotating part is operated on a shaft which needs to connect to the motor or actuator outside the pump chamber, so that it required a bearing to transfer torque and seals to prevent leakage; but these components are susceptible to exposure to high shear forces which in long-term use could cause problems such as a leaking seal, gastrointestinal bleeding, or red blood cell damage, and thus limit the life span of the pump (Gregory et al., 2011).

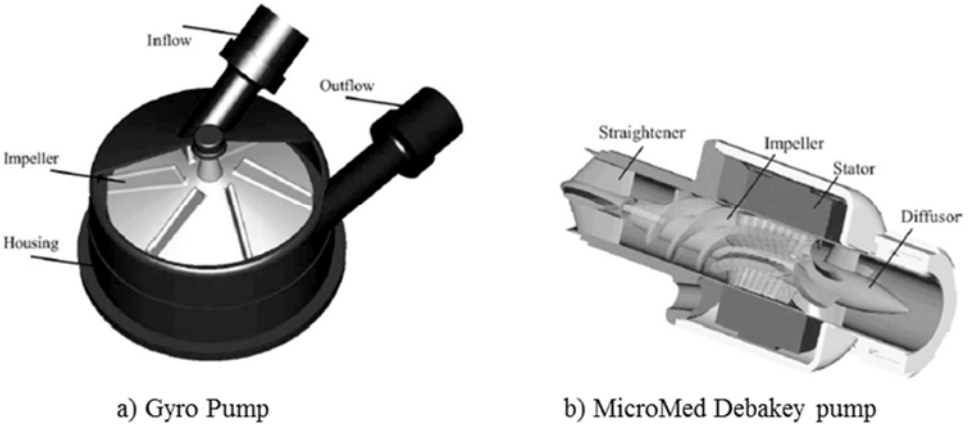

Figure 2-8: Gyro (a) and DeBakey (b) heart pump (Behbahani et al., 2009).

The pump from the second generation is still the most common blood pump available for clinical usage, and it is generally based on either a centrifugal or axial pump structure. Examples of these pumps are the Heartmate II, MicroMed DeBakey and Gyro pumps.

2.3.1.3) 3rd Generation

The target of VAD development was for a device that is able to permanently support the heart and, therefore, the heart pump is expected to have a life expectancy of at least 2 years (Nosé & Motomura, 2005; Olsen, 1999). To increase the durability of the rotary pump, developments were focused on removing the seals and bearings which are vulnerable to damage under high shear forces on prolonged application. Several designs of both centrifugal and axial flow with a magnetically driven pump were proposed on the hydraulic and magnetic bearing concepts with the hope that they would provide enough suspension forces to keep the rotor levitated within the chamber and eliminate all the mechanical contacts in order to reduce the mechanical wear as well as the shear stress exerted on the red blood cells, and hence improve the hemolysis performance and increase the lifetime for the pump's long-term support (Olsen, 1999).

There are many issues that still cause problems for the heart pump in this generation. The major problems that related directly to the pump mechanism design are blood damage from shear stress and blood clot, which is still a problem in the long-term, despite the pump having been greatly improved from the previous

generation. More details of these issues will be covered in later sections of this literature review. Others problems are related to the controlling, powering and unit cost. All the current VADs require a drive line that connects to the control unit and power supply outside the body. This exposed driveline often causes infections that became fatal in many cases (Maniar, Kondareddy, & Topkara, 2011; Park et al., 2012). Another issue is the high power consumption of the VAD which is an issue especially when the current aim of the pump is to provide long-term support. Currently, each battery can last for only 4-6 hours ("HeartWare Ventricular System: Instruction for use," 2012) so it needs to be replaced and recharged frequently which is not effective for use in daily life. The high cost of a long-term blood pump is also an issue that limits the accessibility of the device to the patient.

Figure 2-9: HeartWare HVAD pump.

Examples of the third generation pumps that are available are the HeartWare HVAD, Thoratec Centrimag, MiTiHeart, BiVACOR, DuraHeart, INCOR and HeartMate III. (HeartWare, 2015).

2.3.1.4) Future Direction

Nosé (Nosé & Motomura, 2005) suggests that development in myocardial treatment using stem cells could later lead to a significant turn in the direction of the development of VADs. As one of the major problems currently for the VADs is that the unit cost is relatively expensive, so preventing patients from having access to these devices, the promise of successful cardiac recovery using stem cell injections could be the future of CHF treatment. Studies have reported that it takes only 6-12 weeks for the heart muscles of heart failure patients to regenerate after injecting

bone marrow cells (Perin et al., 2004; Wysoczynski, Hong, & Moore, 2014). If this technology becomes available, it would reduce the requirement of long-term support such as the BTC and DT while shortening the waiting time for patients on the BTT. Therefore, the development of implantable VADs for long-term support that are more durable but yet expensive should have less significance, and instead there should be more focus on a wearable blood pump which could provide support for up to only 6 months. The cost per unit should also be lowered greatly to at least one-fifth of the cost of a current commercial pump to make it become more widely accessible for patients.

However, with uncertainty about alternative treatments in the future, the target for the near future development of heart pumps would still be for the permanent support to supplement heart transplantation in order to relieve the limited supply of donor hearts by mainly focus on increasing durability, output performance, and improving the hemolysis performance (Nishimura, 2014; Olsen, 1999), while any research should also focus on a miniature pump for better implementation on pediatric patients (J Timothy Baldwin et al., 2006; Kido et al., 2006; Throckmorton & Untaroiu, 2008; J. Wu, Antaki, Verkaik, Snyder, & Ricci, 2012).

Other than the pump structure, many authors (Mancini & Colombo, 2015; Manolis & Manolis, 2014; Ohuchi & Takatani, 2006; Stone, 2007) have suggested that some additional improvements could also be done in the control and power systems such as the implementation of remote monitoring , total implantability, and the re-introduction of pulsatility to continuous flow (CF) VADs to reduce the risk of adverse effects from the long-term lack of pulse pressure such as clot formation above the native heart valves and the development of arteriovenous malfunctions.

2.3.2 Classification of VADs

At present, the rotary pump has replaced the displacement type of VADs due to advantages in almost every aspect. The design of a rotary heart pump can be classified into 2 types based on the pump's structure: the axial flow pump and the centrifugal pump.

2.3.2.1) Axial flow pump

An axial flow pump is operated by an axial propeller type of impeller running in a straight pipe casing which allows the fluid to flow in and to be discharged axially. With this design characteristic, the axial flow pump is suitable for low head and high capacity pumping applications, while the axial rotor structure also makes it possible for this type of pump to achieve a more compact design that is suitable for a VAD application in exchange for a higher operating speed. The typical operating speed of an axial flow heart pump at the designed flow rate ranges around 6,000-12,000 rpm and could exceed 30,000 rpm in the miniature designs (Kafagy & Gitano-Briggs, 2013a; Song, Throckmorton, Untaroiu, et al., 2003).

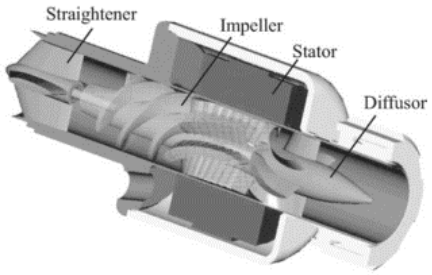

Figure 2-10: Structure of the MicroMed DeBakey axial blood pump (Behbahani et al., 2009).

Advantages: The compact size of the axial flow pump allows the implantation to be less intrusive with a lower trauma of implantation while it is also easy for it to be designed and implemented for pediatric use. In addition, the axial pump also has less power consumption which means the power supply units could be smaller and lighter; thus, it will be more comfortable for patients to wear it on a daily basis (J Timothy Baldwin et al., 2006; Kafagy & Gitano-Briggs, 2013a; Song, Throckmorton, Untaroiu, et al., 2003).

Disadvantages: The axial flow pump operates at a very high speed, so that it could lead to excessive shear stress and cause hemolysis of the red blood cells. In addition, the drive mechanism is also prone to higher stress and heat generation so the lifespan could be shorter. The stationary diffuser guide vanes that are usually required for controlling the axial position of the impeller create a vulnerable region for thrombus formation (Bottrell et al., 2014; Daniel Timms, 2005).

2.3.2.2) Centrifugal pump

The structure of a centrifugal pump is comprised of an impeller and a spiral casing. The impeller is a disc with a series of blades attached to it, where the number and the design of the blades vary but typically they are designed to curve to the opposite side of the rotating direction. During the operation, the inflow fluid flows into the suction inlet which is normally located at the eye of the impeller, then the inflow fluid will be exposed to the centrifugal force generated by the rotating impeller which pushes the fluid circumferentially through the vanes between the impeller blades and thus accelerates the fluid to flow along the curved path of the volute within the spiral housing and through the discharge outlet (Palgrave, 2005).

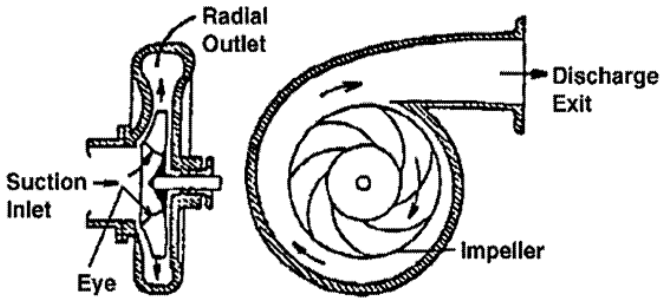

Figure 2-11: Basic structure of a centrifugal pump (Wilson et al., 2006) (K. C. Wilson, Addie, & Sellgren, 2006).

*Advantages***:** As a blood pump, the centrifugal pump has good efficiency so that it could produce a high head pressure at a low flow rate under a relatively low operating speed, typically around 2,000 - 4,000 rpm. This means that a low shear stress is exerted on the red blood cells and there is a lower chance of hemolysis (Bottrell et al., 2014; Kafagy & Gitano-Briggs, 2013a); in addition, this type of pump is also less susceptible to mechanical wear due to its lower operating speed.

Disadvantages: The spiral housing of the centrifugal pump is inevitably larger than the cylindrical casing of the axial pump which makes it harder to implant within the patient's abdomen especially in a person who has a small body or in children. In addition, the large housing combined with the larger impeller results in more weight and it consumes more power to drive the pump.

The difference in the properties of the axial and centrifugal types of blood pump are summarized by Kafagy et al., (Kafagy & Gitano-Briggs, 2013a), as shown in Figure 2-12.

	Pulsatile Pump	Centrifugal	Axial Flow
Speed	~ 60 bps	2000-4000 RPM	6000-12000 RPM
Size	Large	Medium	Small
Hemolysis (NIH)	High	0.0007 – 0.009	0.0028 – 0.03
Thrombosis	Low	Medium	High

Figure 2-12: Comparison of the important parameters of three types of blood pump (Kafagy & Gitano-Briggs, 2013a).

2.3.3 VAD Hydraulic Performance Parameters

Heart pump designs are generally based on general pump structures that have been used for general purpose applications such as with water and other fluids pumps. The hydrodynamic performance calculation is based on the same basis and the structure has a similar concept with some additional concern for the hemolysis performance.

2.3.3.1) Head pressure

Hydrodynamic performance of the pump is typically identified by the difference in pressure across the inlet and outlet designated as "head pressure" which represents the work that a pump performs on the liquid and can be calculated from the following equation:

$$H = \frac{\Delta P}{\rho g} \qquad [2\text{-}1]$$

Where: H = Head pressure

ΔP = Pressure difference

ρ = Fluid density

The plot between the head pressure and volumetric flow rate known as the H-Q plot is one of the pump performance curves that present the performance characteristic of each pump.

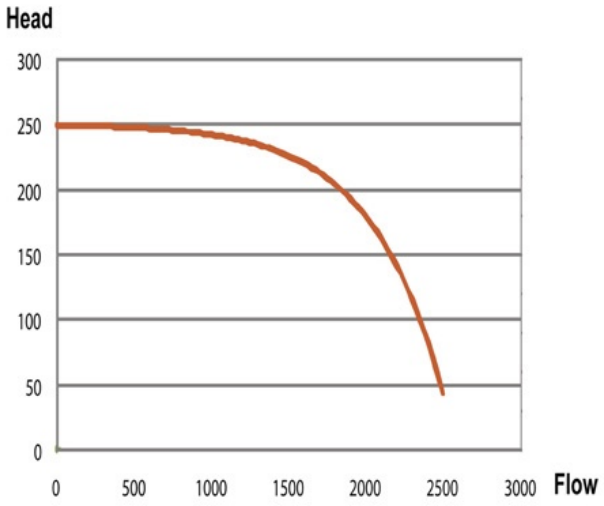

Figure 2-13: H-Q curve (Vogel, 2013).

2.3.3.2) Hydraulic Power

Hydraulic power is a parameter which indicates the amount of fluid that the pump can move in one cycle, as calculated in the following equation:

$$P_h = \rho g Q H \qquad [2\text{-}2]$$

Where:
- H = Head pressure
- ΔP = Pressure difference
- ρ = Fluid density

2.3.3.3) Hydraulic efficiency

The hydraulic efficiency identifies how well the mechanical power of the pump is transferred into hydraulic power. For the continuous flow pump, the efficiency is the ratio of fluid power (output) to the shaft power (input), as follows:

$$\eta_h = \frac{P_h}{P_s} = \frac{\rho g Q H}{T\omega} \qquad [2\text{-}3]$$

Where:
- η_h = Hydraulic efficiency
- P_h = Hydraulic power
- P_s = Shaft power
- T = Impeller torque
- ω = Impeller angular velocity

The hydraulic efficiency can be plotted against the volumetric flow rate, as in the example illustrated in Figure 2-7. It can be observed that the pump's efficiency can gradually increase along with the flow rate up to a point where the turbulence intensity becomes dominating and the efficiency starts dropping as the flow rate continues to increase. The flow rate that allows the pump to operate at the highest efficiency is called the "best efficiency point" (BEP), and the pump should be designed to operate at this point to obtain the best performance.

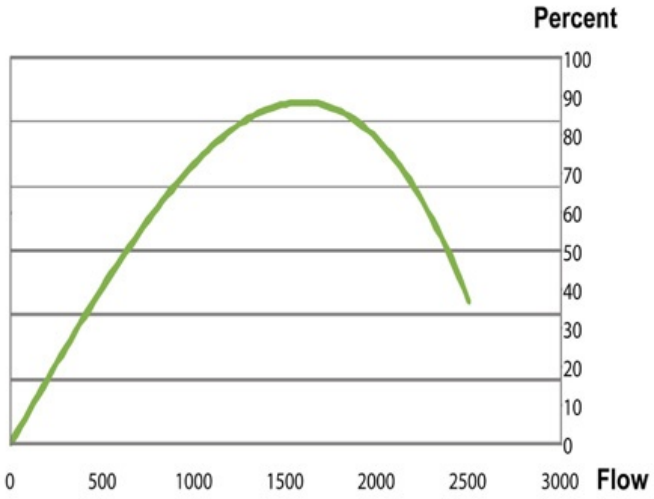

Figure 2-14: Efficiency-Q curve (Vogel, 2013).

Generally, the efficiency of a heart pump is in the range of 20-30% (Throckmorton et al., 2004; Untaroiu et al., 2005; Y. Zhang et al., 2008). Since the pump needs to be operated under a wide range of conditions, it is preferable that the efficiency should have a low variation over the VAD's operating range (Apel, Neudel, & Reul, 2001) and the BEP of a heart pump or the nominal design point is typically designed to be at the average flow rate of a normal heart condition (Throckmorton et al., 2004; Y. Zhang et al., 2008).

2.3.4 VAD Design Concerns

The common targets of the development of most of the current VADs are to create a compact implantable pump that has a high hydrodynamics performance and causes minimum hemolysis and thrombosis with low maintenance and at an inexpensive price (Capdeville & Smedira, 2013; Michael E. DeBakey, 1997; Frazier et al., 1992; Gregory et al., 2011; May-Newman, 2010; Nosé & Motomura, 2005; Nosé et al., 2000; Olsen, 1999, 2000; Stone, 2007; Tang et al., 2009; Yamane et al.,

2010). In order to archive the development objectives, there are several aspects of the VADs' properties that need to be considered.

2.3.4.1) Life Expectancy / Durability of the pump

In the present development of blood pumps, the developers typically expect the device to be durable enough for permanent support (Goldstein, Oz, & Rose, 1998; Porepa & Starling, 2014; Watanabe et al., 2004). Therefore, the service life of this pump type is expected to be at least 5-10 years which is the average survival length of heart transplant recipients (Sorensen, 2007). This could be achieved by increasing the stability of the mechanical components, and by avoiding the risks of thrombosis and hemolysis which are the main factors that limit the blood pump's life span.

I. Mechanical failure

The main factor that limits the heart pump's lifetime is mechanical failure, especially on the contact surfaces of parts that are subjected to repetitive stress that would make it more vulnerable to failure from wear; thus, the first generation of blood pumps that used mechanisms like rollers and a diaphragm, including the non-return valves, which are important components to direct the flow in the pulse flow pump had a limited lifetime of only 2-3 years (Burke et al., 2001). The REMATCH trial also found that there were many problems related to the device's complication that demonstrated a substantial risk of mechanical failure over the course of the program, and as many as 65% of those patients who survived up to 2 years in the trial had to undergo device replacement relating to these failures (Pagani, 2008).

There were many attempts to increase the reliable lifetime of the pump which led to the development of the 2nd generation of the pump. One of the important changes is the removal of a complex pulse generation mechanism that should have made it possible for the pump to achieve a 2-year lifetime. The life expectation of this 2nd generation blood pump should be sufficient to provide enough time for the BTT patients to receive a donor heart for transplantation, and long enough to support the recovery of dilating cardio myopathic hearts in the BTR application. However the axial pump design is unable to achieve this expected

lifetime as the high rotational speed causes high wear of the support bearing systems (Sciolino, 2012; Daniel Lee Timms & Queensland University of Technology. School of Engineering, 2005).

The levitating impeller design of the 3rd generation pump could largely resolve the mechanical failure problem by removing all the contact surfaces; hence, it is expected to greatly improve the durability over the previous design generations. However, the long-term evaluation of this type of pump is mostly still ongoing so that the actual lifetime cannot be confirmed. The most recent report on the durability of the 3rd generation blood pumps is on the data from the clinical trials of the INTERMACS program using HeartWare HVAD devices. It has recently been reported as achieving 4 years (2009 to 2013) without a report of a mechanical breakdown (Özalp et al., 2014).

II. Thrombosis

Thrombosis is the formation of a blood clot initiated by the body's hemostatic mechanism to prevent bleeding. This process can be triggered by many factors such as blood flow interruption, vascular wall abnormalities and alteration of the blood constitution (Behbahani et al., 2009). The formation of thrombosis in the VAD may compromise its mechanism causing a drop in flow and pumping power leading to failure of the VAD, if left unattended. This blood clot, if it is dislodged and circulates in the blood stream, might disturb the flow or occlude the blood vessels in vital organs and cause internal damage that could be fatal.

Currently, thrombosis is a major problem for the long-term VADs on both pulse flow and continuous flow designs as it is found to be one of the primary causes of death for patients with VAD support (Behbahani et al., 2009), and was reported to contribute up to 10% of the total device failure events during the 2 years trial of the HeartWare HVAD which is one of the most advanced 3rd generation heart pumps for the BTT patients (Najjar et al.).

The complication of thrombus formation in the VADs makes it difficult to prevent as it is involved with many factors from the pump flow rate, pump speed, level of anticoagulation and much more (Nakata et al., 2000). However, the risk of thrombosis could be reduced by designing a proper washout mechanism to avoid

stagnation, especially in the low flow region at the gap beneath the impeller in the centrifugal pump that has a high risk of stagnation, or by reducing the chance of flow recirculation over the whole pump operation flow range, while the foreign material surface of the pump that could also cause a blood clot can be overcome by the use of an anti-coagulation coating material or medical therapy (Najjar et al.).

III. Hemolysis

Hemolysis is the breakage of the membrane of the Red Blood Cells (RBC), causing the release of hemoglobin and other contents into the plasma. The leakage of hemoglobin in the blood can deteriorate the patient's condition or cause kidney dysfunction resulting in multiple organ failure (Behbahani et al., 2009). Hemolysis could occur as a result of shear stress exerted on the RBC where the degree of damage is proportional to the exposure time and the magnitude of the shear force. Therefore, it is one of the major concerns in the design of artificial organs especially in the rotary blood pump, where the high shear stresses could occur due to high rotational speed, and the small clearances between the rotor and housing may lead to RBC damage under certain conditions (Katharine H Fraser, Zhang, Taskin, Griffith, & Wu, 2012; Paul et al., 2003).

Paul et al. (Paul et al., 2003) investigated the threshold of blood damage on the shear stress and exposure time based on the evaluation on the Couette device in the shear stress range of 30-450 Pa and the exposure time from 25-1,250 ms; the result indicated the blood damage threshold at the shear stress of 425 Pa and the exposure time of 620ms.

The INTERMACS 2012 third quarter (Cowger et al., 2014) reported the hemolytic events in 363 of the 448 patients with the LVAD implanted, out of the total of 6,033 patients in the program, and it was found that 8 deaths were directly related to hemolysis incidents; the number of events were unclear in the later reports but the total of hemolysis-related deaths were stated to have increased to 14 cases by the end of 2014 ("INTERMACS Quarterly Statistical Report 2014 Q4," 2015). Katz et al. (Katz et al., 2015), suggested that the introduction of CF-VADs does not fully resolve the hemolysis problems, which still affect up to 8% of patients who

were under the device support for two years. Hence, it is still necessary for further studies to improve the devices and implantation methods.

Hemolysis index:

Hemolysis from medical devices such as the VAD with continuous blood flow can be evaluated by using either of two indexes outlined in the ASTM F1841-97 standard: the Normalized Index of Hemolysis (NIH), and the Modified Index of Hemolysis (MIH) (ASTM, 1998) (ASTM, 1998).

These indices are respectively expressed as:

$$NIH\ (g/100\ L\ blood) = \frac{\Delta fHb}{\Delta t}\frac{V}{Q}\ (1 - Ht)\ 100 \qquad [2\text{-}4]$$

$$MIH\ = \frac{1}{Hb}\frac{\Delta fHb}{\Delta t}\frac{V}{Q}\ (1 - Ht)\ 10^6 \qquad [2\text{-}5]$$

And the relationship between the NIH and MIH is given as the following equation:

$$MIH\ =\ NIH\ \frac{10^4}{Hb} \qquad [2\text{-}6]$$

Where: ΔfHb = Increase of plasma free hemoglobin concentration (g/L) over the sampling time interval

V = Circuit volume (L)

Q = Flow rate (L/min)

Ht = Hematocrit (%)

Δt = Sampling time interval (min)

Hb = Total blood hemoglobin concentration at time zero (mg/L)

The NIH index is often used to compare the blood damage generation rate across the devices.

2.3.4.2) Output Requirements

The VAD needs be able to provide sufficient head pressure to compensate for the pressure loss due to the weakened ventricle in all the degrees of heart failure and also must be able to provide sufficient perfusion during the different daily activities of the patients such as sleep, rest, exercise etc. Therefore, the pump is normally designed to have the head pressure the same as the systemic pressure (for

the LVAD) plus some additional pressure to compensate for the vascular resistance at the BEP point, while the flow rate for the CF-VAD typically refers to the average volumetric flow rate for normal people estimated at 5-6 L/min (Daniel Timms, 2005).

2.3.4.3) Size

The commercial VADs normally have a recommendation value for the appropriate patient's body size depending on the pump size and outflow performance. The blood pumps in the first generation are typically large and heavy, so that many of them required a minimum body surface area estimated 1.5m^2 which makes them ineligible for many women and children (Fuhrman & Zimmerman, 2011; Gagnon, Petty, & Lahpor, 2000; Tang et al., 2009). The rotary VADs' design allows the pump to be much smaller and more suitable for implantation even for the very small body size of pediatric patients.

2.4 COMPUTATIONAL FLUID DYNAMICS (CFD)

Computational fluid dynamics simulation is the use of finite element numerical methods to solve and analyse fluid mechanical problems. While it could be considered as a branch of fluid mechanics, it is particularly dedicated to the study of fluid dynamics or the fluid flow interaction with restriction surfaces and the influence of the fluid behavior such as heat transfer or chemical reactions in combustion flows.

CFD has been established since the 19th century in the form of fundamental mathematical equations that can describe the physical characteristics of fluid in motion, known as the "governing equations", but the complexity of geometry and boundary conditions require high computational power which limited the usage of these calculation techniques until the advancement of digital computers that became efficient, affordable and reliable enough for solving such complex flow equations in the early 20th century (Bates, Lane, Ferguson, John, & Sons, 2005). The advancement of CFD makes the simulation result accurate enough to be accepted as one of the three approaches in problem solving in fluid dynamics that traditionally

used only experimental and analytical methods and continues to be greatly relied on, particularly for complex flow analysis (Tu, 2007).

In the early era of CFD simulation, study was limited to the engineering area of aeronautics and astronautics which had large amounts of funding to acquire the powerful equipment to support problem solving; however, now it is widely adopted in many engineering fields because of the increase in computer power and performance as well as several other advantages compared to the traditional methods. These advantages are mainly the ability to provide highly detailed, visualized, and other comprehensive information that could substantially reduce lead times and the cost of production compared to the experimental based method. Meanwhile, it also offers the ability to solve complex flow problems that could not be achieved by the analytical approach. CFD also has the capacity for simulating flow that is not reproducible in an experimental test such as a dangerous chemical flow or a large event like a tsunami (Tu, 2007).

CFD has been used in VADs' development since the age of the first generation of pulse flow (PF) VADs (König, Clark, & Mokhtarzadeh-Dehghan, 1999; Medvitz et al., 2007; Moosavi, Fatouraee, & Katoozian, 2009; Okamoto, Hashimoto, Inoue, & Mitamura, 2003) and has become widely used in this field along with an increase in the popularity of the CF-VADs. In recent studies, CFD has been used to calculate hydraulic parameters such as the fluid forces on the rotor, torque and efficiency, including hydrodynamic related characteristics such as the vortex and stagnation in the flow fields, as well as shear stress for the prediction of hemolysis (May-Newman, 2010).

2.4.1 Geometry modelling of VADs

The simulation of VADs could be divided into the PF and the CF types of VADs that have different basic structures and require different approaches in simulating the flow.

2.4.1.1) Pulse flow VAD (PF-VAD) modelling

The CFD simulation of the PF-VADs is relatively complicated because it involves many moving parts and there is a large flow variation during the pump

cycle; thus, the pump models are often simplified to reduce the computational cost (König et al., 1999; Moosavi et al., 2009). The most difficult part to simulate in this type of pump is the flexible diaphragm which moves up and down in simulating the systolic and diastolic ventricle phase. Instead of actually moving the wall that requires a dynamic grid motion, several authors simulated the effect by directly injecting and removing the blood at the diaphragm surface. The inlet and outlet valves are other issues for CFD modelling that are difficult to replicate with the actual movement in the CFD model; thus, some authors assume that the valves are always in an open position and blood can flow freely in and out the chamber, but instead increase the fluid density to block the flow at the valve locations (Medvitz et al., 2007).

2.4.1.2) Continuous flow VAD (CF-VAD) modelling

Most of the recent VAD simulations have been conducted on the CF-VADs as they are the majority of the pump types under development. The fluid model, which is the computational domain of pump simulation, is normally divided into the stationary part and the moving part; the stationary domain comprises the fluid around the static surfaces like the inlet pipe, volute casing and outlet diffuser, while the moving or rotational domain reflects the movement of the fluid surrounding the pump rotor; however, some authors also further divide the stator and rotor into smaller subdomains for easier mesh generation and to reduce skewness (Selgrade, 2010; Selgrade & Truskey, 2012). The surfaces between the domains are specified as "domain interfaces" which provide connections between the domains (ANSYS, 2009).

2.4.2 Meshing scheme

The governing equations of the fluid flow and heat transfer in CFD are in the form of partial differential equations which are only available for the calculation of very simple cases. Therefore, the computational domains are divided into small subdomains with which the governing equations can be discretized and solved. These small subdomains are called elements while the collection of elements in the whole domain is called a mesh. The accuracy of a CFD simulation is strongly

dependent on the number of elements and increasing the number of elements will generally improve the accuracy of the computational solution. However, the trade-off of an increase in accuracy is the demand of computational power which is limited by the hardware performance and the calculation turnover time. Consequently, it is suggested that the mesh should be refined where the flow conditions change abruptly, while coarse meshes are used for the less complex regions for balancing the accuracy and the required resources (Tu, Yeoh, & Liu, 2013).

Aside from the element density in the domain, the solution accuracy is also influenced by the mesh quality. The type of mesh is one of the most important factors that affects the mesh quality and accuracy of the results as well as the computational resources required for the simulation.

2.4.2.1) Classification of mesh

The type of mesh can be categorized by either connectivity between the elements or the structure of the elements.

I. Connectivity-based classification

If it is classified based upon the connectivity, the mesh type can be either structured, unstructured or a hybrid mesh. The structured meshes are characterized by the regular connectivity between the elements, hence creating a uniform pattern of elements in the domain. A good alignment of the grid helps the solver to converge more easily, but it is not possible to fit this grid type onto some complex geometry.

The unstructured mesh is the type that has an irregular connectivity which has the advantage of better flexibility to fit onto most geometries and allows automated generation but it usually requires more cells and takes more time to converge. In addition to these mesh types, it is possible to apply the hybrid or mixed mesh which is a combination of both the structured and unstructured meshes. The structured meshes are normally applied to regular shaped geometries such as the inlet pipe or the diffuser while the unstructured meshes are used on the more complex areas such as the impeller blades (Kido et al., 2006).

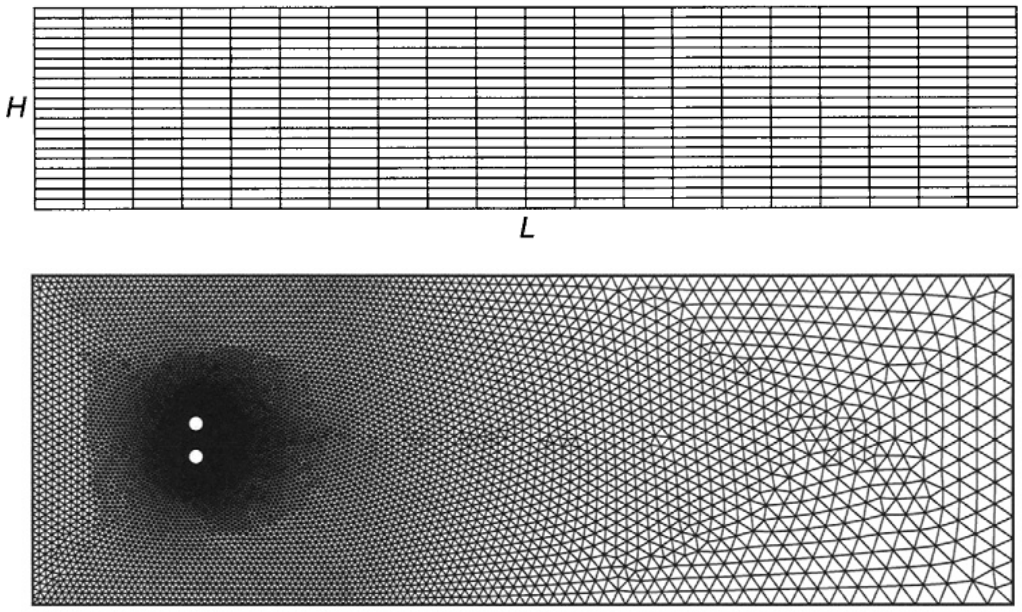

Figure 2-15: Structured mesh (top) and unstructured mesh (bottom) in 2D domain (Tu et al., 2013).

II. The element-based classification

Meshes of the CFD simulation could be generated in either 2-dimensional (2D) or 3-dimensional (3D) space depending on the type of the solving domain. For the 2D mesh, the elements are commonly formed in quadrilaterals or triangles. In the 3D element form, the common structures are hexahedral, tetrahedral, square pyramid and extruded triangles, as shown in Figure 2-16.

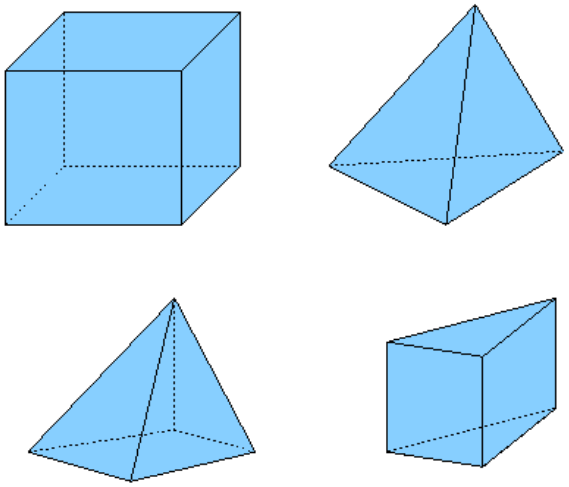

Figure 2-16: Common 3D mesh type for CFD analysis.

Much of the commercial CFD software has a module or function for mesh generation but limited to only the tetrahedral element type on either unstructured or hybrid cells that allows some degree of control over the element sizing, while there are some specialized grid generation packages that are specifically designed for turbo machinery application and could provide the structured meshes with a better mesh quality for the pump (Katharine H. Fraser et al., 2011). Both types of mesh generation tools could provide accurate results under the appropriate configurations. Currently, unstructured and hybrid mesh with tetrahedral and hexahedral elements has tended to become the more common option for CFD simulation in recent pump research for its flexibility and conformability to the complex geometry (Burgreen et al., 2004; Kido et al., 2006; Legendre et al., 2008; Taskin et al., 2010a; Zhou, Zhao, Lee, & Winoto, 2003). Good quality mesh can be generated without a requirement for manual control over the grid generation which is a time consuming process, especially for design comparison or selection that is usually involved with mesh generation and simulation of several different models at a time (Katharine H Fraser et al., 2012; Taskin et al., 2012).

2.4.3 Physical setup and boundary conditions

In order to accurately simulate the flow process in CFD, it is imperative to specify the physical parameters such as the fluid properties and flow environments. The items in the flowchart in Figure 2-17 highlight the various flow physics that often are considered for the simulation setup.

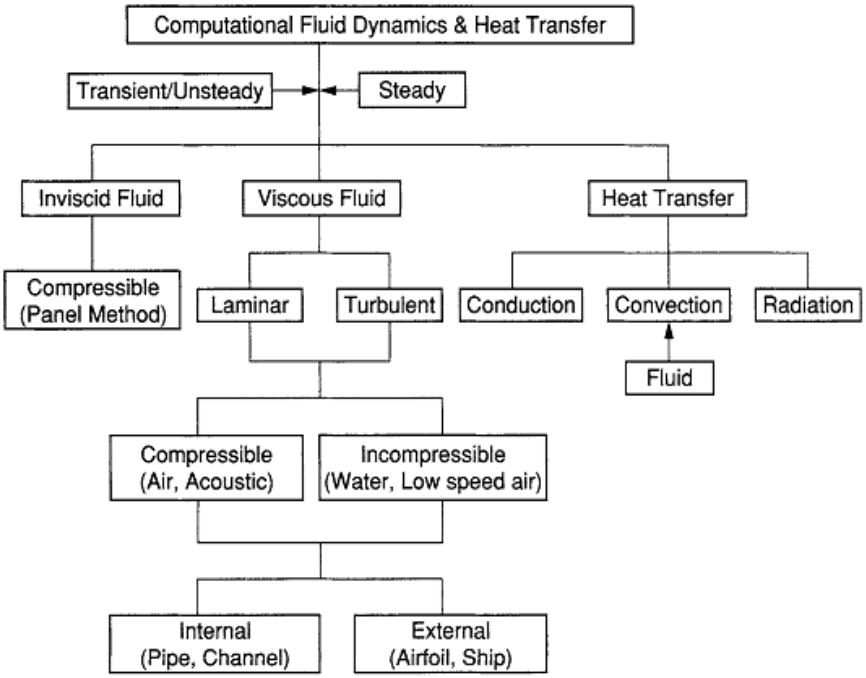

Figure 2-17: Flowchart of physics for the CFD configuration (Tu et al., 2013).

In the CFD application these physics items can be specified to the solver via several configuration options such as the frame of reference, fluid modeling, wall conditions, and boundary conditions.

2.4.3.1) Boundary conditions

Boundary conditions are the set of parameters applied to the domain surfaces to define the flow condition entering and leaving the domain, as well as the border of flow geometries such as the surrounding walls and internal obstacles within the domain (Tu et al., 2013).

For the heart pump application the inlet and outlet boundaries are often set to either flow velocity or pressure when the value of these parameters are set to mimic the flow condition of either the left or right heart support function, but the steady flow condition is commonly assumed for the inlet and outlet boundaries instead of applying time varying boundary conditions to simulate the pulsatility of the inflow blood. The boundary conditions of VAD simulations by different authors are summarized in Table 2-1.

Table 2-1: Boundary settings and turbulence models used by different authors in CFD simulation of CF-VADs.

Author and year	Pump Type	Application	Flow boundary conditions	Turbulence Model
Tsukamoto et al., 2000	Centrifugal	LVAD	Inlet : Q = 5.0 l/min, Outlet : P = 300 mmHg	k-ε
Apel et al., 2001	Axial	LVAD	Inlet = Constant velocity, Outlet = Static pressure	k-ε
Morsi, Yang, Witt, Ahmed, & Umezu, 2001	Centrifugal	LVAD	Inlet : Q = 6.0 l/min	k-ε
Song, Throckmorton, Wood, Antaki, & Olsen, 2003	Centrifugal	LVAD	Q = 6.0 l/min, H = 100 mmHg	k-ε
Song, Wood, Day, & Olsen, 2003	Centrifugal	LVAD	Inlet : Q = 6.0 l/min Outlet = Static pressure	k-ε / k-ω
Burgreen et al., 2004	Centrifugal	LVAD	Q = 3, 7, 10 l/min	- (Laminar)
Song, Throckmorton, Wood, Antaki, & Olsen, 2004	Centrifugal	LVAD	Q = 6.0 l/min, P = 100 mmHg	k-ε
Song, Wood, & Olsen, 2004	Centrifugal	LVAD	Inlet : Q = 2-10 l/min, Outlet: P = 20,000 Pa (150 mmHg)	k-ε
Untaroiu et al., 2005	Axial	LVAD	Q = 2-10 l/min, H = 80-160 mmHg	k-ε
Kido et al., 2006	Centrifugal	LVAD	Inlet : Q = 0.5-3l/min, Outlet: P = 0 Pa	SST k-ω
J. Zhang et al., 2006	Centrifugal	LVAD	Q = 1, 3, 5, 7 l/min	- (no information)
Throckmorton & Untaroiu, 2008	Axial	LVAD	Inlet : Constant velocity (Q = 0.5-4 l/min) Outlet : P = 20,000 Pa (150 mmHg)	k-ε
Masuzawa, Ohta, Tanaka, Qian, & Tsukiya, 2009	Centrifugal	LVAD	Q = 3, 5, 7 l/min	k-ε

Medvitz, Boger, Izraelev, Rosenberg, & Paterson, 2011	Centrifugal	LVAD	Q = 6 l/min	- (Laminar)
H. Wu, Wang, & Lv, 2011	Axial	LVAD	Q = 6 l/min, H = 100 mmHg	k-ε
J. Wu et al., 2012	Axial (Paediatric)	LVAD	Q = 1.5 l/min	SST
Selgrade & Truskey, 2012	Centrifugal	LVAD	Q = 4, 7 l/min	SST k-ω

2.4.3.2) Fluid modelling

For the CFD simulation, it is necessary to specify the accurate properties of the working fluid so that the solver can accurately calculate the flow behaviour including the interaction of the fluid to the surrounding boundaries. The basic properties of the fluid that typically need to be determined before conducting the simulation are phase, density, viscosity and compressibility, while other additional properties such as conductivity, specific heat and vapour pressure could be required depending on the level of details that are considered for the problem such as heat transfer, phase change or cavitation simulation. Therefore, the properties of human blood, which is a working fluid, for the heart pump need to be reviewed to accurately model the simulation.

Human blood is a complex fluid comprised mainly of liquid plasma which is the fluid matrix of blood making up about 55% of total blood volume. The main components of plasma are water, proteins, ions, and dissolved nutrients. Erythrocytes or so called red blood cells (RBCs) is the second major component in blood that accounts for about 45% of volume while the remainder (<1%) are leukocytes or white blood cells and platelets. RBCs have a biconcave disk shape containing enzyme and hemoglobin. The cell wall is a soft membrane that allows the cell to be remarkably flexible and able to compress into various shapes and squeeze through narrow capillaries during circulation. There are an estimated 5 million RBCs in a microlitre of blood, but the amount of RBCs is commonly expressed as a percentage of cells in total blood volume called **hematocrit** and is estimated in a typical range to be 40-54% for a human male (Silverthorn, 2014).

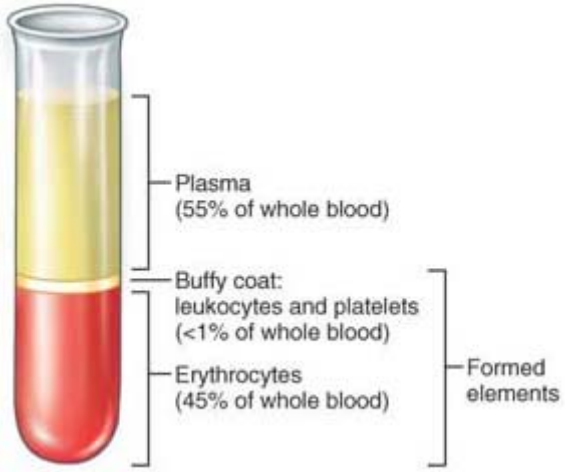

Figure 2-18: Human Blood Composition (Marieb & Hoehn, 2007).

From the fluid mechanics point of view, blood is a non-Newtonian compressible fluid which, nevertheless, expresses Newtonian behaviour when the exerted shear rate is above 100 s^{-1} (Wells & Merrill, 1961, 1962; Woodcock, 1976) and, as most of the CF blood pumps generate a higher shear stress than this threshold, it is commonly defined as incompressible in the CFD simulations. In addition, blood in modelling is normally simplified and assumed to be a pure substance to avoid the complexity of the blood composition. The density and viscosity are typically considered as bulk properties referring to the value of real blood with estimated ranges of 1,040 – 1,060 kg/m^3 and 0.0030 - 0.0036 Pa, respectively (Behbahani et al., 2009; Carswell et al., 2013; Kido et al., 2006; Masuzawa et al., 2009; Medvitz et al., 2011; Selgrade & Truskey, 2012; Song, Throckmorton, Wood, Antaki, et al., 2004; J. Wu, Paden, Borovetz, & Antaki, 2010).

2.4.3.3) Flow modelling

In fluid dynamics, the fluid flow can be categorised based on the velocity distribution and the motion path into laminar and turbulent flow types. At the low Reynolds number flow where the inertia forces in fluid flows are smaller than the viscous force, the disturbances that occur during the flow are overcome by viscous forces and dissipated away which allows the flow to be smooth without disturbance. This type of flow and is called *laminar flow*. The laminar flow is simple and smooth so its flow properties can be simply described using the continuity and momentum equations. However, at a high Reynolds number, the inertia forces can lead to a

large disturbance that becomes dominant and influences a random and chaotic flow motion described as *turbulence flow*. This type of flow is much more complex and harder to predict as it associated with a random swirling flow motion called eddies or vortices that cause random velocity fluctuation.

In the rotating pump, the flow regime can be identified by the Reynolds number calculated from the equation:

$$Re = \frac{\rho \omega D^2}{\mu} \qquad [2\text{-}7]$$

Where: Re = Reynolds number

ρ = Fluid Density

ω = Angular velocity of the impeller

D = Outer diameter of the impeller

μ = Fluid viscosity

For the rotating pump the transition from laminar to turbulence flow occurs around Re = 10^5 (Song, Throckmorton, Wood, Allaire, & Olsen, 2004) . The nature of the rotating blood pump involves a high impeller speed which causes high disturbance to the flow, and hence turbulence flow is typically assumed for the CF blood pump (May-Newman, 2010).

I. Navier-Stokes equations

The Navier-Stokes equations developed by Claude-Louis Navier and George Gabriel Stokes are a set of governing equations that are most commonly used to describe the motion of viscous fluid. The foundation of these equations is the conservation laws, specifically the conservation of mass, momentum and energy. It is useful for describing many flow applications in scientific and engineering interests as it could provide a description of the chaotic nature of turbulence flow, although it would require a large computational effort or some special technique for complex flow problems.

The main continuity equations in the stationary frame can be written as follows:

Conservation of mass

$$\frac{\delta \rho}{\delta t} + \nabla \cdot (\rho U) = 0 \qquad [2\text{-}8]$$

Conservation of momentum

$$\rho g - \nabla\rho + \nabla \cdot \tau_{ij} = \rho \frac{dU}{dt} \quad [2\text{-}9]$$

Conservation of energy

$$\rho \frac{dh}{dt} = \frac{dP}{dt} + \nabla \cdot (k\nabla T) + \phi \quad [2\text{-}10]$$

Conservation of scalar quantities

$$\frac{\partial(\rho\phi)}{\partial t} + \nabla(\rho\phi V) = \frac{dP}{dt} + \nabla \cdot (k\nabla T) + \phi \quad [2\text{-}11]$$

In addition to these main equations, fluid flow can be fully described with other additional equations in which the number or type of the equation needed depends on the required information, which may include the boundary data, heat flux, conservation of mass or an equation of state.

II. Reynolds average equations

There are several approaches to solving the Navier-Stokes equations for the simulation of turbulence flow. The method known to be the most accurate flow simulation and with the simplest concept is the Direct Numerical Solution (DNS) which directly solves the Navier-Stokes equations without using approximating or averaging parameters other than numerical discretizations (Ferziger & Peric, 1996; Tu et al., 2013). However, solving complex Navier-Stokes equations requires a large amount of computational power so it is not a practical approach for most applications.

Another method for modelling the turbulence is called the Large Eddy Simulation (LES) method, which focuses on solving the large scale eddy that is more dominant in turbulence flow. This method is much less costly than the DNS method but still too demanding for complex geometry and high turbulence flow (Tu et al., 2013).

In most engineering applications, only a few quantitative flow properties are of interest and need to be accurately identified. The high accuracy approaches like DNS and LES would waste more resources than necessary. Therefore the Reynolds-

averaged method that produces less information but sufficient engineering approximation values is often considered to be a more flexible option for the complex flow and hence has been the most popular approach for the turbulence simulation.

In this method, the time averaging of all the variables is used in the calculation to avoid the fluctuations in the flow properties. The Reynolds decomposition technique is used for this averaging calculation under the assumption that any flow property (ϕ) can be written as the sum of a time-averaged value ($\bar{\phi}$) and a fluctuation about that value (ϕ') (Ferziger & Peric, 1996):

$$\phi(x_i, t) = \bar{\phi}(x_i) + \phi'(x_i, t) \quad [2\text{-}12]$$

Where $\bar{\phi}(x_i)$ is the steady flow described as:

$$\phi(x_i) = \lim_{T \to \infty} \frac{1}{T} \int_0^T \phi(x_i, t)\, dt \quad [2\text{-}13]$$

For the unsteady flow, the averaged variables are described as:

$$\bar{\phi}(x_i, t) = \lim_{T \to \infty} \frac{1}{N} \sum_{n=1}^{N} \phi(x_i, t) \quad [2\text{-}14]$$

Where: t = unit of time

T = the averaging interval

N = the number of the members of the ensembles (must be large enough to eliminate the fluctuations)

With the Reynolds decomposition in equation [2-12] the instantaneous velocity $u_i(x, t)$ can also be expressed as the sum of the mean velocity and a fluctuation part (Figure 2-19) so that:

$$u_i(x, t) = U_i(x) + u_i'(x, t) \quad [2\text{-}15]$$

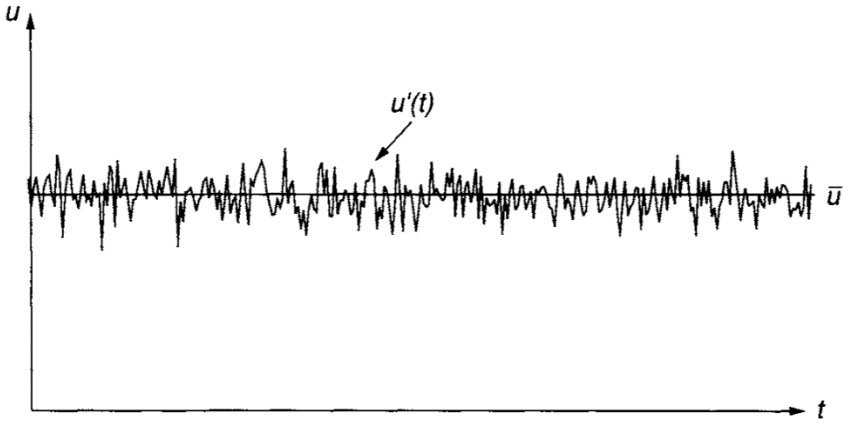

Figure 2-19: Velocity plot of turbulence flow compared to the steady mean velocity component (Tu et al., 2013).

Applying these averaged velocity components of the Navier-Stokes equations to the conservation of mass and momentum under the assumption of an incompressible and constant property flow yields the equation called a **Reynolds-averaged Navier-Stokes** (RANS) equation:

$$\rho \frac{\partial U_i}{\partial t} + \rho U_j \frac{\partial U_i}{\partial x_j} = -\frac{\partial P}{\partial x_i} + \frac{\partial}{\partial x_i}(\tau_{ij} - \rho \overline{u'_j u'_i}) \qquad [2\text{-}16]$$

Where: τ_{ij} = Viscous stress.

The term $\rho \overline{u'_j u'_i}$ in equation [2-16] has a fluctuating contribution to the non-linear acceleration terms and acts as though it was a stress, hence it is called the "Reynolds stress tensor" (George, 20013). Introducing this term results in six unknown quantities and, along with the pressure and three velocity components, there are a total of ten unknowns. However, the available equations are only the mass conservation and the three components of the RANS equation (equation [2-16]), which sum up to four equations in total. This means there are currently more unknowns than the available equations and the system is not closed or unsolvable (David C. Wilcox, 1998) . In normal problems, a straightforward solution would be to develop an extra partial differential equation (PDE) for each term from the original NS equations, but for this case it will introduce more correlations for the unknowns (Saad, 2011). Therefore, an alternative approach is to introduce an approximation to the Reynolds stress term, which is called the "turbulence model".

2.4.3.4) Turbulence model

There are several types of turbulence modelling to close the equations; one of the common approaches for CFD applications is the "eddy viscosity model" which assumes that turbulence consists of small eddies and the Reynolds stresses have a proportional relation to the mean velocity gradients, and the stress at a point of an interested time is the result of velocity everywhere from the past time to that certain point (Davidson, 2003; George, 20013). Therefore, the transport equations need to incorporate nonlocal and flow history effects of the eddy viscosity (μ_t); hence the turbulence kinetic energy, k, was chosen for the velocity scale in the energy equation (David C. Wilcox, 1998).

The eddy viscosity is described as:

$$\mu_{eff} = \mu + \mu_t \qquad [2\text{-}17]$$

Where: μ_{eff} = Local effective viscosity

μ = Local molecular viscosity

μ_t = Local turbulent viscosity

The turbulence kinetic energy relationship to the velocity scale is given as:

$$k = \frac{1}{2}\overline{u'_\iota u'_\iota} = \frac{1}{2}(\overline{u'^2} + \overline{v'^2} + \overline{w'^2}) \qquad [2\text{-}18]$$

Turbulence energy equation

To form the equation of turbulence energy, the Boussinesq eddy viscosity assumption was used to approximate the momentum transfer caused by the turbulence eddy. This assumption states that the Reynolds stress tensor, τ_{ij}, has a proportional relationship to the strain rate tensor, σ_{ij} , as follows:

$$\tau_{ij} = 2\mu_t\sigma_{ij} + \frac{2}{3}\delta_{ij}\rho k \qquad [2\text{-}19]$$

For the compressible flow σ_{ij} = 0, hence the equation is reduced and contracted to $\tau_{ii} = -2k$.

According to these assumptions, the equation of the turbulence energy and eddy viscosity was developed on the basis of the RANS equation in the following form:

$$\frac{\partial \rho k}{\partial t} + U_j \frac{\partial \rho k}{\partial x_j} = \rho \tau_{ij} \frac{\partial U_i}{\partial x_j} - \rho \varepsilon + \frac{\partial}{\partial x_j}\left[\left(\mu + \frac{\mu_t}{\sigma_k}\right)\frac{\partial k}{\partial x_j}\right] \qquad [2\text{-}20]$$

Where: ε = Eddy dissipation rate

σ_k = Closure coefficient.

The experiment results suggests $\sigma_k = 1.0$ (David C. Wilcox, 1998).

This equation is known as the "**turbulence energy equation**" which is an important equation that is used as a basis for all turbulence energy equation models.

The variable "ε" in this equation is the turbulence eddy dissipation which is defined as the dissipation rate of *k.* It could be assumed as:

$$\varepsilon \sim \frac{k^{3/2}}{l} \qquad [2\text{-}21]$$

Where: l = Turbulence length scale; describes the size of large eddies

There are two unknown parameters in this equation which are ε and l. The methods of approximating these variables are provided with the turbulence models.

In the eddy viscosity turbulence models, the method available for approximating the unknowns in the RANS equation could be categorized by the number of the additional PDEs that are used for closing the equations, which range from the zero-equation model which introduces no additional PDE to the two-equation model that adds two PDEs for solving the unknowns.

I. Zero-equation models (algebraic models)

As the name suggests, this approach does not employ any additional PDEs to describe the transport equation; instead, the turbulent viscosity or so called eddy viscosity is calculated as a global value from an algebraic equation as a product of a turbulent viscosity scale, U_t, and a turbulence length scale, l.

$$\mu_t = \rho f_\mu U_t l \qquad [2\text{-}22]$$

Where f_μ is a proportionality constant and the length scale is calculated from the formula:

$$l = \left(V_D^{1/3}\right)/7 \qquad [2\text{-}23]$$

Where: V_D = Volume of the fluid domain.

Solving the transport equations using the zero-equation models requires the least computational effort, but it is not recommended as it does not adequately incorporate the physical foundation of the system, and hence is not accurate enough for use in general flow problems, except only for simple flow geometries or as an initial computation for the more complex methods (ANSYS, 2009).

II. One-equation models

Prandtl's (Prandtl & Wieghardt, 1947) model is one of the most widely known original one-equation turbulence models. It solves the transport equation for a turbulent quantity using the turbulence dissipation, ε, which is the function of turbulence kinetic energy, *k*, and the length scale that is described as an estimated function in equation [2-21], but the closure coefficient, C_D, was introduced for the approximation as follows:

$$\varepsilon = \frac{C_D k^{3/2}}{l} \qquad [2\text{-}24]$$

Where: C_D = Closure coefficient. The empirical data estimate this value between 0.07 and 0.09 (David C. Wilcox, 1998).

l = Turbulent length scale.

The eddy viscosity is then described as:

$$\mu_t = k^{1/2} l = C_D k^2/\varepsilon \qquad [2\text{-}25]$$

Therefore, the turbulence energy equation from equation [2-20] can be written as follows:

$$\frac{\partial \rho k}{\partial t} + U_j \frac{\partial \rho k}{\partial x_j} = \rho \tau_{ij} \frac{\partial U_i}{\partial x_j} - \frac{\rho C_D k^{\frac{3}{2}}}{l} + \frac{\partial}{\partial x_j}\left[\left(\mu + \frac{\mu_T}{\sigma_k}\right)\frac{\partial k}{\partial x_j}\right] \qquad [2\text{-}26]$$

Where: σ_k = 1.0

III. Two-equation models

In this approach the transport equations are derived from two scalar parameters, the first value often relies on the turbulence kinetic energy while the second value could be turbulence length scale or another equivalent. The two-equation models that are often used in CFD simulation are the k-ε and k-ω models in which the second values are turbulence eddy dissipation (ε) and specific rate of dissipation (ω), respectively.

k-ε model

As mentioned above, in the k- ε model**,** the turbulence kinetic energy and the turbulence eddy dissipation are used to derive additional transport equations by relating to the turbulent viscosity (μ_t) as follows:

$$\mu_t = \rho C_\mu \frac{k^2}{\varepsilon} \qquad [2\text{-}27]$$

and expressed to the turbulent kinetic energy equation given in Equation [2-26].

$$\frac{\partial \rho k}{\partial t} + U_j \frac{\partial \rho k}{\partial x_j} = \rho \tau_{ij} \frac{\partial U_i}{\partial x_j} - \rho \varepsilon + \frac{\partial}{\partial x_j}\left[\left(\mu + \frac{\mu_t}{\sigma_k}\right)\frac{\partial k}{\partial x_j}\right] \qquad [2\text{-}28]$$

The second equation is written in terms of the dissipation rate as:

$$\frac{\partial \rho \varepsilon}{\partial t} + U_j \frac{\partial \rho \varepsilon}{\partial x_j} = C_{\varepsilon 1} \frac{\varepsilon}{k} \rho \tau_{ij} \frac{\partial U_i}{\partial x_j} - C_{\varepsilon 2} \rho \frac{\varepsilon^2}{k} + \frac{\partial}{\partial x_j}\left[\left(\mu + \frac{\mu_t}{\sigma_\varepsilon}\right)\frac{\partial \varepsilon}{\partial x_j}\right] \qquad [2\text{-}29]$$

Where the closure coefficients suggested by Wilcox (David C. Wilcox, 1998) are as follows:

$C_{\varepsilon 1}$ = 1.44, $C_{\varepsilon 2}$ = 1.92, C_μ = 0.09, σ_k = 1.0, σ_ε = 1.3

The k-ε model is one of the most widely used turbulence models for CFD simulations in various fields of study, including the CF heart pump simulation (Table 2-1), with many successful results with validations. It is known for its robustness, ease of implementation and being computationally cheap. However, the major weakness of this model is the lack of sensitivity to the adverse pressure gradient and strong flow separation as well as low performance in analysing the viscous sublayer (Davis, Rinehimer, & Uddin, 2012; Florian R Menter, 1993; F. R.

Menter, 1994). With these pros and cons, the k- ε model is suitable for design comparison and optimization which are involved with comparing several conditions or geometries, while it should be avoided for implementation on an application with a drastic pressure gradient.

k-ω model

The standard k- ω model was originally developed by Wilcox (David C Wilcox, 1988; David C. Wilcox, 2008) . As well as the k-ε model, it attempts to predict turbulence by two PDEs and also solve the turbulence kinetic energy, *k*, as a first parameter, but it introduces ω which is described as "the rate of dissipation of energy in unit volume and time" (David C. Wilcox, 1998) or the so called **specific dissipation rate** or **turbulent frequency** as the second parameter in the model.

The relation of k and ω with the eddy viscosity is written as:

$$\mu_t = \rho \frac{k}{\omega} \qquad [2\text{-}30]$$

For this model, the turbulence eddy dissipation is related to the specific dissipation rate, ω, as follows:

$$\varepsilon = \beta' k\omega \qquad [2\text{-}31]$$

Therefore, the turbulence kinetic energy equation [2-26]) can now be written as:

$$\frac{\partial \rho k}{\partial t} + U_j \frac{\partial \rho k}{\partial x_j} = \rho \tau_{ij} \frac{\partial U_i}{\partial x_j} - \rho \beta' k\omega + \frac{\partial}{\partial x_j}\left[\left(\mu + \frac{\mu_t}{\sigma_k}\right)\frac{\partial k}{\partial x_j}\right] \qquad [2\text{-}32]$$

And the second equation to describe the specific dissipation rate is:

$$\frac{\partial \rho \omega}{\partial t} + U_j \frac{\partial \rho \omega}{\partial x_j} = \alpha \frac{\omega}{k} \rho \tau_{ij} \frac{\partial U_i}{\partial x_j} - \beta \rho \omega^2 + \frac{\partial}{\partial x_j}\left[\left(\mu + \frac{\mu_t}{\sigma_\omega}\right)\frac{\partial \omega}{\partial x_j}\right] \qquad [2\text{-}33]$$

Where the model coefficients are given as (ANSYS, 2009):

$\beta' = 0.09$, $\alpha = 5/9$, $\beta = 0.075$, $\sigma_k = 2.0$, $\sigma_\omega = 2.0$

This model performs better in predicting the complex boundary layer flows under an adverse pressure gradient, so it is suitable for external aerodynamics and turbomachinery with a large pressure difference. However, implementation is slightly more complex and more computationally costly as it requires a fine mesh resolution near the wall; moreover, the prediction of separation tends to be early and overestimated.

SST k-ω model

The SST k-ω model is a variation of the k-ω model developed by Menter (Florian R Menter, 1993). It is the combination of the k-ε and k-ω by employing the k-ω formulation in the viscous sub-layer and switching to the k-ε in the free stream.

The k-ε, k-ω and SST k-ω models have been used in VAD studies and have all been reported to have successfully predicted the flow in the pump, but yet there is no study that conducts a full investigation or provides the standard to compare the accuracy between these models. Song et al. (Song, Wood, et al., 2003) suggested that the flow visualization plot from the k-ω model in the near-wall regions has better agreement with the particle image velocimetry results than what is observed from the k-ε model. However, Throckmorton et al. (Throckmorton & Untaroiu, 2008) later made a suggestion, based on their verification data of a miniature axial blood pump, that the bulk flow parameters from the k-ε model correlated more closely to the experimental results than the SST k-ω model.

2.4.4 Unsteady Flow and the Moving Domain

In the operation of CF-VADs, the change of flow rate and pressure including the rotation of the impeller causes the flow and hydraulic forces variations to the pump. These variations of the in-flow properties can be simulated by either applying the time varying boundary conditions in the transient analysis or using the average flow condition in the steady state simulation.

The motion of the CF-VAD impeller is generally limited to the rotation about the axis and there are two approaches available for the calculation of the

moving domain; these are the **multiple frames of reference** (MRF) and **sliding mesh** methods. The MRF method does not physically move the grid of the moving domain but instead approximates the impeller motion using the relative velocity between the static and rotating domains under the assumption of constant velocity; therefore, this method is used on the steady state simulation. The sliding mesh method has a different approach for solving the rotating domain by updating the mesh position periodically based on the defined time step, so it is used for modeling the transient effects (Katharine H. Fraser et al., 2011).

In order to find the necessity of the transient settings in the CF-VAD simulation, Song et al. (Song, Throckmorton, Wood, Allaire, et al., 2004) conducted a series of simulations comparing between a steady state simulation and three transient simulations in the first of which the condition simulated blade rotation under the average inlet flow using a sliding interface technique on the rotor (Transient Rotational Sliding Interfaces - TRSI) , while in the second the condition incorporated a time varying inlet volumetric flow rate (time varying boundary condition - TVBC) over one heart cycle, and, finally, in the third the condition combined both the TRSI and TVBC so that it simulated the closest condition to the VAD operation in the heart pulse environment. The results showed that the disturbance of the flow and forces caused by the varying inlet flow rate were insignificant, however the effect of blade rotation in the TRSI setting was much greater and shows a significant influence over the results.

Despite the large effect of the flow variation from the impeller rotation, there are very few studies which have adopted the transient model for CF-VAD simulations (Burgreen et al., 2004; Chua, Song, Lim, & Zhou, 2006; Curtas et al., 2002; Morsi et al., 2001; Yamane, Miyamoto, Tajima, & Yamazaki, 2004) as most of the VAD studies use a CFD simulation as a preliminarily overview of the pump geometry designs and the steady state could provide sufficient information with lower computational resources.

2.4.5 Blood damage model

As previously discussed, blood damage is one of the major concerns for pump design that should be optimised during the design and evaluation phase of

development; it is, however, one of the most difficult factors to assess because of the large biological diversity and chemical properties that could easily be affected by a small variation in the test conditions or handling during blood preparation, and hence the test results are almost non-reproducible. Moreover, the blood damage generation of the devices is typically evaluated in the test loop that needs a large volume of testing fluid to operate, and human blood would be ideal for obtaining an accurate result; however, it rarely is available in a large enough quantity for the experiment, hence animal blood, such as bovine, is often the preferred option for most studies (Katharine H Fraser et al., 2012; Goubergrits & Affeld, 2004; Gu & Smith, 2005; Song, Throckmorton, Wood, Antaki, et al., 2004; T et al., 2003; Taskin et al., 2012; T. Zhang et al., 2011). However, the blood of different animal species has difference rheological properties and RBC membrane fragility (Jikuya, Tsutsui, Shigeta, Sankai, & Mitsui, 1998) which could cause a large variation or error in the results. Therefore, there have been several attempts to govern the transport equation to predict the breakage of RBC for the CFD simulation to compare the damage during design optimization without having to undertake the complications in the experiment.

The first model for damage calculation in artificial organs, which was widely accepted and became the foundation of many later developed models, was proposed by Giersiepen et al. (Giersiepen, Wurzinger, Opitz, & Reul, 1990). It was a power law established on empirical data obtained by Wurzinger et al. (Wurzinger, Opitz, & Eckstein, 1986) under the assumption that blood damage is only dependent on shear stress and exposure time, and it is formulated as:

$$D = \frac{dHb}{Hb} = C\,\tau^{\alpha} t^{\beta} \qquad [2\text{-}34]$$

Where : D = Damage fraction

dHb/Hb = Ratio of plasma free hemoglobin to total hemoglobin

τ = Shear stress

t = Exposure time

C, α, and β denote constants which have the values originally proposed by Giersiepen as $C = 3.65 \times 10^{-5}$, $\alpha = 2.416$ and $\beta = 0.785$. This set of constants has been widely used but is also thought to be overestimated (Grigioni et al., 2004), hence it has been

replaced several times by some investigators for different applications and conditions; one of the most widely used sets is proposed by Heuser et al. (Heuser & Opitz, 1979) with the values of 1.8×10^{-8}, 1.991 and 0.765 that are available for $t < 0.6$s and $\tau < 700$ Pa. However, Wu et al. (J. Wu et al., 2010) conducted a simulation and experiment on centrifugal blood pumps comparing Giersiepen and Heuser's constants and found that both models yield no significant difference and could closely estimate the value of hemolysis generated by the heart pump.

In CFD simulation of VADs, this power law is also widely implemented for the estimation of blood damage generated from the devices via the post processing techniques. The implementation of a blood damage model can be categorized by the frame of reference in either Lagrangian or Eulerian coordinates. The Lagrangian method relies on calculating the shear stress exerted on each individual blood cell particle as it flows through the device, while the Eulerian method considers the damage over the whole domain at a certain point of time.

I. Lagrangian method

The blood damage estimation using the Lagrangian method could be done by the particle tracking technique which releases particles at the inlet of the pump and integrates the damage function along the pathlines; then, the total blood damage is calculated from the average damage to the individual particles. Since each blood cell particle could have a large variation in the shear stress and exposure time due to the various numbers of trajectory paths in many different flow channels, the accuracy of this method is dependent on the number of the tracked particles where the more particle numbers could cover more possible trajectories of the cell and hence more accuracy of the result. In a recent study, it was found that an estimated 1,100 particles are sufficient for the calculation in the blood pump (Taskin et al., 2012) ,but this number could be varied with different sizes of the device.

According to Giersiepen's power law model in Equation [2-34], the total damage along the pathline from the inlet to the outlet of the device can be calculated as follows:

$$D = \int_{inlet}^{outlet} C \cdot dt^{\alpha} \cdot \tau^{\beta} = \sum_{i=1}^{N} C \cdot \Delta t_i^{\alpha} \cdot \tau_i^{\beta} \qquad [2\text{-}35]$$

Where: N = Number of observation points along the pathline.

t_i = Time that the particle spent from the starting point to reach the ith observation point.

This equation has been adopted by several authors with various sets of constants (W. K. Chan, Wong, Ding, Chua, & Yu, 2002; Mitoh et al., 2003; Pinotti & Rosa, 1995; Song, Throckmorton, Wood, Antaki, et al., 2004; T et al., 2003; J. Wu et al., 2012; Y. Zhang et al., 2008). However, Grigioni et al. (Grigioni et al., 2004; Grigioni, Morbiducci, D'Avenio, Benedetto, & Gaudio, 2005) suggested that the method of summing the individual damage along the pathline with Equation [2-35] could not reflect the cell with sub-lethal damage that may later be destroyed under the sustaining shear stress. Therefore, Equation [2-36] which could add up the damage contribution as the erythrocyte moves along the pathline was proposed:

$$D = \sum_{i=1}^{N} Ca \left[\sum_{j=1}^{i} \tau(t_j)^{b/a} \Delta t \right]^{a-1} \tau(t_j)^{b/a} \Delta t \qquad [2\text{-}36]$$

The accuracy of these 2 equations was compared by Fraser et al. (K. H. Fraser, Taskin, Zhang, Griffith, & Wu, 2010) using both the centrifugal and axial types of blood pump and using Taskin's constant set. The results from the centrifugal pump simulation showed that Equation [2-35] yields less than a 10% error compared to the experimental results while Equation [2-36] over-predicted the hemolysis for this pump. It is unfortunate that the results from the axial pump in this study were not clearly reported, thus it is not possible to verify whether the hemolysis prediction was accurate for the different shear range.

Another hemolysis estimation method on the Lagrangian frame that takes the shear loading history into account was proposed by Goubergrits et al. (Goubergrits & Affeld, 2004). This method modified Giersiepen's power law model (Equation [2-34]) by dividing the pathline into small increment time steps, so that the shear stress can be assumed to be constant in each step. The damage index D along the pathline can then be given by:

$$D\ (t + \Delta t) = C \cdot \left(t_{eff} + \Delta t\right)^{\alpha} \cdot \tau(t + \Delta t)^{\beta} \qquad [2\text{-}37]$$

Where t_{eff} is defined as a virtual time step which can be calculated as:

$$t_{eff} = \left(\frac{D(t)}{C \cdot t(t + \Delta t)^{\beta}}\right)^{\alpha} \quad [2\text{-}38]$$

The C, α and β constants in this model were based on the original Giersiepen's constant; however, the experiment by Taskin et al. (Taskin et al., 2012) shows that it considerably over-predicted the damage on both the axial and centrifugal pump while Heauser's constant set yielded closer results but they were still slightly lower than those obtained from the actual experiment.

The accuracy of this method depends on the number of particles that are released to the pump but it takes more computational power as more particles are tracked.

II. Eulerian method

In the Eulerian approach, the damage index is calculated by an integration of the damage function over the entire fluid domain which is usually done by transforming the equation from the Lagrangian to the Eulerian frame. This approach generally requires less computational power than the Langrangian method as it is not required to calculate the particles' trajectories, and the accuracy of damage prediction is hence relying on the mesh structure.

Garon and Farinas (Garon & Farinas, 2004) proposed the hemolysis estimation method based on Giersiepen's empirical model in Equation [2-34] with the original constant set, by proposing the linear damage (D_I) as follows:

$$D_I = D^{1/0.785} = (3.62\ x\ 10^{-7})^{1/0.785}\ \tau^{2.416/0.785}\ t \quad [2\text{-}39]$$

This equation was formed from the experimental results of blood exposed to different levels of constant shear stress and exposure time. Therefore, it could be simplified by the time derivative to remove the time dependency and thus the equation could be transformed from the Lagrangian to the Eulerian frame under the assumption of incompressible fluid, resulting in the average linear damage generated by the device ($\overline{D}_I$) :

$$\overline{D}_I = \frac{1}{Q} \int_V \sigma \, dV \qquad [2\text{-}40]$$

Where: V = Finite volume

σ = Scalar shear stress

In the Eulerian frame, the damage D from the device is then given by:

$$D = (\overline{D}_I)^{0.785} \qquad [2\text{-}41]$$

This study also gives the relation of the damage function D and the normalised index of hemolysis (*NIH*) which is available when the quantity of plasma-free haemoglobin is small in relation to the amount of total haemoglobin by reducing Equation [2-4] to:

$$NIH = Hb \times D \times 100 \qquad [2\text{-}42]$$

This hemolysis calculation approach was employed by several research groups for blood pump developments (Medvitz et al., 2011; J. Zhang et al., 2006), and yields close results to the experimental measurement of hemolysis conducted by Taskin et al. (Taskin et al., 2012).

The calculation of blood damage with this approach is conducted in the post-processing, therefore it can be done without adding to the computational load required during the simulation process. However, the drawback is it that it cannot identify the location of the damage source because it only provides a global index over the whole device.

Another hemolysis estimation method in the Eulerian frame is proposed by Taskin et al. (Taskin et al., 2010b) which introduced a scalar function of plasma-free haemoglobin ($\Delta Hb'$) that is defined as:

$$\Delta Hb' = \Delta Hb^{1/\alpha} \qquad [2\text{-}43]$$

And the scalar transport equation is formulated as follows:

$$\frac{d(\Delta Hb')}{dt} + v\rho\nabla(\Delta Hb') = S \qquad [2\text{-}44]$$

Where S in the above equation is the source term which is defined as:

$$S = \rho\,(Hb \cdot C\,\tau^{\beta})^{1/\alpha} \qquad [2\text{-}45]$$

Along with the new hemolysis model, Taskin et al. also obtain a new set of constants from the experiment on the shearing device from bovine blood as C = 1.21 x 10-5, α = 0.747 and β = 2.004. The damage index (*D*) of the device could then be calculated from the mass-weighted average of Hb at the outlet divided by Hb.

This hemolysis model calculated the post-processing process as well as Garon and Farinas' model, but its advantage is that it can directly provide localized information on the high hemolysis regions which is valuable information for the design optimization of the devices. However, the validation of this model on the experimental results that was later conducted by Taskin et al. (Taskin et al., 2012) with three different set of constants found that it had made a considerable over-prediction. Fraser et al. (Katharine H Fraser et al., 2012) later optimized this model by suggesting a new set of constants: C = 1.745 x 10^{-6}, α = 1.963 and β = 0.7762 which could greatly improve the accuracy of the hemolysis prediction for both the centrifugal and axial pump designs.

Comparison of Lagrangian and Eulerian approaches

The comparative investigation and experimental validation of the three Lagrangian and two Eulerian approaches reviewed here were conducted by Taskin et al. (Taskin et al., 2012) with three different sets of constants (proposed by Giersiepen's, Heauser's and Zhang's constants) on an axial blood flow shear device that was designed based on the Jarvik 2000 heart pump and the Centrimag heart pump. However, for the Garon and Farinas' model, the authors used the nonlinear damage form (equation [2-39]) in the Langragian frame in the study; hence, the result of the Eulerian model (equation [2-40]) was not confirmed.

According to the results, Giersiepien's model (equation [2-34]) tends to predict the highest hemolysis value compared to the other models in both pump designs, while the rest of the models (equations [2-35], [2-36], [2-37], [2-39] and

[2-44]) give smaller difference values between the models. The accuracy of the blood damage prediction in this study was greatly affected by the constant used with the model. Giersiepen's constants overestimated the damage as well, as was seen in other previous studies, while Heauser's constants have overall results slightly closer to the experiments than Zhang's set of constants.

All the available damage models presented too large a percentage of errors to be viable options for the damage prediction of the device, as the minimum error from the Lagrangian method was 57% while it was as high as 91% in the Eulerian method. Furthermore, the prediction results from these studies also show a different percentage of error compared to the model validation in other studies (K. H. Fraser et al., 2010; Gu & Smith, 2005; Song, Throckmorton, Wood, Antaki, et al., 2004), which could be caused by variation of the blood handling and the testing procedures that are uncontrollable (Goubergrits & Affeld, 2004); moreover, currently there is no standard procedure available for the blood shear test. However, it is still possible to use these simulation methods for the relative prediction of hemolysis in the comparative studies such as the design optimization or ranking the damage generation of different heart pumps.

2.5 REVIEW SUMMARY

The number of heart failure patients has been increasing and has become one of the greatest global healthcare concerns, while the effective treatment for severe cases is still limited to the heart transparent which is greatly restricted by the availability of donor hearts. The VADs have become an alternative option to relieve the requirement for heart replacement with the flexibility to support both sides of ventricle failure, although use as a biventricular support still faces complications as it requires two devices to be implanted. Long-term clinical trials have confirmed the advantages of VADs over medical therapy for sustaining patients in temporary support for the BTT and BTR while having the potential to become the preferable option for use as a permanent support or DT in the near future.

The recent development of VADs has been focusing on improving the reliability and hemodynamic capability to increase the device’s life span while attempting to reduce the pump size to be implantable in the small body of a

paediatric patient. The review has included the essential design concerns that need to be considered for heart pump development, starting with the mechanical durability which has improved from the pulse generation mechanism used at the dawn of VAD development to a more reliable rotating impeller and, eventually, a magnetically levitating impeller that completely removes the mechanical wear and that has been in development and is in clinical trials at present. The hemolysis or blood damage generation from the pump is also a major concern as it is still a major contributor to the problematic incidents that reduce the survival rate of long-term patients. It is caused by the exposure of RBC to the excessive shear stress over the period of time. In the CF pump this shear stress generation is related directly to the blade design and the impeller's rotating speed, so the high risk regions, such as the leading edge of the impeller and the volute tongue, must be carefully designed and a design with a lower specific speed would be more preferable. Another hemodynamic concern is thrombosis or blood clot that is likely to form in the recirculation and stagnation region of the pump and could cause a performance drop or mechanical failure and could be lethal if the clot breaks free into the blood stream; hence, flow visualizations are typically employed to ensure that recirculation and stagnation are not present in the pump.

This literature review included a comparison between two common designs of the current generation of CF VADs, the axial flow and centrifugal pumps. The axial flow pump has a more compact design but the trade-off is a lower capacity and performance, so that it requires a much higher pump speed than the centrifugal pump to deliver the same head and flow rate. This also leads to a higher risk of mechanical wear if the pump has a contact surface or bearing, and also increases the chance of shear stress induced hemolysis; so, the centrifugal pump tends to be a more preferable option for the design of a VAD that is aimed for long-term support.
In the development of the heart pump, CFD has proved to be a powerful tool that provides the detailed results that cover most of the design aspects from hydrodynamic estimation to hemolysis and thrombosis prediction, as well as design selection and optimisation. Employing CFD for heart pump development could help to save costs and time by reducing the number of prototypes required for initial evaluations; hence, the latter part of this literature review outlined the current use of

CFD for VAD design and the simulation techniques for heart pumps to effectively obtain significant information from the CFD simulation.

The CFD analysis of VADs starts with creating the fluid model that reflects the fluid domain within the pump. For the CF-VADs, the model is typically divided into the rotating domain, which is the fluid within and around the impeller hub, and the stationary or other areas in the pump. The domain is then subdivided into smaller elements with the mesh generation process to simplify the model for the numerical calculations. The unstructured mesh offers better flexibility over the complex geometries and allows automatic generation with some degree of control over the element size, so it is often preferred for the VAD simulation, but some prefer the hybrid mesh for better element quality.

The pre-processing or simulation setup is one of the most important stages that greatly influence the accuracy of the simulation results. The physics set up for the flow problems could be done via the configuration of boundary conditions, fluid properties, turbulence model and frame of reference. From the literature review, most of studies have been focusing on LVAD simulation, and the boundary conditions are typically set to the BEP of the pump while some also included the off-design conditions by varying the flow rate and pump speed. The properties of blood in the simulation are usually assumed to be incompressible according to the high shear stress within the pump, and are considered as a pure substance for simplicity.

The rotation of the impeller in CF-VAD causes high disturbance to the fluid flow, hence the turbulence flow nature is common in most pumps. The Navier-Stokes equations that are commonly used to describe the flow could also predict the turbulence flow model with a great amount of detail. However, solving the equations in a 3D frame within the complex geometry of a heart pump is a huge computational demand and hence impractical. Consequently, the Reynolds-averaged method is typically employed to obtain the approximated value of the relevant parameters which could reduce the computational load with the trade-off of a lower accuracy but which is still sufficient for the engineering applications. However, this approach leads to the situation where the equations could not be closed as there are more unknown variables than the available equations. To resolve this problem, the

turbulence models technique has been used for calculation of the unknown Reynolds stress term. The type of models has been classified by the number of additional transport equations introduced for the calculation. This review discussed the turbulence models with emphasis on the two-equation model as it can sufficiently describe the physics of flow and has many verification studies which support the accuracy of the calculation. The k-ε model is commonly used for heart pump simulation because of its robustness and ease of implementation, while the limitation of this model is that the drastic change in pressure gradient does not impose on the low pressure head in the heart pump. Another model discussed in this section was the k-ω; this model, and its variations, was also implemented in some studies for its strength in the accuracy of the near-wall region but it requires higher computational power for the near-wall mesh resolution. The weakness of this model lies in the prediction of the flow separation regions which tend to be overestimated. The pulsatile nature of blood flow and the fluctuation from impeller rotation could affect the solution results. The transient simulation with a time varying boundary condition could closely simulate the flow effect at a high computational cost, so the magnitude of the effect from different configurations of the transient simulation was compared against a steady state simulation. The review supports the use of the sliding mesh method of transient simulation with the steady state, as the effect of fluctuation from the blades appears to be significant to the results. However the steady state is more widely used for its lower computational resources despite the lower accuracy.

The method of hemolysis estimation has been thoroughly discussed as it is one of the major design concerns that are difficult to accurately predict. The damage models are established on either the Lagrangian or Eulerian frame of reference, where the Lagrangian method computes the blood damage from the shear stress exerted on the sample particles that flow through the pump while the Eulerian method focuses on the calculation of shear stress on the elements over the whole domain. With several results for comparison and validation, both methods still present a large error as neither could reflect the actual damage from the pump, but the calculation methods are still valuable for design comparison and optimization to reduce the risk of damage generation from the heart pump.

2.6 CONCLUSION

According to the literature review, it is clear that a VAD is a strong alternative for CHF patients as it is more effective than the optimal medical treatment and more flexible than heart transplantation. Improvements in mechanical reliability and hemocapability could reduce the limitations of the current long-term blood pump.

CFD is an important tool to achieve the objectives of new heart pump design and development and helps to predict the design issues, so it is possible to create several pump designs and use the information from CFD to select the best optimum design that suits the requirements without having to produce several working prototypes for actual comparison. The selected design can then be further analysed in greater detail for further optimisation to obtain the best hydraulic performance and minimise the risk of hemolysis and thrombosis before making a prototype for experiments.

From the literature review, it is notable that the VADs are commonly designed for the left ventricle support function, although some are capable of providing the right ventricle support by lowering the pump speed, and there are very limited studies on the BiVAD as a single module. It could prove to be useful if the pump is carefully designed to equally support both sides of the ventricles with the assistance of CFD simulation to provide an insight into the pump geometry.

To complete the development process, the human mock circulation loop is still required for the verification of the final pump design which is the final stage in the scope of this research. Beyond this stage it will involve the development of the driving, controlling and suspension mechanism before in vitro tests in animals and clinical trials which are the last stage in the VAD development cycle.

Chapter 3: Design and Development of the VAD

This section is about the design concept and optimisation of the BiVAD and the CFD simulations to predict the hydrodynamic and hemodynamic performances for the design of a working pump ready for verification and the evaluations within the human mock circulation loop.

3.1 INTRODUCTION

Turbo machinery has long been used in industrial and general pump applications. However, the development of these pumps focuses only on the hydraulic performance aspects such as improving the efficiency at the pump operating point. The requirements are different for ventricular assist devices which have more factors to consider, including hemocompatibility which is highly significant as the blood is a sensitive fluid with complex properties that could affect the patient's circulatory system. To achieve the hemodynamic requirements, the heart pump needs to be carefully designed to avoid causing high shear stress that could damage the red blood cells and cause blood trauma, which is not a major concern in general pump design. Damage to blood may lead to thrombus formation and could be fatal to patients if it breaks free into the blood stream and migrates to vital organs.

The variation in pump operating conditions is also an important factor which makes the design of a VAD more complicated. In general application, pumps are usually designed to operate at the best efficiency point (BEP) where they have the highest efficiency while also being least prone to failure. The VAD operating condition, however, is hard to determine as it is greatly varied by many uncontrollable functions. These variations are caused by flow variation due to the pulsatility nature of the heart's cycle, or the degree of heart failure which requires a different level of support for each individual patient. The requirement is also caused by the physiological requirements of basic daily activities such as sleep, rest or exercise. In some cases, the heart condition of a patient with VAD support could

worsen, and the pump would need to be able to be adjusted to provide sufficient support for the patient's perfusion needs. Meanwhile, if the patient's heart recovers, the pump also needs to be able to respond to the changes and reduce the level of support accordingly. Aside from these variations in operating conditions, the VAD design aims to cover a wide range of operations to function as an LVAD and RVAD to be able to support both the left and right ventricle with the same pump model or to function as a BiVAD which supports both sides at the same time.

The VADs that are designed for long term support such as bridge to transplantation (BTT), bridge to recovery (BTR) or destination therapy (DT) are expected to be implantable so that the patients can carry on their daily activities while under the support of the device. Therefore the size of this type of pump needs to be small enough to fit into the patient's pericardial cavity or abdomen; meanwhile, it also needs to have a strong structure and a reliable mechanism that could extend the pump's life expectancy without requiring any internal maintenance of the pump.

With all these sensitive requirements, it usually takes a long time for the development of the pump and requires a lot of expense to carry out the heart pump development. The pump's initial design needs to be evaluated and optimized many times with much trial and error in the process to produce an effective prototype. The pump needs to pass both in vivo and in vitro tests before it could be used in a clinical trial. A new pump design often takes a few years of clinical trials before it can be approved for real clinical use and commercial production.

CFD is a powerful tool for fluid flow analysis that could be adopted for the heart pump development to reduce the time and cost from design initiation to prototype evaluation. It can be used to provide details of the pump flow and helps the designer to predict the pump's performance, compare the flow dynamics between difference choices of designs, and identify the flow problems that might occur in the pump. The information obtained from CFD simulation is not limited only to the hydraulic pump's performance, but it is also possible to use it to analyse the hemodynamic parameters such as blood damage and thrombosis which are design concerns for heart pump development. With this information, the designer can investigate the different design choices without having to go through the long and repetitive work of trial and error on real prototypes, which is a time and resource

consuming process. In addition to the use of CFD to establish the working prototype, it can also be used to provide information for the design optimization throughout the rest of the final stages in the development process, like making minor refinements that might help to improve the pump's performance during the in vivo or the clinical trial stages.

To achieve the aim of this thesis, this chapter describes the design of the BiVAD in aiming to achieve all the requirements of the heart pump's functions, as described above, with the employment of CFD techniques to analyse the pump's performance. The design was then modified to operate on the single-sided motor as a prototype for the performance evaluation in the test rig, by taking advantage of the symmetrical design of the LVAD and RVAD. This modification yields a single-sided pump that can work in both the left and right heart support applications, while the information from this evaluation could be used for the full prototype of the BiVAD in the future.

3.2 STRUCTURE OF THE VAD

3.2.1 VAD Design background

As discussed in Chapter 2, the third and later generations of heart pumps are commonly built on an axial flow or a centrifugal pump as the pulse generation mechanism has proved to be not necessary. Each type of pump has different advantages that need to be considered for the design of the VAD. The axial flow pump structure offers the advantage of compact size with the same performance; however, the trade-off is a very high impeller rotating speed which could cause excessive shear stress and thus blood damage. The life span of the pump is also shorter because of the mechanical wear if there is any contact with the surface or seal (Kafagy & Gitano-Briggs, 2013b). For all these reasons, the centrifugal pump is a more preferable choice for long term usage for the heart pump which is required to be durable and to generate minimum blood damage.

The design of the centrifugal VAD is based on the general centrifugal pump; however, the pump's requirements are not only dependent on the hydrodynamic performance like the net positive suction head (NPSH), radial or axial thrust, but also

on the hemodynamic effects such as shear stress induced blood damage and recirculation, and the pump size needs to be carefully considered.

3.2.2 Centrifugal VAD structure

The VAD design in this study is based on the BiVAD concept structure previously designed by Jianping Yuan[1], as shown in Figure 3-1. The pump has been redesigned to incorporate the driving mechanism as well as optimised to suit the making of the prototype pump and further evaluation in the human mock circulation loop. The structure of this pump, including the design choices and decisions, is discussed below:

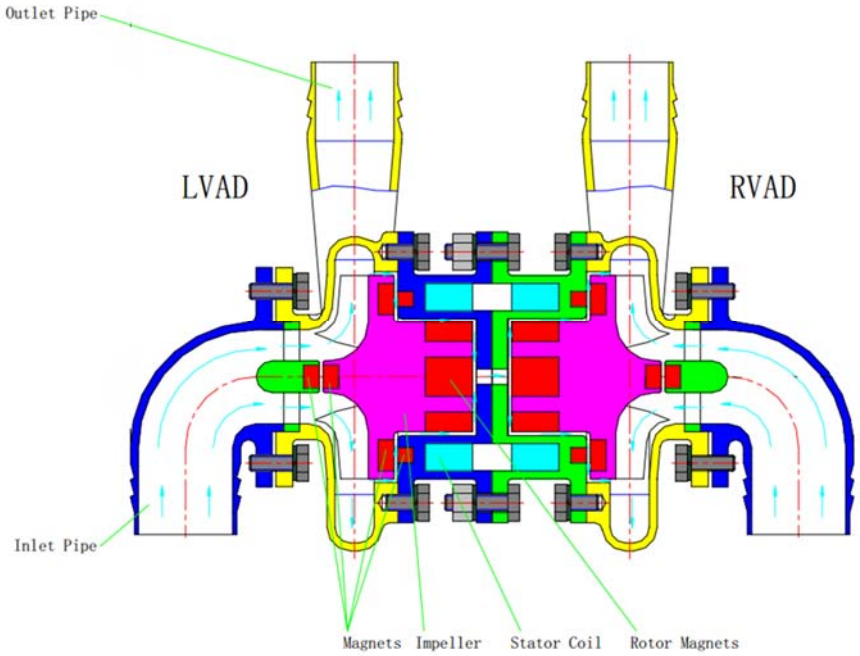

Figure 3-1: BiVAD concept design schematic.

I. Inlet pipe

The inlet pipe of the VAD is the part which connects to the ventricle via the inflow cannula and guides the blood to the impeller eye. The common design of the inlet pipe is a basic straight pipe that guides the flow directly to the centre of the impeller eye; this is the most effective and has low boundary layer losses. However, some designs would slightly shift the inlet pipe position due to the restriction of the impeller shaft or bearing placement.

---

[1] *This BiVAD concept was designed by Prof. Jianping Yuan when he was a visiting research fellow at QUT in 2012*

The original concept design of this pump has a 90^{o} elbow structure to reduce the space required in the implantation and to be suitable for the placement of cannulas. Right after the elbow corner, there is a flow straightener that helps to eliminate disturbances in the incoming flow before entering the impeller area.

II. Impeller

The impeller is the rotating part that transfers mechanical energy to fluid energy and thereby increases the flow velocity and pressure. The fluid flow into the impeller at the centre, known as the eye of the impeller, is pushed away from the centre with centrifugal force through the blades or shrouded vanes on the impeller. The number of blades or vanes is an important factor for the performance of a centrifugal pump as a large number of blades generate more centrifugal force and, thus, a higher head pressure. However, there will be fewer volute spaces between the vanes and, hence, a reduced flow capacity of the pump. Therefore, the design of the blade numbers in a VAD is significant for balancing between a sufficient flow rate to meet a patient's perfusion while also generating enough head to compensate for the pressure loss from the weakened ventricle.

The design of the impeller can also be classified by the way that the impeller blades are attached to the hub, as follows:

i) Open impeller

The open impeller type only has blades attached to the cylinder hub. This type of impeller has a low performance as the fluid can leak from both above and below the impeller blades. However, the open structure allows easy cleaning and there is a larger flow channel compared to other types, so that it is suitable for fluids with large particle as there is a lower chance of blood clot formation.

ii) Shrouded impeller

The shrouded impeller has shroud plates attached on both sides which enclose the impeller blades within. This structure can eliminate leakage across the vanes, and it improves the performance of the pump significantly. However, the small clearance above the shroud allows leakage from the inlet pipe and risks generating shear stress

and the formation of recirculation flow, as the centrifugal force might not work effectively to wash out this area without the guide vanes.

iii) Semi open impeller

The semi-open impeller only has a circular plate attached to the bottom side of the blade; thus, the leakage flow can occur only above the impeller, and the performance is in between the shrouded and open type of impellers. The only major concern of this impeller as a VAD design is the clearance under the impeller that could cause a recirculation flow and leads to stagnation without a proper flow design. The semi-open impeller design was considered to be the most suitable for this VAD design. In order to achieve the highest performance, 5 designs of impeller with common hub structures but different blade configurations were created for a comparison between the effect of the blade numbers and the twisted / cylindrical blade alignment, as follows:

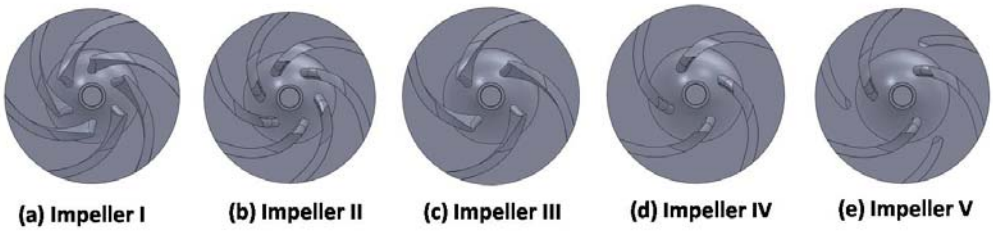

Figure 3-2: Five impeller designs for the performance evaluation.

Figure 3-2 shows the different impeller designs for evaluation. Impeller II and impeller IV have a normal cylindrical blade alignment, the only difference being that impeller II has 6 blades while impeller IV has the blade number reduced to 4 to increase the flow capacity.

Impellers I and III have 6 and 4 blades, respectively, but incorporate the twisted blade alignment design.

Impeller V has a unique structure among the designs as it has 3 cylindrical blades and 3 smaller splitter blades.

The impeller of this pump is to be driven by the magnetic force between the stator coil and the permanent magnet embedded at the base of the impeller hub. The permanent magnets (shown in red in Figure 3-1) also added to the impeller eye, inlet support, and around the impeller hub, help to suspend the impeller and levitate it within the chamber.

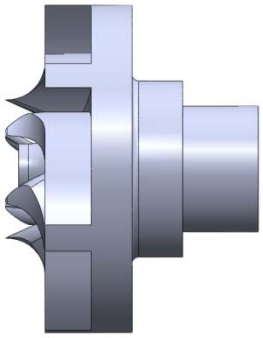

Figure 3-3: Side view of the impeller with the extended part to accommodate the magnet for the driving and suspending the mechanism.

III. Volute casing and chamber

The blood flow from the impeller vanes is collected in the volute casing which gradually reduces the flow velocity and gains the dynamic pressure along the expanding cross-sectional area in the process known as velocity diffusion. A good volute design must be able to conduct this velocity conversion with minimum losses. There are many volute designs of centrifugal pumps available depending on the application; however, the common designs of VAD are single volute, double volute and circular volutes.

i) Single volute

The single volute is the most basic and common design of a centrifugal pump for its simplicity and good efficiency. However, the disadvantage of this type of volute is the considerable radial force when operated at a flow rate lower or higher than the best efficiency point (BEP) due to the imbalance in the pressure distribution around the impeller. The excessive radial force could cause fatigue on an internal structure such as a bearing or shaft and thus reduce the life time of the pump.

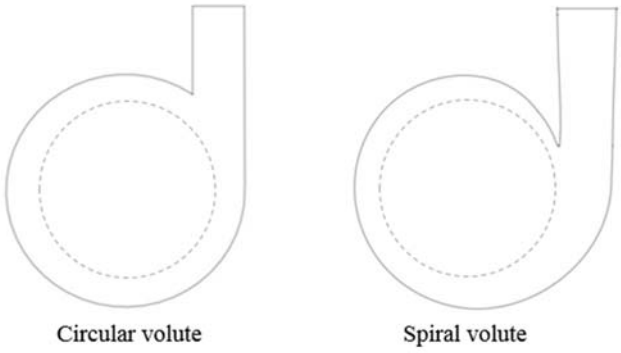

Figure 3-4: Circular and spiral volute

The variations of the single volute type are the circular volute and spiral volute. The circular volute is a type of concentric volute casing around the periphery of the impeller. It can provide better pump efficiency compared to the spiral volute design at specific speeds below 600 rpm; however the efficiency is lower at a higher specific speed (Lobanoff & Ross, 2013). Some of the VADs that use the circular type of volute are NEDO BVAD(Nosé et al., 1999) and BiVACOR (Daniel Timms et al., 2008).

ii) Double volute

The double volute design has a similar structure compared to the single volute but it has a dividing rib to split the flow before exiting to the outlet diffuser. This volute design provides a lower radial force on the impeller so it is often used in applications or pump designs with a high radial force that could cause an excessive shaft and bearing load. However, the small structure of the splitter rib could cause some difficulty in production, especially for a small VAD design.

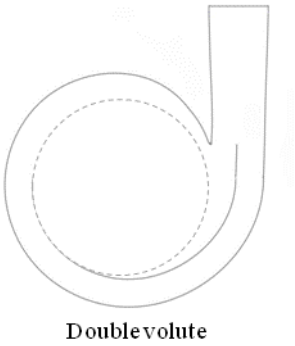

Figure 3-5: Double volute

The original concept design of this pump is made on a single spiral volute design with a 30 mm volute basic circle diameter. Underneath the impeller there is a small clearance of 0.5 mm that allows the rotor to levitate within the chamber by means of magnetic suspension without touching down or rubbing on the internal chamber surface. This area, however, has a risk of creating recirculation flow which could cause blood coagulation; therefore, a small passage was created as a link between the chambers that generates the small flow from the LVAD to the RVAD side. This secondary flow is designed to create a washing effect to wash the small clearance area along the side and underneath the impeller and eliminate all recirculation flow; in addition, it could also provide the hydraulic bearing effect that reduces the axial thrust on the impeller. The issue of this concept structure is the leakage flow that could reduce the efficiency of the LVAD; in addition, it also allows the oxygen rich blood to flow into the RVAD that leads to the pulmonary system. Therefore, the amount of the leakage flow must not be too large to disrupt the pulmonary function while the flow needs to be sufficient to effectively wash out the stagnation or recirculation flow.

IV. Outlet diffuser

The outlet diffuser in the VAD is the part from the volute throat that guides the outflow from the volute to the outlet port. The static pressure of fluid is gradually increased in this part as the cross-section area is expanding along the flow path toward the outlet port.

The key design parameters of this pump are summarized in the Table 3-1.

Table 3-1: Design parameters of the BiVAD pump

Diameter of impeller inlet	D_i	11 mm
Diameter of impeller hub	D_h	4 mm
Diameter of impeller outlet	D_2	26 mm
Width of impeller outlet	b_2	3.5 mm
Number of impeller blades	Z	4 or 6
Wrap angle of impeller blades	ϕ	110^o
Diameter of volute basic circle	D_3	30 mm
Width of volute inlet	b_3	5 mm
Diameter of volute outlet	D	10 mm

3.3 VAD DESIGN CRITERIA AND REQUIREMENTS

3.3.1 Hydrodynamic requirements

The average mean aortic and pulmonary pressure of a healthy adult are estimated at 93 and 15 mmHg, respectively, and the average flow rate is 5 l/min (Marieb & Hoehn, 2007). As the pump needs to be able to support different degrees of failure of the ventricle, including the need to overcome the variation of vascular resistances, the design operation point was set to be higher than the average pressure at 100 mmHg (1.36m) for the LVAD and 20 mmHg (0.68m) for the RVAD.

Another design problem for the heart pump is the variation of the flow rate that passes through the pump and which is influenced by many factors such as age, severity of the CHF condition, and physical activities of the patients. As these factors are uncontrollable, the pump must be able to deliver the required head pressure with a wide range of flow rate to maintain perfusion for the patients.

This evaluation was done in the CFD simulation software along with the impeller design selection. As the left and right side of the BiVAD design are identical and they work independently, it was safe to consider the configuration as a single pump that operates under different conditions. Therefore, the pump evaluation was done independently to find the optimum rotation speed that could deliver the head pressure under the variation of flow rate.

3.3.2 Hemodynamic requirements

As previously discussed in Chapter 2, the major hemodynamic concerns of the heart pump are shear stress induced damage and thrombus formation from the recirculation flow.

Although blood damage generated by the pump is an important factor that affects the pump's lifetime for supporting patients, there is no clear standard for the acceptable blood damage caused by a heart pump. Nosé (Nosé, 1998) suggested the blood damage threshold of a heart pump by categorizing the clinical needs of the heart pump into 3 categories: 2-day pumping, 2-week pumping, and longer than 6 months. The short term support pumps for 2 days and 2 weeks are required for cardiopulmonary bypass and post-cardiotomy heart failure support, respectively,

while the 6-month pump is intended for long term support such as bridge to transplant. Nosé recommended that the pump which was considered to have anti-traumatic property should have a normalised index of hemolysis (NIH) less than 0.01 g/100L for the long term or 2- week pumps that operate under a flow rate 5 of L/min and head pressure 100 mmHg. It was also recommended that the pump should have a lower NIH than 0.004 g/100L to reduce the chance of the red thrombus that could form during a patient's bioadaptation on the first 2 days of operation and to be considered as antitraumatic for short term operation support; however, this is generally not a requirement for clinical practice (Behbahani et al., 2009). These standard values have later been used as a design reference and development targets for several heart pump developments (Bock et al., 2007; Carswell et al., 2013; C. H. H. Chan et al., 2015; Farinas, Garon, Lacasse, & N'Dri, 2006)

Aside from shear stress, the flow dynamics within a pump need to be carefully designed to avoid stagnation and recirculation which could cause thrombosis that leads to pump failure or breaks off into the blood stream and causes an ischemic attack.

3.4 INITIAL SINGLE-SIDED VAD SIMULATION

The initial simulation was conducted on the Ansys CFX 12.1 software to confirm availability of the impeller design in delivering the required head pressure and briefly investigate its efficiency. In this stage, the simulations was conducted on the simplified model of the independent single-sided pump of all five impeller designs under different flow rates at the nominal designed pump speed.

After this initial simulation a more detailed simulation on the full model of the BiVAD would be conducted in the next step to find the optimum rotating speed for each impeller design and provide a detailed analysis of pump performance. The most suitable impeller design would be selected, for further development and the information was also used in further optimization for creating a pump prototype.

3.4.1 Fluid model

The CFD analysis was performed on the simulation domain which in this case is the simplified fluid model of the pump that was created for the initial simulation to

study the efficiency of each impeller design. The fluid domains of the centrifugal pump and VAD simulation can be divided into two types: the rotating domain which is the fluid in the vanes and around the impeller area, and the static domain which in this study comprises three parts: the inlet pipe, side chamber or ring diffuser, and volute, as shown in Figure 3-6. A total of 5 impeller models were placed in the static domain for each simulation.

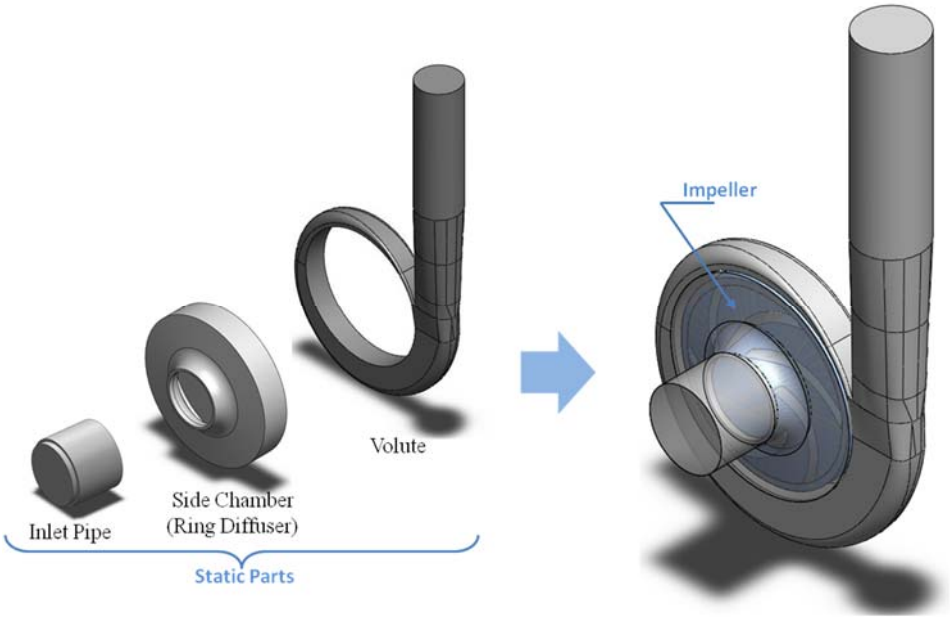

Figure 3-6: Fluid assembly model of the single-sided VAD.

3.4.2 Meshing method

Mesh creation is a method to subdivide the computation domain to a number of small elements for finite calculation methods. The mesh generation of this model was done in Ansys 12.1 ICEM using the CFX-mesh method. The process of meshing was done separately between the stationary domain and the impeller so that all the simulation could be done on the same stator.

The mesh type selected for the simulation was the unstructured tetrahedral-shaped element for its ability to effectively generate a valid mesh on the model with small angles such as for the blade tips without highly skewed element angles. The element size was controlled by the face spacing method that allows control over the mesh size on each surface area via the specification of the angular resolution, the range of edge length, and the expansion factor. The angular resolution is an option to control the edge length to vary over the face curvature; the smaller value for this setting allows a smaller edge length and finer elements. The range of edge length is

specified by the minimum and maximum length that allows for the element generation, and it is applied with the angular resolution to control the mesh size. As these functions were applied to constrain the mesh size on the local surfaces, the expansion factor was used to specify the rate at which the mesh length scale returns to its global value as the elements moved away from the surface. The large expansion factor allows the mesh to coarsen more rapidly from the specified surface.

By utilising this face spacing feature, the constraints were set to generate a finer mesh near the walls, on the side chamber, on the volute tongue and on the impeller, especially near the blade surface area which requires a more accurate calculation of the results, and is coarser on the area with a more uniform flow at the inlet port and outlet diffuser.

With the specified method and constraint configurations, the total number of mesh elements generated on the static domain is 532,615 elements, while the impeller is composed of an estimated 544,000 - 785,000 elements depending on the design structures. The mesh structures on the static and rotating models are shown in Figure 3-7 and Figure 3-8 respectively, while the number of elements is summarized in Table 3-2.

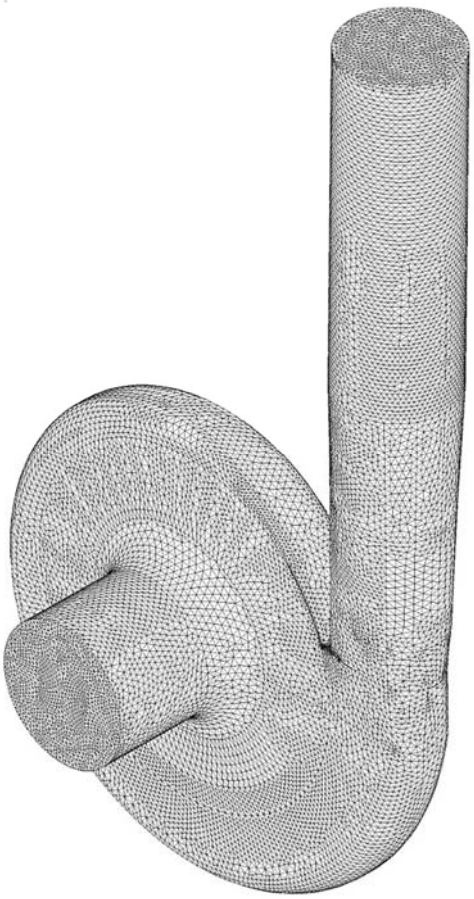

Figure 3-7: The tetrahedral meshes generated on the stator model.

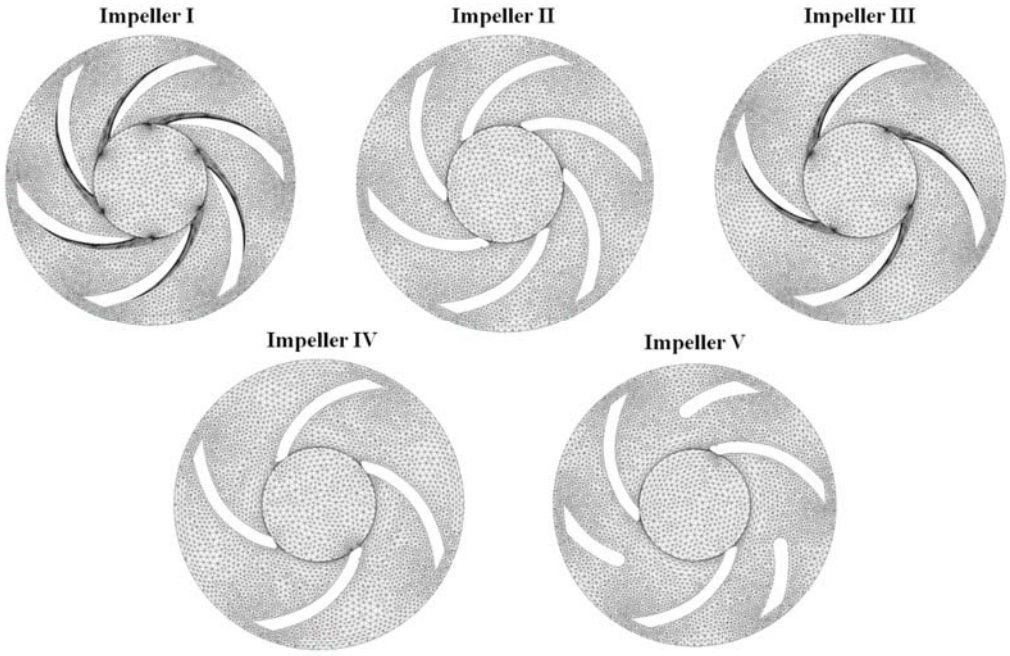

Figure 3-8: Meshes of single sided VAD impeller.

Table 3-2 : Number of elements on each part.

Fluid Model	Number of Elements
Stator	532,615
Impeller I	785,597
Impeller II	709,286
Impeller III	626,164
Impeller VI	544,316
Impeller V	715,965

3.4.3 Material properties

Blood is known to be a non-Newtonian fluid, however it behaves as a Newtonian fluid when the shear rate is above 100 s^{-1}; therefore, the pumping fluids of VADs are often modelled as Newtonian due to the high shear rate nature of the blood pump and aorta (Wells & Merrill, 1961, 1962) and this assumption has been experimentally validated in several research studies (Steven W. Day et al., 2001; Steven W Day et al., 2002; J. Zhang et al., 2006).

Therefore, to simulate the blood flow through this blood pump, the fluid was assumed to be Newtonian and the properties were specified to replicate the blood density at 1,056 kg/m^3 and the viscosity at 0.004 Pa.s.

3.4.4 Boundary conditions

The boundary conditions for this initial simulation are specified by aiming to find the efficiency for each impeller design over a variety of flow rates. Therefore, the volumetric flow rate was varied from 0.15 to 0.42 m^3/h over a designed pump speed of 4,000 rpm. This flow rate was converted to flow velocity (v) by the equation, v = A/Q, where Q is the flow rate and A is the cross-sectional area of the inlet pipe, and is applied to the pump inlet as the normal velocity profile. The boundary type of the outlet pipe is specified as the "opening" which has no restriction on the flow direction; and, since the flow rate between the inlet and the outlet are equal, the Cartesian velocity components were used to specify the flow velocity at the outlet boundary based on the same flow rate at the inlet pipe to direct the flow out of the pump in the normal direction to the outlet diffuser.

The standard k-ε turbulence model was chosen for this simulation and specified as an initial turbulence boundary for both the inlet and outlet of the pump. The turbulence kinetic energy was calculated from the equation:

$$k = 0.05u^2 \qquad [3\text{-}1]$$

where k = Turbulence kinetic energy (m^2/s^2)

u = Flow velocity (m/s)

The initial turbulence eddy dissipation (ε) was specified by the function:

$$\varepsilon = \frac{C_{\mu}^{0.75} k^{1.5}}{0.07D} \qquad [3\text{-}2]$$

where ε = Turbulence eddy dissipation rate (m^2/s^3)

C_{μ} = Constant parameter for k-ε model, = 0.09

D = Pipe diameter (m)

The connecting surfaces of the impeller and volute model (Figure 3-9) were specified as the general connection domain interface to allow the fluid flow to pass through between the models, and the mixing model on these interfaces was specified as the "frozen rotor" which is the calculation option for the quasi-steady state simulation without changes in the relative position between the components across the interface (ANSYS, 2009). Other surface areas were specified as no slip, and smooth wall.

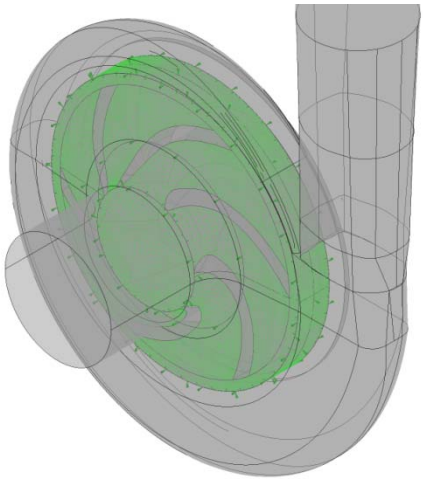

Figure 3-9: Interface at the connecting surface between rotating and stationary domain.

The boundary conditions for this initial simulation are summarised in Table 3-3.

Table 3-3: Boundary conditions of single-sided VAD simulation.

Boundary Conditions		
Inlet	**Boundary type**	Inlet
	Boundary Detail	Normal Speed: 'Flow Velocity$_{inlet}$' m/s
	Initial Turbulence	k-ε
Outlet	**Boundary type**	Opening
	Boundary Detail	Cartesian Velocity Components: u = 0 m/s v = 'Flow Velocity$_{outlet}$' m/s w = 0 m/s
	Initial Turbulence	k-ε
Impeller	**Speed**	4000

3.4.5 Solver control

The solver control was set to the high resolution advection scheme to obtain better accuracy for the current unstructured meshes. The convergence criteria were to reach either 2,000 iterations or to reduce the RMS residual below 1 x 10^{-5}. This solver control setting was also used in all the simulations in this study.

3.4.6 Initial simulation results and discussion

With the method explained above, the simulations were conducted on 5 impeller designs under 6 flow rates, so that a total of 30 simulation cases were completed in this initial simulation.

The performance parameters considered for this initial simulation are head pressure, hydraulic power, and hydraulic efficiency. The comparison of these parameters across the impeller designs are shown in Figure 3-10, Figure 3-11 and Figure 3-12.

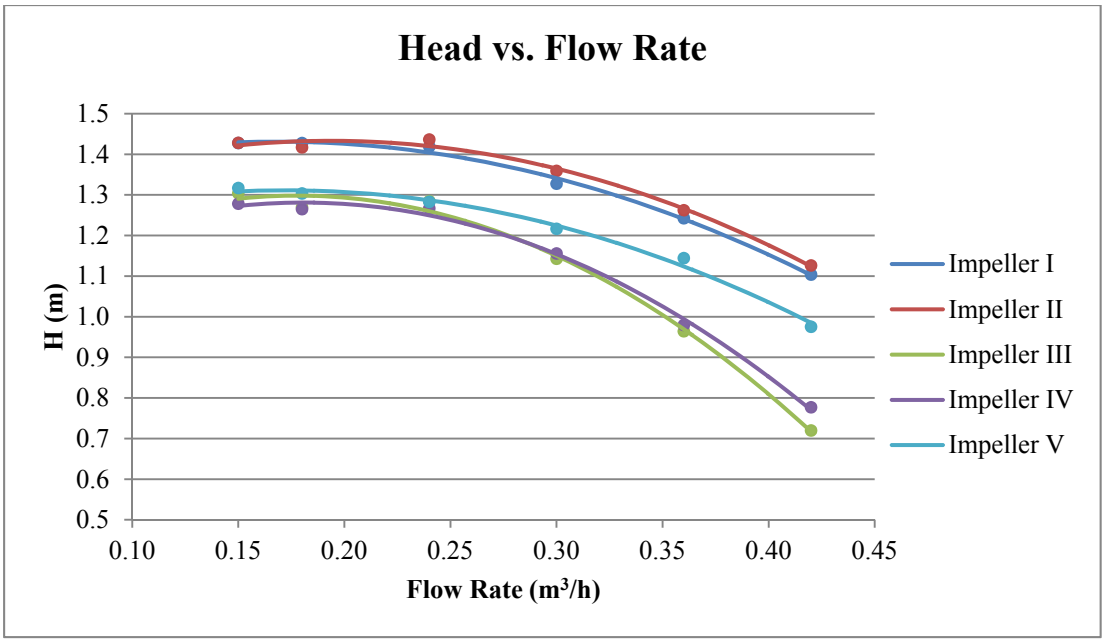

Figure 3-10: The predicted pump head vs. flow rate across the impeller designs.

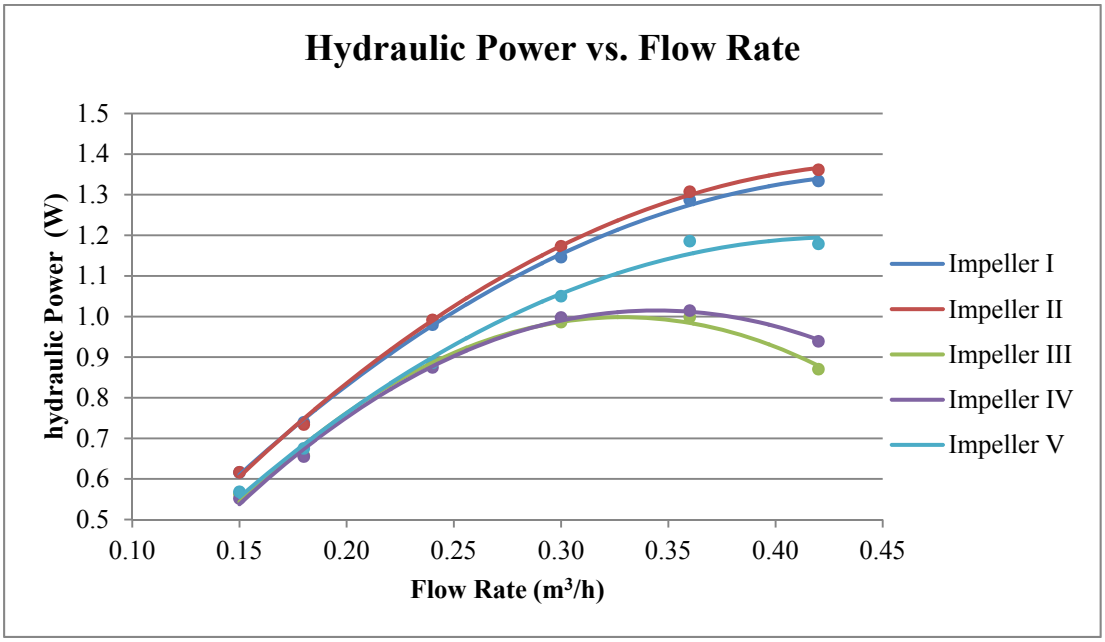

Figure 3-11: The predicted hydraulic power vs. flow rate across the impeller designs.

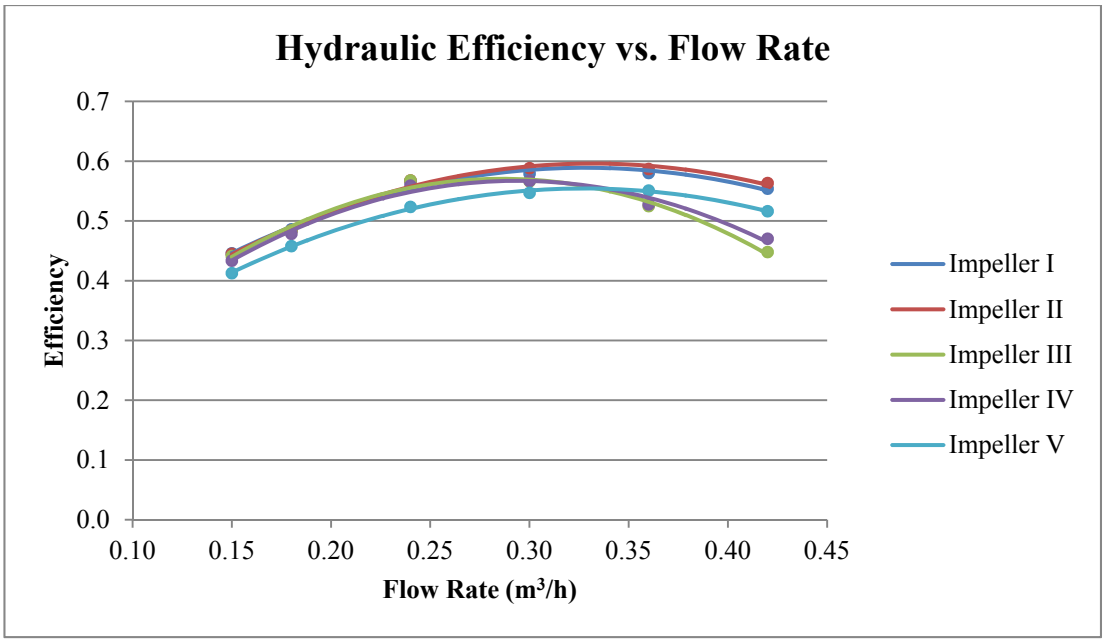

Figure 3-12: The predicted hydraulic efficiency vs. flow rate across the designs.

According to the performance plots, impeller numbers I and II which have 6 blades are the best design which could generate the highest head and hydraulic power and, hence, better efficiency compared to the designs with 4 blades and the short splitter blades design. Design V is the third best design but the efficiency is about 8% lower than designs I and II under the whole flow range in this simulation. Designs III and IV have close performances to design V at a flow rate lower than 0.24 m^3/h, but the head pressure drops more rapidly above the designed flow rate. At the design flow rate (0.3 m^3/h), both designs I and II could deliver the estimated head pressure up to 1.42m while other designs generate a significantly lower head at the same flow rate for all the conditions and could not achieve the LVAD required head of 1.36 m (100 mmHg) at this designed speed; however, this could be achieved by optimizing the rotation speed of the pump in later stages.

In addition to the performance parameters, the pressure, velocity and shear stress distribution contour within the pump at the designed flow rate (0.3 m^3/h) are shown in Figure 3-13. According to the pressure contour in this Figure, the pressure is distributed almost equally between the vanes. The rate at which the pressure is raised is higher in the designs with six blades and the splitter blades compared to the four blade designs, which is in agreement with the higher head pressures from designs I, II and V. However, designs I, II and V present a large low velocity region

in the diffuser area, as shown in the velocity contour, which could not be observed in the four-blade designs. The high shear stress region was found at the tongue and leading edge of the impellers, especially on the splitter blades of impeller V, but the effect of this shear stress needs to be investigated further to explain whether it affects the red blood cells (RBC).

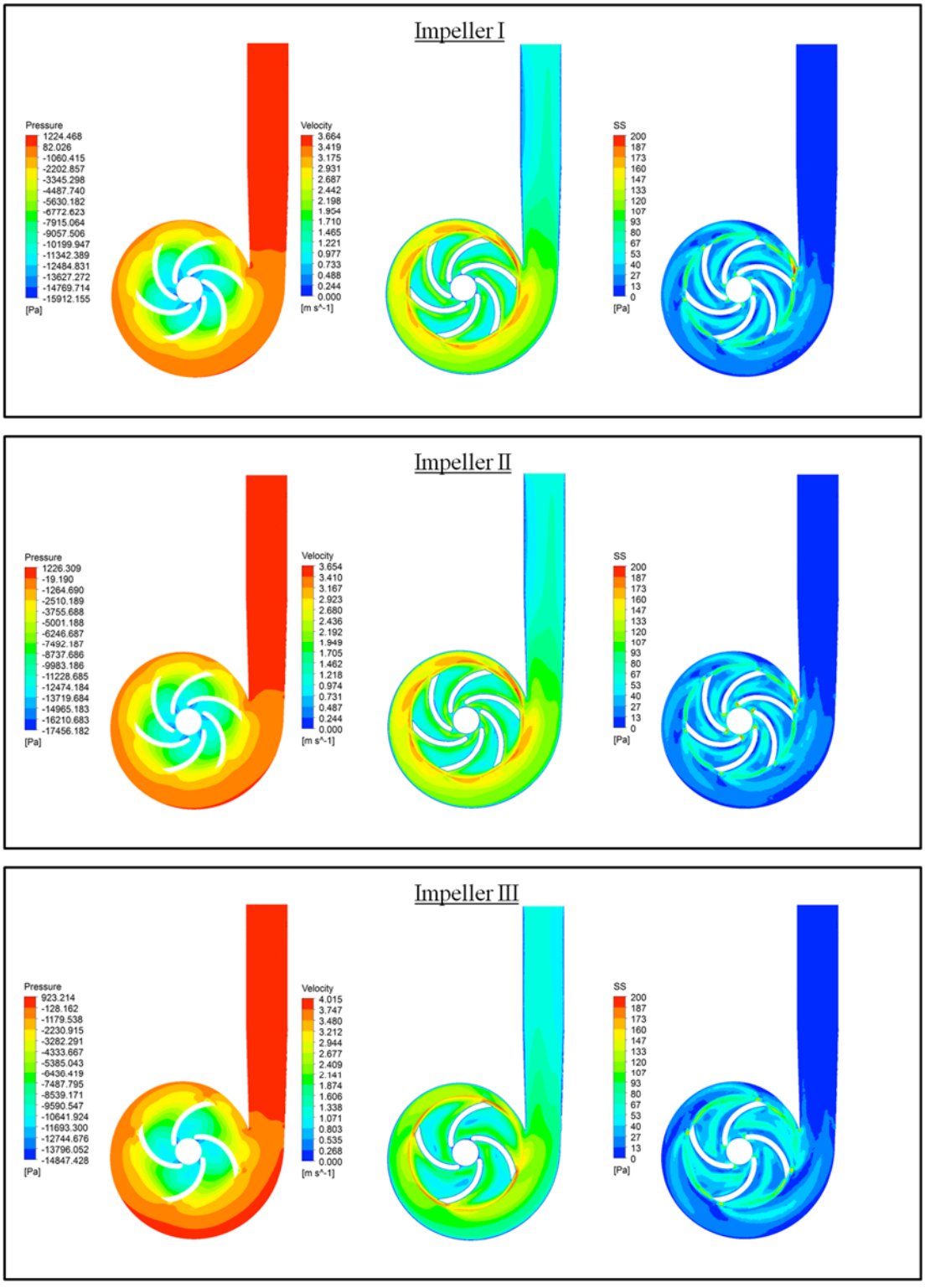

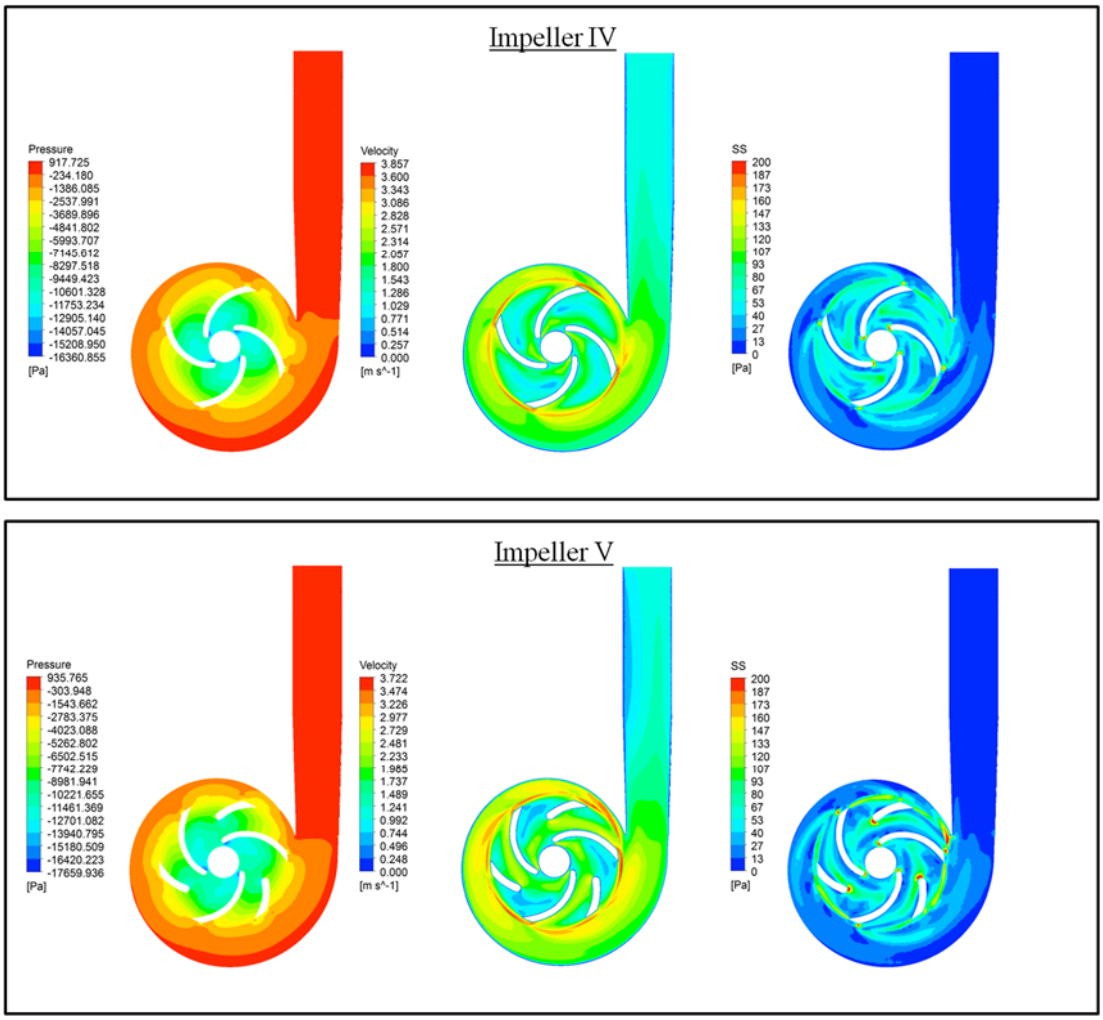

Figure 3-13 : Pressure, velocity and shear stress contours of each impeller.

In conclusion, all the designs show no significant problem at this stage of the initial evaluation. In the next section, all the impellers will be evaluated as a BiVAD under the designed flow rate to find the operating speed that could deliver the desired head pressure for the LVAD and RVAD environments. There will also be further investigation of the low flow region and the effect of the generation of shear stress.

3.5 BIVAD SIMULATION

As stated in previous sections, the simulation of the BiVAD at this stage is aimed at acquiring information on the operating speed, performance specification, and possible design problems for the impeller selection and the development of the prototype pump.

3.5.1 BiVAD fluid model

The fluid model of the BiVAD was created on the same principles as the single-sided VAD but with inter-connection details of the BiVAD's internal structure. The model comprises 8 parts, with 3 parts for the stationary domain (inlet pipe, side chamber, and volute) on each side and 2 rotating domains that represent each impeller. This fluid model is shown in Figure 3-14 and the solid model in Figure 3-15.

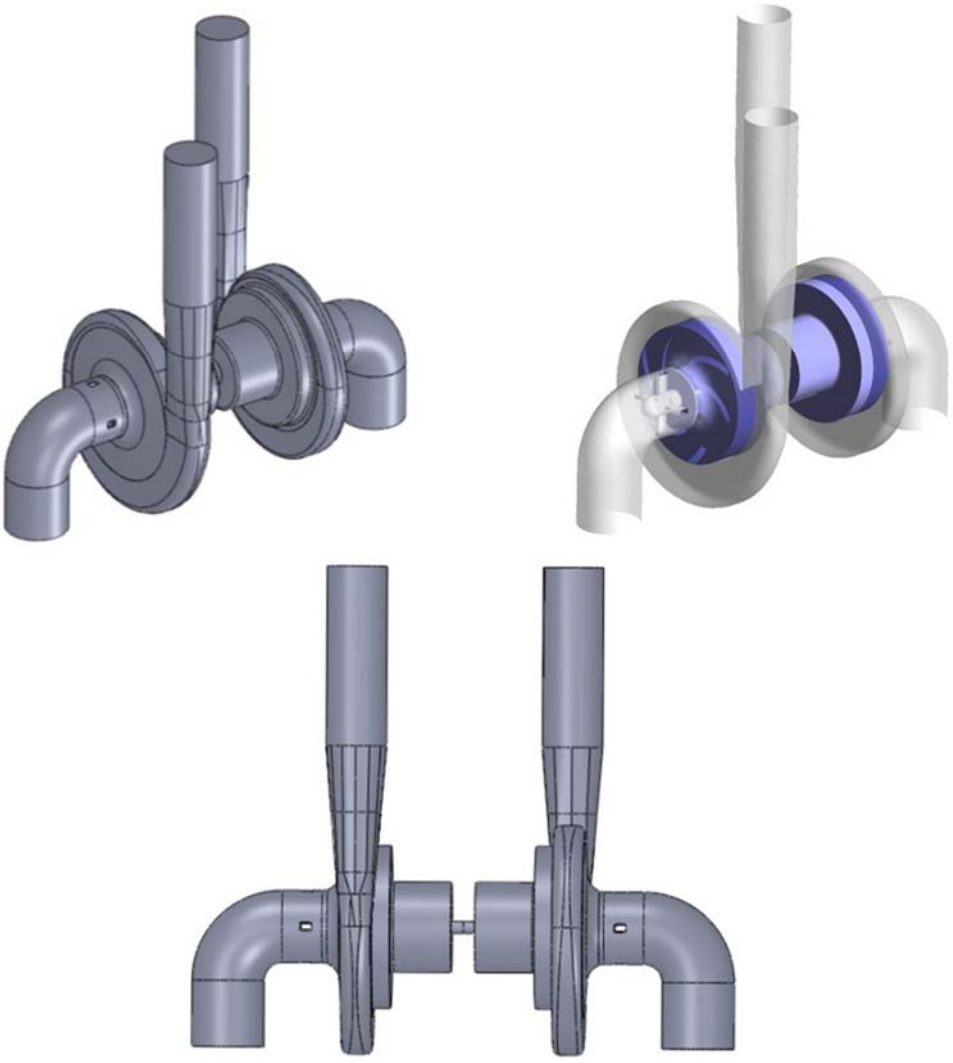

Figure 3-14: Fluid Model of BiVAD.

Figure 3-15: BiVAD solid concept model.

3.5.2 Meshing model

The mesh generation for this BiVAD simulation was still based on the face spacing method. However, due to the larger model size, the elements scale has been adjusted to keep the number of elements close to the previous simulation to maintain the reasonable computational power and the simulation time. The high density mesh was maintained on the sensitive areas such as near the blades' region, the tongue and the wash-out hole between the chambers, while reducing the mesh density on the straight flow areas such as the inlet pipe and the outlet diffuser.

The stator model contains a total of 822,505 elements while the impellers, which have an identical structure, contain an estimated 190,000 - 215,000 elements in total, or about 40% of the total elements on the model, depending on the impeller design. The meshed models on the rotor (impeller I) and stator are shown in Figure 3-17 and Figure 3-16, respectively.

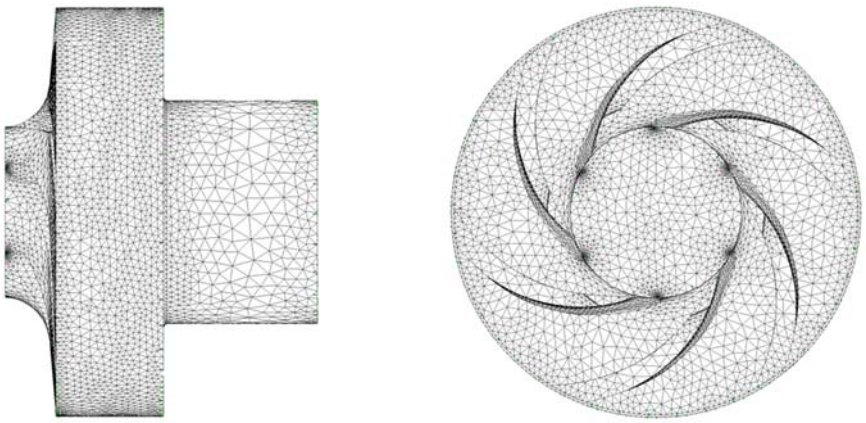

Figure 3-16: Meshed model of BiVAD rotor (Impeller I)

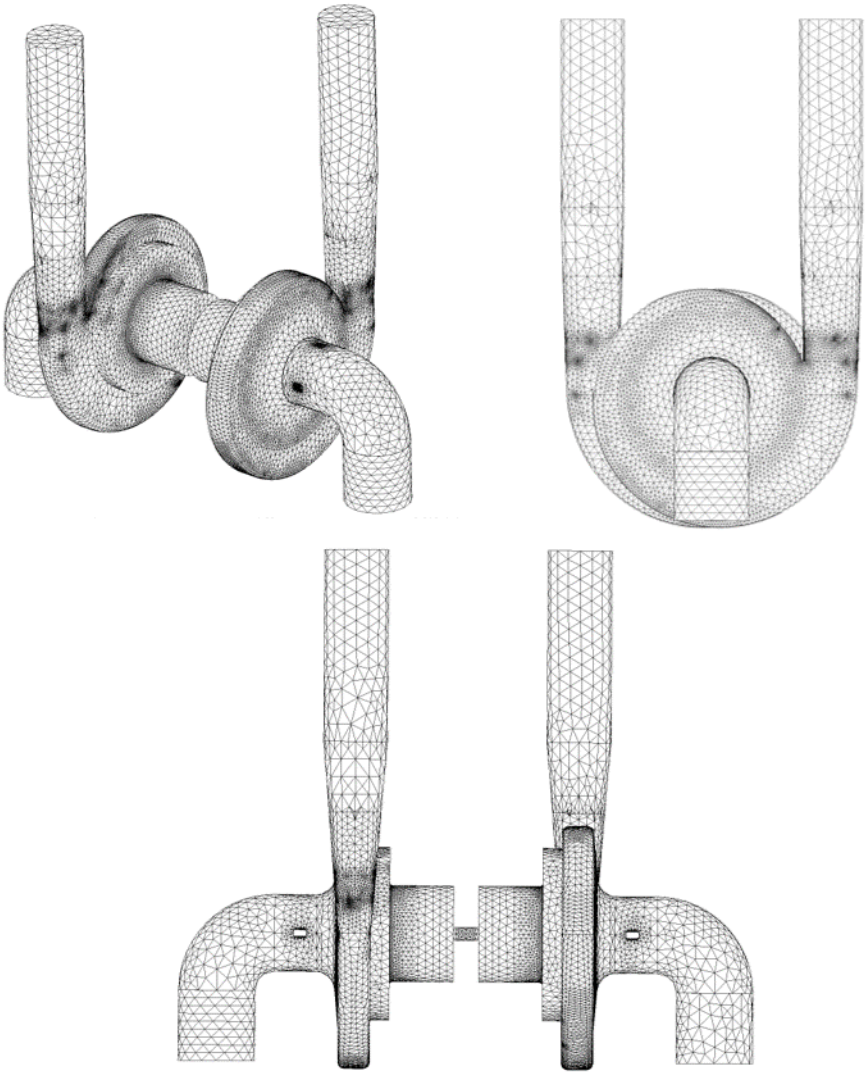

Figure 3-17: Meshes on the BiVAD stator.

Mesh independence test was conducted to ensure that the element density is sufficient to obtain the accurate solution and the accuracy of the result is independent on the element size. The test was done by varying the number of elements from approximated 250,000 to 1,500,000 elements while maintaining the mesh ratio 2:1 between stator to rotors. Head pressure was used to represent the result from simulation and the relation between head pressure and the number of element is shown in Figure 3-18. According to this result, the head pressure is tend to be steady when the number of element is above 700,000. Consequently, the current mesh density is verified to be sufficient for this study.

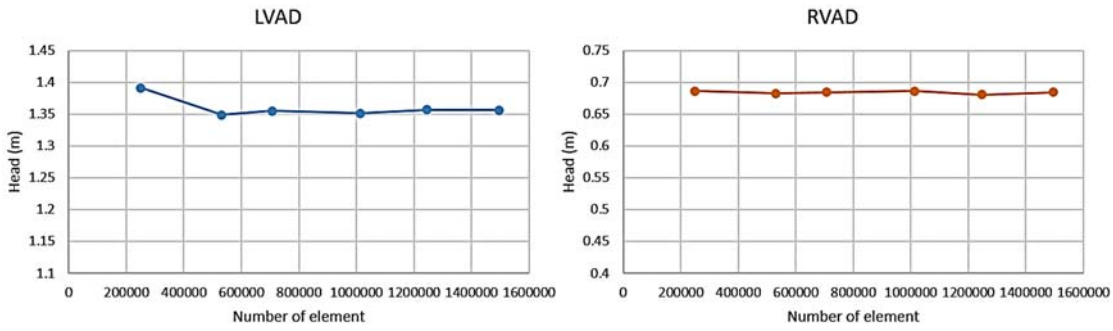

Figure 3-18: Head pressure vs. number of element.

3.5.3 Simulation settings and boundary conditions

In this simulation, the pump is set to operate at the design conditions with variable pump speed to find the specific speed that could deliver the required head pressure. The flow rate on this simulation is thus set to the designed condition at 5 L/min by specifying the outlet boundary as a Cartesian velocity components, while the static pressure is used as the inlet boundary condition. The inlet pressure was set to 20 mmHg which is the estimated filling pressure from atrium in case of congestive heart failure.

3.5.4 Simulation Results and discussion

By varying the pump speed of the simulation condition as specified above, a series of simulations were conducted and the relationships between the pump head (H) and rotation speed (n) of all the impeller designs were plotted, as shown in Figure 3-19.

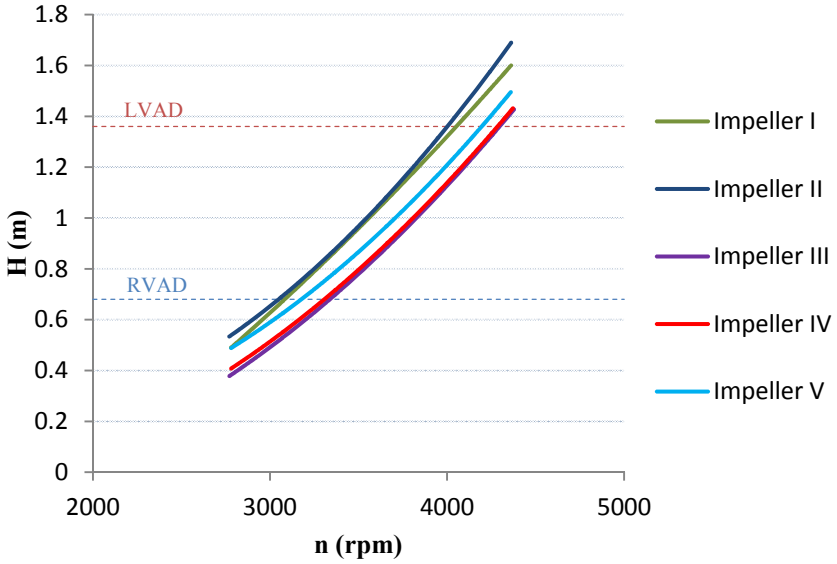

Figure 3-19: The plot of the head pump vs. pump speed.

Since the required head pressures for the LVAD and RVAD are 1.36 m and 0.68 m, respectively, the required rotation speed was derived from the plot, as shown in Table 3-4.

Table 3-4: The required rotation speed for each impeller design.

	Impeller rotation speed (rpm)				
	Impeller I	**Impeller II**	**Impeller III**	**Impeller IV**	**Impeller V**
LVAD	4062	4000	4298	4283	4196
RVAD	3111	3054	3336	3304	3181

I. Hydraulic efficiency

With these specified speeds, a total of five simulations were made. The hydraulic performance of each side of the pump and the total performance are summarized in Table 3-5.

Table 3-5: Predicted hydraulic performance of heart pump from the Simulation.

	Parameters	Case I	Case II	Case III	Case IV	Case V
LVAD	$n_L(rpm)$	4062	4000	4298	4283	4196
	$Q_{L-outlet}(m^3/h)$	0.29	0.29	0.29	0.29	0.29
	$H_L(m)$	1.367	1.357	1.359	1.359	1.358
	P_h(W)	1.149	1.141	1.144	1.143	1.142
	η_{hL}	0.529	0.551	0.514	0.522	0.509
RVAD	$n_R(rpm)$	3090	3054	3336	3304	3181
	$Q_{R-outlet}(m^3/h)$	0.29	0.29	0.29	0.29	0.29
	$H_R(m)$	0.682	0.681	0.676	0.679	0.678
	P_h(W)	0.574	0.573	0.569	0.571	0.570
	η_{hR}	0.511	0.532	0.487	0.501	0.496
BVAD	$Q_{gap}(m^3/h)$	0.0037	0.0027	0.0025	0.0041	0.0046
	η_{hR}	0.523	0.545	0.505	0.515	0.504

According to Table 3-4 and Table 3-5, the simulation results of this BiVAD are in good agreement with the results from the initial simulation on the single-sided pump. Impeller II requires the lowest speed to deliver the required head pressure to both sides of the pump at 4,000 rpm for the LVAD and 3,054 rpm for the RVAD. Impeller I required a slightly higher speed at 4,062 and 3,090 for the left and right sides, respectively, while impellers II and IV need the highest speeds among the designs to generate the required head.

The hydraulic power of the pump generated from the impeller is relatively close on both sides and show no significant difference in these simulation conditions. However, Impeller II shows the highest efficiency among the cases, 55.1% on LVAD, 53.2% on RVAD, and overall of 54.5% for the whole pump, which is slightly higher than Impeller I with 52.3% efficiency and approximately 5% better efficiency than the rest of the designs.

With the design of the washout hole between the left and right chambers, some of the blood was allowed to leak from the LVAD to the RVAD to generate a washing effect to prevent stagnation under the impeller. The fluid transfer rate from the left to the right side of the pump is shown in Table 3-5 as the volumetric flow rate "Q_{gap}". It can be observed that approximately 0.003-0.004 l/min of the oxygen rich blood from the systemic circulation leaks to the pulmonary system. At this pump flow rate, the leakage is considered to be a small amount at approximately only 1.5% of the pump flow and should not cause any problem to a patient's circulatory system. The

effectiveness of the washing effect is to be considered and discussed based on the flow visualisation in the next section.

II. Hydraulic force

The magnitudes and direction of the hydraulic forces on the impeller are critical to the magnetic suspension design of the pump to avoid contact between the impeller and the internal surface of the chamber which could cause wear and reduce the pump's lifetime. Therefore, an accurate prediction of the radial and axial thrusts in the simulation phase of the pump development could help reduce time and cost in the prototype's evaluation. From the information gathered in this simulation, the radial force (F_r), is calculated from the accumulated force between F_x and F_y and can be identified by the equation:

$$F_r = \sqrt{F_x^2 + F_y^2} \qquad [3\text{-}3]$$

The direction of F_r can be obtained as follows:

$$\theta = tan^{-1}\frac{F_y}{F_x} \qquad [3\text{-}4]$$

The radial force (F_r), axial thrust (F_y), and the torque (τ) about each axis that are applied on the impeller and the whole pump are summarized in Table 3-6.

Table 3-6: Hydraulic forces and torques on the BiVAD.

Case	Location	F_r(N)	θ(°)	F_z(N)	T_x (N.m)	T_y (N.m)	T_z (N.m)
I	**LVAD Rotor**	0.054	304.05	13.80	-0.00027	-0.00027	-0.00511
	RVAD Rotor	0.085	282.15	-12.89	-0.00261	0.00032	0.00347
	Stator	5.741	182.37	-0.59	0.00476	0.10998	-0.00902
II	**LVAD Rotor**	0.061	300.75	11.89	-0.00034	-0.00019	-0.00494
	RVAD Rotor	0.067	284.37	-11.00	-0.00202	0.00047	0.00336
	Stator	5.765	182.13	-0.62	0.00413	0.10996	-0.00899
III	**LVAD Rotor**	0.038	320.49	9.76	-0.00018	0.00029	-0.00494
	RVAD Rotor	0.089	265.11	-8.90	-0.00265	-0.00035	0.00334
	Stator	5.748	182.30	-0.63	0.00521	0.11092	-0.00901
IV	**LVAD Rotor**	0.046	309.17	8.42	-0.00024	0.00026	-0.00489
	RVAD Rotor	0.090	269.74	-7.67	-0.00268	-0.00028	0.00329
	Stator	5.727	182.46	-0.55	0.00517	0.11002	-0.00878
V	**LVAD Rotor**	0.052	300.30	10.53	-0.00039	-0.00029	-0.00511
	RVAD Rotor	0.082	294.08	-9.66	-0.00212	0.00074	0.00345
	Stator	5.747	182.48	-0.61	0.00518	0.10878	-0.00940

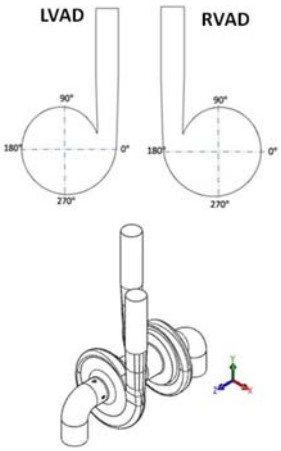

According to the results from Table 3-6, the axial thrust is the dominant force in all cases for both the LVAD and RVAD sides. The axial thrust is estimated to be 200 - 250 times greater than the radial forces, which is the result of the inflow that passes directly onto the impeller's rotating axial. The results from this simulation show that the impellers with a higher number of blades have a larger axial force compared to those with fewer blades, while the twisted-blade designs have a slightly larger axial force compared to the cylindrical blades structure. The design that has the largest axial force is impeller I which has 13.80 N on the LVAD and 12.89 N on the RVAD. This is followed by impeller II which has the same number of blades, and impeller III that also has a total of 6 blades but 3 of them are the shorter splitter blades. Impellers III and IV have an estimated 30% lower axial forces applied on the impellers compared to the same structure with more blades.

The radial force on the rotors is very small compared to the axial thrust. The largest radial force is observed on the RVAD side for impeller IV with a magnitude of 0.090 N. The smallest force among all the cases is 0.038 N which is observed on the left impeller of impeller III. The directions of these radial forces are variable. By comparing the radial forces' direction to the volute diagram shown in Table 3-6, it

can be seen that impellers I, II and III have the same direction of force at approximately 300^{o} on the left impeller and 280^{o} on the right side. They are all in the fourth quadrant and near the diffuser area of the volute; meanwhile, the radial forces' direction of impellers III and IV, which have 4 blades each, are also placed in the fourth quadrant for the left impeller but slightly backward to the third quadrant for the right impeller.

The highest torque on this BiVAD is the torque about the z-axis which is the result of the difference in pump speed on the left and right sides and the placement of the outlet diffuser. Since the magnitude of this torque is very small, it is considered insignificant and negligible.

III. Flow visualisation

Figure 3-20 through Figure 3-24 present the distribution streamlines and contours of the turbulence kinetic energy, velocity, pressure and shear stress, respectively. Since all the impeller designs show a relatively close flow distribution, the information presented in these Figures is depicted from the BiVAD with impeller II only. More simulation results of other cases are shown in Appendix 3-1.

Streamlines: Streamlines of the fluid flow through the pump are plotted in Figure 3-20. It was found that blood can flow smoothly through the inlet pipe of both the LVAD and RVAD side, although the flow speed is reduced at the 90 degree elbows but there is no sign of recirculation. The fluid then flows through the straighteners to the impeller without any major disruption to the stream flow. Inside the chamber, the flow is distributed to each vane and accelerated out to the volute and outlet port. The flow in the outlet port is not fully uniform especially on the RVAD side where it can be seen that the stream circulates around the outlet pipe while flowing toward the outlet. This flow motion leads to losses in the pump's performance and increases the residence time of the blood which might increase the blood damage. The angle and dimension of the outlet port can be further optimized to improve the pump's performance.

The streamlines also show some of the fluid flow paths that leaked and circulated down along the impeller hub in the same direction as the impeller rotation of the LVAD. This leakage allows the fluid from the LVAD side to flow through the

washout hole to the RVAD side. The characteristic of the fluid flow through this washout hole will be further discussed in the later part of this section with additional information from other flow parameters.

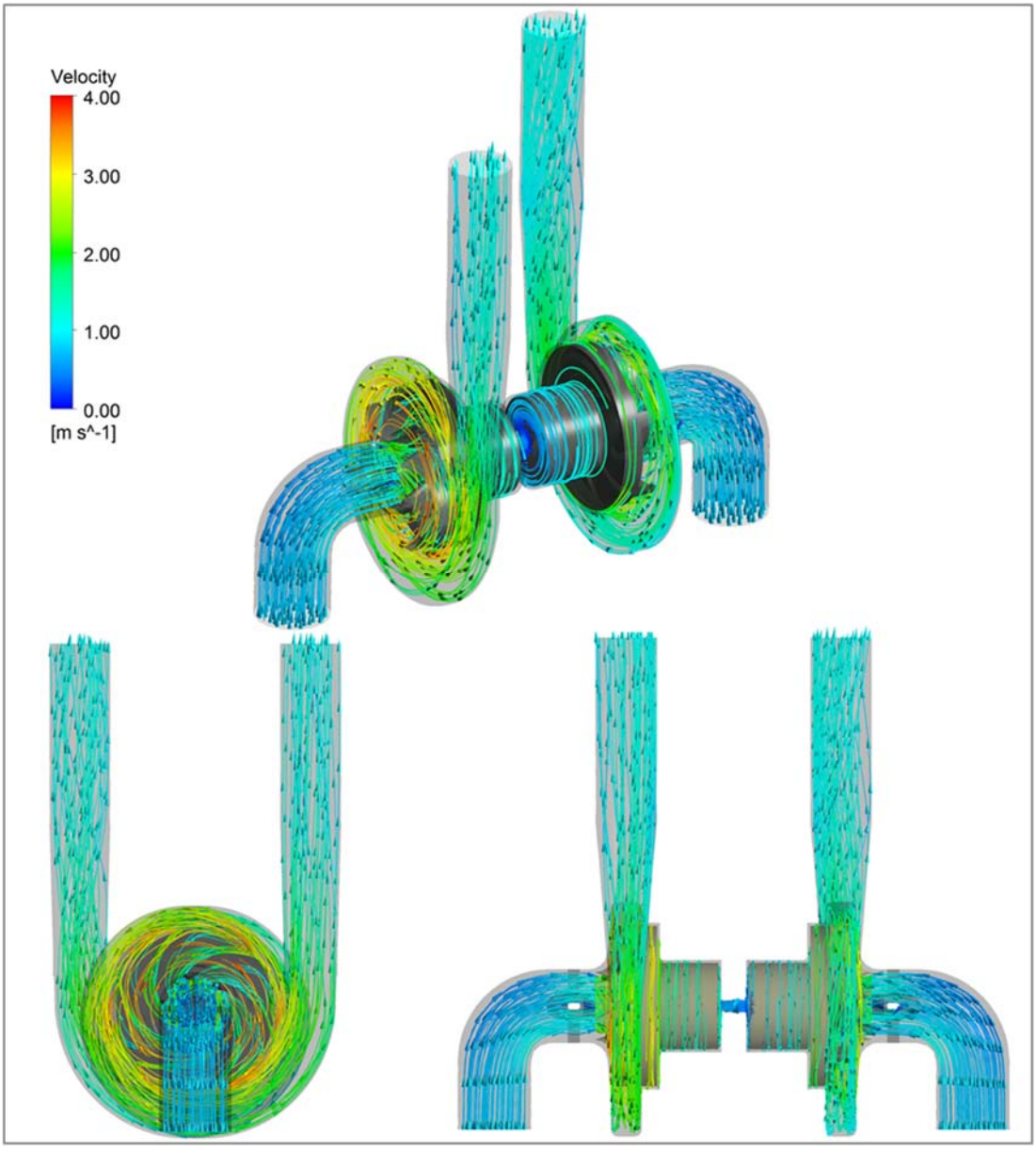

Figure 3-20: Streamlines through the BiVAD.

Turbulence kinetic energy: The turbulence kinetic energy (TKE) is the kinetic energy associated with the eddy and can be used to identify vortices in the pump flow. According to Figure 3-21, the TKE is relatively low in the inlet pipe, which indicates a uniform inflow to the impeller and outflow from the pump despite having to flow through the 90° elbow and the top bearing of the impeller. The only high TKE regions can be observed in the impeller vanes, blade tips and near the volute

tongue which is a common effect of turbulence from the flow separation caused by the rotating impeller. The TKE is reduced in the gap behind the impellers and the diffuser area, which means that the flow becomes more uniform before exiting the pump.

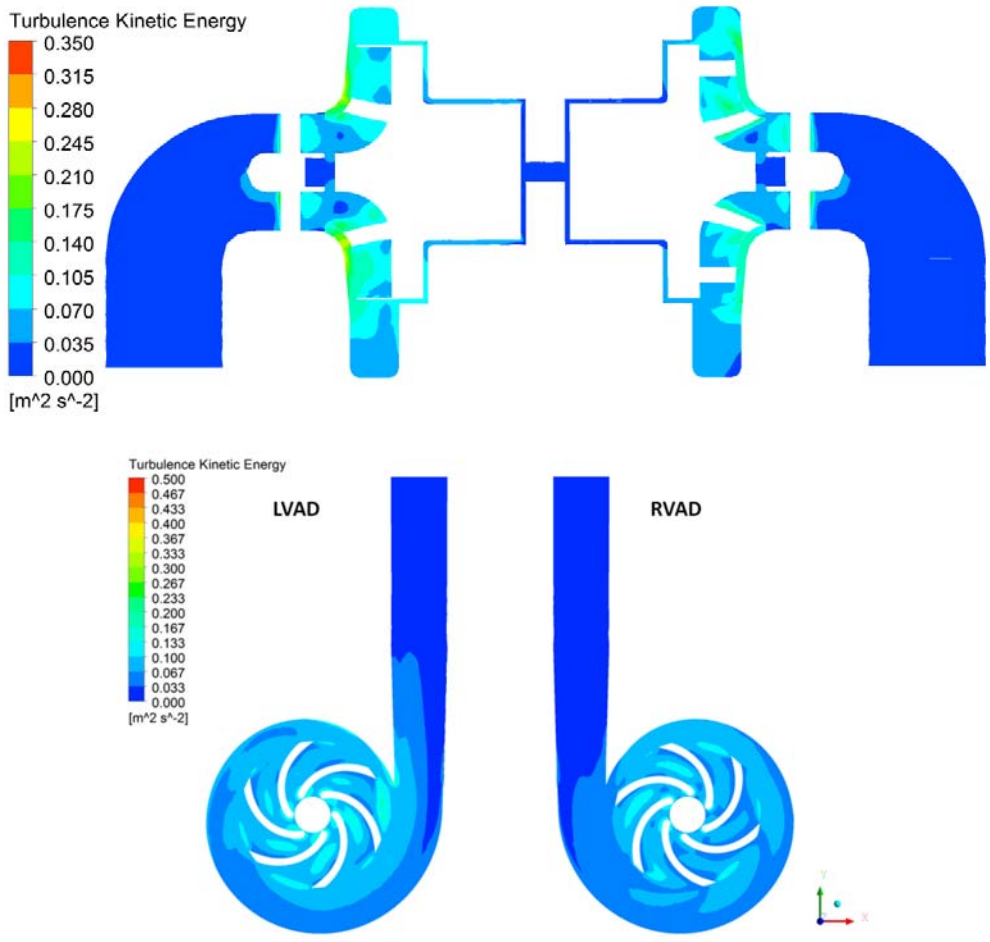

Figure 3-21: Turbulence kinetic energy distribution gradient in section view of the LVAD, RVAD and across the whole pump with Impeller II.

Flow velocity: According to the velocity contour plot (Figure 3-22), the velocity of the fluid is highest at the area of the blade tips and gradually reduces near the volute wall and the outlet diffuser while the pressure is raised in these areas. The low velocity region is near the wall of the inlet elbow and the outlet diffuser; however, it shows that the uniform velocity distribution and the turbulence kinetic energy in these areas are relatively low. The flow is expected to be uniform and not likely to have any stagnation or formation of coagulation in these areas. However, the performance of the pump can be improved by optimising the inlet elbow for better flow distribution to the impeller.

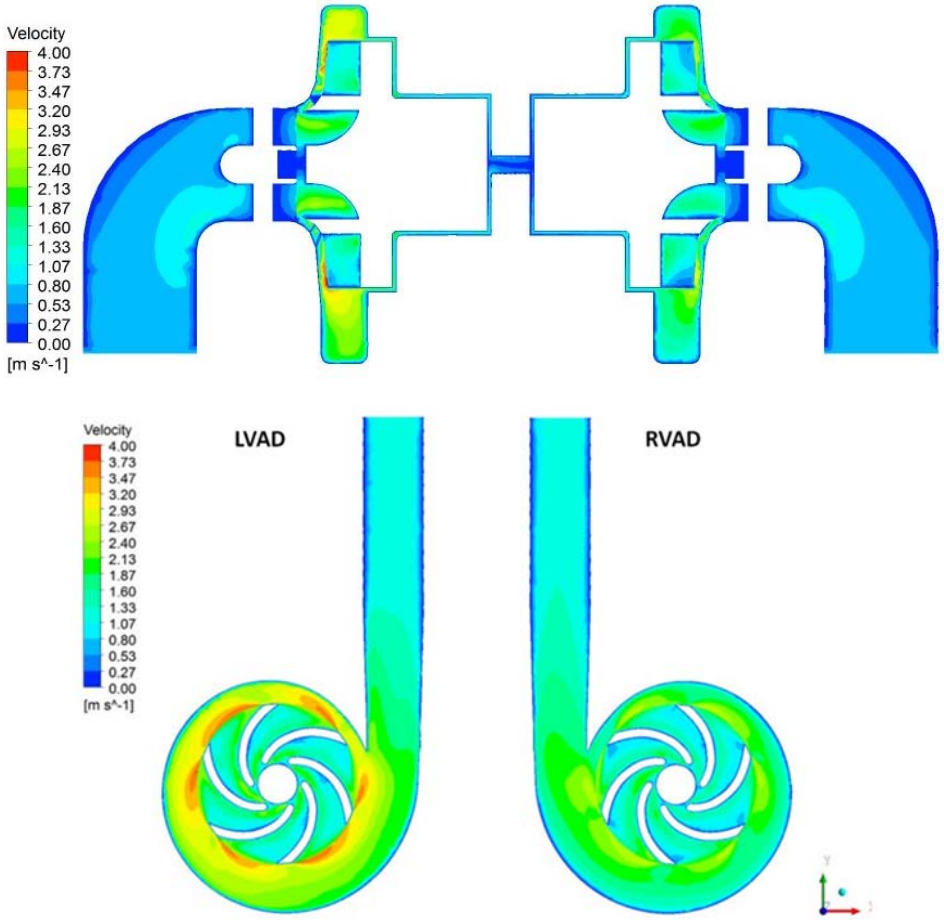

Figure 3-22: Velocity contour in section view of the LVAD, RVAD, and across the whole pump with Impeller II.

Pressure: The pressure distribution is uniform in the bend section of the inlet pipe and increases as the flow exits the vanes to the volute and diffuser area, which is the same trend as observed in the initial simulation of the single-sided VAD. In the gap around and underneath the impeller the pressure is slightly reduced, but it can be noticed that the overall pressure in this area of the LVAD is higher than in the RVAD, and this difference in pressure pushes the blood to flow through the flow passage.

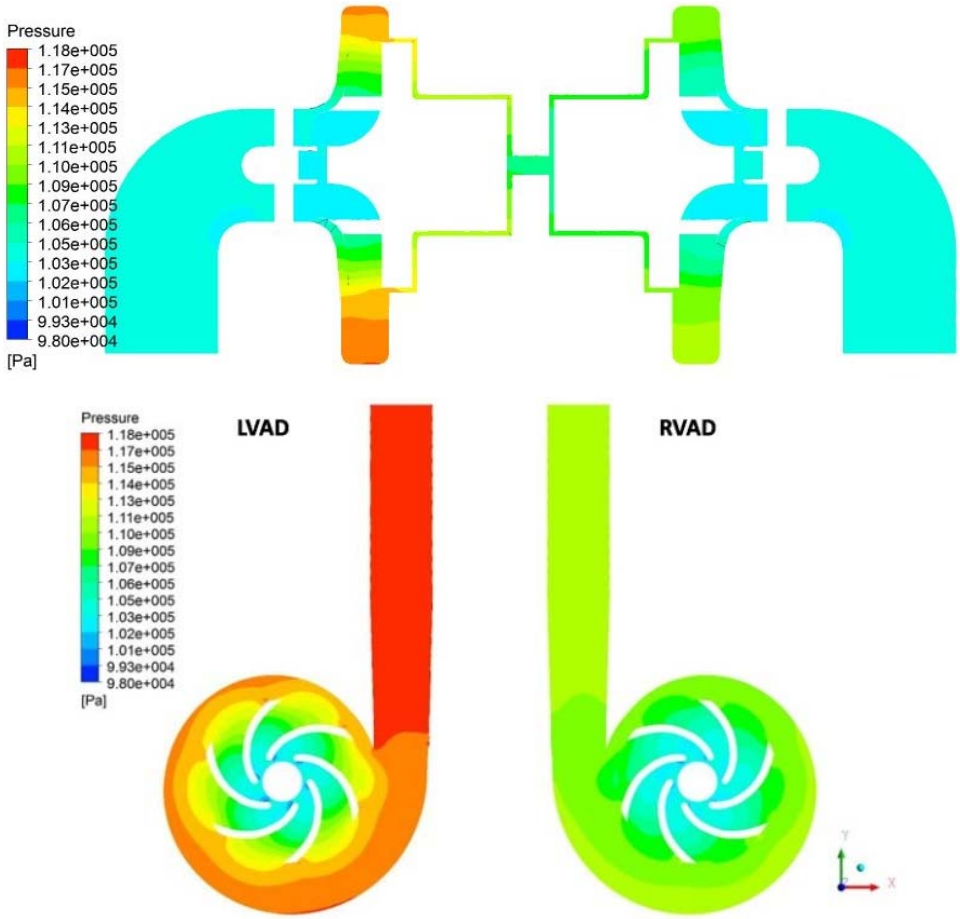

Figure 3-23: Pressure distribution gradient in section view of the LVAD, RVAD, and across the whole pump with Impeller II.

Shear stress: Shear stress is distributed similarly between the LVAD and RVAD, as shown in Figure 3-24, but the regions of high shear stress are slightly larger on the LVAD side due to the higher speed. The regions with high shear stresses are above 125 Pa and can be observed on three small areas: at the inlet magnet support parts which are above the impellers, on the leading edges of the impeller, and at the volute tongue. The information of this shear stress can be used for the blood damage calculation for the pump which will be discussed in the next section.

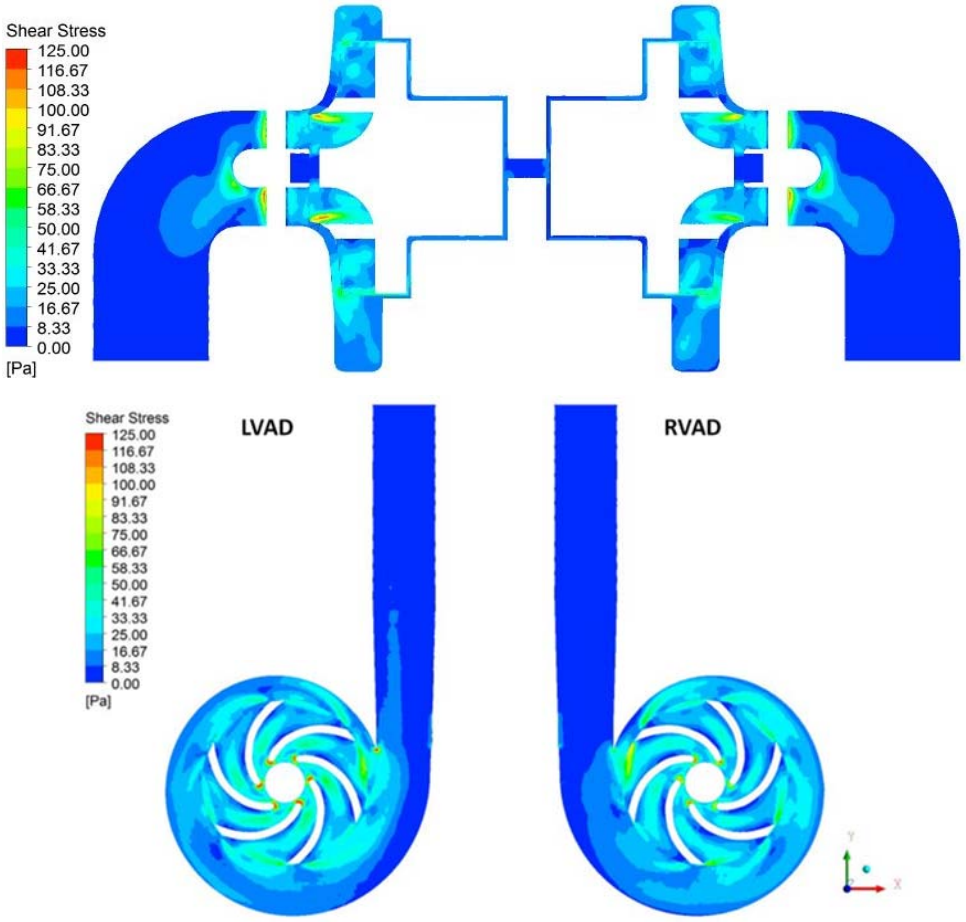

Figure 3-24: Shear stress distribution gradient in the transverse-mid plane view of the LVAD, RVAD, and across the whole pump with Impeller II.

Washout passage flow: The flow through the connecting passage can be observed from the streamlines in Figure 3-25. The leakage of blood from the LVAD rotates with the impeller movement down along the gap between the impeller and the chamber. This flow path is induced by the effect of the pressure difference between the LVAD and RVAD, as presented in the pressure distribution contour in Figure 3-26. At the bottom of the chamber, blood continues to swirl to the centre of the rotation, where it then pushes through the flow passage and continues to swirl in the same direction until the end of the passage. At the end of the passage on the RVAD side, the swirling direction of the blood then turns in a counter-direction to move along with the right impeller upward to the volute region. This flow passage could generate the washout effect smoothly without any recirculation observed on the streamlines; however, there are small regions underneath both impellers that have low flow velocity, as shown in blue colour in Figure 3-27. These areas may have the

risk of stagnation formation and should be optimized further before making the prototype.

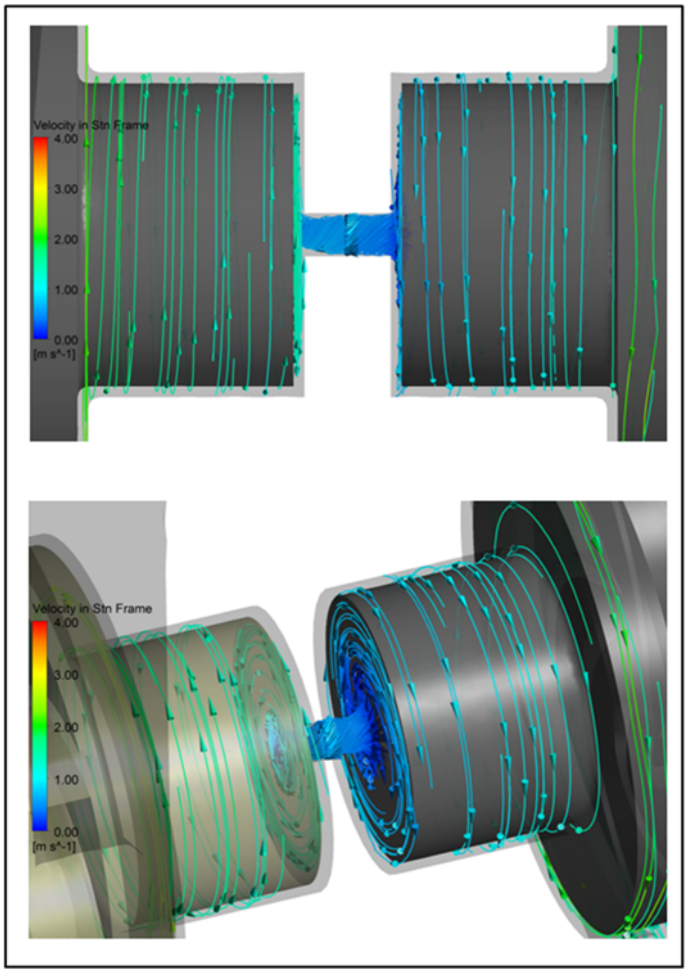

Figure 3-25: Streamlines of the blood flow from the LVAD to the RVAD.

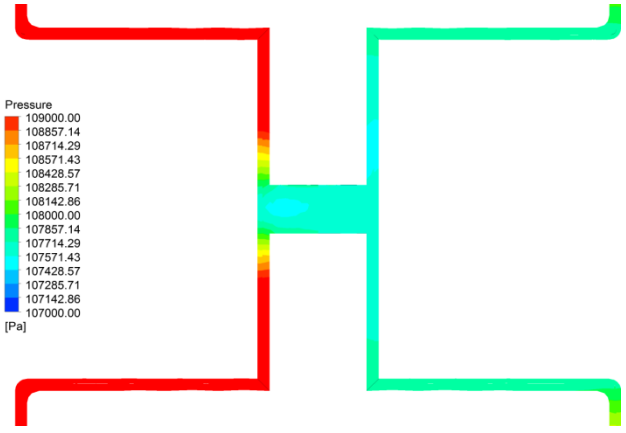

Figure 3-26: Pressure distribution in the flow passage.

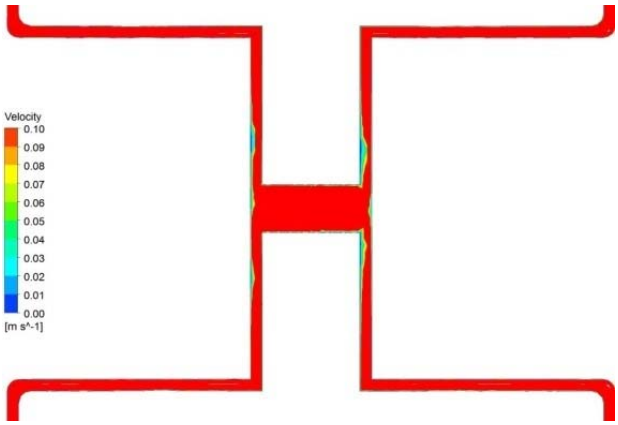

Figure 3-27: Velocity gradient in the section view of the flow passage between the the LVAD and RVAD.

IV. Hemolysis estimation

The shear stress induced hemolysis, which is the breakage of red blood cells, providing high shear stress over the time period. In reality the damage is assessed by the amount of haemoglobin released to the plasma by the damaged cells, but for the CFD simulation it could be predicted by the damage threshold which is a function of the shear stress and the exposure time of RBC.

The Eulerian method introduced by Garon & Farinas (Garon & Farinas, 2004) was used for the predicting blood damage in this simulation. In this method the blood damage was considered to be time independent and the total blood damage from the device can be calculated by the function of the average linear damage over the whole calculation domain. The NIH is then calculated and the benchmark against Nosés anti-traumatic threshold for a long term and short term blood pump at 0.01 and 0.004 g/100L, respectively (Nosé, 1998), the comparative results are shown in Figure 3-28.

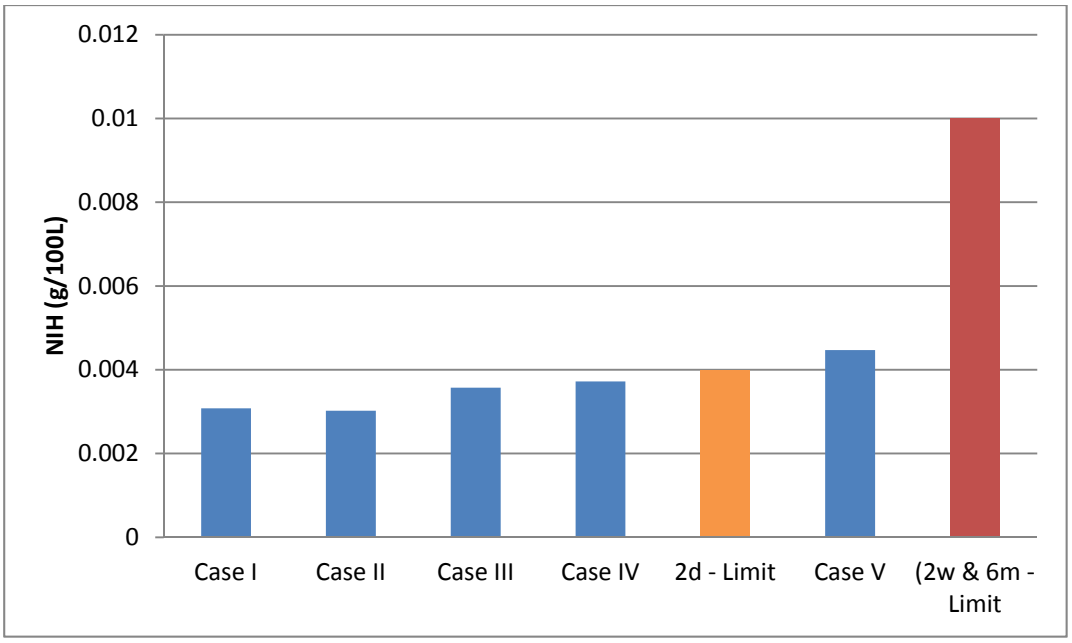

Figure 3-29: NIH prediction of all the impeller designs compared to the anti-traumatic limit.

According to the blood damage calculations, although all the impellers could pass the clinical threshold for long term use for a blood pump at 0.01 g/100L, impeller V is the only design that causes higher blood damage than the short term anti-traumatic threshold. The design of the impeller that generates the lowest blood damage is impeller II which has an NIH value of 0.00302 g/100l, while impeller I causes slightly higher blood damage with an NIH value of 0.00308g/100l. Impellers III and IV which have the 4-blade structure also generate lower damage than the limit at 0.357 and 0.00372 g/100 L, respectively.

3.5.5 BiVAD simulation conclusion

The comparison of the simulation results among the five impeller designs has presented a similar flow profile across the pump. The flow passage design could generate a smooth wash-out effect from the LVAD to the RVAD without a vortex or recirculation. Improvement to the design could be done in the low velocity region under the impeller which has the risk of forming thrombosis, and the 90^{o} inlet elbow can be improved to deliver a more uniform flow velocity to the impeller which could improve the overall performance of the pump.

The performance analysis shows that the 6-blade designs (Impellers I and II) of the pump have better performance compared with the 4-blades (Impellers III and IV) and

the splitter blades design (Impeller V) while also requiring a lower operating speed to achieve the required head on both sides of the pump. Aside from the number of blades, the cylindrical blade design has a slightly higher efficiency than the twisted blade design in this simulation condition.

Impeller II is also the best design in terms of hemodynamic efficiency as it generates the lowest blood damage and could achieve the anti-traumatic property along with impellers I, III and IV. Impeller V, although it could not be designated as an anti-traumatic short-term blood pump, is still clinically acceptable for both short and long term use on patients.

According to the hydrodynamic and hemodynamic efficiency from the simulation results, impeller II was the best design that could outperform the other designs in most aspects. Therefore it was adopted for further development of this blood pump.

3.6 DESIGN OPTIMISATION AS A SINGLE-SIDED VAD

This BiVAD concept requires a specifically designed motor which is unavailable in this stage of development. Therefore, the pump was split in half and a study was conducted on an individual side of the pump. This was possible because the pump has a symmetrical design between the LVAD and RVAD sides and the only difference is the impeller's rotating speed. This analysis was to provide insight information on the pump in a systemic and pulmonary circulation operating environment, which would be used in the design optimization before the pump could be combined together as a full BiVAD once the driving mechanism design is ready. However, splitting the pump for individual analysis meant that the washout mechanism for removing stagnation underneath the impeller needed to be redesigned as the flow passage between the chambers was no longer available. To solve the stagnation problem a new flow passage was introduced in the middle of the impeller. In this design, the centrifugal force generated from the rotating impeller will generate a secondary flow that can eliminate the stagnation by drawing the leakage of blood from the gap around the bottom of the impeller hub and then push out the primary flow at the outlet passage on the top of the impeller hub between the impeller blades.

Two designs for the passages were evaluated against the control design in this simulation to verify the change in the pump's efficiency and the fluctuation of the radial force which is significant for the magnetic suspension design. The first design has a single outlet port and the second design has two outlet ports in opposite directions. The fluid model of the passage designs is shown in Figure 3-30.

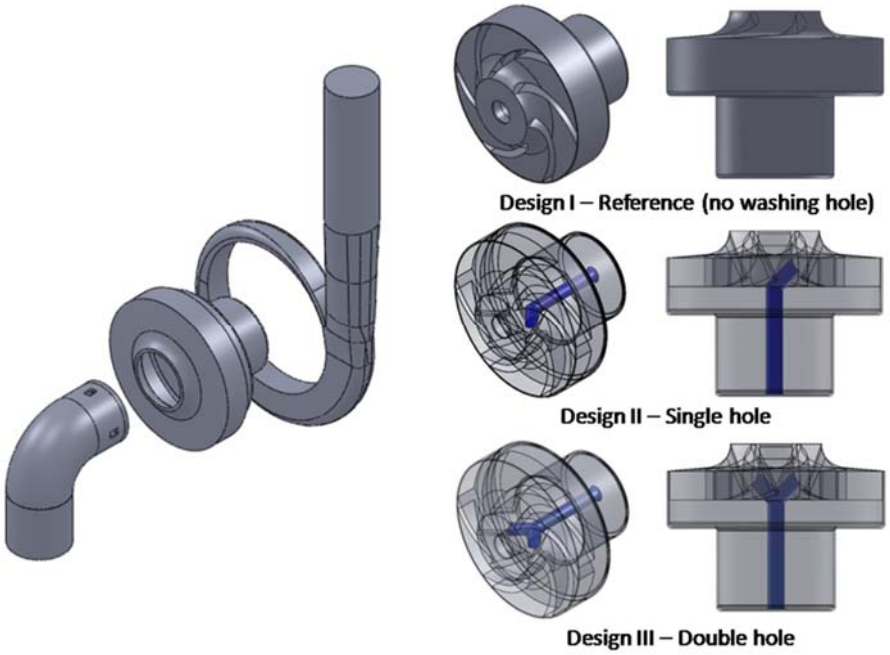

Figure 3-30: The design of the flow passage on the LVAD.

This new design of the passage, especially the single outlet design, introduced an asymmetrical structure to the impeller which could cause fluctuation of the radial force due to the outflow stream. This fluctuation needs to be closely examined as an excessive radial force could cause damage to the internal structure of the pump. In addition, the investigation of the radial force is also important for the design of the magnetic suspension system which could be implemented in this pump in the future. Therefore, the transient simulation was employed to examine the pump's operation.

3.6.1 Simulation setup

In the simulation the impeller speed was set to the design point at 4,000 rpm, the inlet and outlet boundaries are at a pressure of 780 mmHg, and the flow rate is 0.3 m^3/h; which these were the designed working conditions of the pump that were used in the previous simulation on the LVAD side.

To apply the transient simulation, the transient rotor stator was used as a mixing model on the domain interfaces. The time frame was set to 0.015 s and a total of 120 time steps were processed within the selected time frame which is equal to one revolution of the impeller. The simulation was initiated by a steady state result obtained from the initial simulation, then the solver allowed the impeller to run for 3 consecutive revolutions to reach a stable condition before starting to record the results.

3.6.2 Simulation results and discussion

I. Hydraulic force

The relationship between the pump head and impeller positions of the three cases is shown in Figure 3-31. It can be noticed that all the cases display the same head pattern over time. The amplitudes in the graph exhibit an increase cyclically of the head pressure when the impeller vanes move across the diffuser port. There is a small shoulder in the signal during the decline of the head pressure as the trailing edge of the blades approach the volute tongue. Both of the designs with the washout holes express a slight loss on the head pressure, presumably due to the leakage flow through the washout hole; however, the loss is very small as it is less than 1% for both designs and, thus, it could be considered as not significant.

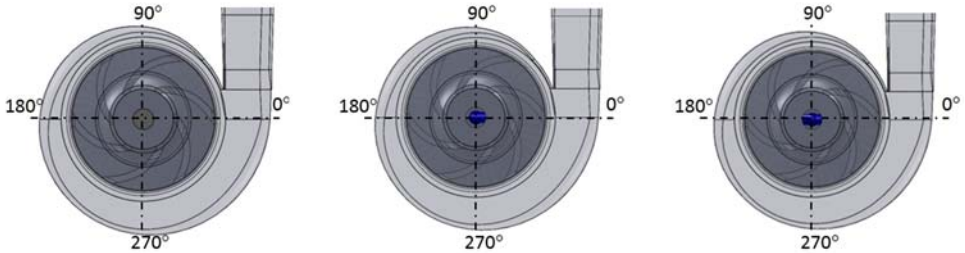

Design I (Ref) Design II Design III

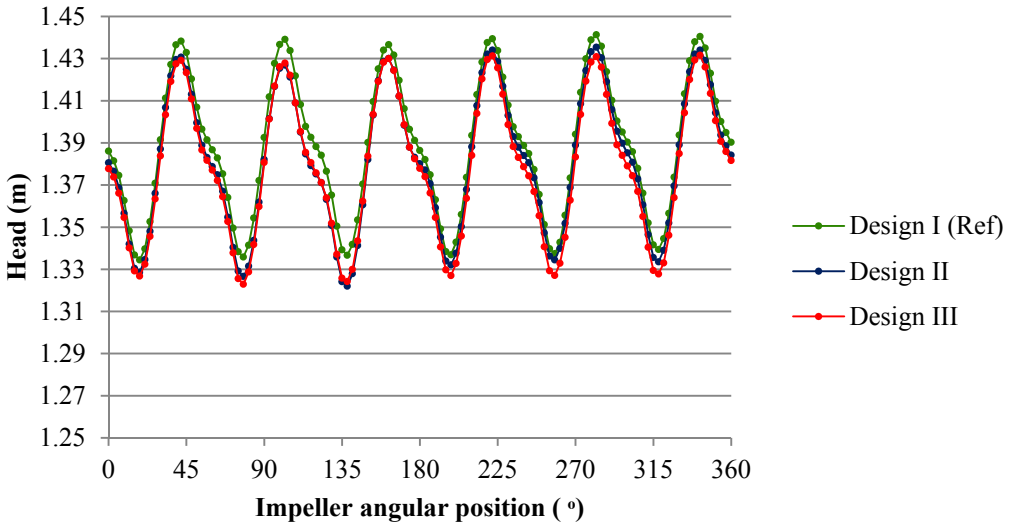

Figure 3-31: Head vs. impeller angular position of 3 washout hole designs

A similar cycling pattern can also be seen in the change in the pump's efficiency over time (Figure 3-32). There is a small fluctuation in the efficiency of the designs with a washout hole, and the leakage flow through this passage also reduces the pump's efficiency slightly. The average efficiency predicted from the simulation on revolution is 56.37%, 56.26% and 55.84% for designs I, II and III, respectively.

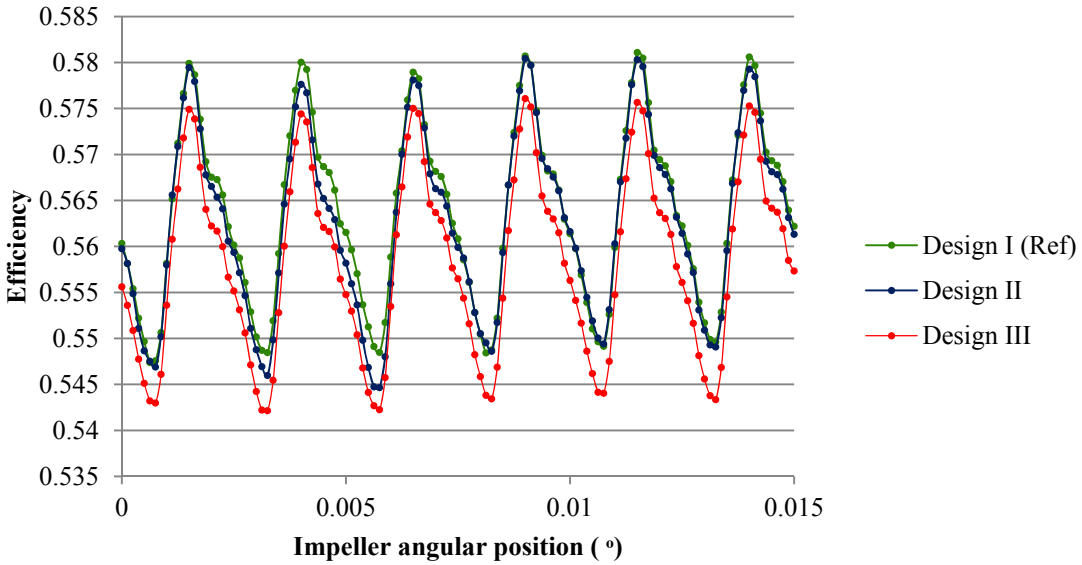

Figure 3-32: Pump efficiency vs. impeller angular position

The outflow from this new washout hole affects the magnitude and direction of the radial force, as shown in Figure 3-33 and Figure 3-34. The reference design

without a washout hole presented an almost steady cyclical pattern of force when the impeller rotates. This force is disrupted by the outflow from the washout hole and causes more fluctuation to the force direction, as clearly seen on the polar coordinate plots. However, the magnitude of force is very small compared to the other forces on the impeller.

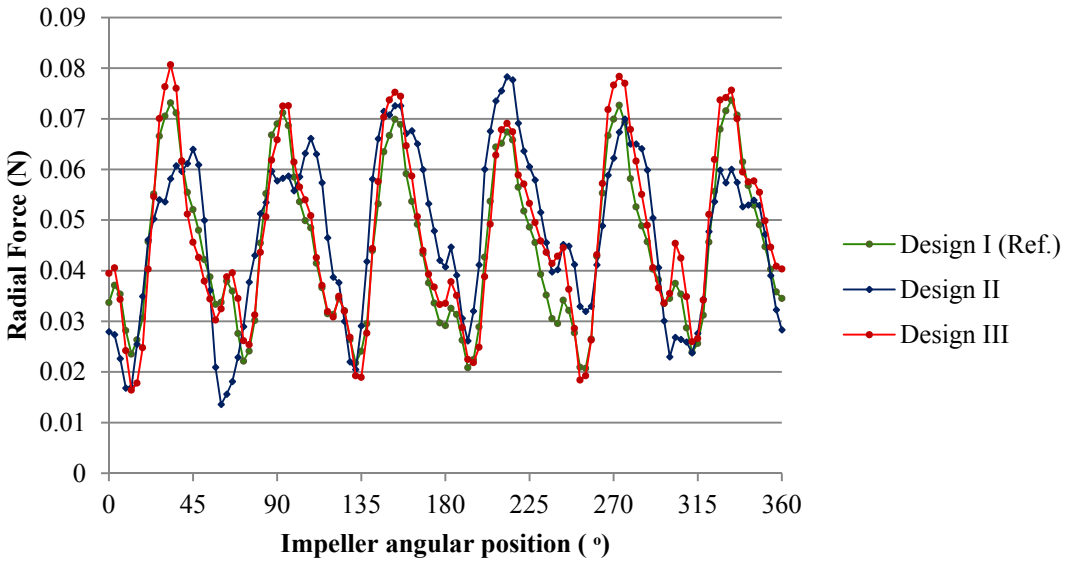

Figure 3-33: Radial force vs. Impeller angular position

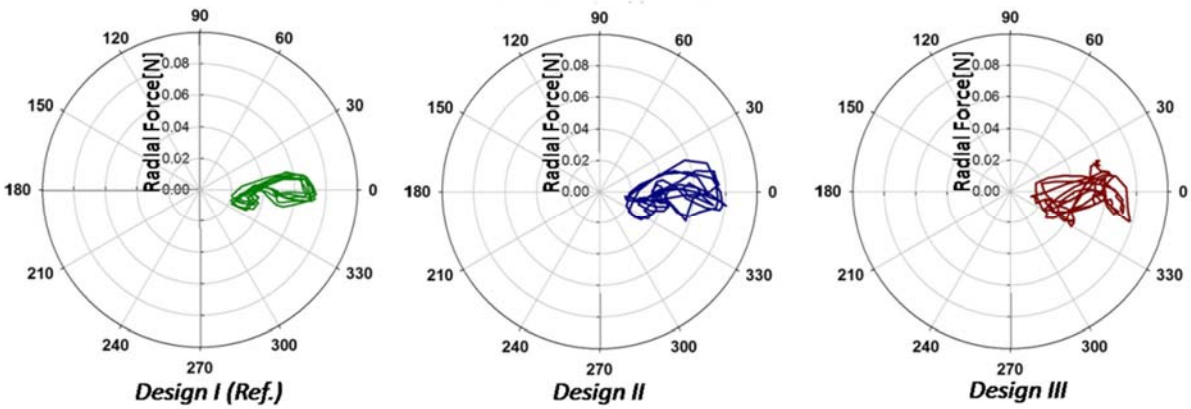

Figure 3-34: Radial force trajectories on the polar coordinates.

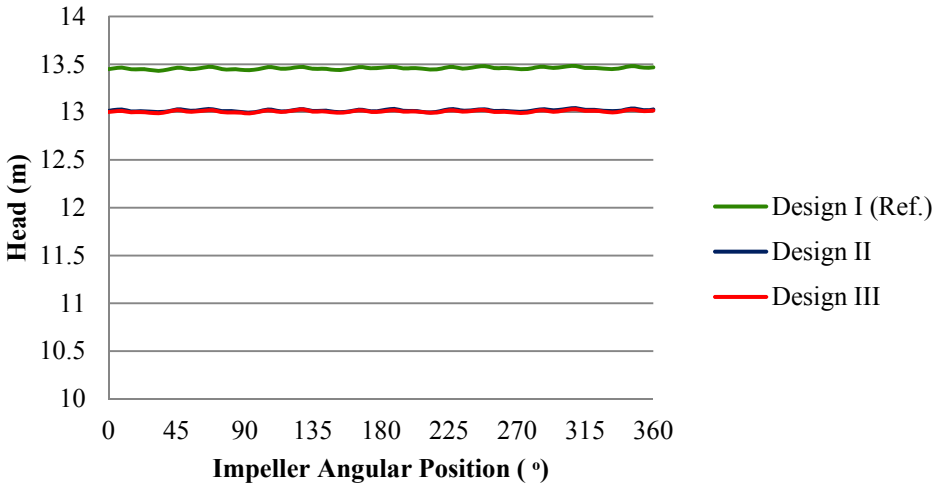

Figure 3-35: Head pressure vs. Impeller angular position

Figure 3-35 shows the axial forces (F_Z) of all designs and they are relatively large compared to the radial forces. The unbalanced design of the washout hole did not cause any significant fluctuation on the axial forces as it did on the radial coordinate. However, the force exerted on the impeller for both designs with a washout hole is lower due to the counter-direction force from the retrograde flow in the passage. According to the results, the axial force of Design III is slightly lower than Design II with average forces of 13.007N and 13.016N, respectively, while the average axial force of the reference design is relatively high at 13.459N.

II. Washout passage flow

The streamlines distribution in Figure 3-36 depicts the flow pattern under the impeller area and inside the washing hole. In the reference design, the fluid circulate in this region at high velocity near the edge of the impeller and at very slow velocity near the center of the rotation without making any progress upwards and back to the top region of the impeller. This stagnant and recirculation flow pattern could cause platelet deposition which leads to a high risk of thrombus formation in this area. The washout passage in design II and design III overcomes this problem by creating leakage flow from this clearance gap upwards to the region of the blades; according to the flow pattern, blood could swirl through this passage towards the outlet near the leading edge of an impeller without a vortex being observed in the flow field. Considering the flow profile in the passage of Design II, blood continues swirling

throughout the passage, while the streamlines of the fluid flow in design III become more uniform after the separation of the passage.

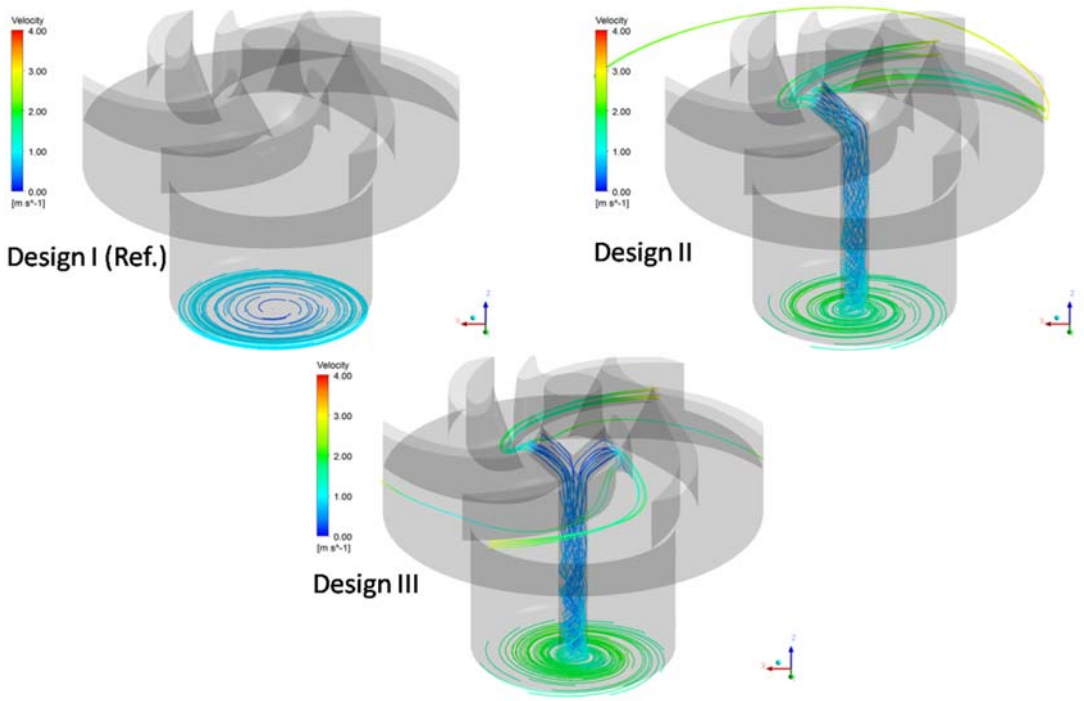

Figure 3-36: Streamlines comparison in each washout hole design

Figure 3-37 displays the velocity contour in the cross-section view of the pump at different impeller positions. The blue regions' appearance near the passage outlets of design III indicate possible stagnation areas which were not washed out during the rotation of the impeller. Stagnation was not found in the washout hole of design II as the single-hole design creates a larger pressure difference across the passage, as shown in Figure 3-38, and thus makes a slightly higher flow rate through the passage, which helps wash out the stagnation flow. The average flow rate through the hole for design I and design II during one revolution is 0.00577 m^3/h and 0.00496 m^3/h, respectively, which is considered to be only about 2% of the blood flow rate through the pump.

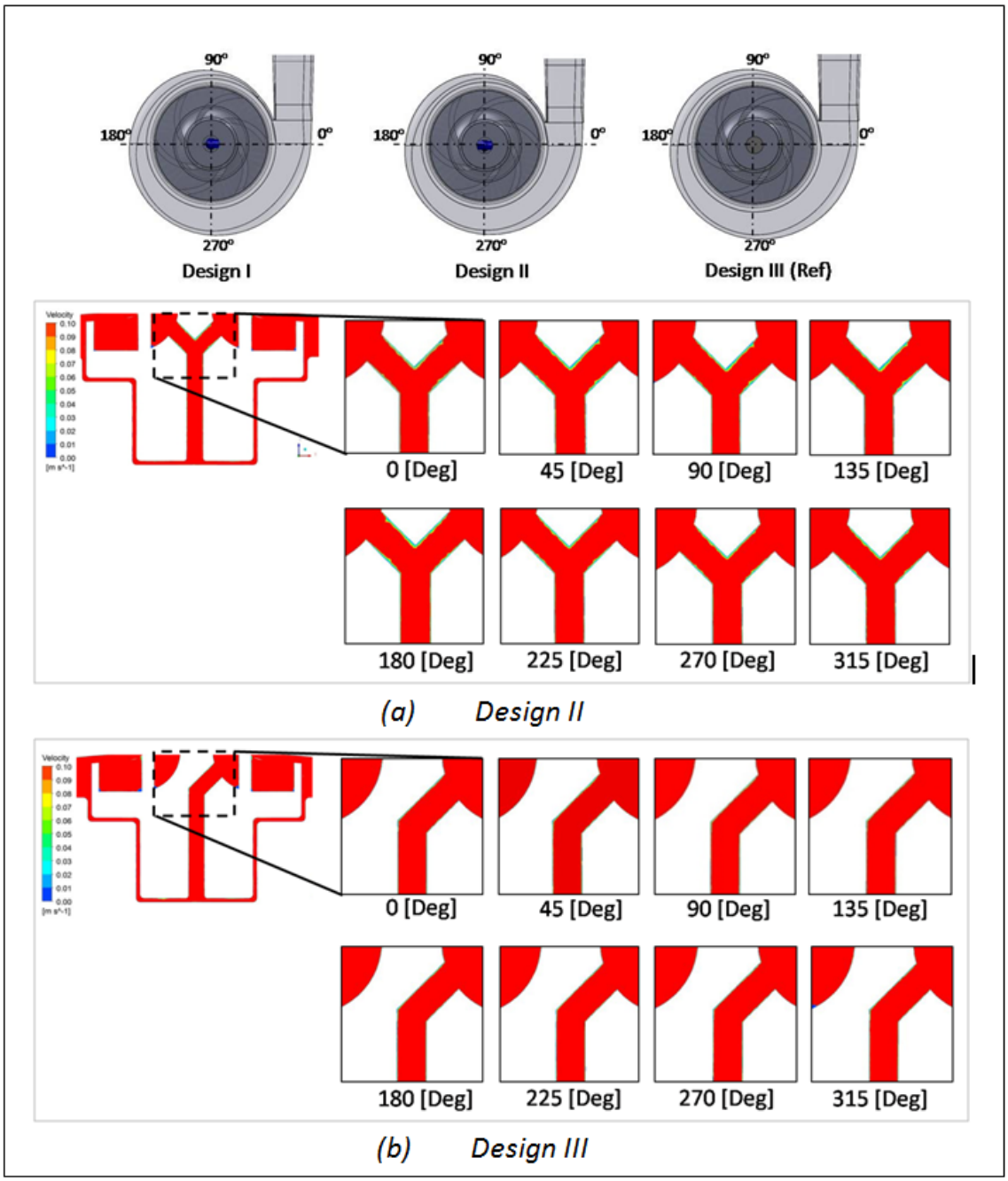

Figure 3-37: The section view of velocity contour within the washout hole at different angular position of impellers.

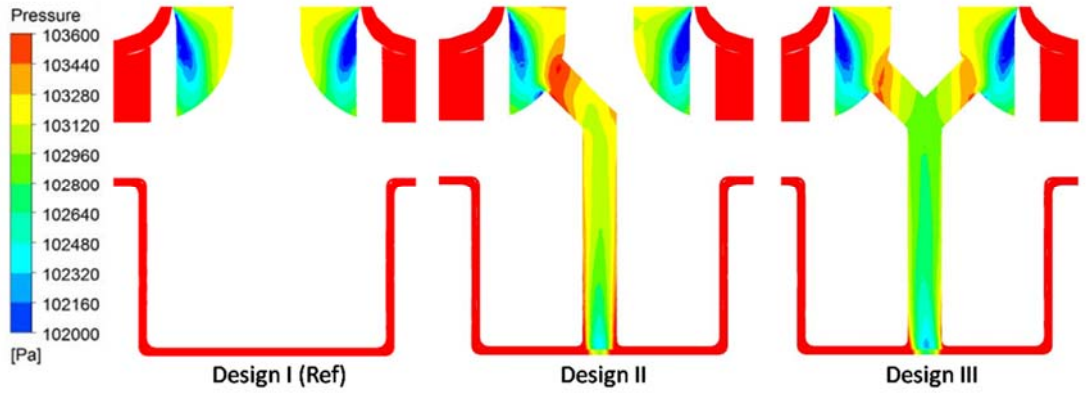

Figure 3-38: Pressure distribution in the vertical-section view of the pump

III. Hemolysis

The hemolysis of this simulation was calculated from the shear stress information at each time step and plotted against the impeller angular position as shown in Figure 3-39.

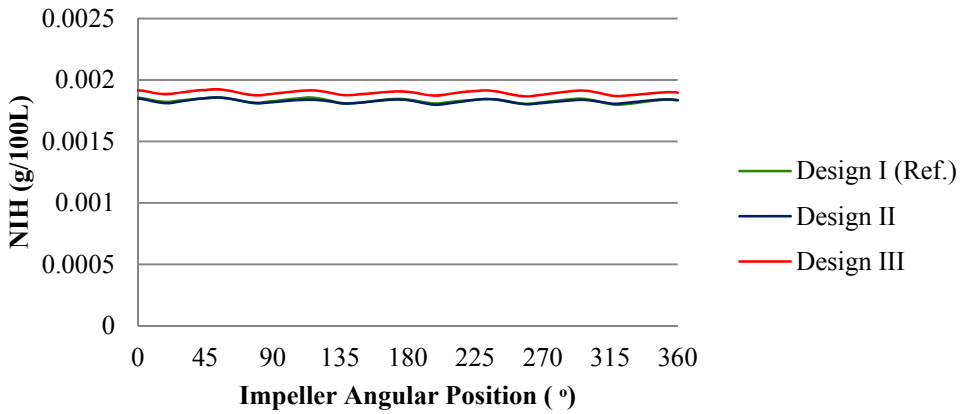

Figure 3-39: NIH vs. impeller angular position

Considering the comparison of the above cases, all the cases can achieve the required hemolysis specification. The reference design and the single hole design generate almost the same level of blood damage with the NIH of 0.001831g/100l and 0.001287, respectively, while design III causes the highest damage to the blood cells. However, the difference between the cases is so small that it can be considered as not significant and all the designs are acceptable in terms of hemolysis.

Summary

According to the simulation results, Design III which has double washout holes presents a slightly lower efficiency than the single hole and the reference designs. Moreover, from the velocity contour in Figure 3-37, there are low velocity regions present on the surfaces within the holes. These regions have a risk of forming thrombosis as the simulation result of the different impeller positions shows that these stagnations could not be washed out by the rotation of the impeller. Therefore, Design II with a single hole was selected as the prototype due to its better hemodynamic performance.

3.7 FINAL REFINEMENTS AND SIMULATION FOR THE PROTOTYPE

The design optimisation at this stage was conducted by aiming to produce the final prototype of the working product by considering the machine capability and available resources as the main priorities.

3.7.1 Pump structure

I. Driving mechanism

With the lack of a proper pump driving mechanism that requires a specifically designed magnetic pump control system, the magnetic levitating function of the impeller cannot be accomplished for the current development. The design for the prototype and in-vitro evaluation were continued based on a single-sided pump by running on the motor of a commercial magnetic drive pump Iwaki MD-10-230GS0 which is a small 30W DC pump for general application. Therefore, the external structure was redesigned to be able to fit on the motor's structure while the impeller hub was adjusted to accommodate the new ferrite ring magnet for the driving mechanism.

Figure 3-40: Iwaki MD-10-230GS0 motor for the VAD

II. Bearing and Shaft design

The magnet of this motor can provide the driving force for the impeller but it is not strong enough to create the magnetic bearing suspension; therefore, the support bearing needed to be redesigned to control the axial position of the impeller while a shaft needed to be added to restrict the radial movement. To solve these problems, a pivot bearing was introduced to support the top of the impeller by adding a truncated cone-shaped tip on top of the impeller which can fit on the female socket that is embedded on the flow straightener to work as a pivot joint, as shown in Figure 3-41. At the bottom of the chamber, 6 small static blades were added to support the impeller and help regulate the blood to flow smoothly to the passage at the impeller's centre (Figure 3-42).

To control the radial position, a small pin was added in the centre at the bottom of the chamber to function as a shaft that restricts the radial movement. The position of the bending angle in the washout hole was moved down towards the pin, as shown in Figure 3-43, so the centrifugal force could effectively pull the vortices that might form at the tip of the pin.

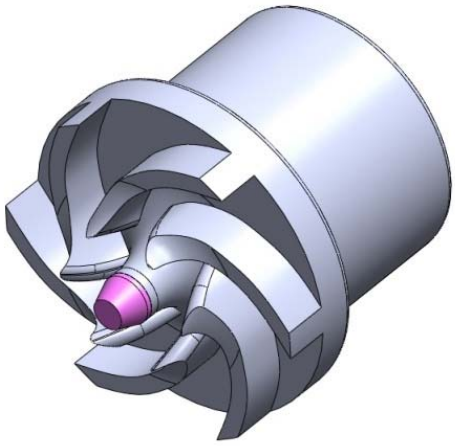

Figure 3-41: An impeller with a truncated cone tip as a pivot bearing.

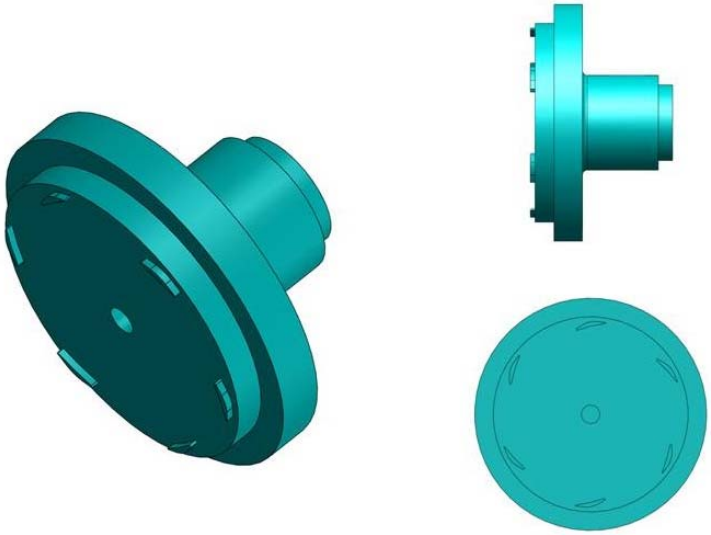

Figure 3-42: Bottom support part of the impeller with static blades.

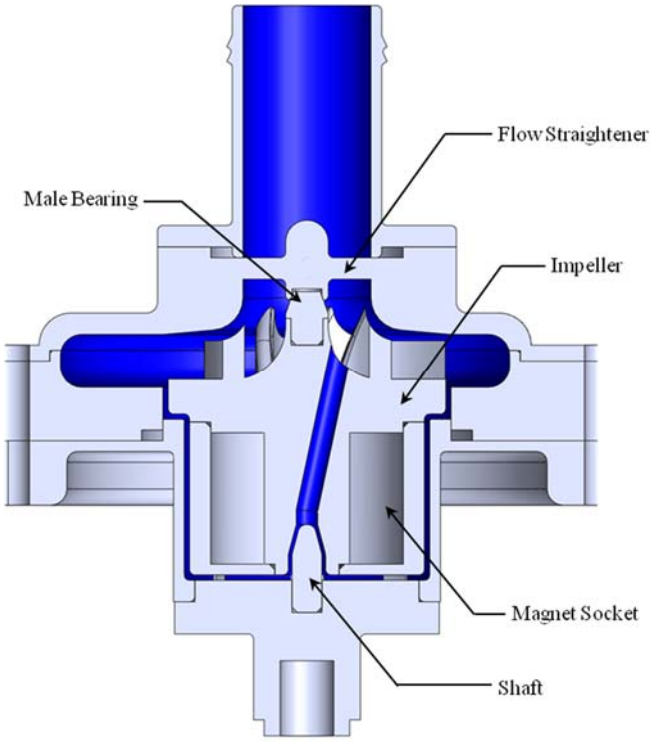

Figure 3-43: Section view of the pump structure.

III. Inlet pipe

As the pump now functions as a single pump, the 90° elbow which was originally designed to provide the same inlet direction to save space in the BiVAD is no longer required. The inlet was changed to a straight pipe which helps avoid the low flow region experienced in the elbow inlet corner and also provides a more uniform flow to the impeller which could improve the overall pump efficiency.

IV. Chamber

The pump was produced by a CNC milling machine as it could produce a highly accurate prototype at low cost which is suitable for further refinements if any minor change needs to be made in the pump design. However, there are several positions in the original pump design that could not be machined by this method such as the internal volute of the pump or the tiny impeller supports at the bottom of the pump for which there is not enough open space to enable the milling cutter to reach the surfaces. Therefore, the chamber was split into 4 parts, as shown in Figure 3-44, while the outlet pipe was also separated to an individual part that can slide to fit on the outlet diffuser to lock the two top parts of the chamber together.

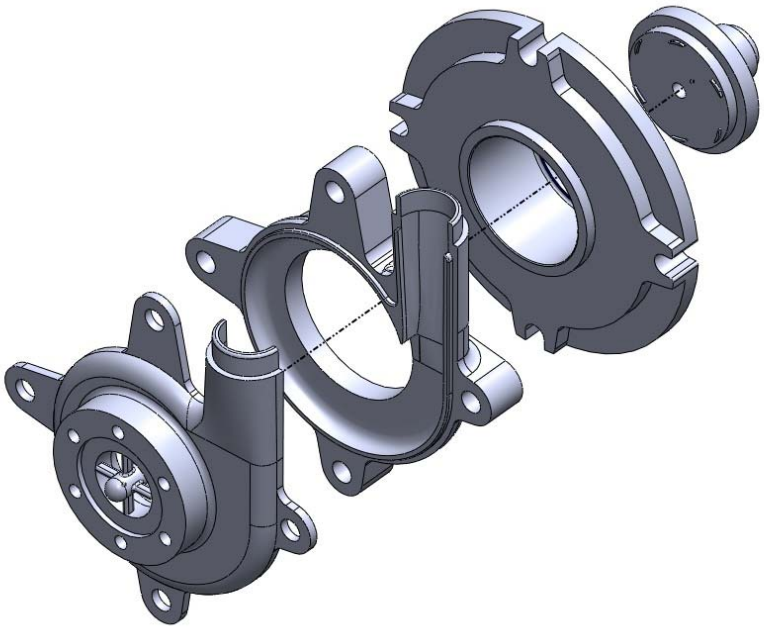

Figure 3-44: Components of the pump chamber.

The complete prototype model of the pump after design optimization is shown in Figure 3-45.

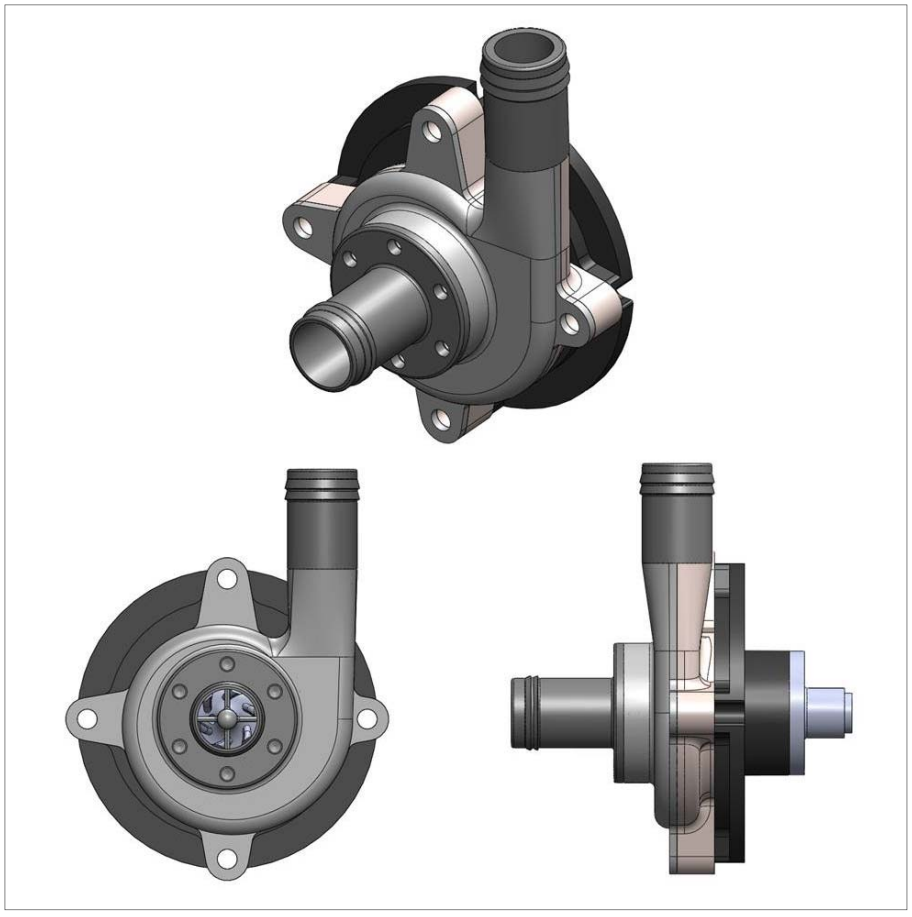

Figure 3-45: Final model for the pump prototype.

This design was based largely on the limitation of materials and the manufacturing capability process. In the final commercial product of this pump, the manufacturing could be changed to a more effective method such as molding injection or 3D printing that is capable of creating a chamber as a single piece without requiring screws and seals to assemble the parts together.

3.7.2 Simulation setup

The simulation of this pump was conducted as a final confirmation to ensure that the new pump design could achieve the required performance before producing the prototype; therefore, the pump was evaluated under the off-design conditions and more analytical analysis was done to ensure that the pump performed as intended and also to gather more information for future improvement. The simulation in this stage was conducted with the updated ANSYS 14.0 version.

I. Fluid model

The fluid model of this new pump design was adjusted according to the changes of the pump's components, as shown in Figure 3-46. It included the new pump design structure which has a straight inlet pipe and a new washout hole structure including the shaft, pivot bearing, and static blades to support the bottom of the impeller.

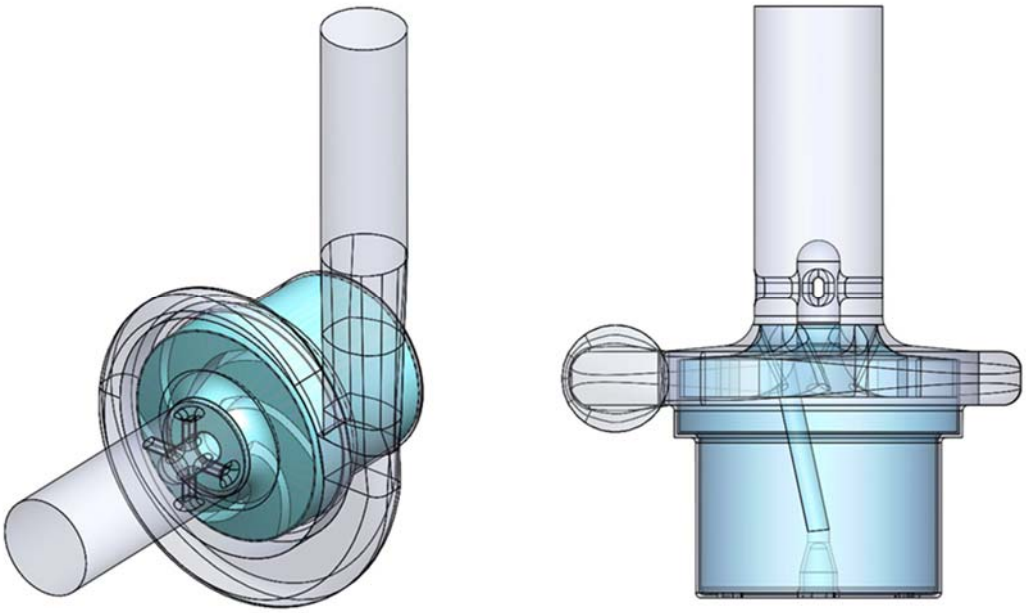

Figure 3-46: The transparent fluid model shows the impeller and the internal flow passage.

II. Meshing model

The meshing continued to be conducted by the ICEM CFD using the unstructured tetrahedral mesh and the mesh size is controlled by the face sizing method on the areas that require fine meshes. The stator model of this VAD contains 1,160,059 elements which is close to the number of elements of the previous simulations. However, on the rotating domain the number of elements was increased to 1,013,883 elements which is almost a 1:1 ratio with the stator elements because of the more complex areas at the bottom support of the impeller, the region around the shaft, and along the washout passage; these areas comprise many small parts and gaps which required a high density of elements to accurately simulate the near wall flow effect. The mesh models of the stator and rotor of this VAD are shown in Figure 3-47 and Figure 3-48, respectively.

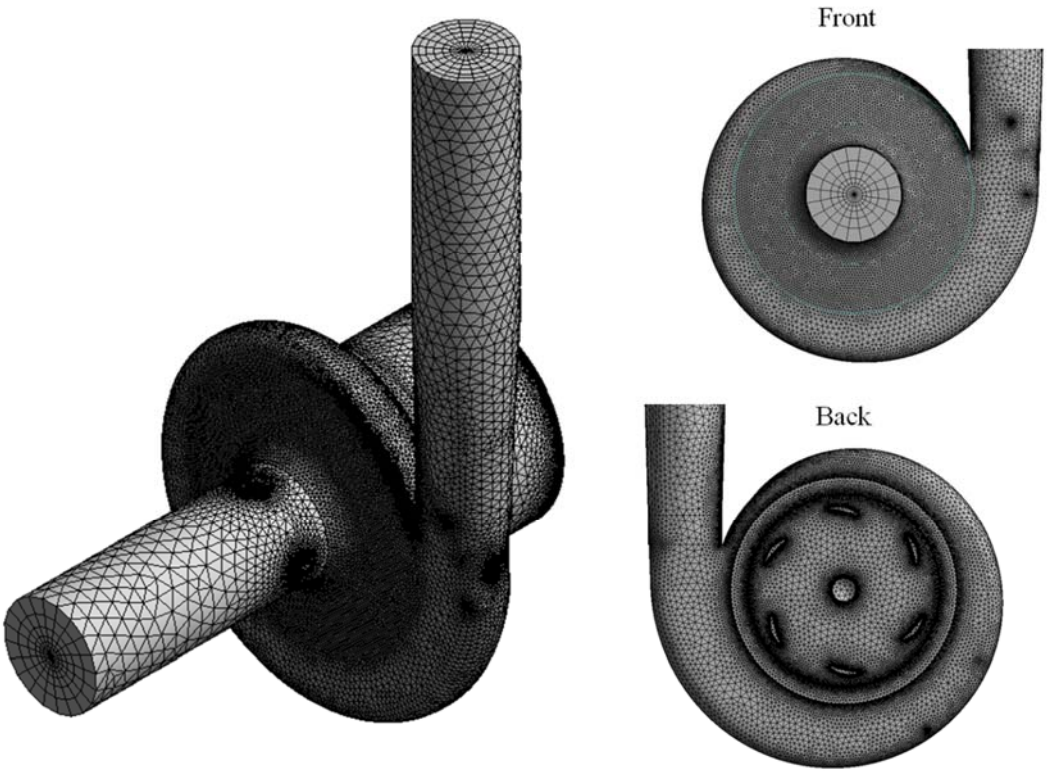

Figure 3-47: Meshes on the stator.

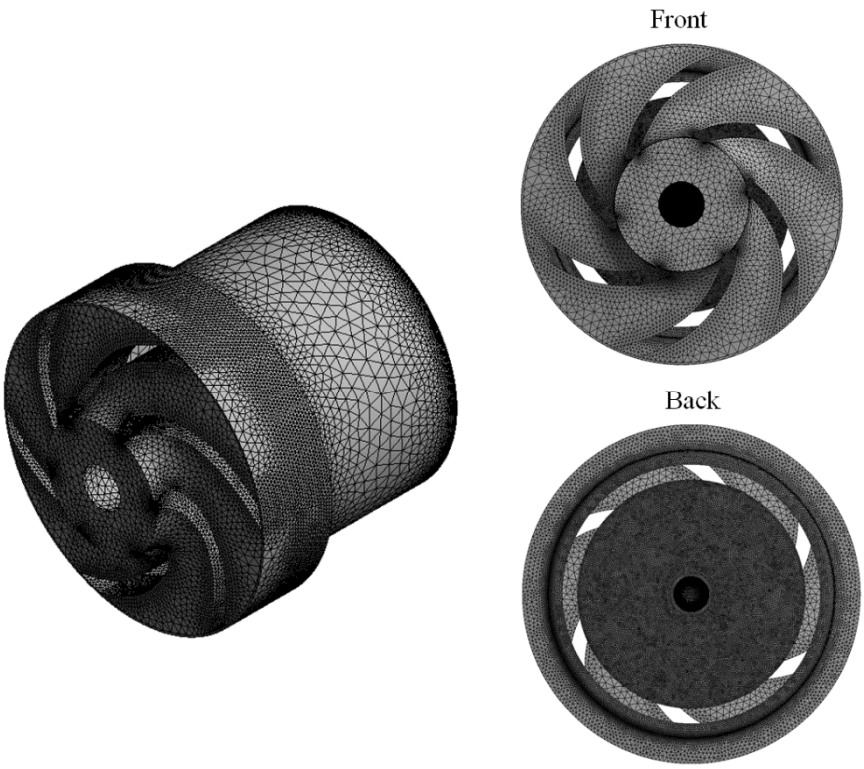

Figure 3-48: Meshes on the rotor.

III. Boundary conditions

As was discussed earlier that the current design of the pump could function as both the LVAD and RVAD by adjusting the pump speed to deliver the required head pressure, the simulation in this stage also needs to be conducted to verify the performance of this prototype design on both pump functions.

In order to improve the accuracy of this simulation for the actual pump within the human body, the boundary conditions have been slightly adjusted to reflect the pump's working environment in the systemic and pulmonary circulations, as follows:

Inlet: At the inlet, the boundary was specified by the Cartesian velocity component of the flow, which is related to the volumetric flow rates that varied between 0.15, 0.18, 0.24, 0.30, 0.36 and 0.42 m^3/h, to find the pump characteristics under the different flow rates. The k-ε model was still used as a turbulence model for this simulation.

Outlet: The outlet boundary is specified using static pressure; for the LVAD, the outlet of the pump has to be connected to the aorta for the systemic circulation

arterial, thus the mean arterial pressure (MAP) was defined for the outlet boundary pressure. Similarly for the RVAD, the right pump is connected from the right ventricle of the patient to the pulmonary venous system; therefore, the mean pulmonary artery pressure (MPAP) (McNeil, Dunning, & Morrell, 2003) was used as the RVAD outlet boundary.

Impeller rotation speed: A series of simulation was conducted to find the new pump speed for this modified pump design to achieve the required head pressure. It was found that the speed has to be slightly increased to compensate for the additional loss of the impeller support fans and the washout hole. Therefore, the pump speed for this simulation was set to 4020 rpm on the LVAD and 3070 for the RVAD to generate the required head pressure.

Table 3-7: Boundary condition of the single sided VAD prototype simulation.

Location		LVAD	RVAD
Inlet	Boundary type	Inlet	Inlet
	Boundary Detail	Normal Speed: 'Flow Velocity$_{inlet}$' m/s	Normal Speed: 'Flow Velocity$_{inlet}$' m/s
	Turbulence Model	k-ε	k-ε
Outlet	Boundary type	Outlet	Outlet
	Boundary Detail	Static Pressure 100 mmHg	Static Pressure 50 mmHg
Impeller	Speed	4020 rpm	3070 rpm

3.7.3 Simulation results

The simulation results are shown and discussed in this section for the current pump's performance and the possibility of future development. However, as the impeller position is almost fully restricted by the shaft, pivot and base supports, the radial and axial force acting on the impeller is thus not considered for this design.

I. Hydraulic efficiency

The hydraulic efficiency shown in the relationship of the flow rate to the head, hydraulic power and hydraulic efficiency are shown in the graphs from Figure 3-49 to Figure 3-51.

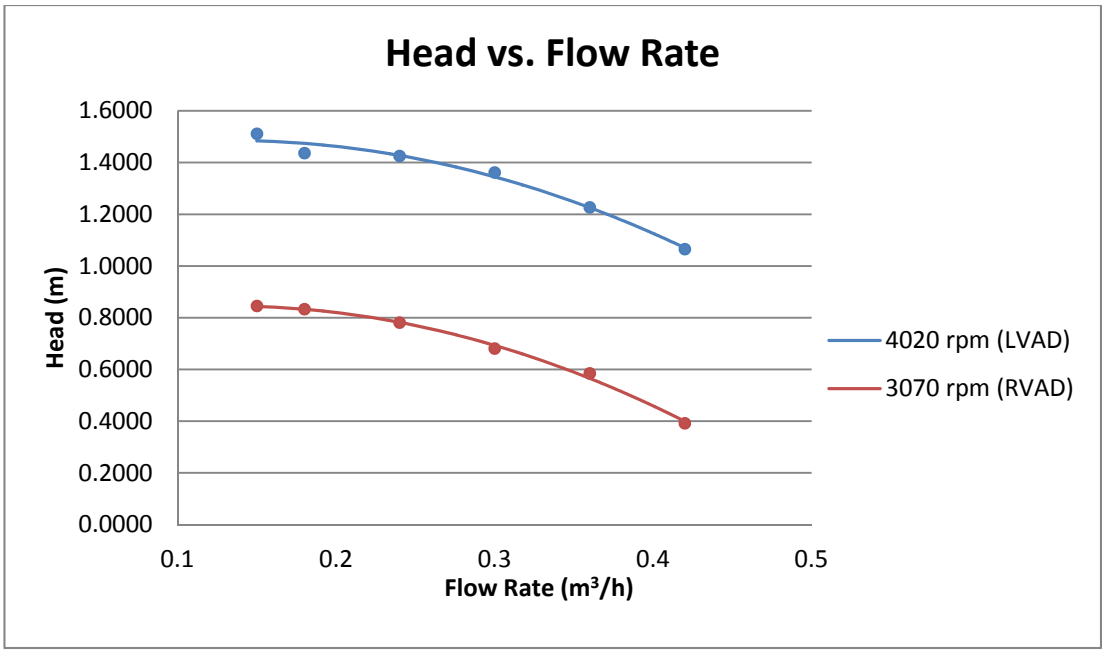

Figure 3-49: The plot between pressure head vs. flow rate on the LVAD and RVAD operating speed

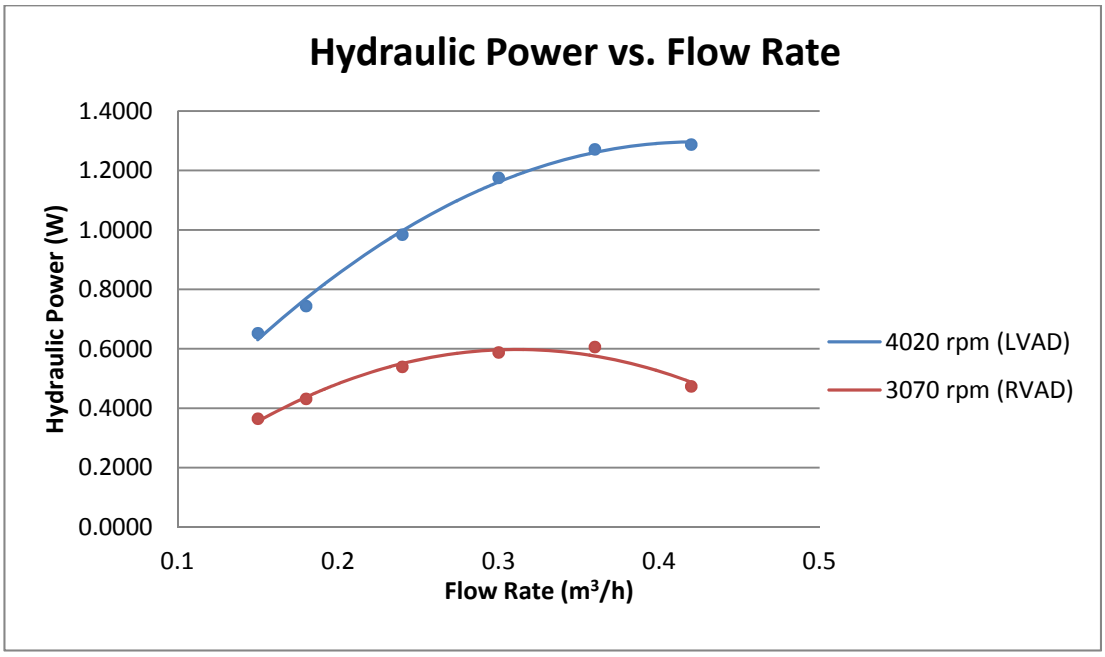

Figure 3-50: The plot between hydraulic power vs. flow rate on the LVAD and RVAD operating speed

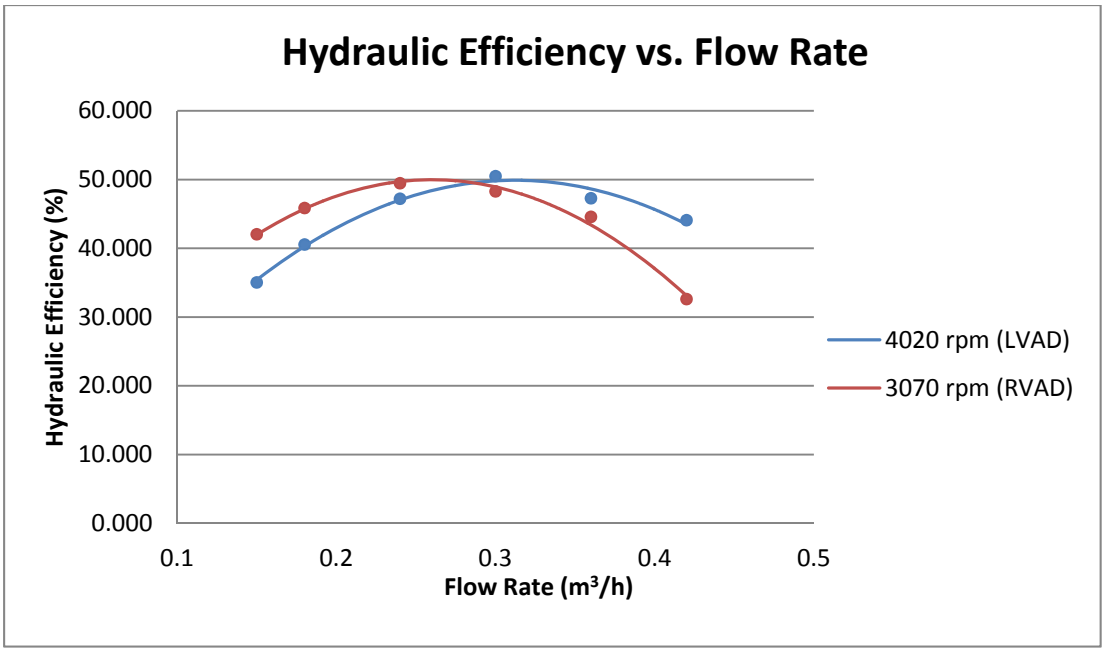

Figure 3-51: The plot between Hydraulic Efficiency vs. Flow rate on the LVAD and RVAD operating speed

In the real operational environment of the pump the LVAD would operate at the estimated flow rate of 5 l/min (0.3 m^3/h) while the RVAD would provide a pulmonary flow at an estimated 4 l/min (0.24 m^3/h). These flow rates were set for the pump operation point although there would be some variation between the conditions of heart failure and physical activities. According to the simulation results, the pump could generate the LVAD with the required head pressure of 1.36 m at a flow rate of 0.3 m^3/h and at a speed of 4,020 rpm while the RVAD head of 0.68 m was achieved by the pump at a speed of 3,070 rpm at the designed flow rate of 0.24 m^3/h. The pump also shows the best efficiency at these operating points with 50.50% and 49.47% for the LVAD and RVAD, respectively.

Comparing these parameters with the levitating impeller in the previous BiVAD concept simulations, the efficiency of this design is reduced by 4.6 % for the LVAD and 3.7 % for the RVAD under the same flow rate.

II. Overview of the pump and passage flow at the design condition

The inflow streamlines in Figure 3-52 represent the overview of the flow distribution within the pump under the design condition of the LVAD. It can be seen that the stream flow in the inlet pipe is distributed uniformly in the design condition. Some of the flow could leak down the impeller-chamber gap to the washout hole and

swirl around the shaft and through the washout passage back up to merge with the primary flow stream in the impeller vanes. The estimated flow rates through this passage on the LVAD and RVAD are 0.0010 - 0.0015 m^3/h and 0.008 - 0.001 m^3/h, respectively.

According to the streamlines plots in Figure 3-52 and Figure 3-53, there is no recirculation of the blood flow observed in this design condition; however, the streamlines show that the flow is not fully uniform when exiting the outlet port. This leaves some possibility for an improvement in the future optimization.

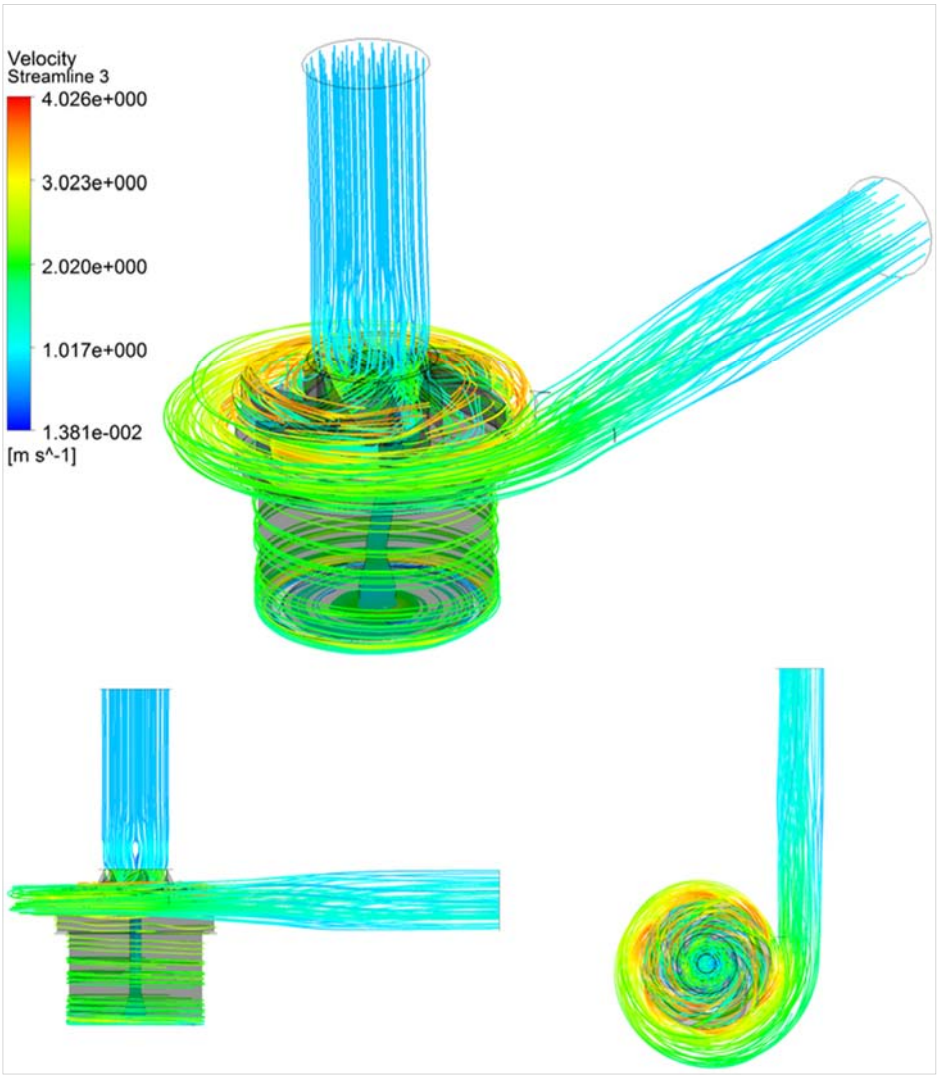

Figure 3-52: Flow streamlines from the LVAD at flow rate 0.3 m^3/h

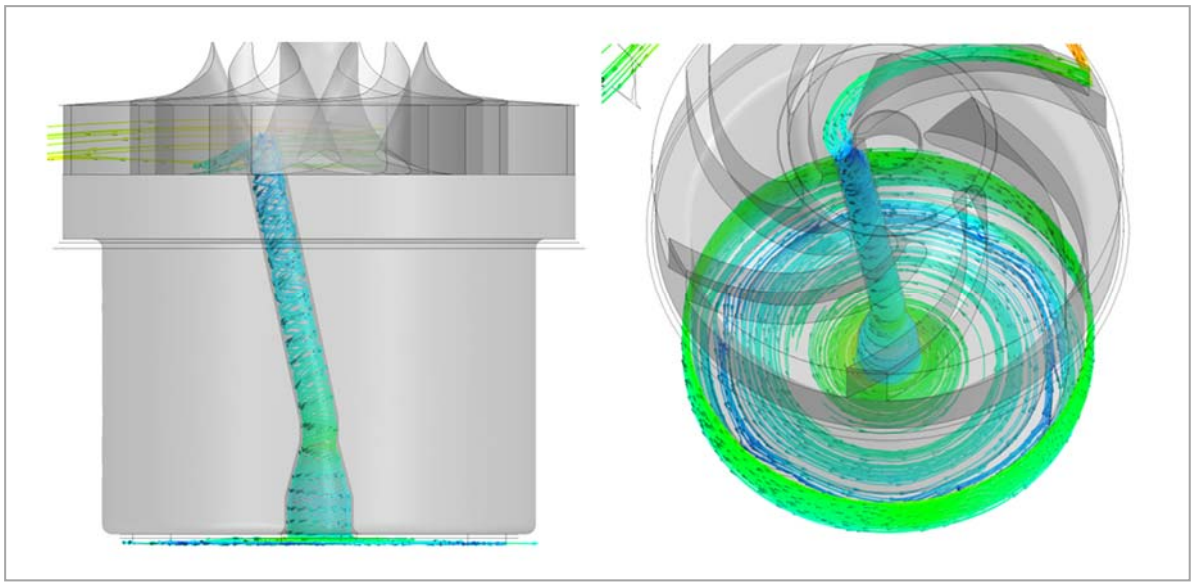

Figure 3-53: Streamlines of the flow from the bottom region of the impeller through the washout hole

III. Pressure distribution

The contour plots of pressure on the transverse-mid plane and vertical plane Figure 3-54 to Figure 3-57) show similar distribution patterns between the LVAD and RVAD with a larger magnitude on the LVAD side in response to the higher pump speed. On the transverse-mid plane (Figure 3-54 and Figure 3-56), the pressure is distributed almost equally in each vane, with a higher pressure on the pressure side of the blades, and it is gradually raised when blood flows toward the vane exit and the outlet port, while there is also observed high pressure in the near wall region of the volute casing when the pump operates at the above design points. On the vertical plane (Figure 3-55 and Figure 3-57), it can be seen that there is a pressure difference between the higher pressure in the bottom area of the impeller and the negative pressure induced by the centrifugal force at the impeller eye and within the washout passage, which creates a suction force that draws the blood flow through the washout passage and creates a secondary flow within the pump, as previously shown in the streamlines plots.

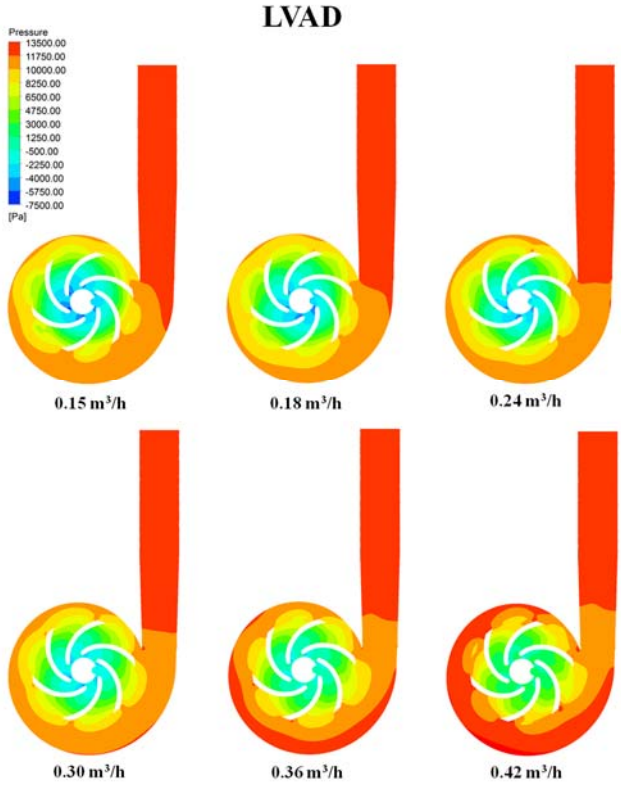

Figure 3-54: Pressure contour plot of the LVAD under different flow rates on the transverse-mid plane

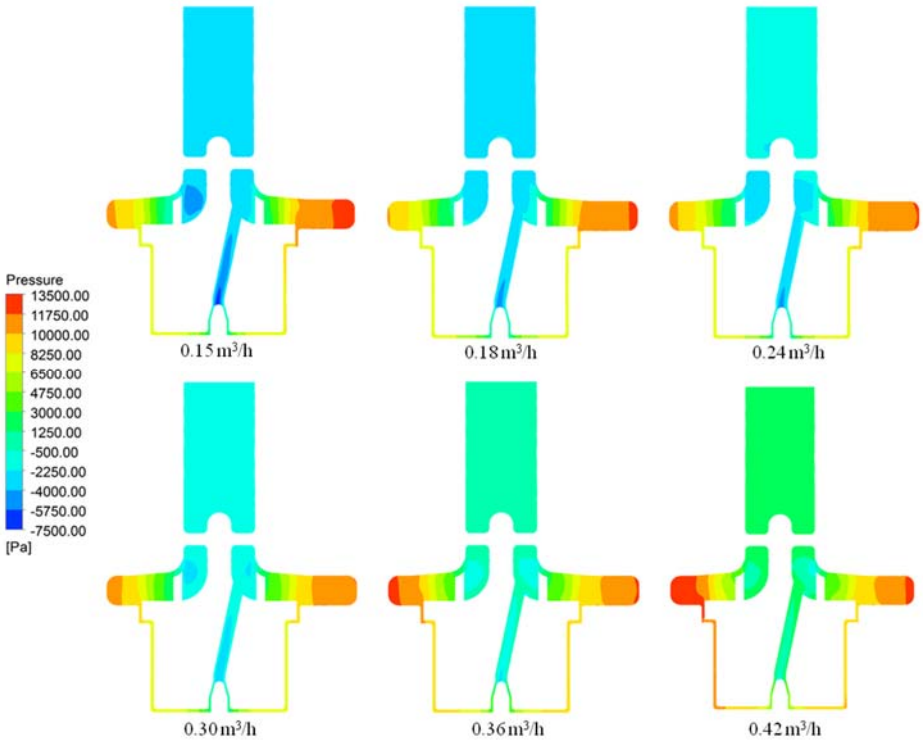

Figure 3-55: Pressure contour plot of the LVAD on the vertical plane

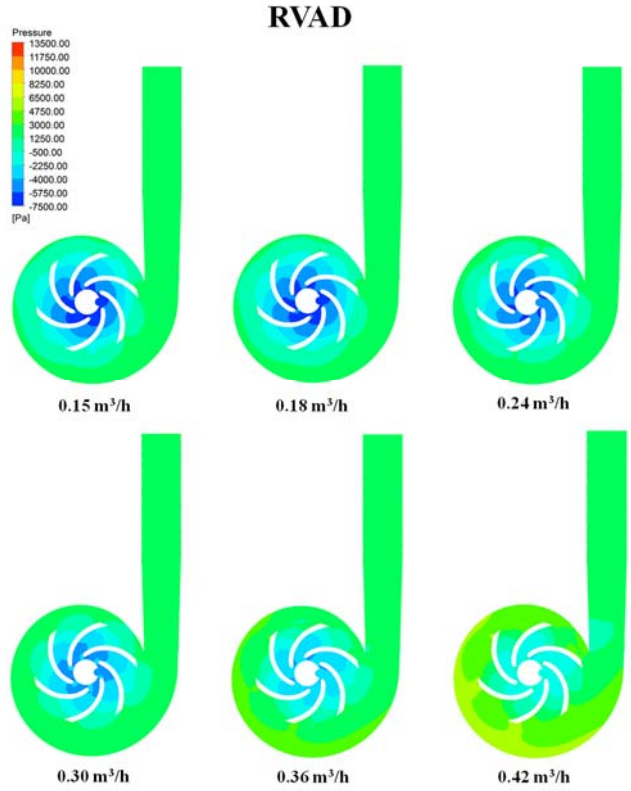

Figure 3-56: Pressure contour plot of the RVAD under different flow rates on the transverse-mid plane

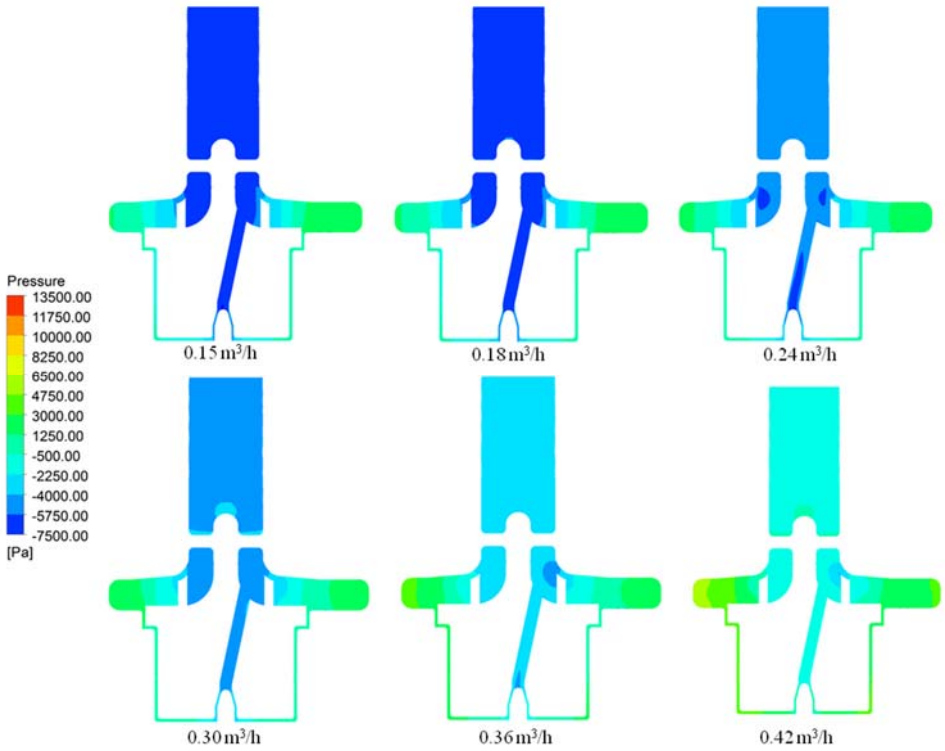

Figure 3-57: Pressure contour plot of the RVAD on the vertical plane

IV. Velocity distribution

LVAD

The velocity distributions of the LVAD at the transverse-mid plane and the vertical plane at different flow rates are displayed in Figure 3-58 and Figure 3-60, respectively. On the transverse-mid plane at the design condition, it can be observed that the velocity is distributed almost symmetrically on each vane where the high velocity is present near the compression side of the blades and the lower velocity is on the suction side. At the mid-section of the blades on the suction side there are small regions which show slightly lower flow rates at 0.4 - 0.8 m/s, but the velocity vectors plot (Figure 3-59) indicates a smooth flow through these areas. The flow speed is highest in the region around the impeller, especially near the volute tongue where the velocity is above 3.6 m/s, and it gradually decreases as the blood flows toward the outlet. There are boundary layers of low velocity flow observed at the near wall area in the outlet diffuser; this is due to the wall friction effect of the no-slip wall boundary and these grow in a symmetrical shape to reach the centre at the end of the outlet port.

At a flow rate above 0.3 m^3/h, the velocity distribution pattern in the impeller region and volute is similar to that observed in the centre condition but low velocities are located at the trailing edges instead of at the middle of the blades. The overall flow velocity is raised along with an increase of the flow rate through the pump, but it is notable that the distribution becomes more uniform since the velocity above 3.6 m/s is no longer present, while the regions of velocities of 2.0-2.8 m/s expand over a larger part of the volute area. A large low velocity boundary layer is observed in the diffuser at the tongue side while the higher velocity is shifted to the opposite side.

In the low flow conditions (0.15, 0.18 and 0.24 m^3/h), large low velocity regions could be observed in the impeller vanes and their size increases when the vanes move toward the diffuser region. The flow in these regions, as shown by the velocity vector plots (Figure 3-59) has a jet-wake structure which is a separation of the streamlines between the flows regions and which develops a recirculation pattern within the area. Under the flow rates of 0.18 and 0.24 m^3/h, the jet-wake presented a clear separation of different flow velocities but the flow is still properly guided out of

the vanes without any recirculation observed, while at a flow rate of 0.15 m^3/h, the areas of low flow become larger with a lower velocity.

In the lowest pump flow condition, the mass flow through the vanes is not enough to provide sufficient momentum to effectively eject the blood to merge with the main flow circulating in the volute casing; thus, the flow from the volute could flow back into the volute regions and develop separations with two large recirculations at the end of the impeller passages. The size and intensity of these vortices increases in the locations where the cross-sectional area of the volute expands near the diffuser. However, these recirculation regions would continue to wash away when the vanes move past the tongue where there is smaller resistance to the flow and allow the blood to fully discharge out of the blades' passage. This washout occurs repeatedly with every revolution of the impeller, so the recirculation cannot persist long enough to form thrombosis within the pump, but it could increase the residence time of the blood which exposes the RBC to shear stress for longer and causes more blood damage.

The velocity distribution contour in the outlet diffuser under low flow conditions showed low flow regions along the pipe at the opposite side of the tongue. The velocity vector plots showed that the flow could pass through this area in the condition with the flow rates of 0.18 and 0.24 m^3/h despite a flow separation with a much larger intensity of separation when the pump flow rate is lowered to 0.15 m^3/h and where the flow near the wall region starts to recirculate and form vortices that dominate a large area in the diffuser. The recirculation in this area could not be washed out by normal pump operation under this flow rate; thus, there is a high risk of forming both thrombosis and hemolysis if the pump is left to operate under this condition for long enough and it also causes loss of energy which reduces the pump's efficiency. Therefore, the angle or dimension of the outlet diffuser should be optimized to cover a wider range for the pump's operation.

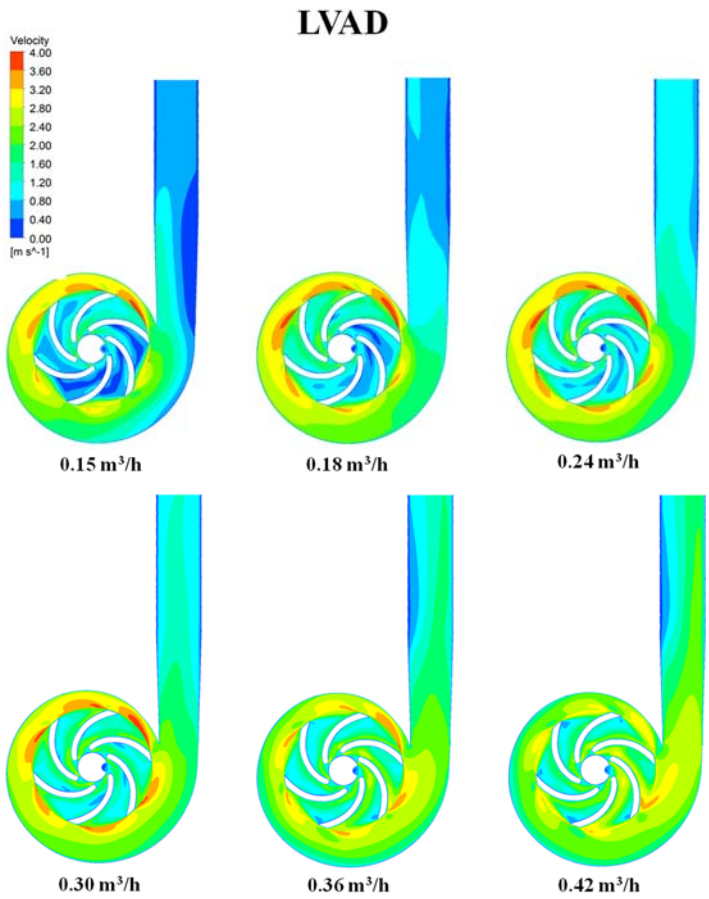

Figure 3-58: Velocity contour plot of LVAD under different flow rates on the transverse-mid plane

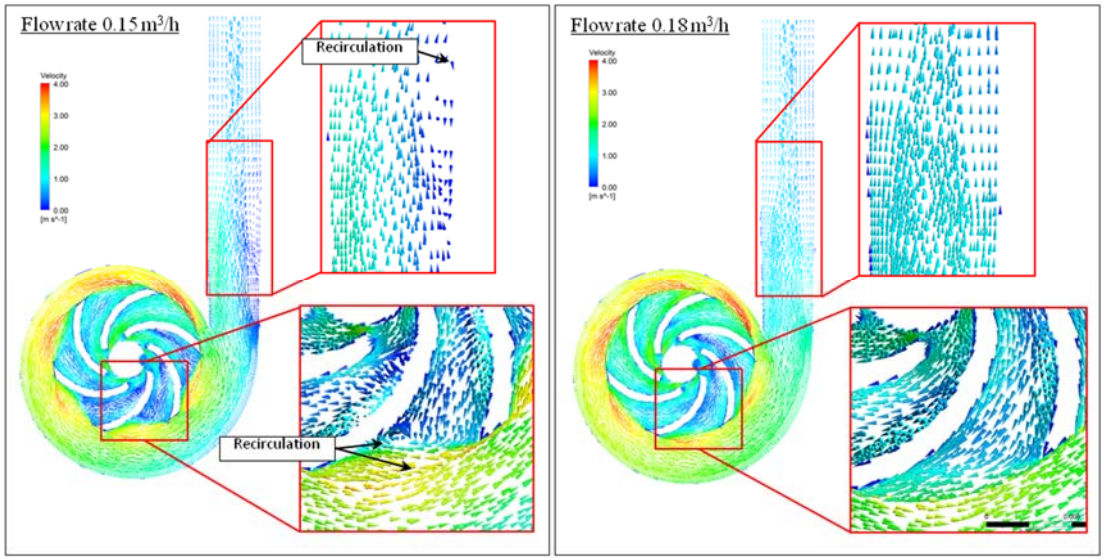

Figure 3-59: Velocity vector fields of LVAD below design flow rate conditions

The contour plot on the vertical plane (Figure 3-60) shows that the boundary layers of the lower flow velocity formed at the near wall regions of the inlet pipe;

this is caused by the effect of wall friction on the uniform velocity flow that was set as an inlet boundary. However, the flow could pass through the pipe without any sign of stagnation or recirculation at all the flow rates. The region that is at risk of forming thrombosis in this pump, as observed from this vertical-section view, is in the area behind the flow straightener bars. Currently there are 4 of these bars built on the top part of the chamber, and each has a thickness of 1 mm which is relatively large compared to the cross-sectional area of the inlet pipe; thus, there could be a blockage of some flow and a cause of stagnation, as shown in the blue region of this Figure. However, with the limitation of the current manufacturing process and the strength of material for the prototype, the size and shape of the straightener could not be reduced or optimized further in this stage but they should be adjusted in the future optimization of this pump.

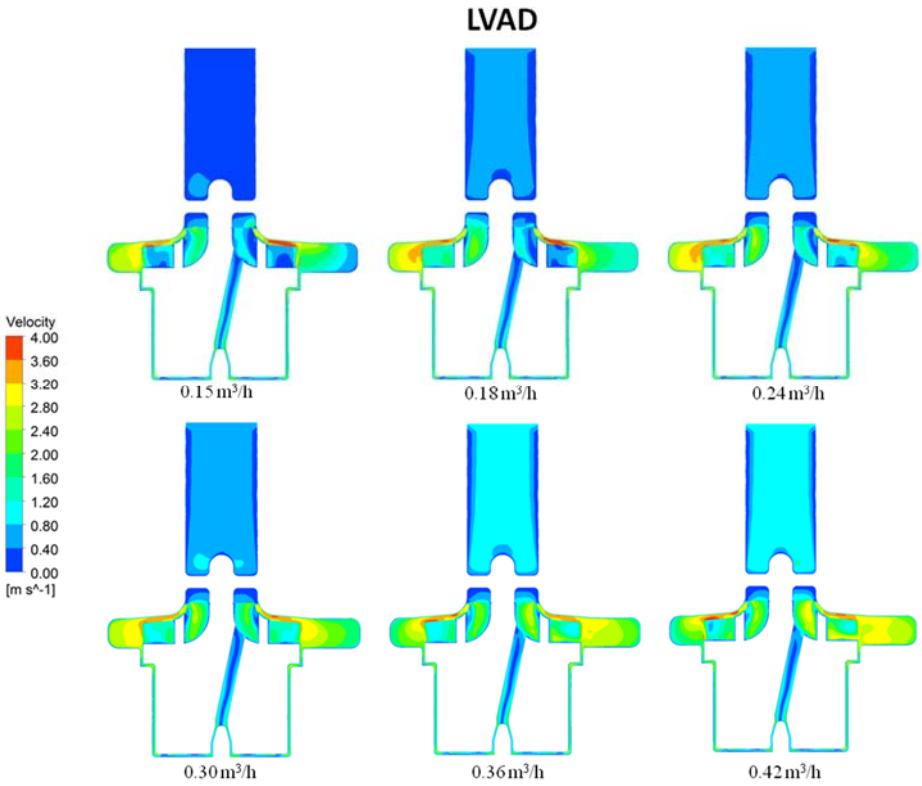

Figure 3-60: Velocity contour plot of the LVAD on the vertical plane

RVAD

When the pump is operating under the RVAD conditions the overall flow velocity is lower than the LVAD under the same flow rate, as shown in Figure 3-61. At the design flow rate (0.24 m^3/h) the pump presented a similar distribution to that

previously observed in the design condition of the LVAD (0.3 m^3/h) where small flow separations are found at the middle of the blades on the suction side. The separation intensity is increased below the design conditions but the velocity vector field plots in Figure 3-62 show that the recirculation was not formed in the vanes, while the diffuser region also developed a well-uniform distribution without any separation.

The flow separation in the diffuser of this RVAD is instead found in a higher flow rate than the design condition at 0.3 m^3/h near the middle area of the outlet diffuser on the tongue side. The separation intensity in this condition is not high enough to generate recirculation and it disappeared when the flow rate was increased to 0.36 m^3/h. However, the separation is observed again at the flow rate of 0.42 m^3/h, starting from the volute tongue with very high intensity. The velocity vector plot (Figure 3-63) shows that the separation in this area is caused by the main flow that hits the tongue at a high contact angle on the volute side, so the flow does not fully cover the tongue on the diffuser side and leaves the low pressure behind the impact region, thus creating a suction force that forms the recirculation in the area.

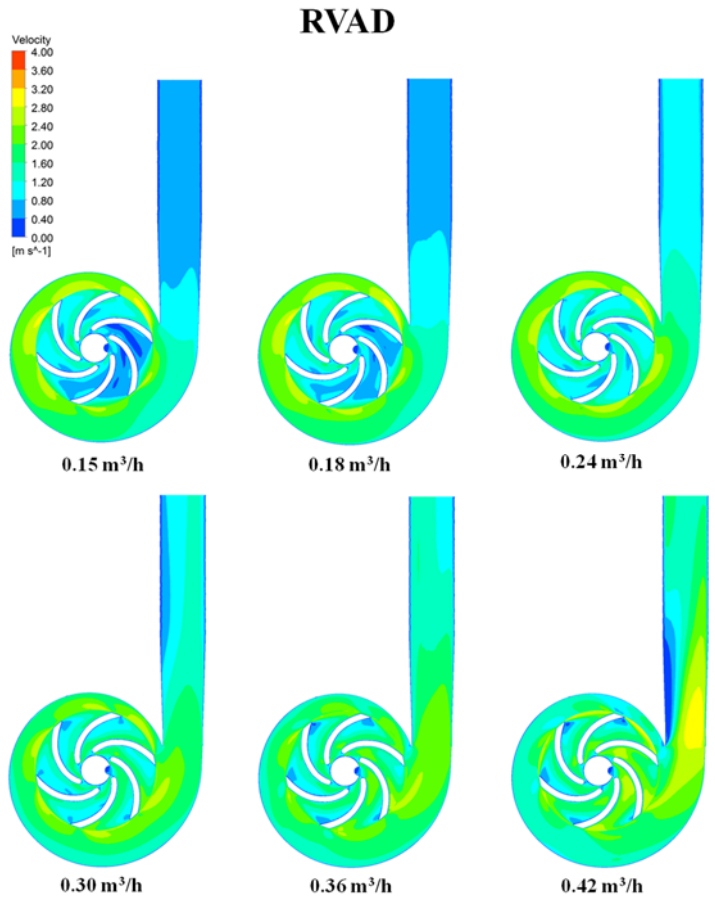

Figure 3-61: Velocity contour plot of the RVAD under different flow rates on the transverse-mid plane

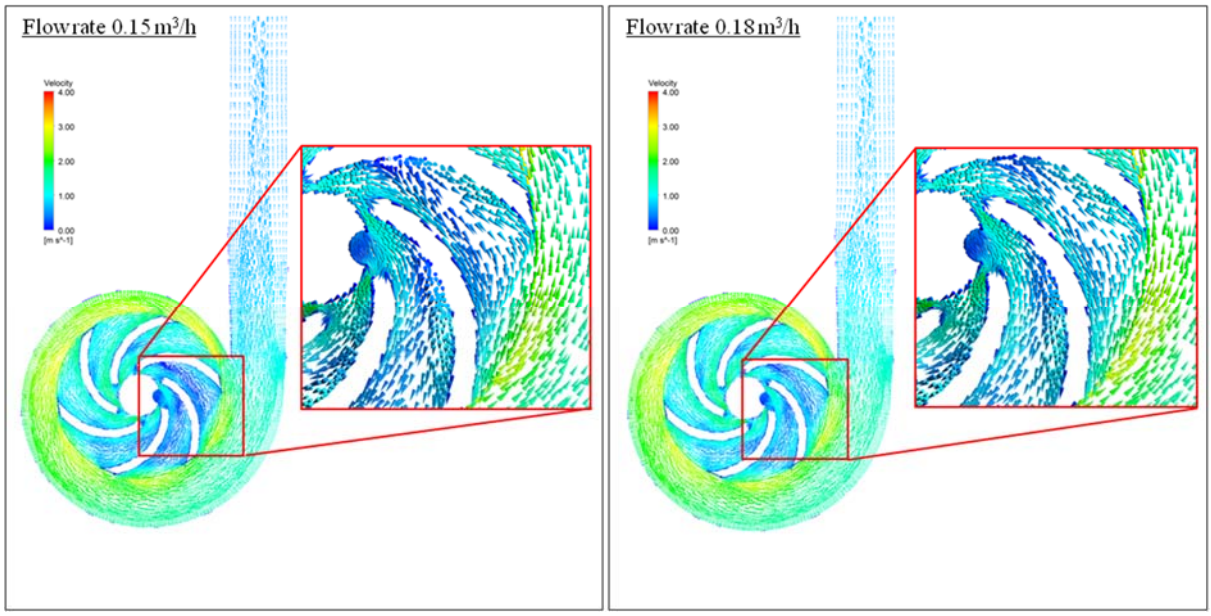

Figure 3-62: Velocity vector fields of RVAD below design flow rate conditions

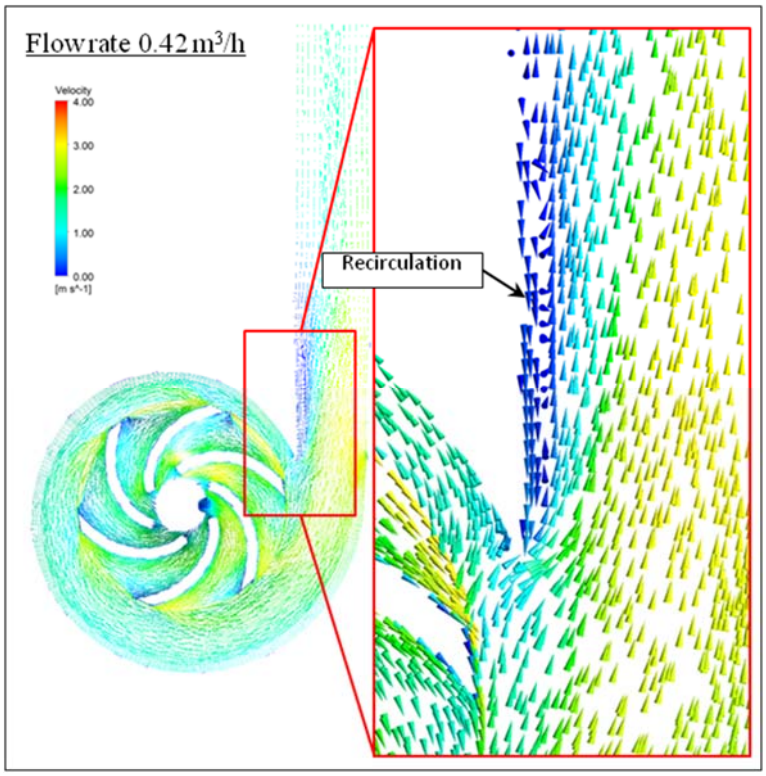

Figure 3-63: Velocity vector field of RVAD above design flow rate

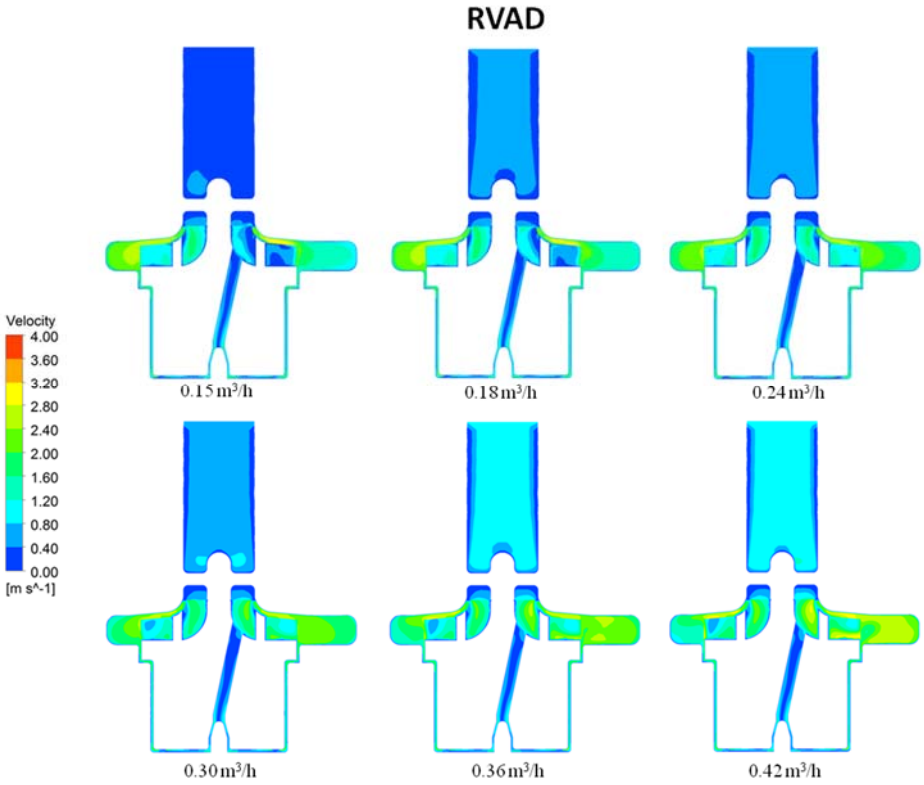

Figure 3-64: Velocity contour plot of the RVAD on the vertical plane

From the vertical plane plot (Figure 3-64), the velocity distribution is similar to the LVAD; boundary layers are also observed in the inlet pipe for all the flow rates. The low velocity is found behind the straightener bars and risks forming stagnation in these RVAD operating conditions.

V. Turbulence kinetic energy

LVAD

The intensity of the turbulence kinetic energy (TKE) is found to be relatively high at the vane on the suction side of the blades in most conditions, while the same or a slightly higher TKE level is also observed behind the trailing edge of the blades due to the wake turbulence; this is common for the flow within the centrifugal pump and could be observed in all the simulation conditions and also in the previous simulation results.

During low flow there is an increase of the TKE intensity around the tongue region but the distribution is still similar in pattern for the flow rates of 0.24 and 0.18 m^3/h. However, when the flow rate is reduced to 0.15 m^3/h a very high intensity of TKE, roughly above 0.6 m^2/s^2, is found at the end of the vanes that move near the tongue. This value of TKE is more than 100% higher than those observed on the same region with a higher flow rate which indicates strong turbulence in the area. If comparing this plot to the velocity contour plot, the high turbulence is found to match the location of the large vortices where the back flow was previously observed at the tip of the impeller vanes. Therefore, it is reasonable that strong turbulence could develop in these areas.

For the above design flow rate conditions, the TKE is raised all over the impeller and volute areas. The left side of the diffuser where the flow separation occurs tends to have more turbulence than the other side where the flow passes through more smoothly. These turbulences observed in the diffuser have no direct impact on the hemodynamic properties of the pump, but an improvement to the design to eliminate these turbulences could reduce the energy loss and improve the pump's performance.

An additional observation on the vertical plane is a small amount of TKE found at the inlet of the washout passage and at the end of the shaft where blood

starts to swirl around in order to flow through the passage but the intensity is lower than that at the impeller and volute areas.

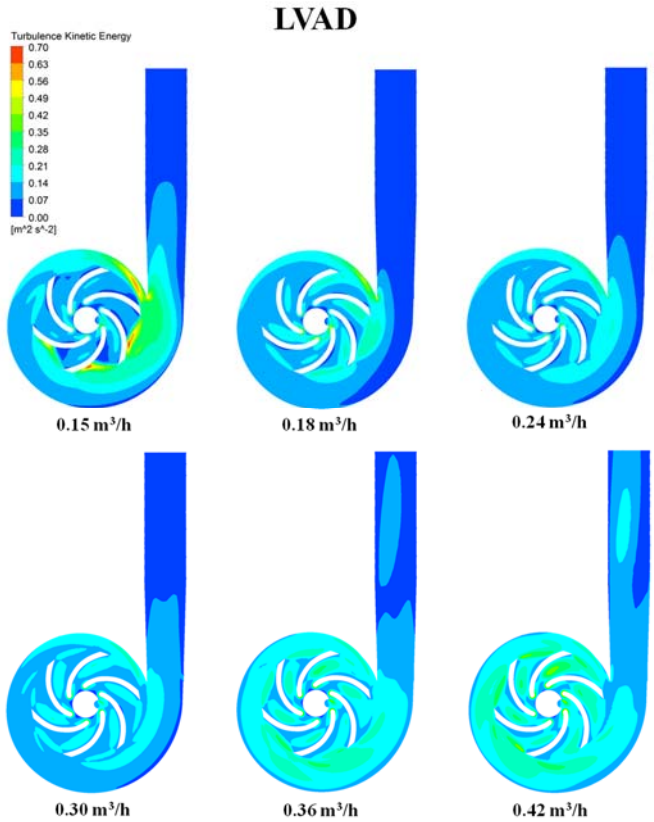

Figure 3-65: Turbulence kinetic energy of the LVAD under different flow rates on the transverse-mid plane

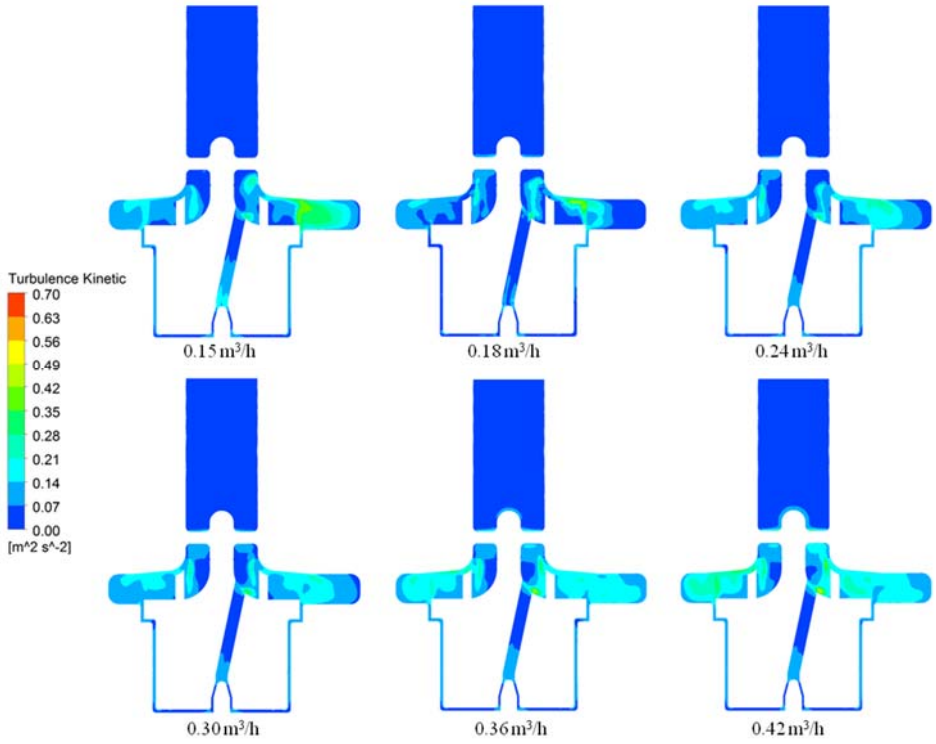

Figure 3-66: Turbulence kinetic energy contour plot of the LVAD on the vertical plane

RVAD

The TKE in the RVAD shown in Figure 3-67 with the design flow rates (0.15 and 0.18 m^3/h) are better distributed than those in the LVAD and there is no sign of strong turbulence being formed at the pump in both flow rates. However, turbulence is starting to form in the middle of the outlet diffuser at the above design flow rate of 0.36 m^3/h with an estimated energy of 0.07-0.14 m^2/s^2 and it becomes highly intense and dominating mostly at the diffuser area when the flow rate is increased up to 0.42 m^3/h; this results in a large recirculation near the tongue area similar to that previously observed in the velocity vector plots.

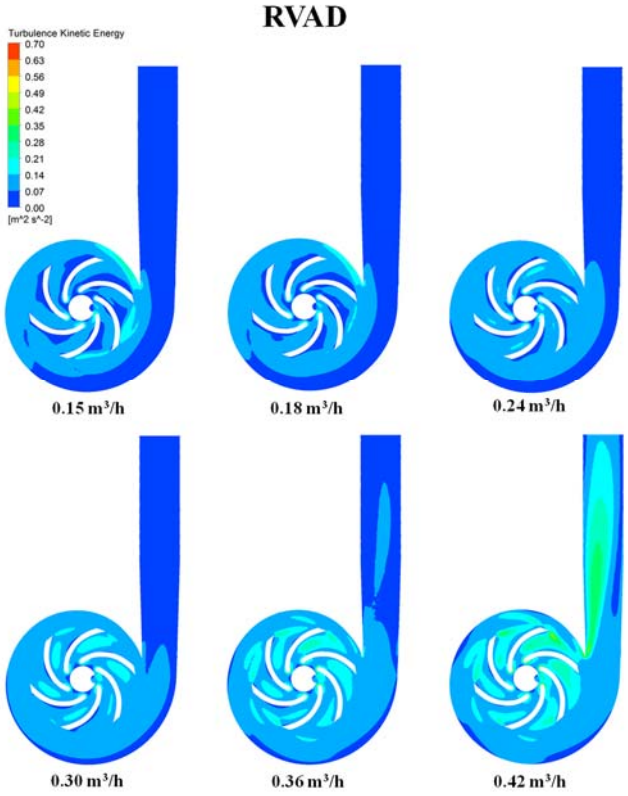

Figure 3-67: Turbulence kinetic energy of the RVAD under different flow rates on the transverse-mid plane

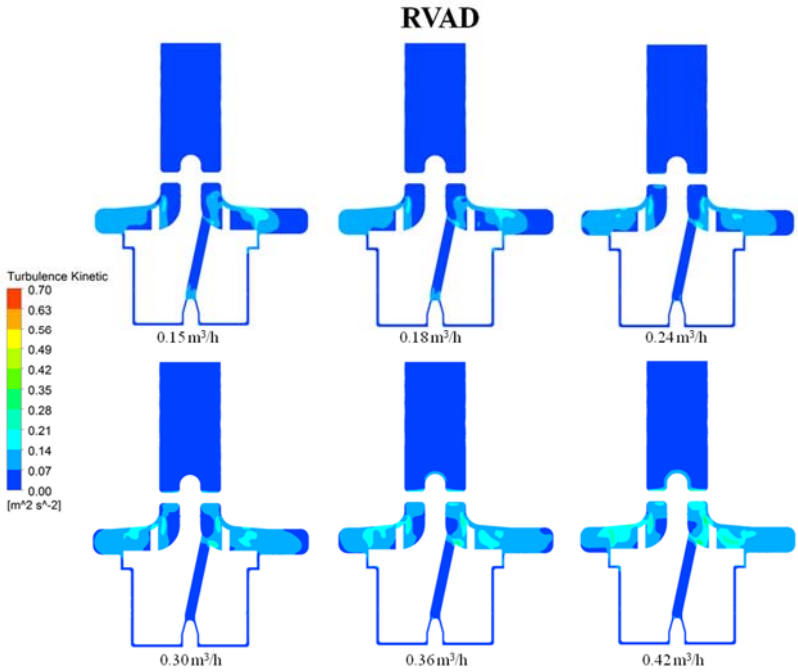

Figure 3-68: Turbulence kinetic energy contour plot of the RVAD on the vertical plane

VI. Shear stress

The shear stress within the pump is generally found to be high in the region of flow diversion or separation; in this case the tongue and leading edge of the blades were found to have the highest shear stress in most of the flow conditions. The level of shear stress is reduced when the flow is directed into the impeller vanes but is still relatively high at the region where turbulence occurs near the suction side of the blades and along the wake turbulence region behind the trailing edges.

The contour plot on the vertical plane reveals that the shear stress could be increased on the flow straightener at the inlet when the flow rate is increased. The additional shear stress of this design was also found to be generated at the inlet of the washout passage where the flow starts to swirl in, and also at the outlet of the passage which currently has a sharp exit corner. This high shear stress at the exit of the flow passage could be improved by adding a small radius to provide a better transition when the blood merges with the main flow and to reduce the stress exerted on the RBC in this area.

The shear stress plot of the bottom plane (Figure 3-73) depicts extra shear stress that is introduced to this design at the leading and trailing edges of the static support blades. However, the magnitude of the shear stress at this region is lower than at the blades' area due to the lower flow speed.

LVAD

When the pump operates at below the flow rate in the LVAD, there is an increase in the shear stress intensity on the left side of the tongue and at the wake turbulence region formed behind the trailing edge of the blades. The shear stress greatly increases at the flow rate of 0.15 m^3/h where this wake turbulence flows back into the vane regions and contacts with the pressure side of the next blade that moves in. This effect was found to cause high shear stress, which is estimated at above 240 Pa, and increased the risk of causing RBC damage as the recirculation also occurs in the same area.

The shear stress was found to be generated in the outlet diffuser in the same region where the turbulence was formed when the pump operates above the design

point. The level of shear stress in this region was the same as the average stress found at the volute casing area but covers a larger area when the turbulence exists in the pipe.

RVAD

The overall shear stress level in the RVAD is only slightly increased at the level below the design flow rate and there was no significant problem from this shear stress level except for a slight increase in the blood damage level.

The high shear stress that forms in the RVAD is only observed in the tongue and diffuser area which previously saw a large turbulence and a retrograde flow. Although the shear stress observed in this area is much lower than that found in the critical regions of the LVAD, the recirculation could increase the exposure time and eventually damage the RBC.

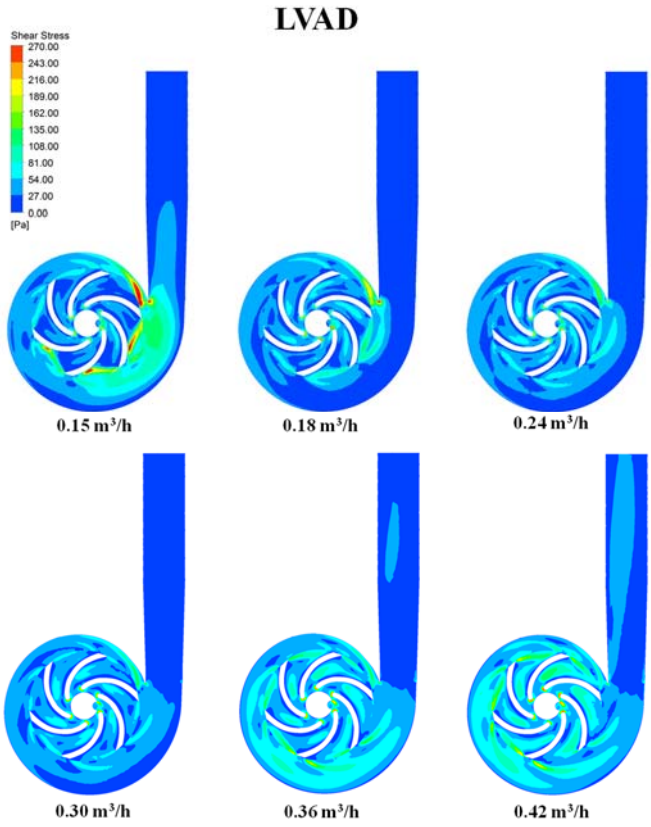

Figure 3-69: Shear stress of the LVAD under different flow rates on the transverse-mid plane

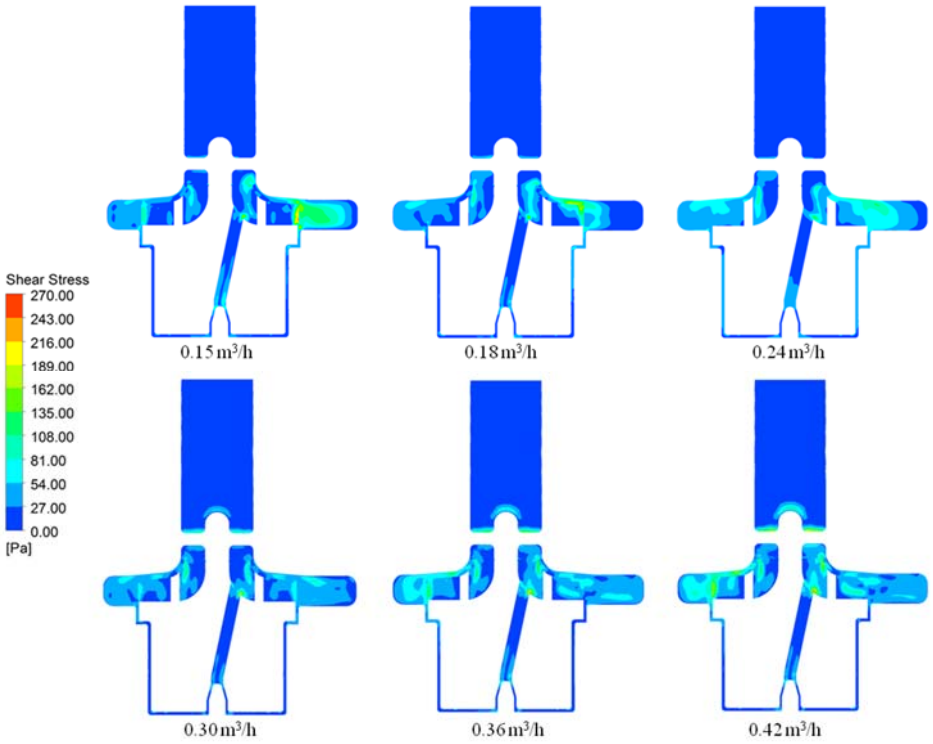

Figure 3-70: Shear stress contour plot of the LVAD on the vertical plane

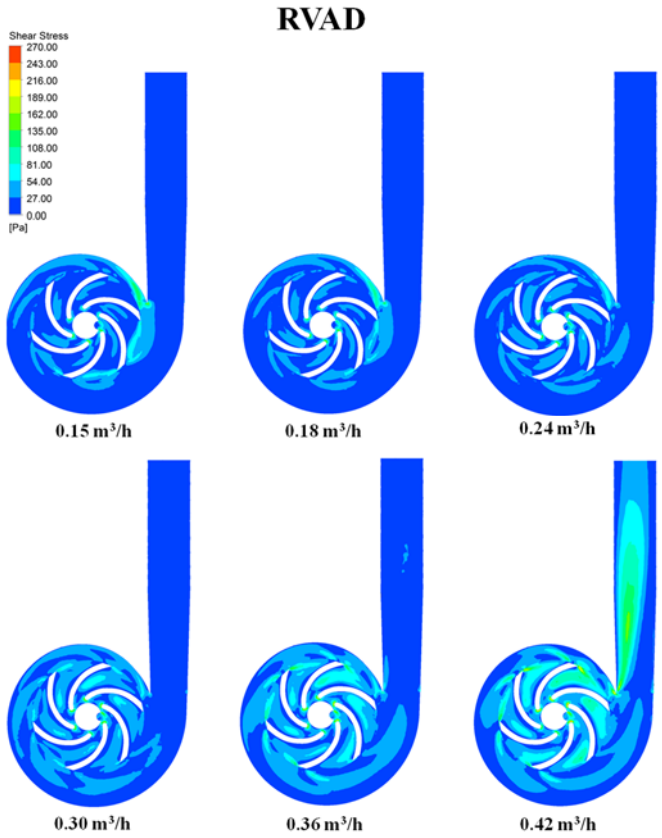

Figure 3-71: Shear stress of the RVAD under different flow rates on the transverse-mid plane

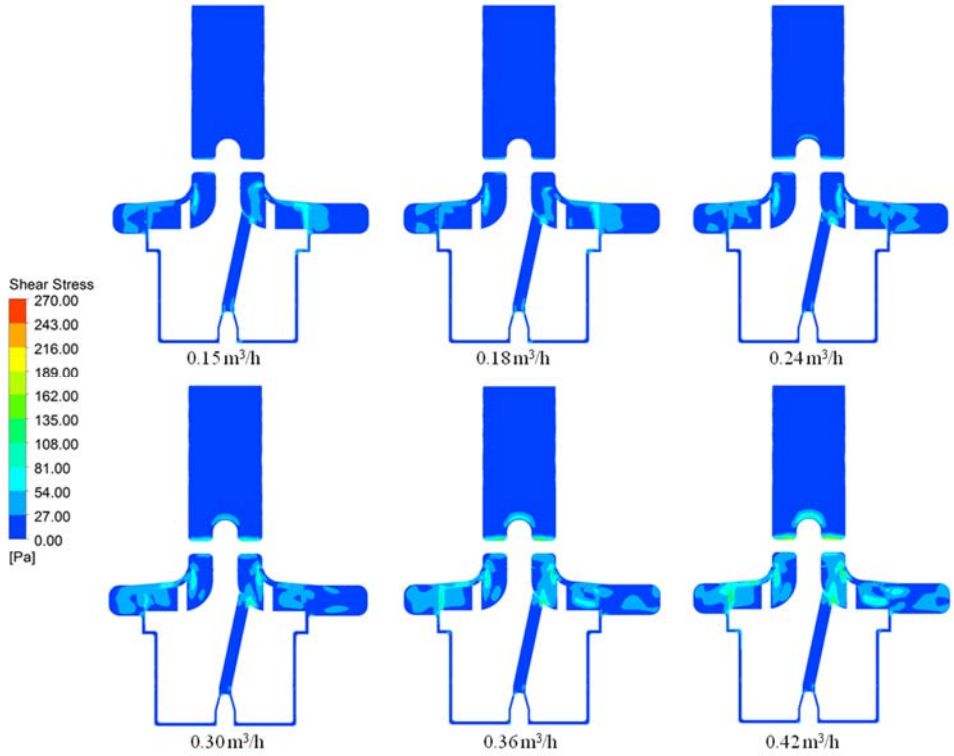

Figure 3-72: Shear stress contour plot of the RVAD on the vertical plane

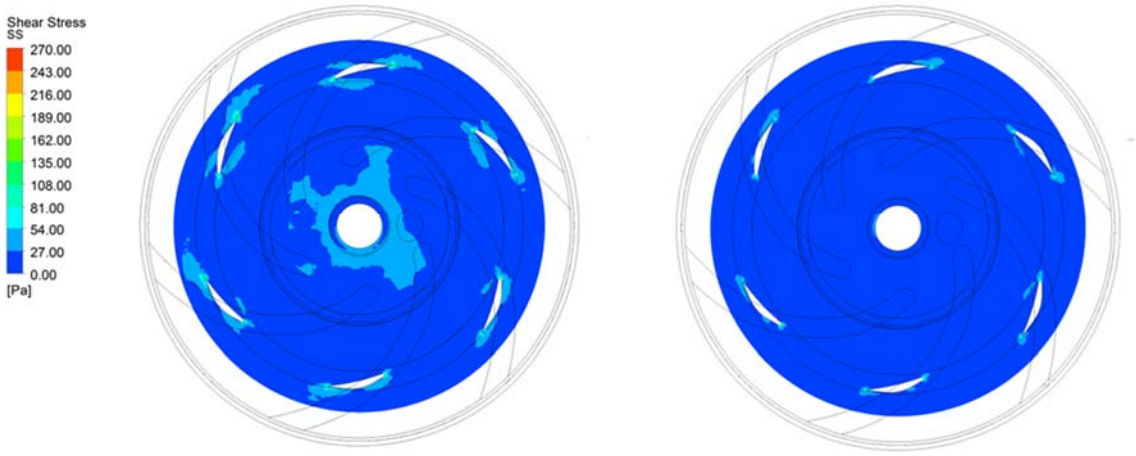

Figure 3-73: Contour plot of the shear stress distribution in a bottom plane of LVAD (left) and RVAD (right) at the design flow rate

VII. Hemolysis estimation

The blood damage assessed from the simulations is shown as the NIH index in Figure 3-74. The pump tends to generate a smaller amount of damage at the BEP

flow rate for both the LVAD and RVAD which has a good agreement with the shear stress that was observed in each flow condition.

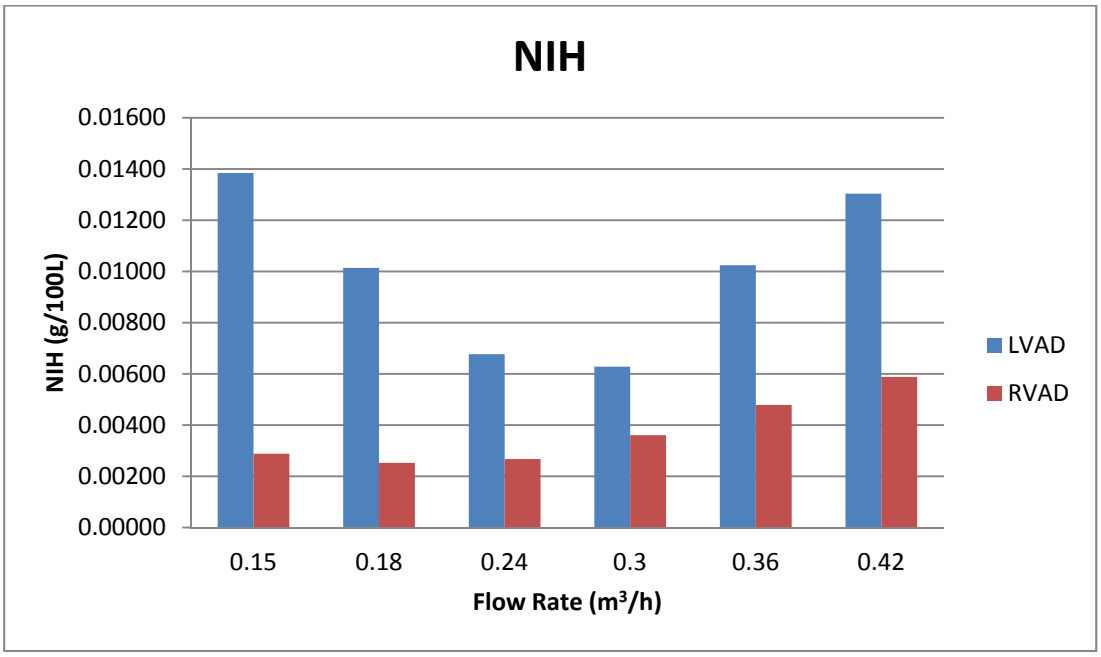

Figure 3-74: NIH index of different flow rates on the LVAD and RVAD functions

At the design operating condition of this pump under the flow rate of 0.3 m^3/h, the NIH index from the simulations is 0.00628 g/100L. This number increased significantly from the previous simulations due to the additional shear stress introduced to the pump with the additional support components. These included the impeller support structure on both the top pivot bearing and the static blades at the bottom, and the extra shear stress at the outlet of the washout passage, as shown in the Figure 3-72 and Figure 3-73.This value of the NIH is higher than the anti-traumatic limit of a short term support pump for cardiopulmonary bypass support; however, it is still within the acceptable clinical range and could be used for both the LVAD and RVAD applications.

The graph in Figure 3-75 represents the hemolysis index of several heart pumps both on trial and commercially available under the standard operating condition at a flow rate of 5 L/min and head pressure of 100 mmHg. This pump at the current stage could operate at the required condition while generating significantly lower blood damage than the clinical limit and maintaining its competitiveness with other pump models at the same generation. This result suggests

that the blood damage generated from this VAD design is at the acceptable level, and this pump should not cause blood damage problems in the long term support.

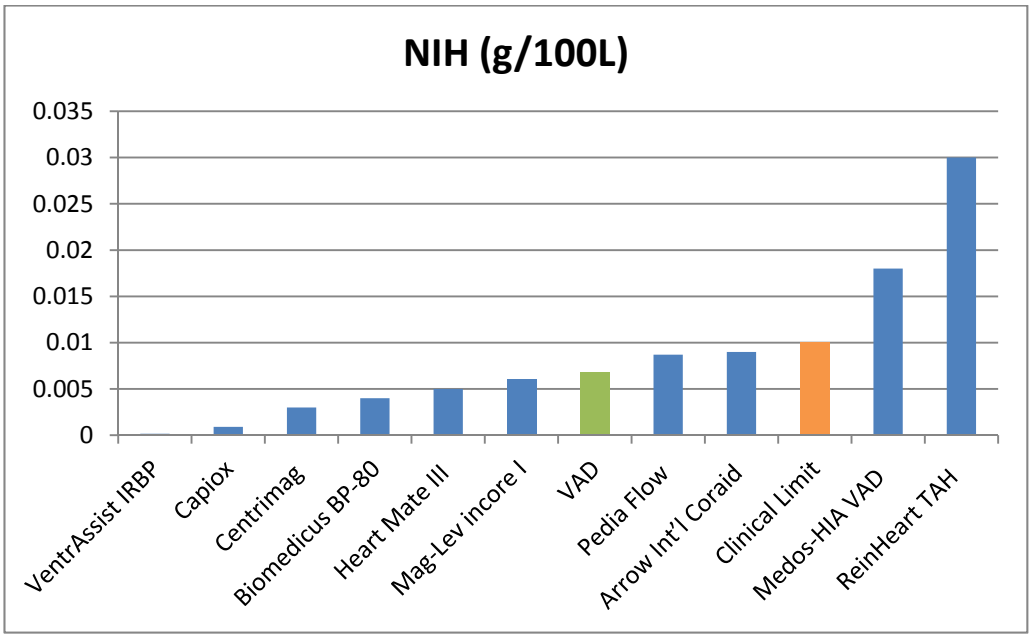

Figure 3-75: NIH comparison across the pumps (Gräf, Finocchiaro, Laumen, Mager, & Steinseifer, 2015; James, Wilkinson, Lingard, Meer, & Woodard, 2003; Johnson Jr et al., 2011; Lin et al.; Throckmorton & Kishore, 2009; J. Zhang et al., 2006)

3.7.4 Conclusion

According to the simulation results, the distribution profile of all the parameters on the contour plots are similar to the results previously observed in the BiVAD simulation, which means that the design refinements did not cause any significant impact on the flow in the volute and impeller areas.

The off-design simulation confirmed that the pump could provide sufficient head pressure over the wide range of flow rates with good efficiency for both the LVAD and RVAD applications, and could achieve the hemodynamic requirements to be used as both a short term and long term blood pump to support cardiopulmonary operations or CHF patients.

The pump still has a risk of forming thrombosis from the recirculation when operating at the flow rate of 0.15 m^3/h and below on the LVAD application, and at the flow rate 0.42 m^3/h and above on the RVAD application. The structure of this pump should be further optimized in a future study to achieve a wider operational

range for the pump. The limitations of the pump also need to be confirmed in a test with real blood to study the actual time at which thrombosis could be formed within the pump when operating under the off-design conditions.

In addition to the items that need to be further studied, there are also some structures in the pump that have potential for minor improvements such as the shape of the flow straightener that could be optimized to prevent stagnation behind it, and the high shear stress at the washout hole which could be reduced by adding a small radius for better transition of the outlet flow.

3.8 DESIGN SUMMARY

The availability of the pump design has been confirmed by the simulation results and revised based on manufacturing requirements; therefore, the pump design is summarised, as shown in Figure 3-77 to Figure 3-79. The pump prototype for design verification was produced on these models and drawings.

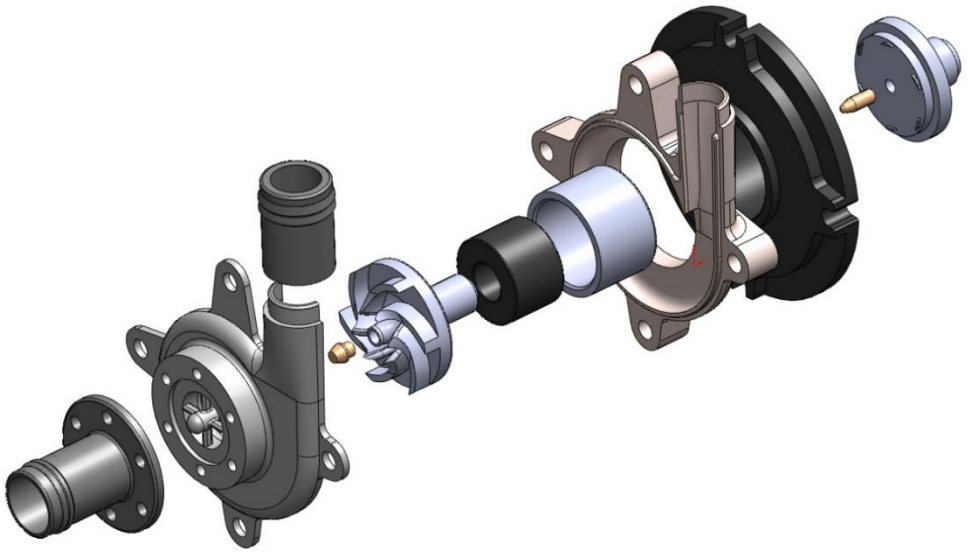

Figure 3-76: Exploded view of the VAD design.

Figure 3-77: Rendered view of the VAD concept model

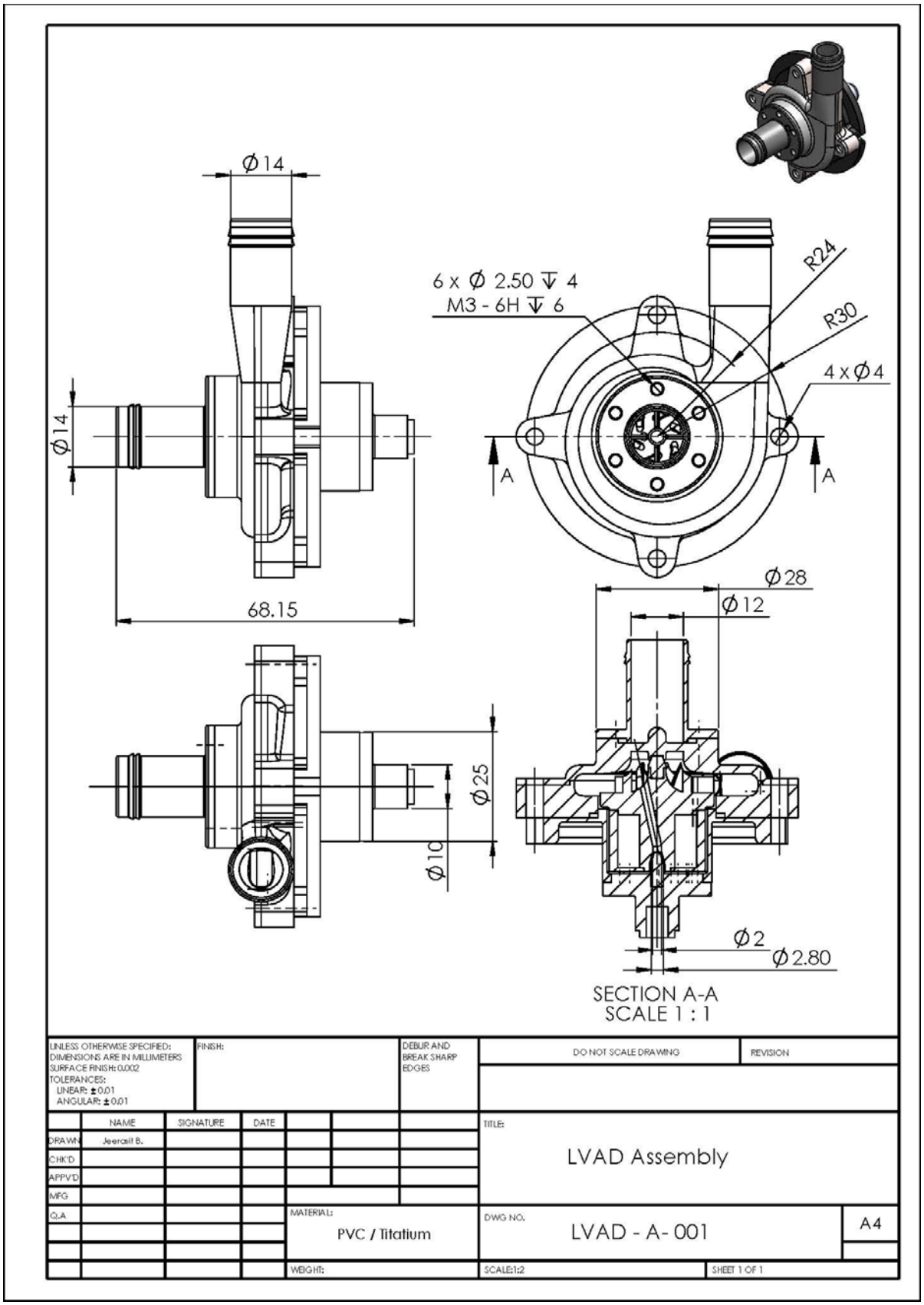

Figure 3-78: Assembly drawing of the VAD design.

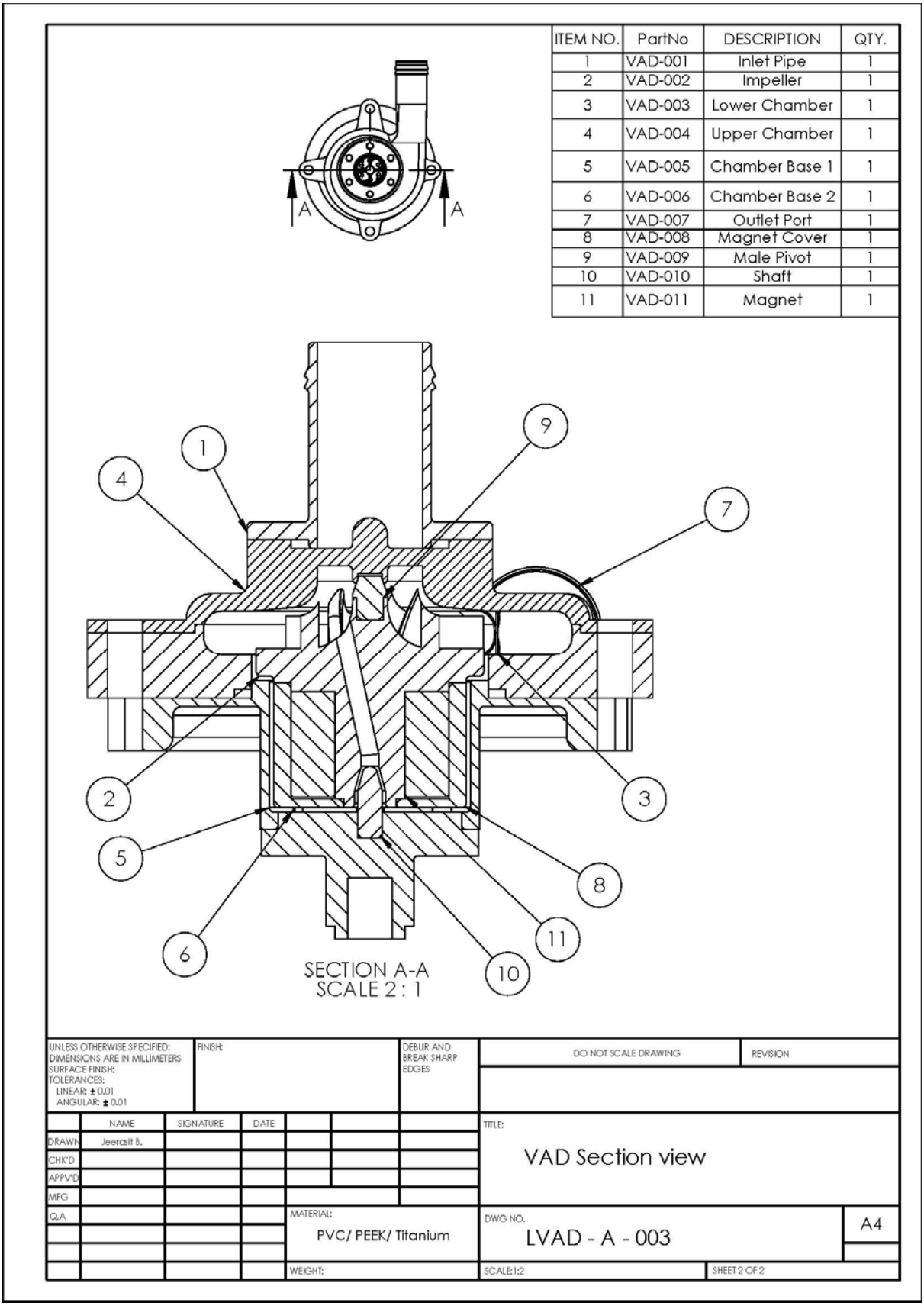

Figure 3-79: The section view drawing of the VAD design

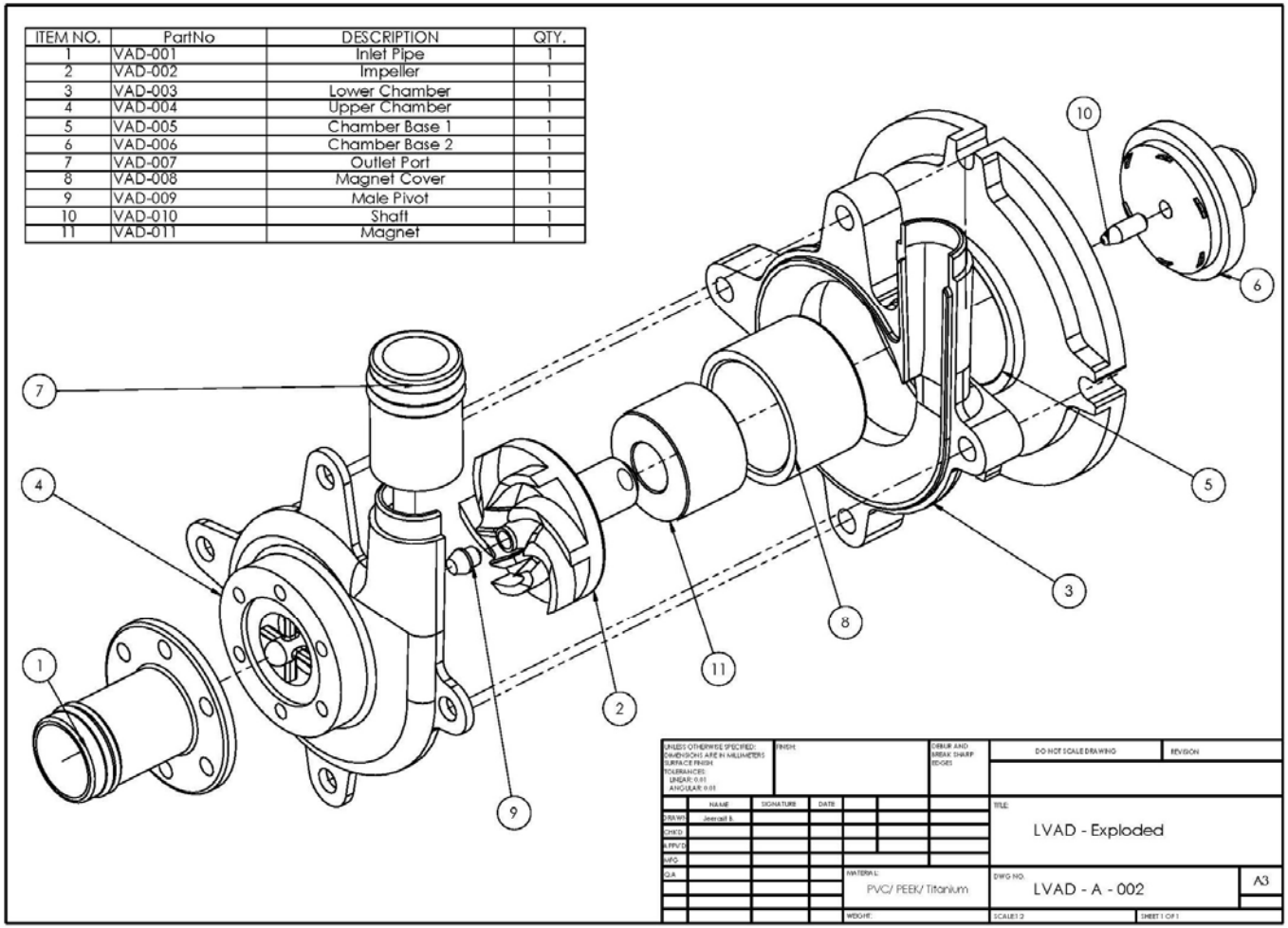

Figure 3-80: VAD exploded sketch with bill of parts

Chapter 4: Design and Construction of VAD Test Loop

This Chapter focuses on the design and construction of the test loop for an in-vitro evaluation of the VADs known as the Human Mock Circulation Loop (MCL). In order to achieve all the aspects of evaluation, the MCL must be able to simulate the basic physiological conditions of a normal heart and the heart functions of CHF which mainly are characterized by the pulsating flow, the compliance of the venous and arterial system, and resistance of the blood vessels.

4.1 DESIGN REQUIREMENTS

The main objective of the MCL design is to create an apparatus for evaluation of the VAD prototype and verify the simulation results. The structure is mainly focused on replicating the pulsatile environment and resistance of the systemic circulation to observe characteristic of the pump under the unsteady flow. Therefore the MCL must be able to simulate the flow condition of a healthy adult as a reference condition, while also capable of reducing the physiological condition to simulate the condition of a heart failure patient.

4.2 PHYSICAL PARAMETERS

In order to mimic the flow characteristics of the human circulatory system, several physical parameters need to be studied and properly selected to achieve, as much as possible, the condition that is close to what really happens within the human body. These parameters include the flow circulation paths, heart functionality, pressure and flow distributions, and compliance and resistance to the flow.

4.2.1 Human Circulatory System

The human heart is a double pump each of which has its own circulation loop encompassing a set of vessels, namely the arteries, arterioles, capillaries, venules and veins. Figure 4-1 shows the human circulatory system where the left part of the heart

pumps blood through the systemic circulation and the right part of the heart pumps blood through the pulmonary circulation.

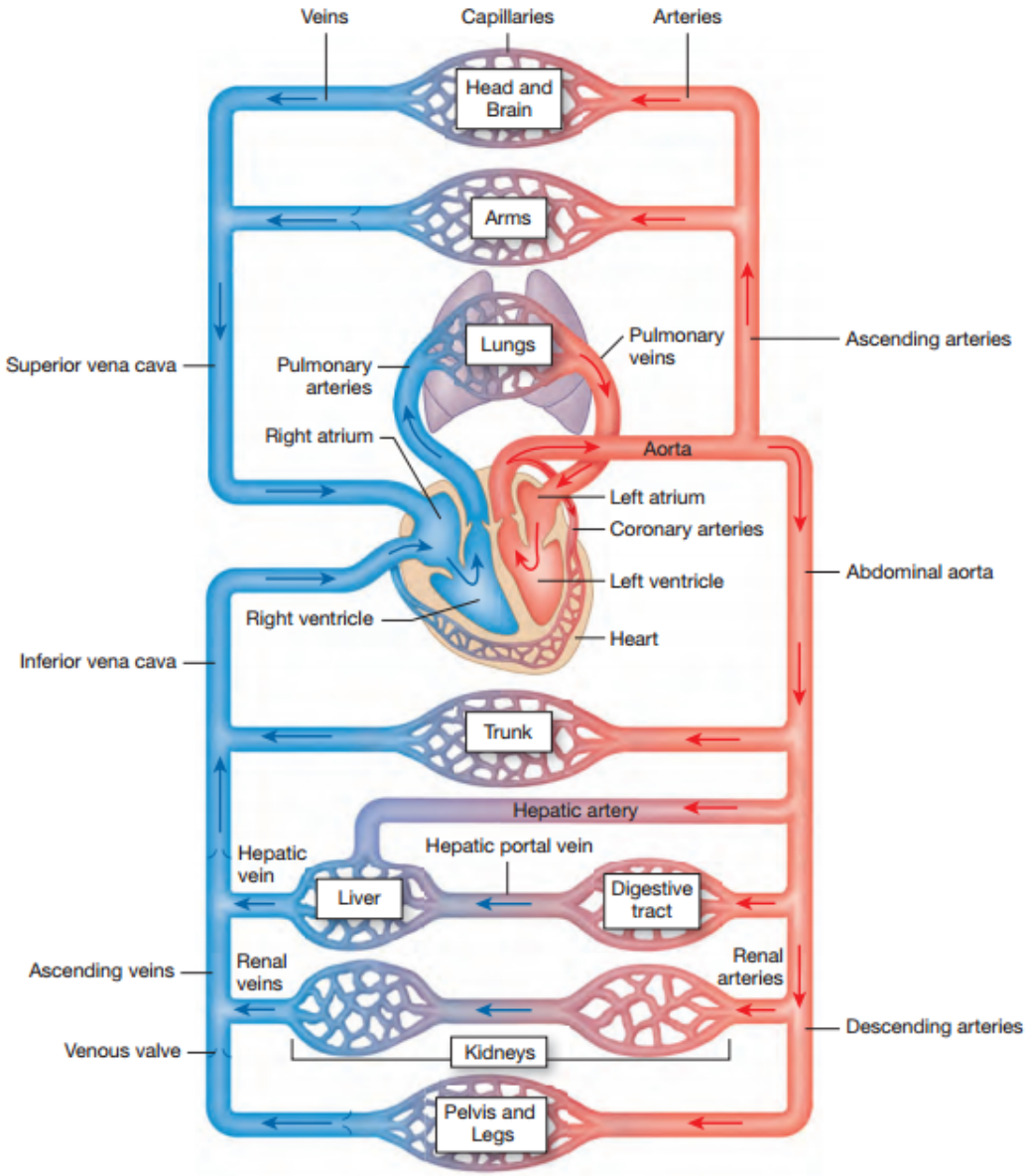

Figure 4-1: Human circulatory system (Brazier, 1988)

The systemic circulation functions in distributing oxygen-rich blood containing nutrients and other substances needed to all the body tissues and organs, while also carrying away the carbon dioxide and organic waste from the cell metabolism back to the heart via the vena cavas. This return blood enters the heart at the right atrium which functions as a weak primer pump to regulate the venous blood to the right ventricle before pumping to the pulmonary circulation.

The pulmonary circulation is a shorter circuit. It carries oxygen-poor, carbon dioxide-rich dark red blood from the end stage of the systemic circulation to the air sacs called alveoli in the lungs to exchange the gas and enrich the oxygen level to the blood cells. As the gases are exchanged, the blood turns bright red and circulates back to the left atrium via the pulmonary veins to enter the systemic circulation again.

4.2.2 Heart Functionality

I. Cardiac Cycle

The human heart pumps blood by the contraction of the heart wall that reduces the volume of the heart cavity during the systolic phase and thus increases the pressure to the blood and propels the blood flow through the heart valves, before the heart muscle is relaxed and allows the blood to fill in the cavity for the next ejection in the diastolic phase. Heart valves have a vital role in regulating the blood flow during the cardiac cycle where they function as non-return valves to prevent backflow to the heart chambers. There are a total of 4 valves in human heart chambers (Figure 4-2); the atrioventricular valves (mitral and tricuspid valves) control the flow from the atriums to the ventricles, while semilunar valves (aorta and pulmonic valves) control the outlet flow of the ventricles.

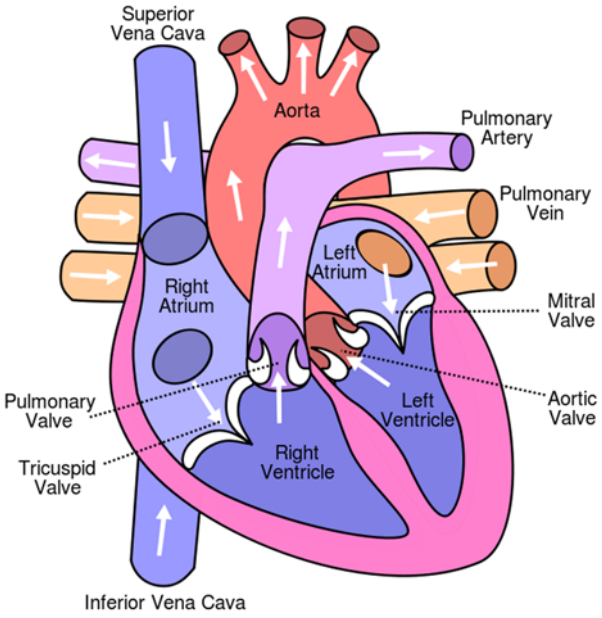

Figure 4-2: Schematic of the human heart (Nordqvist, 2014)

The full cycle of the cardiac function consists of five phases. Figure 4-3 shows the pressure and volume of a heart over two complete cycles, while Figure 4-4 outlines the events of the cardiac cycle.

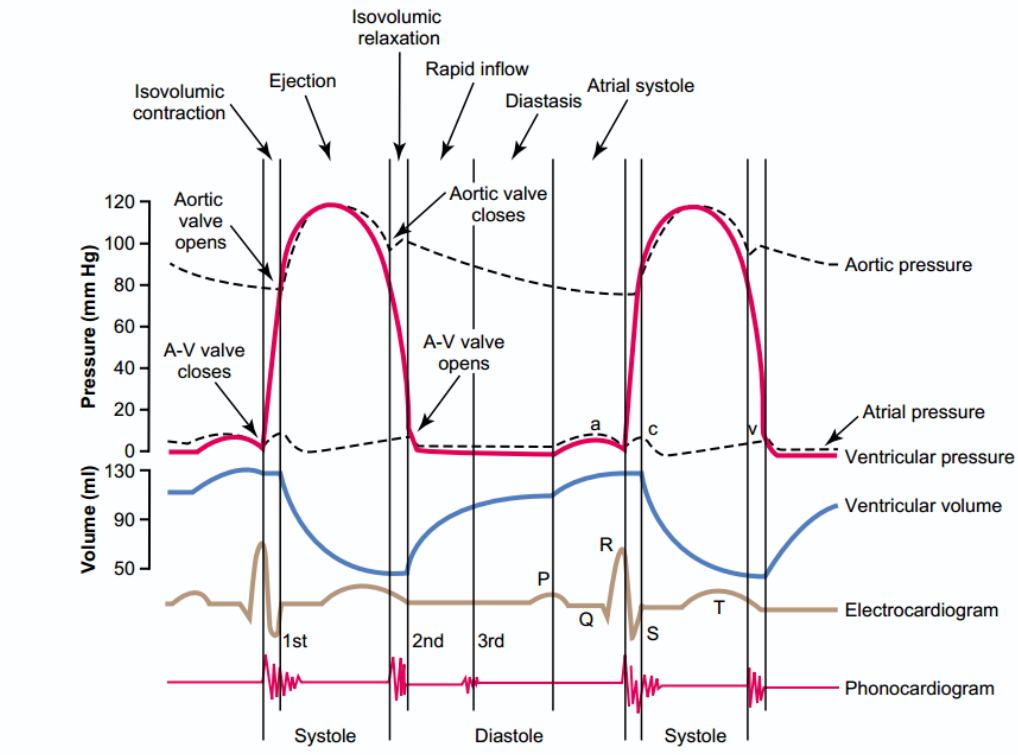

Figure 4-3: Pressure and volume of heart during systolic and diastolic phases (J. E. Hall & Guyton, 2011).

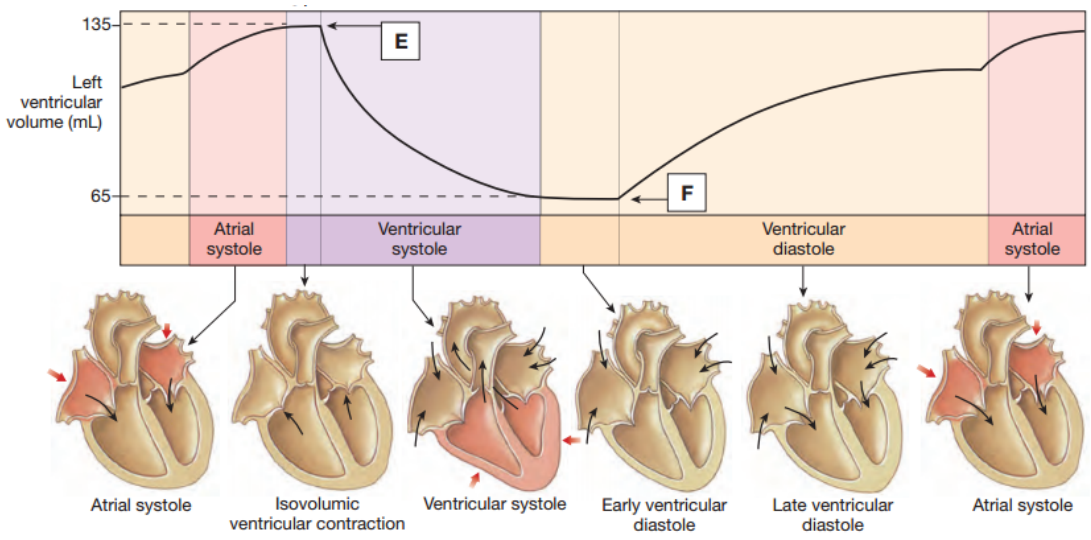

Figure 4-4: Heart events and left ventricle volume during the cardiac cycle (Brazier, 1988).

Phase 1: Ventricular Filling

During the filling stage, the artrioventricular (AV) valves are open, while the semilunar valves are closed. Blood flows into the heart and about 70% of the ventricle is passively filled in this phase.

Phase 2: Arterial Systole

In this stage, the arterials' contraction forces the blood to flow through the tricuspid and mitral valves to the ventricles. The inertia still keeps the blood flowing into the heart while preventing backflow to the veins.

Phase 3: Isovolumetric Contraction

There are 2 stages in the ventricular systole. At the beginning of the phase the aortic valve is closed, and the ventricular muscle starts to contract and reduce the volume; therefore, the pressure is sharply increased until the ventricle pressure is raised above the aortic pressure and pulmonary pressure at an estimated 80 mmHg and 10 mmHg, respectively. The aortic and pulmonary valves then open while the ventricle continues to contract and thus the pressure is raised further at a slightly lower rate.

Phase 4: Ventricular Ejection

The volume ejection begins as the aortic and pulmonary valves open. The high flow rate starts at an early phase due to the high ventricle pressure and then slows down as the systole progresses. The aortic and pulmonary pressures at the end of this ejection phase could slightly exceed the ventricle pressures but the momentum keeps the blood flow forward without a retrograde flow.

The estimated peak pressures in the aorta and pulmonary artery are about 120 and 25 mmHg, while the cardiac output is around 70 to 90 mL per stroke at resting condition, which is an ejection fraction of about 65% of the end-diastolic ventricular volume.

Phase 5: Isovolumetric Relaxation

The ventricular pressure continues to drop rapidly while the aortic and pulmonary valves close to prevent the backflow (Barrett, 2010).

II. Heart Rate

Heart rate is the measure of the heart cycle per unit of time which generally is measured as beats per minute (bpm). The heart rate can be varied depending on the physical needs of the oxygen and carbon dioxide exchange; therefore, the heart rate could have a large variation from 60-80 bpm for a normal adult during rest to above 180 bpm during intensive exercise.

This mock circulation loop is capable of varying the heart rate between 60-120 bpm. The heart rate of 60 bpm is set for the normal heart function, while 90 bpm is used for the heart failure condition to simulate the increase of the heart rate in attempts to compensate for the loss of cardiac output.

4.2.3 Distribution of Flow and Pressure

I. Pressure in the Heart Chambers

The contraction of the heart chambers makes the pressure varied throughout the cardiac cycle. The pressure distribution and the range of an average healthy adult during rest is shown in Table 4-1

Table 4-1: Pressure distribution in heart chamber

Heart Chamber	Pressure (mmHg)
Right Atrium	0-4
Right Ventricle	25/4
Pulmonary Artery	25/10
Left Atrium	8-10
Left Ventricle	120/10
Aorta	120/80

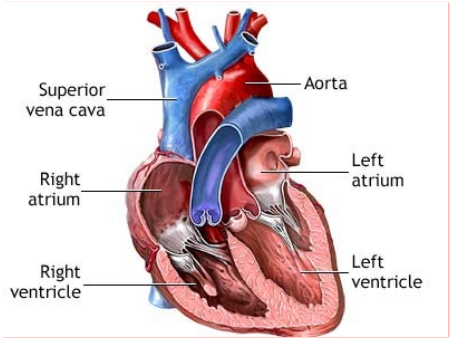

The left ventricle has the highest diastolic pressure among the chambers as it pumps blood through the systemic circulation. The maximum left ventricle pressure is estimated at 120 mmHg which is equal to the pressure in the aorta at the same phase of the heart cycle, while the pressure is lowest during the filling phase at about 10 mmHg and the aortic pressure is around 80mmHg. Blood from the systemic circulation then returns to the heart via the right atrium at a very low pressure ranging from 0-4 mmHg. The blood from the right ventricle is then pumped through the pulmonary circulation by the right ventricle in the same manner as the left ventricle does in the systemic circulation but at a significantly lower pressure, which is about 25 mmHg during the systolic phase and 4/10 mmHg during the diastolic phase in the right ventricle and pulmonary, respectively. The pressure in the left atrium, which receives the blood returned from the pulmonary circulation, slightly varies with respiration from 8-10 mmHg.

II. Stroke Volume

The amount of blood volume pumped during one contraction is called stroke volume. It can be calculated by measuring the difference in the blood volume in the ventricle at the end of the diastolic phase and at the end of the systolic phase:

$$SV = EDV - ESV \qquad [4\text{-}1]$$

where EDV is the end-diastolic volume and ESV is the end-systolic volume. The EDV of the left ventricle for normal people is about 120 ml and the ESV is 50ml; therefore, the estimated stroke volume (SV) is about 70 ml or around 60% of the blood volume in the chamber. However, the actual value of the stroke volume can range from 55-100 ml depending on the activities and physiological condition of normal people. Figure 4-5 shows the relation between the left ventricular volume and the stroke volume during one cardiac cycle.

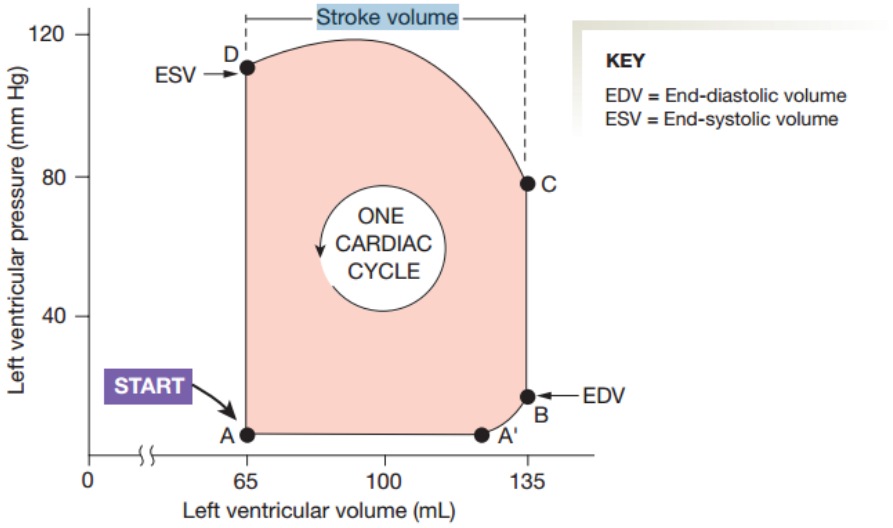

Figure 4-5: Left ventricular stroke volume (Brazier, 1988).

III. Cardiac Output

The cardiac output (CO) refers to the volume of blood pumped by the left or right ventricle. It can be calculated by the following equation:

$$Cardiac\ Output = Heart\ rate\ x\ Stroke\ Volume \qquad [4\text{-}2]$$

Normal cardiac output is approximately 5L/min which is generally the same for both ventricles. During exercise, the reflex mechanism increases the cardiac output by either increasing the heart rate, stroke volume, or even both at the same time to pump enough blood volume to meet the required perfusion for the tissues and organs. These mechanisms may raise the CO rate up to 30-35 l/min (Brazier, 1988; Marieb & Hoehn, 2007).

IV. Arterial Pressure

The contraction of the heart during the systolic phase ejects blood into the aorta at high pressure. For an average healthy adult, this arterial pressure is typically as high as 120 mmHg and 25 mmHg for the left and the right ventricles, respectively. This peak pressure is called the **systolic pressure** (P_{sys}).

During the diastole, after the aortic valve closes, the aortic pressure drops to the lowest level at approximately 80 mmHg for the left ventricle and 10 mmHg for the right ventricle for a healthy adult. This pressure is referred as **diastolic pressure** (P_{dias}). The difference between systolic and diastolic pressure is defined as the arterial **pulse pressure (PP)**. This relationship is shown in Equation [4-3]:

$$PP = P_{sys} - P_{dias} \quad [4\text{-}3]$$

The pulse pressure is the measure of force per unit area that the heart generates at each contraction; therefore, it is used as a strong indication of heart problems. In normal people the pulse pressure is estimated at 40 and 15 mmHg for the systemic and pulmonary circulation, respectively. An arterial pulse pressure lower than 25 mmHg caused by low stroke volume could be a sign of cardiovascular disease, while a pressure consistently greater than 40 mmHg could indicate poor heart functions like heart valves' leakage. Pulse pressure is directly related to the stroke volume and the heart rate, thus it increases during exercise as the systolic pressure is increased with a stronger ventricle contraction while the diastolic pressure remains about the same.

V. Mean Arterial Pressure

Due to the fluctuation of pressure according to the nature of pulse flow, an average pressure is often used as a reference for the studies and calculations of arterial pressure. However, as the diastolic phase is normally longer than the diastole, the mean arterial pressure (MAP) is calculated based on the diastolic pressure plus one-third of the pulse pressure.

$$MAP = P_{dias} + \frac{PP}{3} \quad [4\text{-}4]$$

The typical value of mean arterial pressure for a healthy adult, whose systolic pressure is 120 mmHg and diastolic pressure is 80 mmHg, is calculated as follows:

$$MAP = 80 + \frac{(120 - 80)}{3} = 93.3\ mmHg$$

The pulmonary artery pressure is approximately 7 times lower than the aortic pressure (Barrett, 2010); therefore, the pressure for the right system is estimated at 13 mmHg .

VI. Venous Blood Pressure

Venous blood pressure is typically measured in terms of mean venous pressure (MVP), also known as central venous pressure (CVP), and is the pressure of blood in the thoracic vena cava. The value of this pressure is steadier compared to the arterial pressure which is pulsated by the left ventricle contraction, and has very little variation during the cardiac cycle. The pressure in the vena cava is only approximately 15 mmHg.

4.2.4 Compliance

Compliance or capacitance is the ability of the blood vessels and internal organs to expand on receiving a pulse pressure of blood flow during the systolic phase and the recoil on the diastolic phase is due to the elasticity of the cell membrane. This flow property creates a damping effect to the blood flow which reduces the pulse fluctuation and helps in maintaining the perfusion supply to the organs during the systolic phase where the flow is paused. Without this effect, the systemic circulation pressure would quickly drop from the systolic pressure to zero which would cause a pause in the perfusion and the heart workload would need to increase greatly to maintain a continuous blood supply to the body. Compliance can be described as the ratio of the change in volume (ΔV) by the change in pressure (ΔP), as expressed in the following equation:

$$C = \frac{\Delta V}{\Delta P} \qquad [4\text{-}5]$$

The compliance property is dependent on the elasticity of the organs or blood vessels' walls by having an inverse relation to the stiffness; therefore, this value varies at different body locations. This relationship can be seen in the plot between pressure and volume of the arteries and veins, as shown in Figure 4-6. The graph suggests that the veins in the venous system are deformed more easily than the arteries under the same pressure; therefore, according to the description of the compliance, the venous system has greater compliance than the arterial system. In addition to the variation of compliance among the blood vessels, the compliance value could also gradually be changed with age as the elasticity of the arterial walls becomes lower and thus the compliance is reduced.

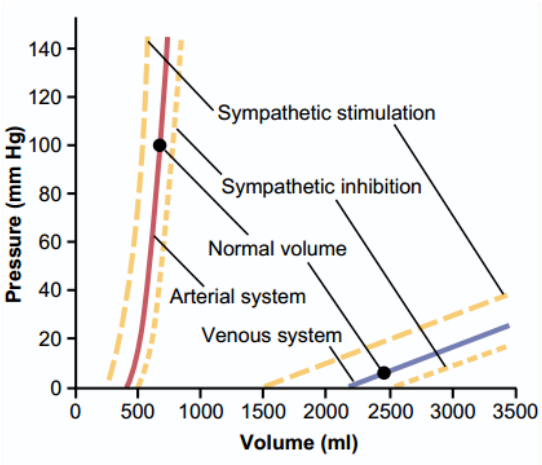

Figure 4-6: Pressure - volume plot of arteries and veins (J. E. Hall & Guyton, 2011).

As the compliance relies on the elasticity of the blood vessels, it is hard to directly measure the values; thus, it is commonly calculated based on the stroke volume and pulse pressure (Chemla et al., 1998; Stergiopulos, Meister, & Westerhof, 1994).

VII. Arterial compliance

Arterial compliance is the compliance of large arteries such as the thoracic aorta, which normally have large elasticity and, thus, small compliance. Several studies have been conducted and the arterial compliance has been documented, as shown in Table 4-2; the average values range from 1-2 ml/mmHg for the systemic arterial and 2-5 ml/mmHg for the pulmonary arterial system.

Table 4-2: Compliance values from different literature.

Literature	Arterial Compliance(ml/mmHg)	Pulmonary Compliance(ml/mmHg)
(Stergiopulos et al., 1994)	1.68	-
(Chemla et al., 1998)	1.46	-
(G. Ferrari et al., 2002)	1.80	4.80
(Liu, Allaire, Wu, Wood, & Olsen, 2006)	2.20	-
(Daniel Timms, 2005)	1.12	2.98

VIII. Venous compliance

The venous compliance is estimated to be from 20 to 30 times greater than the arterial compliance (Berne, Levy, Koeppen, & Stanton, 1998; Gelman, 2008); therefore, the estimated venous compliance value of a healthy adult is about 50ml/mmHg.

4.2.5 Resistance

The resistance to the blood flow is one of the significant effects on the circulatory system. It is mainly influenced by the blood's viscosity, and the length and/or change in the size of the vessels that the blood passes through. Higher viscosity makes the fluid thicker and stickier as it become harder for the molecules to slide between one another; the high viscosity of blood compared to water makes this property become more significant. The longer the length of the vessels, the greater the resistance, and the large radius of a vessel like in the aorta means a lower resistance compared to the resistance in the smaller vessels such as arterioles or capillaries. These relationships can be expressed by the formula:

$$R = \frac{8\eta L}{\pi r^4} \qquad [4\text{-}6]$$

The resistance also has a relationship with the flow rate and flow pressure. A large flow resistance causes a large pressure drop on the flow path. This relationship is described by the following equation:

$$R = \frac{\Delta P}{Q} \qquad [4\text{-}7]$$

The resistance value can be presented in different units but most commonly is displayed in dyne.s.cm^{-5} or mmHg.min/l.

The flow resistance is predominantly encountered in the systemic circulation which includes the resistance of blood flow incurred by the arteries, capillaries and veins. These resistances are often lumped to a single parameter called systemic vascular resistance (SVR) or total peripheral resistance (TPR). Based on Equation [4-7], the SVR can be calculated from the pressure drops between the MAP and the mean right arterial pressure (mRAP), divided by the cardiac output (CO), as shown in the following Equation (Marieb & Hoehn, 2007):

$$TPR = \frac{MAP - mRAP}{CO} \qquad [4\text{-}8]$$

According to Equation [4-8], the TPR is calculated based on the MAP of 93 mmHg, mRAP of 3 mmHg, and the CO of 5 L/min, which yield an estimated TPR of 1.09 mmHg.min/l.

4.2.6 Frank-Starling Mechanism

Frank-Starling is the circulation mechanism of the heart that increases the stroke volume in response to the venous blood that returns to the heart. This means that the heart naturally works harder to eject the excessive blood volume that is filled in the ventricle, leading to an increase of stroke volume and, hence, cardiac output. Figure 4-7 shows the Starling curve; it is the left ventricle contraction force via the stroke volume on the y-axis which increases, along with the end of the diastolic volume on the x-axis.

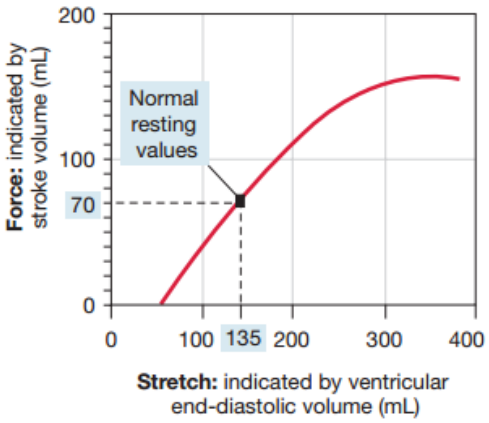

Figure 4-7: A Starling curve (Brazier, 1988).

4.2.7 Physiological condition of CHF patients

As described in Chapter 1, CHF is the condition in which the heart muscles, especially in the ventricle, are weakened, thus losing the contraction force that is required to pump blood in the circulation system. In the aspect of physiological parameters, one can see a reduction of stroke volume and, thus, of cardiac output, which means the ventricle cannot effectively remove the blood volume from the ventricle. If this occurs in the left ventricle, the excessive blood will start to accumulate in the pulmonary system, the right side of the heart and the lungs, thus increasing the MAP and LAP which leads to pulmonary edema. Meanwhile, the blood that is backed up in the right side of the heart will trigger the Frank-Starling mechanism that leads to more blood being accumulated in the lungs and left ventricle and causes even more edema. In addition to the pulmonary problem, the consistently high workload on the right ventricle due to the Frank-Starling response could induce the development of right-sided heart failure, and thus lead to a worsening CHF condition.

4.3 LITERATURE REVIEW OF MOCK CIRCULATION LOOP STRUCTURE & MECHANISM

The mock circulation loop (MCL) is a mechanical circulation system capable of simulating the physiological conditions of the human circulatory system. It could be used as a test rig for in-vitro evaluation of cardiac prosthetic devices such as heart valves, balloon pumps, TAH or VAD. There are several designs of MCL that serve

different purposes and with different components and which have the capability of replicating the circulation characteristics. They can vary from the basic system that only consists of the preload chamber and a resistance valve that can deliver a continuous but constant flow rate, to the more advanced versions which simulate the pulse flow and comprise both systemic and pulmonary circulation systems. Some of these advanced systems can accurately replicate other important characteristics such as compliance, ejection fraction, fluid inertia or the different levels of the body's workload during exercise, rest or sleep. Examples of the structure of a basic and an advanced MCL configuration are shown in Figure 4-8.

4.3.1 Basic structure and flow generation

Several basic MCL systems have been developed for the evaluation of a heart pump as the MCL is a quick and efficient way to verify the pump's performance. The common feature of the basic loop is the ability to deliver a constant flow which is usually achieved by a preload tank with a clamp or valve to adjust the resistance before it flows into the pump, while the pressure is controlled by the water level (Yoshino et al., 2001). However, the lack of pulsatility behaviour from this type of loop limits the ability to evaluate the hemodynamic performance and it is not possible to evaluate the fluctuation of the pump's performance due to the variation of flow that occurs in a real human circulatory system.

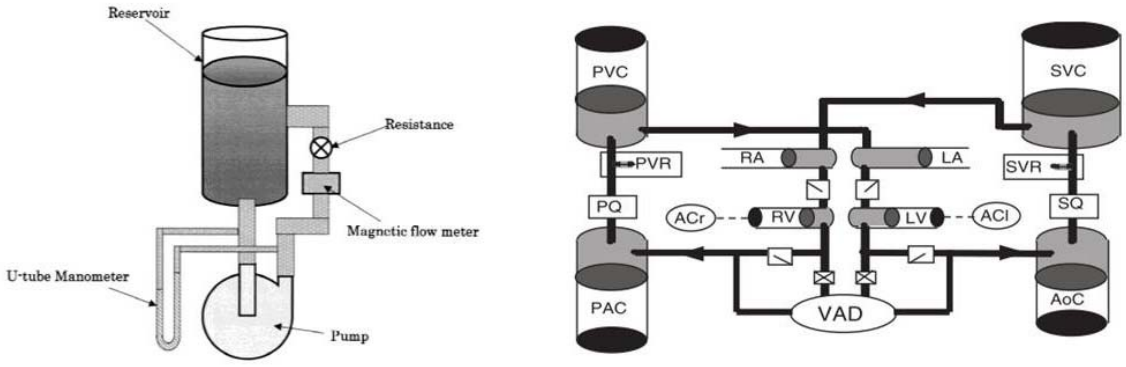

Figure 4-8: Diagrams of a basic mock circulation loop by Yoshino et al. (Yoshino et al., 2001) (left) and a more advanced version by Timms et al. (Daniel Timms, Hayne, McNeil, & Galbraith, 2005) (right)

The advanced mock circulation loop has been constantly developed to be more flexible and capable of reflecting the real physiological conditions. An important function of the advanced MCL is the simulation of the pulsatile flow environment from the artificial ventricle. Scotten et al. (Scotten, Walker, & Brownlee, 1979) created a left ventricle for a mitral prosthetic valve with a cone-shaped polyurethane sheet enclosed in a transparent hydraulic chamber. The ventricle is driven by a positive displacement pump that transfers the pressure to the sheet via the fluid within the chamber.

Cassot et al. (Cassot et al., 1985) attempted to improve the physiological pressure, especially within the left ventricle, to simulate an accurate condition for a heart valve evaluation which required a higher detail of the flow characteristics than the traditional MCL could generate. The study focused on redesigning the ventricle simulator by trying to mimic the real shape of a ventricle using a flexible ventricular sac suspended within the top part of the transparent rigid chamber (Figure 4-9). The driving force was still delivered by means of hydraulic pressure like the system of Scotten et al. but the piston pump was replaced with a volumetric gear pump running on a servomotor controlled by a synthesiser that could produce the pressure to regulate the flow for the required shape, amplitude and frequency profile.

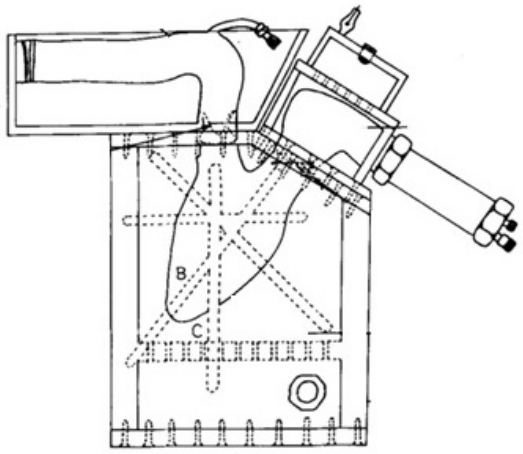

Figure 4-9: An artificial ventricle by Cassot et al. (Cassot, Morvan, Issartier, & Pelissier, 1985)

The designs of a ventricle with a flexible membrane within the chamber were adopted and improved many times by several researchers to suit the requirements of the testing subjects with consideration about compromising between the accuracy and the complexity of the mechanism. One of the most common designs for this type of ventricle simulator is the replacement of the hydraulic chamber with an air pressurised chamber fitted with a pneumatic regulator to control the pressure; this was used by Verdonck et al. (Verdonck, Kleven, Verhoeven, Angelsen, &

Vandenbogaerde, 1992), Pentalos & Konig et al. (Koenig et al., 2004; Pantalos, Koenig, Gillars, Giridharan, & Ewert, 2004), Liu et al. (Liu et al., 2006) and Garcia et al. (Garcia, Enriquez, Dembitsky, & May-Newman, 2008),

The simulation of the pulse flow effect can also be accomplished by means of a simpler mechanism, such as a piston or bellows in the displacement pumps. An example of a piston-driven ventricle is the mock circulation loop designed by Zannoli et al. (Zannoli, Corazza, & Branzi, 2009) (Figure 4-10), with a 1:20 downscaled model of the systemic circulation system built as a simple but effective design for teaching and general research purposes. The piston in this system is driven by a simple crank and slider mechanism that operates at a constant speed of 66 rpm and a fixed stroke volume of 1.0 ml. To control and vary the stroke output, the pressure-volume relationship of the ventricle needs to be controlled, and a more sophisticated driving mechanism is needed. Baloa et al. (Baloa, Boston, & Antaki, 2001) incorporated this pressure-volume relationship in their mock loop for VAD testing by using a voice coil actuator (VCA) which could control the speed and displacement of the bellows pump directly controlled by the computer program. The piston or bellows displacement control can also be achieved by other different means of driving mechanism such as a servo motor and a screw-driven mechanism (Colacino et al., 2008; Vosse et al., 2011).

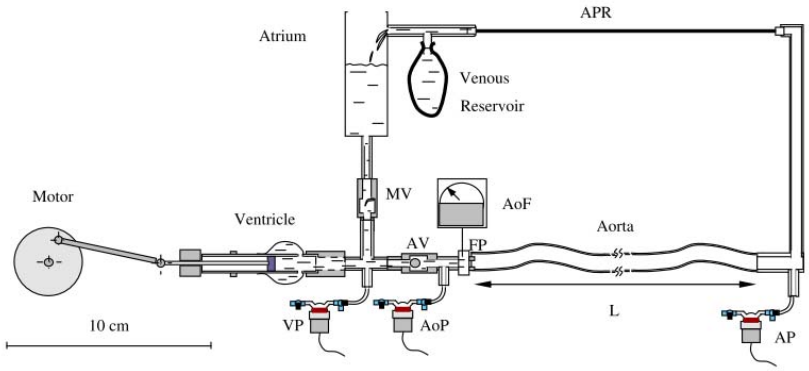

Figure 4-10: The MCL with piston-driven ventricle by Zannoli et al. (Zannoli et al., 2009)

Timms et al. (Daniel Timms et al., 2005; Daniel L. Timms et al., 2011) have a different approach to create the pulsatile flow in their complete mock loop for

BiVAD testing by using pneumatic actuators to compress the air directly to the ventricle chambers, which is an air-sealed vertical tank constructed from clear flexible PVC piping. This method allows the ventricle pressure to be simulated more efficiently as it allows the passive diastolic filling and does not induce negative pressure in the chamber like other mechanisms.

4.3.2 Compliance simulation

The compliance effect is one of the important parameters that reduces the fluctuation of the flow rate and pressure due to the pulsatile flow environment. However, as the rigid wall of tubing and other components could not reflect the compliance from the elastic property of the blood vessels, many researchers attempted to replicate this effect in their advanced loop by introducing a damping effect via several mechanism structures. The notable designs include the use of a spring, flexible membrane and air trap tank.

One of the most widely accepted MCLs was the Pennsylvania State University mock circulation system (Rosenberg, Phillips, Landis, & Pierce, 1981) which was originally designed in 1971 and has undergone several improvements and became the standard used by the American National Institutes of Health in 1985. This MCL consists of many components that were innovative designs at the time; one of the important features is the application of a leaf spring-loaded bellows to a compliance chamber which allows the compliance to be relatively small and adjustable by replacing the spring with another different spring constant.

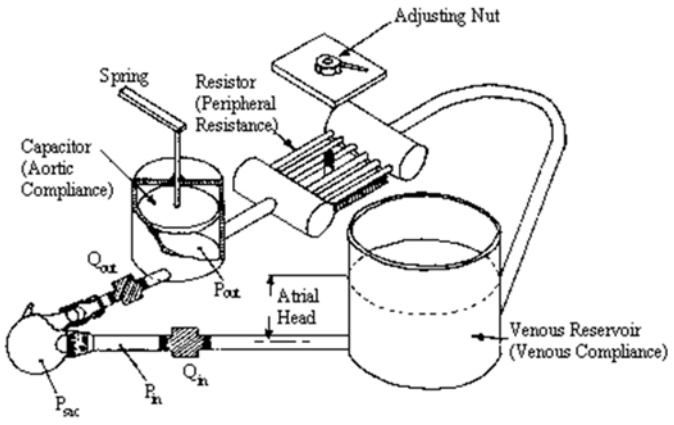

Figure 4-11: The Pennsylvania State University mock circulation system.

The concept of this compliance was revisited by Woodruff et al. (Woodruff, Sharp, & Pantalos, 1997), which focused on improving the compliance mechanism for the required microgravity environment evaluation to study an astronaut's cardiac function under weightless conditions. The Penn State mock circulation system was used as a base design and improvement was done by replacing the original leaf spring with a spring coil, resulting in a significantly smaller size and lighter weight. Figure 4-12 shows the design of this compliance chamber with an internal spring structure and a knob on the top which can be used to adjust the spring constant to change the compliance value of this chamber. The test was conducted in comparison with the original Penn State loop and the compliance was set to 0.5, 1.0 and 1.5 mmHg/ml for the arterial compliance, and 5, 10 and 15 ml/mmHg for the venous compliance. The results show the limitation of the available springs that could not provide the exact required spring constant and thus there is some error in the actual compliance value. Another major drawback of the spring compliance chamber is that the adjustable range of spring constant was not wide enough to cover all the target compliance values, thus the test rig needs to be stopped for spring replacement which could cause an error to other parameters of the circulation loop.

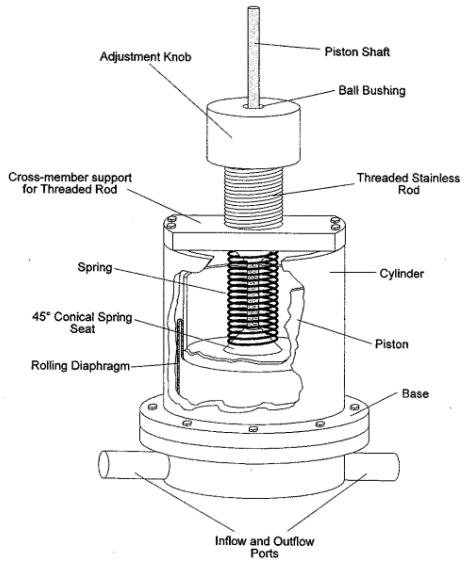

Figure 4-12: Compact compliance by Woodruff et al. (Woodruff et al., 1997)

Pentalos et al. (Pantalos et al., 2004) used the spring compliance concept for the venous and systemic compliance chamber that was specifically designed for VAD

testing. The compliance design was similar to the chamber of Woodruff et al. with a spring-loaded piston pressed on the roll sock diaphragm which was fitted inside the enclosed chamber. This compliance can be varied by adjusting the spring stiffness, but the value was set to 1.3 ml/mmHg to simulate the real human condition for assessing the MCL performance.

The use of a flexible membrane to provide a compliance is incorporated in the basic circulation loop for artificial lung testing which was designed by Haft et al. (Haft et al., 2003). This loop has a simple structure design where the pulse flow is generated from a Thoratec LVAD instead of a dedicated design of a ventricle simulator and adjustable resistance is not included in the system. A flexible polyurethane bag in a pressurised chamber is used as a compliance chamber, as shown in Figure 4-13. The compliance is adjustable by using the air pressure compressed into the chamber by a pneumatic compressor; in this test, the pressure was varied from 0 to 16 mmHg while the volume of the chamber also varied between 50, 100, 200, 250 and 500 ml.

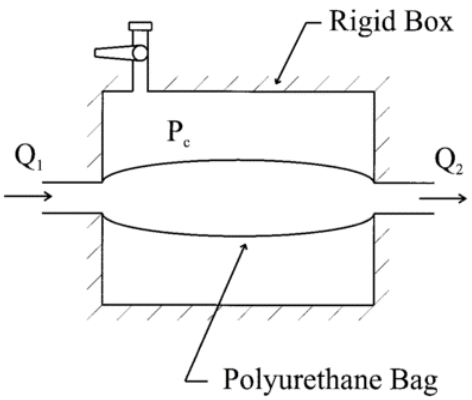

Figure 4-13: Flexible membrane compliance by Haft et al. (Haft et al., 2003)

One of the most common approaches to simulate this effect is using the air trapped inside the chamber to replicate the elastic property of the blood vessels. This method was utilised by Donovan (Donovan, 1975) on the mock circulation loop for VAD testing that was constructed as an acrylic tank that contains 4 internal chambers of which the 2 small chambers are used as the systemic and pulmonary arterial chambers while the larger chambers are the systemic and pulmonary venous chambers. The compliance was set at 10 ml/mmHg, 1 ml/mmHg, 5 ml/mmHg and 1 ml/mmHg for the systemic venous, pulmonary arterial, pulmonary venous and systemic arterial chambers, respectively. The compliance was adjustable by changing the volume of the air trapped above each individual chamber.

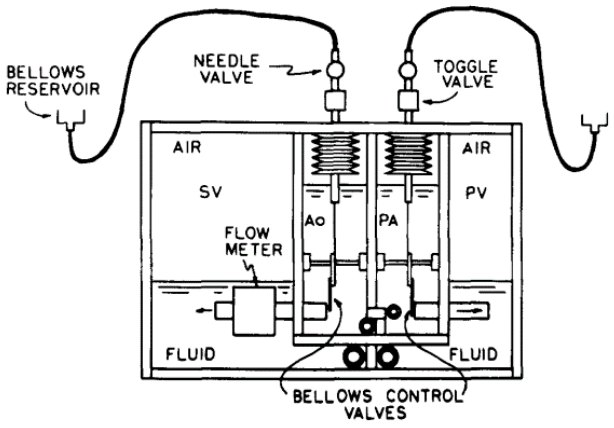

Figure 4-14: Mock circulation loop by Donovan (Donovan, 1975)

The concept of the chamber with the air trapped inside is known to be a simple but effective design, but the size of the tank needs to be relatively large to trap enough volume of air that can give the required compliance. However, as MCLs are often developed for laboratory use where usually the size is not a critical consideration in the design, the basic chamber with the air trapped inside which is less complicated and easier to develop is, thus, still a preferred option for many researchers to use in their test loop (Andrade et al., 1999; Athanassiou, Hancock, & Mahajan, 2005; Avrahami, Rosenfeld, Raz, & Einav, 2006; Ayre, Lovell, & Woodard, 2003; Bowles et al., 1991; Garcia et al., 2008; Liu et al., 2006; Daniel Timms et al., 2005; Vosse et al., 2011).

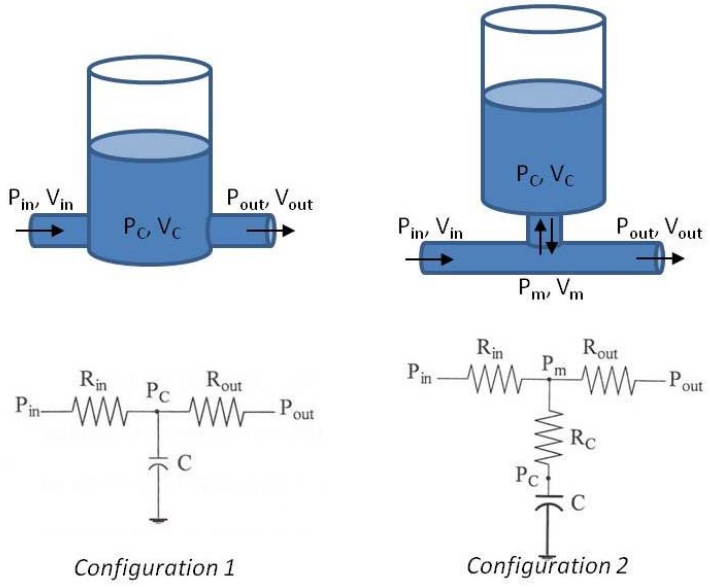

Figure 4-15: Compliance tank configurations and its equivalent electrical analog diagram.

Among the air trapped inside the chamber designs, two configurations of the windkessel tank, as shown in Figure 4-15, have been widely used in several studies. While both configurations have proved to accurately replicate the human circulatory system, Liu et. al. (Liu et al., 2006) compared both configurations on the Matlab/Simulink mathematical simulation model and suggested that the 90 degree elbow connector between the tank and the main pipe introduces extra resistance and cause pressure loss from ventricle to aorta, so the configuration 1 was used in his complete circulation loop for VAD testing (Figure 4-16). Therefore, this configuration was adopted for the MCL in this thesis for the same reason.

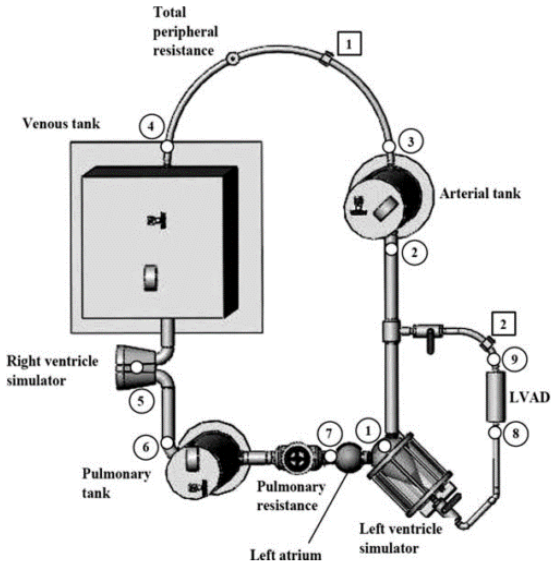

Figure 4-16: The complete mock circulation loop by Liu et al. (Donovan, 1975)

4.3.3 Resistance simulation

Resistance is a significant basic flow property in the simulation of human circulation; therefore, most MCLs include a component that can both vary this value in the designs to mimic the ability of the body and that can vary the resistance in response to the physiological conditions such as the reduction of resistance during exercise to increase the blood circulation.

A concept of resistance, as discussed in the previous section, is defined as the ratio of the pressure drop to the volumetric flow rate. Therefore, the simulation of resistance often relies on reducing the cross-sectional area of the pipe to generate the pressure drop across the pipe section. Donovan's (1975) MCL, shown in the previous section (Figure 4-14), adopted this concept for the systemic and pulmonary resistance. The resistance module in this MCL shows an innovative design structure as the resistance can be varied automatically in response to the variation of arterial and pulmonary pressure. As shown in Figure 4-17, this resistance module is situated inside the aortic and pulmonary compliance chamber. The cross-sectional area of the flow tube is adjusted by the valve plate located on the lever arm that moves about the pivot connection, while another arm of the lever connected to the bellows is filled with water so that the water pressure can be controlled by a toggle valve and a needle

valve outside the chamber. As the air pressure within the tank increases above the water pressure, the bellows are compressed and force the water to flow through the valves back to the bellows' reservoir. The contraction of the bellows pulls the lever arm which causes the valve plate to move about the pivot and open more of the cross-sectional area to the flow tube, resulting in the reduction of the flow resistance while also reducing the arterial pressure.

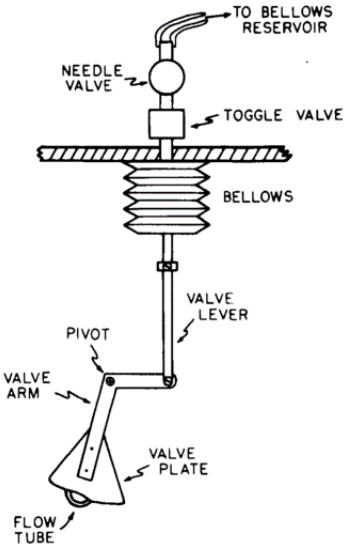

Figure 4-17: Bellows-operated resistance mechanism by Donovan (Donovan, 1975)

The Pennsylvania State University mock circulation system (Rosenberg et al., 1981) creates a pressure drop for peripheral resistance using the same concept of changing the cross-sectional area of flow but with a different approach. The system was fitted with a resistance module containing a series of small flexible tubes situated between two flat plates. The plates can be clamped together by the adjusting nut which reduces the flow area and thus raises the flow resistance.

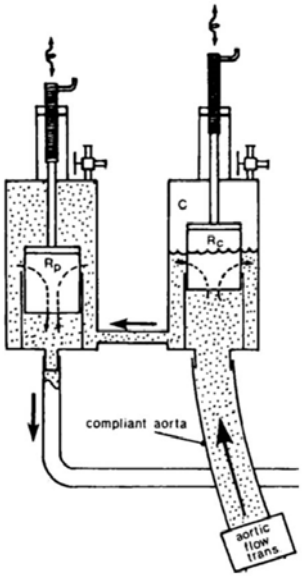

Figure 4-18: Resistance unit inside the compliance chamber by Scotten et al. (Scotten et al., 1979)

The approach of Scotten et al. (Scotten et al., 1979) of simulating the resistance is slightly different from those directly adjusting the section area of the tube; instead, a cellulose fibre filter was inserted into the vertical inflow tube within the compliance chamber (Figure 4-18). The filter is attached to a threaded rod inserted into the threaded hole on top of the tank which allows the vertical position to be adjustable and, therefore, the active length of the filter and hence the resistance can be directly altered. Pantalos et al. (Pantalos et al., 2004) used a similar method of simulating the resistance by filling the chamber with the open cell form in the sealed chamber with an adjustable compression piston to create the required flow resistance.

While the resistance mechanism as shown above is reliable and capable of simulating the human vascular resistance, the more recent research often relies on simpler components such as an adjustable clamp used by Andreade et al. (Andrade et al., 1999), Liu et al. (Liu et al., 2006) and Vosse et al. (Vosse et al., 2011), or various type of valves such as Baloa et al. (Baloa et al., 2001) and Inoguchi et al. (2006) (Inoguchi, Tanaka, Maehara, & Matsuda, 2006).

A more advanced control over the resistance valve is the design of Timms et al. (Daniel Timms, 2005) which incorporated a pinch valve with a proportional input voltage controlled under an algorithm that is capable of varying the resistance in response to the change of arterial pressure in the circulation loop.

4.3.4 Summary of Physical Parameters for the MCL

I. Healthy - Rest

According to the MCL literature and the calculations of physiological parameters that were reviewed in the previous sections, the condition of a healthy adult for the mock circulation loop is summarized in Table 4-3.

II. CHF

CHF caused by left ventricular failure which reduces the capability of the heart to eject sufficient blood out of the left ventricle, reduces the end-diastolic pressure, cardiac output, MAP and the mean circulatory pressure. Meanwhile, an imbalance between the flow in the systemic and pulmonary circulation causes excessive blood to back up in the lungs and increases pulmonary pressure.

To reflect the weak ventricle of CHF patients, the aortic pressure is reduced by about 30% and the cardiac output is reduced by approximately 40%. The heart rate was raised by 50% to simulate the attempts of failing heart to compensate the loss of cardiac output.

Table 4-3: Physiological parameters for the mock circulation loop.

Parameters	Healthy	CHF
Heart Rate (HR) (BPM)	60	90
Stroke Volume (SV) (ml)	80	30
Cardiac output (CO) (L/min)	5	2.5
Left Ventricular Peak Systolic Pressure (LVPPS) (mmHg)	120	80
Left Ventricular Peak Diastolic Pressure (LVPPD) (mmHg)	0-8	0-8
Aortic Systolic Pressure (AOP_{sys}) (mmHg)	120	80
Aortic Diastolic Pressure (AOP_{dias}) (mmHg)	80	55

Arterial Compliance (C_{art}) (ml/mmHg)	1.28	0.96
Total Peripheral Resistance (TPR) (mmHg/ml/s)	1	1

4.4 COMPONENTS AND FUNCTIONS

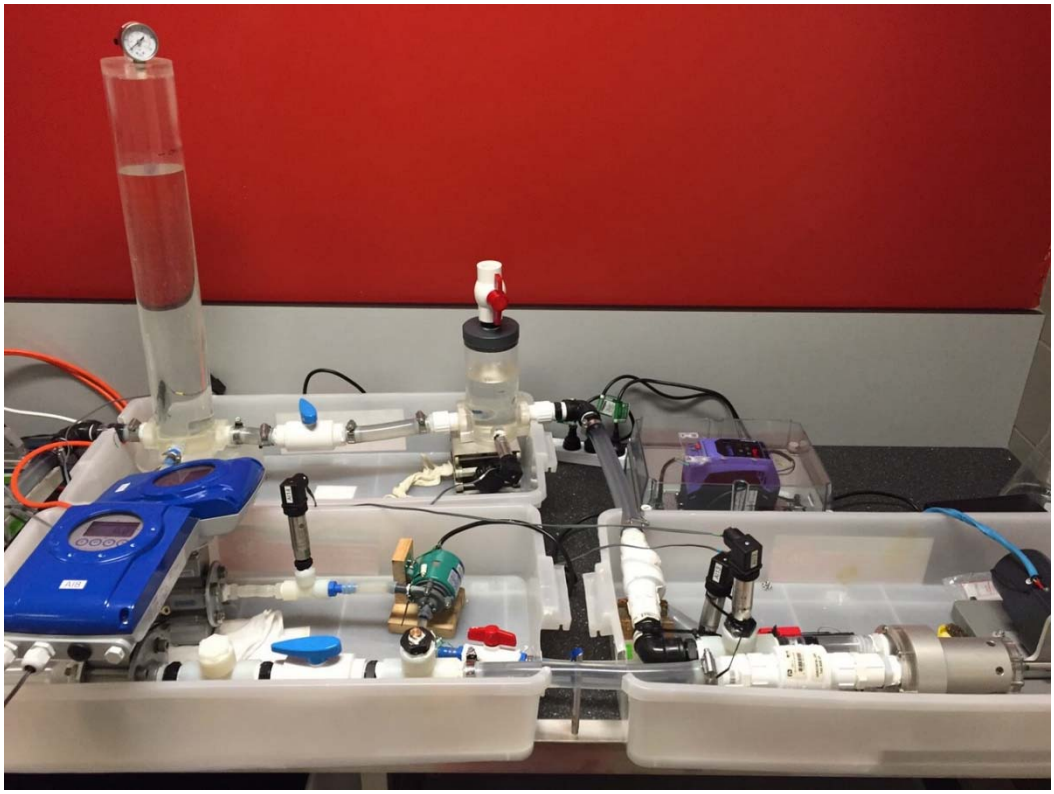

Figure 4-19: The human mock circulation loop in this study.

The mock circulation loop in this study is shown in Figure 4-19 and the components diagram is shown in Figure 4-20. This MCL is comprised of three main components: the ventricle simulator (1), the compliance tank (2) and the arterial tank (3). All the components are connected by 1in diameter clear vinyl tubes with adjustable ball valves to simulate the peripheral resistance. Two check valves are installed at the inlet and the outlet of the ventricle simulator to regulate the blood flow direction. The VAD is connected to the MCL in the secondary flow circuit using ½in tube fitted to an extra outlet of the ventricle simulator to the compliance chamber and has a valve to cut off the flow for the evaluation of the loop without the VAD. The test rig was placed on three large plastic containers to contain any spill or leakage of fluid that might accidentally occur.

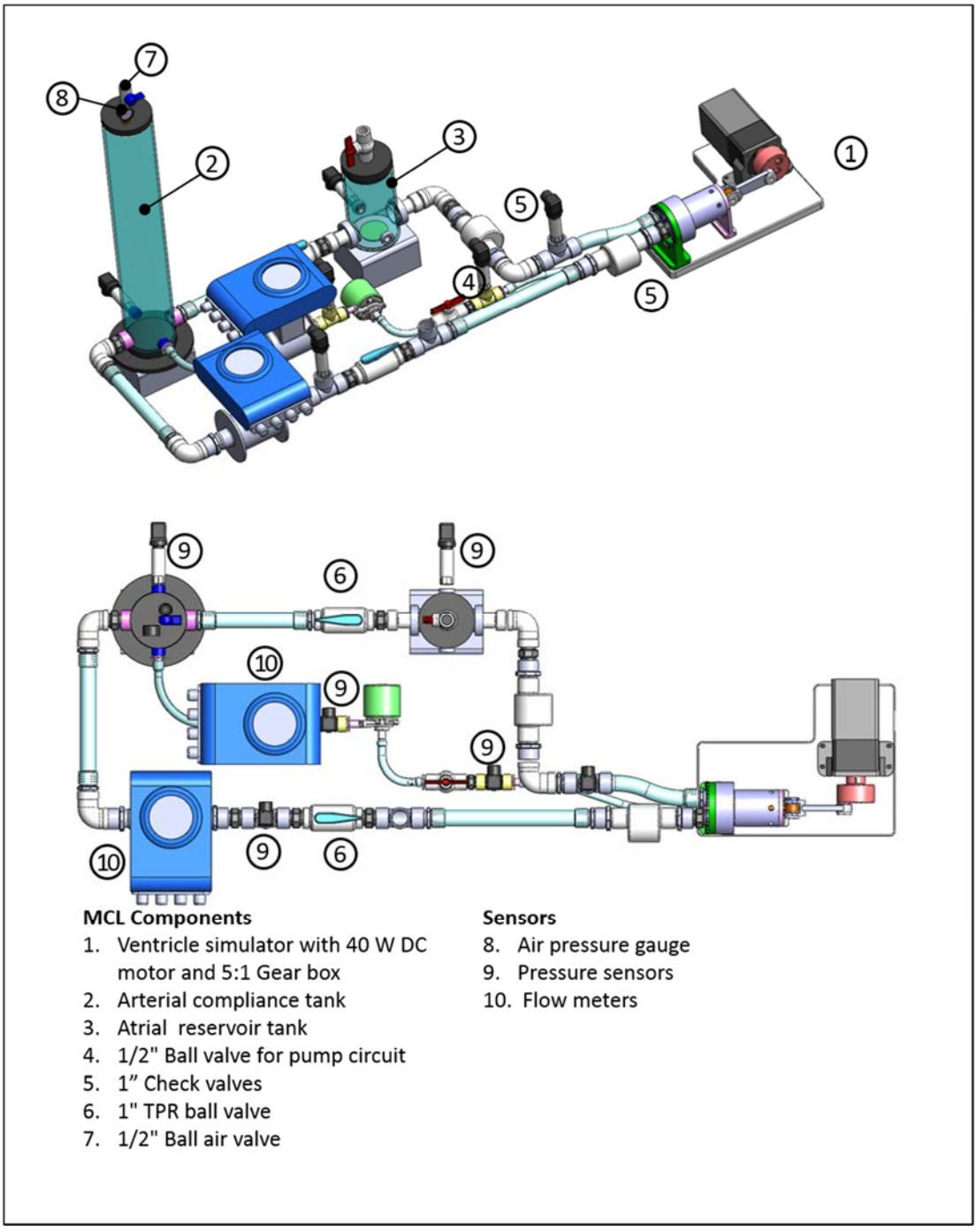

Figure 4-20: Diagram of mock circulation loop.

I. Ventricle Simulator

The function of the ventricle simulator in this mock circulation loop is to simulate the pulse flow to mimic the heart pulse from the left ventricle. The structure of this ventricle simulator is based on a piston pump driven by a scotch-yoke mechanism powered by a 40W DC motor with 5:1 gear box to increase the output torque. The speed is adjustable via the variable speed controller to achieve the heart rate of different physiological conditions. The cylinder, made of structured anodized aluminium, has 2 parts; the larger part of the cylinder has a diameter of 100mm covered by an acrylic lid with 2 x 1in sockets for the inlet and outlet ports of the pump and a 1/2in socket connected to the VAD circuit. The smaller part of the cylinder has a diameter of 80mm and contains the sliding piston that pumps the fluid. The fly wheel of the ventricle simulator has 3 threaded sockets with different distances from the centre of the wheel; the ejection volume of the pump can be adjusted by moving the pin of the scotch-yoke mechanism to these holes (Figure 4-21 & Figure 4-22).

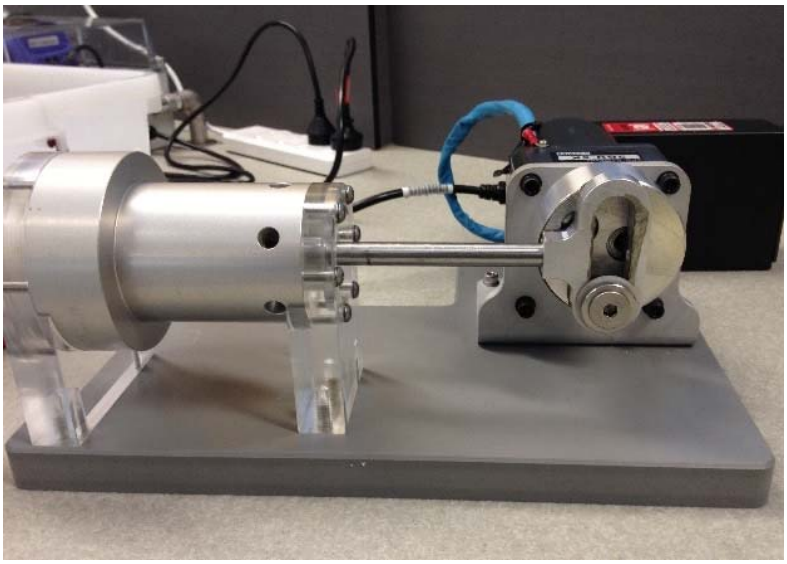

Figure 4-21: Ventricle Simulator.

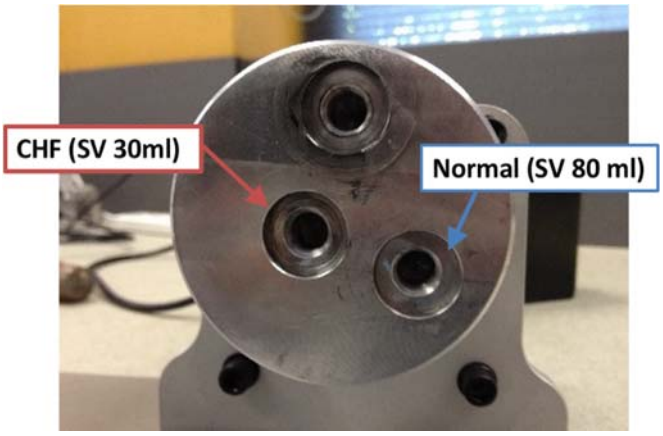

Figure 4-22: Threaded sockets on the fly wheel of ventricle simulator for adjusting the ejection volume.

II. Arterial Compliance Tank

The compliance tank of this mock circulation loop is designed to simulate the arterial compliance effect. It is an airtight tank constructed from clear PVC with an inner diameter of 100mm, wall thickness of 4.5mm, and height of 645mm. The top lid of the tank is fitted with a ball valve and a pressure gauge for measuring and adjusting the air pressure according to the required compliance value. The bottom of the tank has two 1in sockets for the barb fittings to connect the main flow tubing, one 1/2in port for secondary flow from the VAD and one 1/4in port for the pressure transducer.

III. Atrial Reservoir Tank

This reservoir tank serves 2 objectives; to supply the water returning to the ventricle simulator, and to create the preload pressure for the ventricle simulator like the atrium. This tank has a basic structure like the compliance tank but has a different size and volume. The top of the tank is fitted with a 1in ball valve for ease of filling the working fluid and pressure adjustment. The bottom of the tank is fitted with two 1in connectors for the inlet and outlet and a 1/4in female threaded fitting where the pressure sensor is connected. The outlet of this tank is connected to the check valve which restricts the flow direction to return to the ventricle simulator. The tank is placed on an adjustable stand for a freely level adjustment of the vertical position to achieve the pressure and compliance of the arterial compliance tank.

IV. Mitral / Aortic Valves

The mitral and aortic valves prevent the back flow of fluid to the atrium and ventricle and are simulated by the 1in flapper check valves which were selected due to their lower resistance compared to other types of non-return valves. The mitral valve is installed near the inlet of the ventricle simulator to prevent the back flow to the arterial tank, while the aortic valve is attached to the outlet of the ventricle simulator to regulate the output flow.

V. Pumping Fluid

To closely replicate the circulatory system, the pumping fluid needs to have similar properties to real human blood which has an estimated density of 1,040 kg/m^3 and a dynamic viscosity 0.004 Pa.s. Water-based solutions are commonly used for the mock circulation loop as the density of water (998 kg/m^3) is close to that of real blood. Glycerol is often used as a mixture for the solution as it can increase the density to be about the same as real blood. A 40% glycerine solution was used as a medium solution for this mock circulation loop to mimic the density of human blood. The comparison of properties between fluid mixtures and human blood is shown in Table 4-4.

Table 4-4: Properties of the fluid for MCL pumping medium

Pumping Fluid	Density (Kg/m^3)	Dynamic Viscosity (Pa.s)
Blood	1040	0.004
Water	998	0.001
Saline	1025	0.001
Glycerine	1261	0.950
Glycerol 40%	1103	0.0039

VI. Measuring Equipment

Pressure transducer: a total of five GE UNIK 5000 pressure sensors (Figure 4-23) were used in this mock circulation loop to measure the pressure at various locations. Two of these sensors were installed at the bottom socket of both air tight tanks to measure the fluid pressures which help in calculation of the compliance values; one sensor was inserted in the 1/2in tee connector next to the check valve at the ventricle simulator outlet to measure the aortic pressure, while the other 2 sensors were positioned across the VAD in the flow circuit that runs parallel to the main flow direction from the ventricle simulator to the compliance chamber in order to measure the ventricle pressure and calculate the head pressure of the pump.

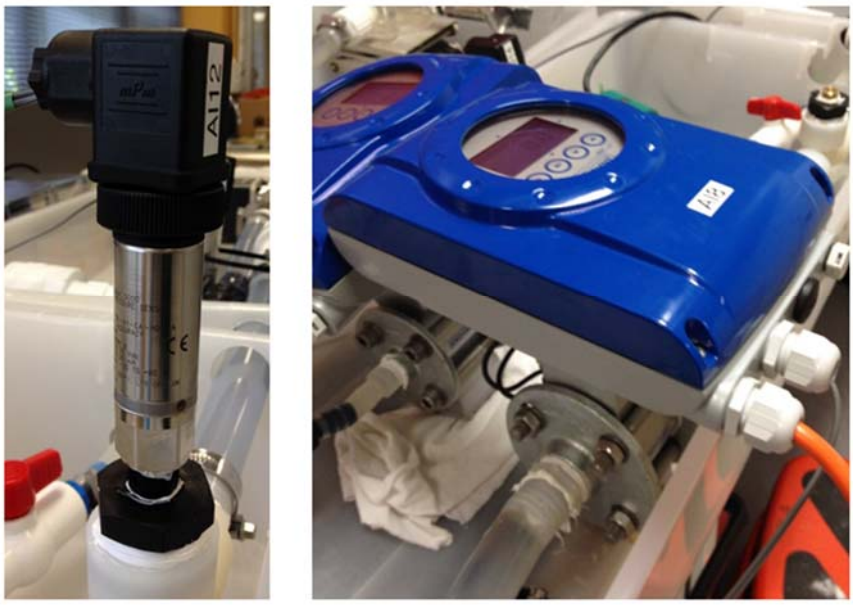

Figure 4-23: UNIK 5000 Pressure Transducer (left) and KROHNE IFC050C Magnetic Flowmeter (right).

Flow meter: Two KROHNE IFC050C magnetic flow meters (Figure 4-23) were installed on the tee fittings next to the TPR ball valve on the main circuit for measuring the aortic flow, and after the VAD in the secondary circuit to measure the pump output flow rate.

VII. Data Acquisition System

Both the pressure sensors and flow meters are powered by the QJE PS3005 power supply unit. All the modules are connected to the National Instrument Real-Time CompactRIO NI 9207 and attached on the NI eDAQ-9172 chassis which is connected to the computer laptop via the USB port, as shown in Figure 4-25. The data acquisition module acquires sampling data from all channels, and then the data are processed and logged directly to the Labview 2013 software installed on the PC at a selected sampling rate of 100 Hz.

The Labview processes and records 2 flow rates from the main circuit and a secondary circuit, and a total of 5 pressure data from the sensors which measure the aortic pressure, ventricle pressure, compliance tank pressure, reservoir tank pressure and the pump outlet pressure. The addition data which include TPR and CO are calculated in Labview using the acquired pressure and flow data. The front panel of Labview in Figure 4-24 shows the real time plot of all the signals displayed.

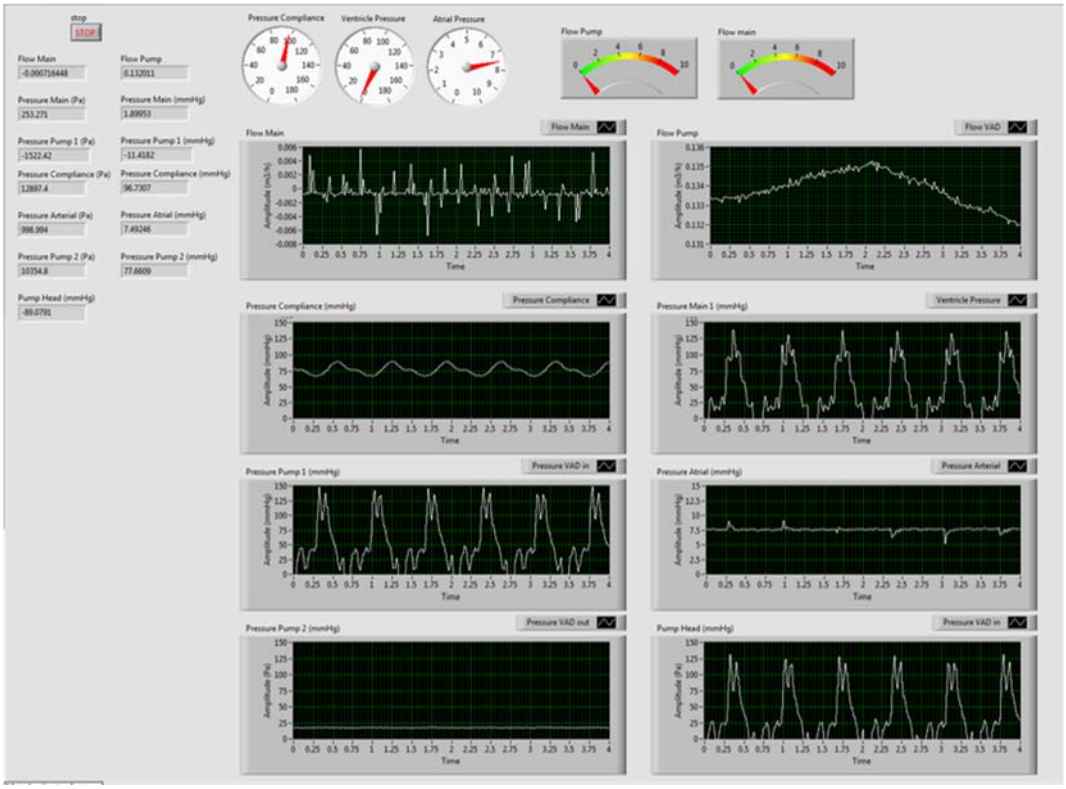

Figure 4-24: The front panel of LabView for monitoring the sensor signals.

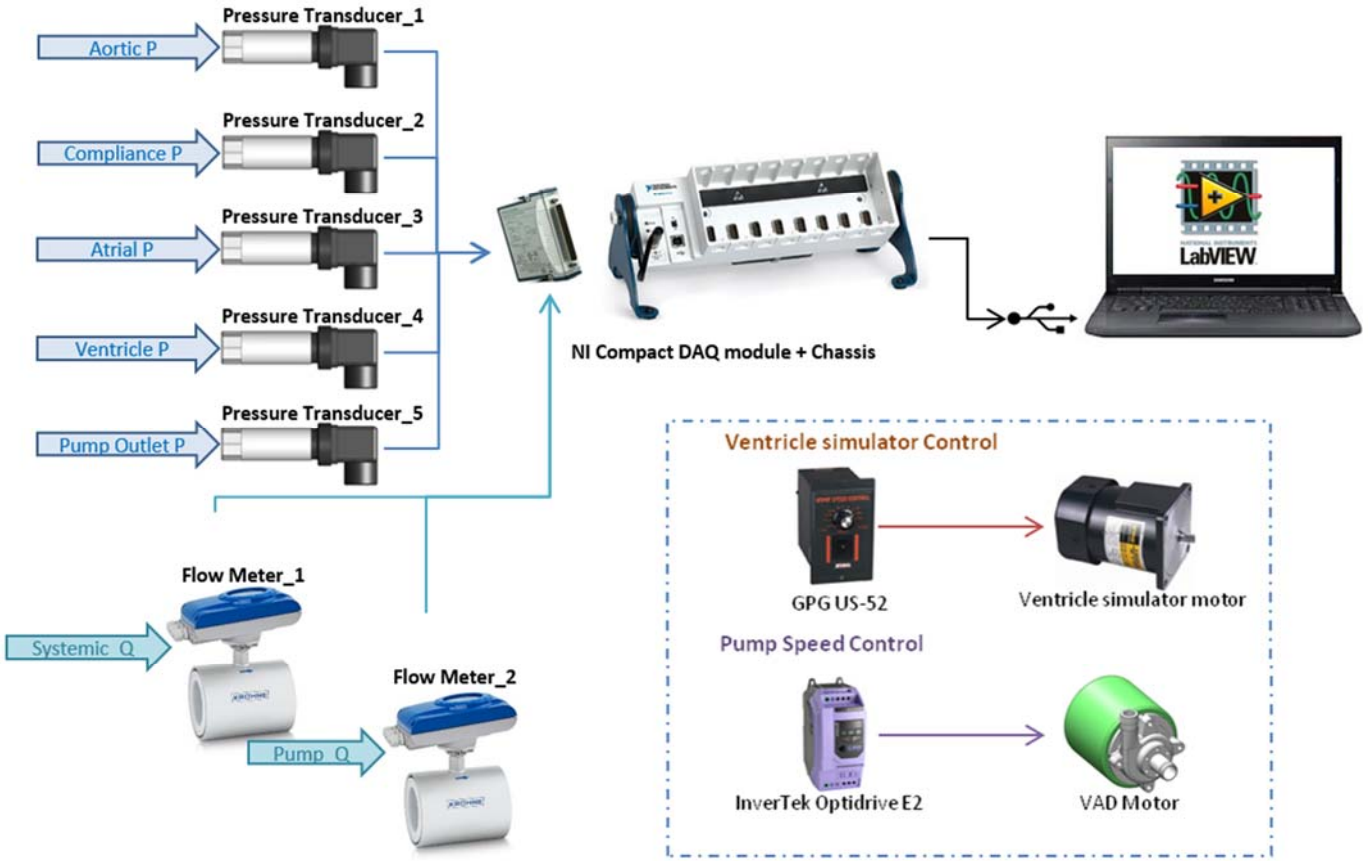

Figure 4-25: The connection diagram of controllers and data acquisition system.

Equipment List

All the equipment and the VAD control module of this MCL are listed in Table 4-5.

Table 4-5: Equipment list of the mock circulation loop.

Equipment	Model	Manufacturer	Quantity
40W DC Motor	5IK40GN-C	GPG	1
5:1 Gear box	5GU-5K	GPG	1
Motor Speed Controller	US-52	GPG	1
Pressure Sensor	UNIK5000	GE	5
Flow Meter	IFC050C	KROHNE	2
Power Supply	PS3005	QJE	1
Compact DAQ Chassis	cDAQ9172	National Instrument	1
DAQ I/O Module	NI 9207	National Instrument	1
Variable Speed Controller	OptiDrive E2	Invertek Drives	1

4.5 COMPONENTS CONFIGURATION AND CALCULATIONS

4.5.1 Compliance tank

The elastic nature of human blood vessels with the damping effect to the blood's properties is called compliance. The airtight tanks in this loop are designed to simulate this elastic property by trapping the air above the fluid level within the tanks, and this compliance value can be controlled by the amount of the volume of air that is trapped, which can be calculated by Equation [4-9].

$$C = \frac{V_{air}}{P_{air}} \qquad [4\text{-}9]$$

Where C = Compliance value of the tank (ml/mmHg)

V_{air} = Initial air volume (ml)

P_{air} = Air pressure (mmHg)

The total pressure at the bottom of an airtight tank is the summation of the air pressure and the fluid pressure which can be written as Equation [4-10].

$$P_{air} + P_{fluid} = P_{tank} \quad [4\text{-}10]$$

where P_{air} is the pressure of air trapped in the tank (mmHg)

P_{fluid} is the fluid pressure (mmHg)

P_{tank} = Total pressure at the bottom of the airtight tank (mmHg)

The fluid pressure can be calculated from the equation P_{fluid} = ρgh, where h_f is the total fluid height and could also be written as:

$$h_f = h_{tank} - h_{air} \quad [4\text{-}11]$$

$$h_f = \frac{V_{tank} - V_{air}}{A_t} \quad [4\text{-}12]$$

According to Equation [4-10], Equation [4-12] can be rearranged as:

$$P_{air} + \rho g h_f = P_{tank} \quad [4\text{-}13]$$

$$P_{air} + \rho g \frac{(V_{tank} - V_{air})}{A_t} = P_{tank} \quad [4\text{-}14]$$

In the normal heart condition, the arterial compliance tank has a target compliance value of 1.28 ml/mmHg while an average human aortic pressure is 100 mmHg relative to the atmospheric pressure (absolute pressure 860 mmHg) and the fluid

density is 1040 kg/m^3. The structural parameters of the tank are; the area (A_t) = 7.85 x 10^{-3} m^2, the tank height (h_t) = 0.635 m, and the volume (V_{tank}) = 4.87 x 10^{-3} m^3. According to these values, solving Equation [4-9] yields V_{air} = 1.04 x 10^{-3}, P_{air} = 1.089 x 10^5 Pa, and h_f = 0.4867 m. This fluid height is used in setting the compliance value of the tank which will be discussed in the next chapter.

4.5.2 Total peripheral resistance valve

In the mock circulation loop in this study, only the resistance from systemic circulation, as specified above, was considered. The simulation of resistance is achieved by adjusting the ball valve between the arterial compliance and the atrial reservoir tank where the resistance calculation is based on Equation [4-7] taking the pressure drop across the tanks divided by the maximum flow rate through the circulation loop.

4.5.3 Arterial reservoir

The arterial reservoir provides the constant preload pressure for the ventricle simulator, and this preload pressure is controlled by the height of the fluid in the tank. The required height of fluid in the tank is calculated from the equation:

$$P = \rho g h \qquad [4\text{-}15]$$

where the density of the working fluid (ρ) is 1040 kg/m^3, and the target preload ventricle pressure (P) is 8 mmHg (1.066 kPa) for all the conditions. The average height of fluid (h) calculated from the above equation is 10.45 cm.

4.5.4 Ventricle simulator

The stroke volume or ejection volume of the ventricle simulator is adjustable by moving the pin of the connecting rod on the fly wheel. The stroke distances of the ventricle simulator are fixed at 40, 45 and 15 mm which can produce the estimated stroke volume of 80, 90 and 30 ml for the normal, exercise and CHF conditions, respectively.

4.6 CONCLUSION

The literature review was conducted on the mechanisms and configurations of human mock circulatory systems that have been used on various applications. A suitable structure has been selected and modified for creating a MCL that meets the requirements for the testing of the new VAD that has been developed in this thesis. This newly designed MCL was aimed at VAD testing to verify the pump performance and identify problems for further optimization. As the pump in this study is a single-sided pump, this MCL was designed as a half circulation loop.

This MCL has the capability of simulating the three main characteristics of the heart's function, which are the pulsatile flow, compliance effect and vascular resistance. The pulsatile flow was simulated by the ventricle simulator which is based on the displacement pump design and has an adjustable stroke volume at 80 and 30 ml/stroke for the normal heart and CHF conditions while the heart rate is adjustable by the motor's speed. The compliance, which is the effect of the elasticity of the arteries in damping the pulse signal, was simulated by the tank with the air trapped inside so that the compliance value was adjustable by the ratio between the volume to the pressure of the air. The vascular resistance was lumped into a ball valve that allows the value to be adjustable. To maintain these characteristics and regulate the flow direction, the swing check valves were installed to the inlet and outlet of the ventricle simulator. The 40% glycerol mixture was used as a pumping fluid in this test rig to replicate the density and viscosity of blood.

This MCL can simulate both the normal heart function for establishing the baseline condition to validate the output from the loop, and the heart failure condition for the heart pump testing. The normal heart condition was simulated with the average parameters from a healthy adult while the cardiac output and aortic pressure are reduced by 20% and 10%, respectively, for the heart failure condition.

The test results of this MCL on both the normal heart and CHF functions along with the prototype experimental evaluation will be provided and discussed in the next chapter.

Chapter 5: Experimentation Evaluation of VAD on Human Mock Circulation Loop

A VAD prototype was produced based on the design shown in Chapter 3. This pump prototype was evaluated in the human mock circulation loop that was designed and constructed based on the information presented in Chapter 4. The target of the pump evaluation was to confirm the hydrodynamic performance of the pump design under the pulse flow environment, and to obtain other information for the later stages of development.

5.1 EXPERIMENTAL DESIGN AND PROCEDURE

This section provides the overview of the equipment's preparation and the experiment's configuration that were used in the evaluation of the mock circulation loop and the VAD performance.

5.1.1 VAD prototype for evaluation

The pump prototype for the experimental evaluation was created with the Solidworks software, as shown in Chapter 3. The 3D model of the pump was used in the prototype construction with the CNC machining process which was done internally by the QUT Design and Manufacturing Centre (DMC) workshop. PVC was used as the main material for this prototype, while polyether ether ketone (PEEK) was used for the male bearing on the top of the impeller to reduce the friction between the contact surfaces. The pump prototype was to be driven by a motor of the Iwaki MD-10-230GS0 magnetic drive pump, so the ferrite magnet from the impeller of this Iwaki pump was embedded into the socket in the impeller hub of this VAD prototype.

5.1.2 Equipment calibrations

The main parts of the equipment for this experiment that required calibration were the pressure transducers and flow meters. Each of these sensors was calibrated using the individual calibration sheet from the manufacturer that provided

information about the actual output range. All the sensors in this experiment have the current output, so the actual range of each sensor was converted to the gain which is mmHg/mA for the pressure transducers and m^3/h /mA for the flow sensors. These gains were then used to correct the real time output data from the sensors during the measurement.

5.1.3 MCL setup

The experimentation was done in two stages. The first stage was to establish the baseline of the mock circulation by simulating the normal heart and CHF conditions. The second stage was the experiment of the VAD under the CHF environment of the MCL from the previous stage.

In the first stage, the MCL was first set to simulate the normal heart function to establish a baseline for the pump experiment. After that, the MCL was adjusted to simulate the CHF condition.

Table 5-1: Target parameters for each MCL configuration

Parameters	Normal	CHF
Heart Rate (HR)	60	90
Stroke Volume (SV)	80	30
Cardiac output (CO)	5	2.5
Left Ventricular Peak Systolic Pressure (LVPSP)	120	80
Left Ventricular Peak Diastolic Pressure (LVPDP)	0-8	0-8
Aortic Systolic Pressure (AOPsys)	120	80
Aortic Diastolic Pressure (AOPdias)	80	55
Pulse Pressure (PP)	40	25
Mean Arterial Pressure (MAP)	93.3	63.3
Atrial Pressure	8-10	8-10
Arterial Compliance	1.28	0.96
Fluid Pressure	35.83	38.63
Air Pressure (kPa)	7.66	2.4

The target parameters for the mock circulation loop for the normal heart and CHF are summarised in Table 5-1, and the configuration procedures are listed as follows:

VAD Installation: Although the VAD is not used in this stage of the experimentation, it can be pre-installed in the secondary flow loop that is the link between the ventricle simulator and the compliance tank. With this setting, the VAD can be either included or removed from the circulation loop by turning on or shutting off the valves that connect the secondary loop from the main flow, as shown as number 4 in Figure 4-20. The VAD installed in the MCL is shown in Figure 5-1.

Figure 5-1: VAD Installed on a motor that is attached to the stand and inserted to the MCL via the bypass flow loop

MCL filling and operating: In this stage the pumping fluid is filled into the atrial reservoir tank. The TPR valve is closed to allow the fluid level in the atrial and compliance tanks to be adjustable independently, while all the other fluid valves and the air valve on the compliance tank are opened during the filling. During this initial filling, the ventricle simulator is turned on to about 5 rpm to remove the air bubbles from the circulation system, then the speed is lowered and the fluid level reaches the required height. With the VAD installed to the MCL, the system is turned on for a few seconds to purge the air. The VAD valves are then turned off to isolate the VAD from the circulation.

Compliance setting: The compliance value of this MCL can be set by closing the air valve and continuing to pump the fluid into the compliance tank. With this

method, the air pressure will be raised to the required compliance effect of the MCL. The air pressure can be read directly from the pressure gauge installed on the top of the compliance tank. Labview needs to be enabled during this step to verify the fluid pressure. This compliance value can be adjusted by releasing some of the air through the air valve and opening the TPR valve slightly. When the compliance value reaches the required level, the reading from the pressure sensor should be equal to the mean arterial pressure.

Atrial Pressure: Atrial pressure can be adjusted directly by altering the fluid height in the arterial reservoir tank. Additional fluid can be added to the required level after the compliance is set, and the atrial pressure can be verified on the Labview panel.

Heart Functionality: The heart function is controlled by the stroke volume and heart rate. The stroke volume can be adjusted by moving the pin position on the fly wheel to the required perfusion of each testing condition. The heart rate is adjusted from the variable speed drive that controls the motor speed, and the output pulse rate can be read on the Labview panel.

Aortic Pressure: Aortic pressure is measured from the pressure sensor in the compliance tank which reads the total pressure of the fluid and the compressed air pressure. With the ventricle simulator open in the previous stage, the aortic pressure will be raised with additional fluid being pumped into the tank. Now the TPR valve can now be opened and adjusted until the aortic pressure reduces to the target level.

After completing the above steps the test rig will be ready for use. The data can now be recorded by the Labview program.

In the second stage of the experiment, the configuration of CHF from the previous stage is maintained. The VAD can now be included in the circulation by opening the secondary loop valves and setting the required speed with the variable speed drive.

5.2 INITIAL EXPERIMENTAL RESULTS OF MCL

The initial test of the MCL was conducted by simulating the normal heart and the CHF conditions to verify the related parameters before proceeding to the tests of

the newly designed VAD. During the tests without the VAD, the valves to the secondary loop were turned off to isolate the heart pump from the system.

5.2.1 Normal heart configuration

In this test, the MCL was set to the target parameters, as previously shown in Table 5-1, in order to replicate the function of a healthy natural heart. The fluid was initially filled into the loop and pumped into the compliance tank until the pressure reached 35.83 mmHg, then the air valve was closed and the fluid continued to be pumped into the tank until the total pressure reached the target MAP at 93.33 mmHg, which is the required compliance. Additional fluid was then added to the arterial tank until the pressure reached 8 mmHg to provide the preload to the ventricular simulator. The speed of the ventricle was then adjusted to generate the pulse flow at the rate of 60 bpm, while the aortic pressure was adjusted from the TPR valve to maintain the range between 80 to 120 mmHg.

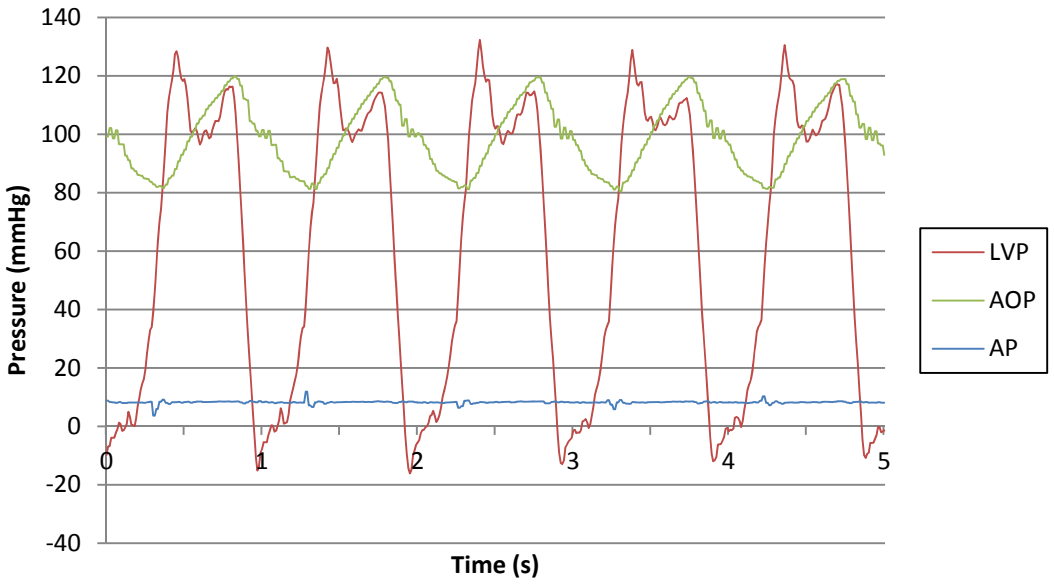

Figure 5-2: The output parameters from the systemic circulation of a normal heart configuration. (LVP: Left Ventricle Pressure, AOP: Aortic Pressure, AP: Atrial Pressure)

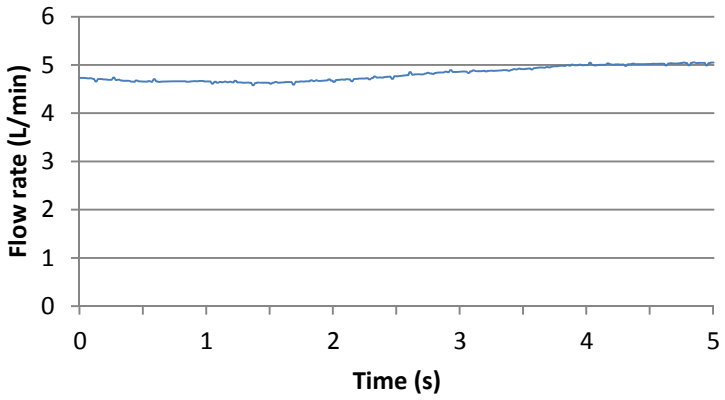

Figure 5-3: Cardiac output from a normal heart configuration

With the normal heart configuration using the above target parameters, the output pressure from the configuration of a normal heart is shown in Figure 5-2 and the cardiac output is shown in Figure 5-3. The output signals of this configuration are discussed as follows:

Ventricle Pressure (VP): According to the Figure, the pressure signal from the ventricle shows the cyclical pulse at approximately 1 Hz or 60 bpm which is the same rate as the target parameter for this configuration. There are large spikes observed in the signal during the end-systolic and end-diastolic phase, which are caused by the water hammer effect from the sudden closure and bounce of the flapper check valves that are used to control the flow direction. A similar fluctuation pattern is also found in some other MCLs such as those developed by Pantalos et al. ((Koenig et al., 2004; Pantalos et al., 2004), Liu et al. (Liu et al., 2006) and Timms (Daniel Timms, 2005). This large fluctuation indicates that the signal is underdamped. In this case, the lack of venous and pulmonary compliance emphasises this fluctuation, so the moving average signal filtering was applied to reduce the effect. According to the graph, the peak pressure of the systolic phase is 126.24 mmHg, while the pressure observed in the diastolic phase is reduced to the negative pressure range so that the diastolic pressure ranged between -15.2 to 1.4 mmHg. The main cause of this negative pressure is the systole filling process that relies on the suction pressure to fill the ventricle chamber.

Aortic Pressure (AOP): According to the Figure, the aortic pressure simulated from this MCL is very close to the desired value at 80/120 mmHg. This loop could simulate the aortic pressure signal ranges between 80.44 to 119.93 mmHg and the

mean arterial pressure (MAP) is 93.60 mmHg. There is almost no spike observed in this signal because it is measured directly from the compliance tank so the signal is well dampened; however, there is a phase delay compared to the signal from the ventricle which is caused by the inertial effects and the distance between the chambers. The systolic ratio is not adjustable due to the mechanism design of the ventricle simulator, so it is fixed at 50% whereas the systolic ratio of an actual normal heart is approximately 40%.

Arterial Pressure (AP): As this mock circulation loop only simulates half of the human circulation system, the venous pressure is assumed to be equal to the left atrium pressure. The arterial pressure is estimated at 8.2 mmHg with a slight fluctuation during the valve opening and closure.

Cardiac Output (CO): The cardiac output measurement is limited by the ability of the magnetic flow meter that can only measure the total flow over a period of time. Consequently, it was unable to capture the pulsatile nature of the flow in the MCL; hence, the cardiac output is plotted as a mean value over a period of time. The average cardiac output in this setting is 4.99 L/min.

The output parameters from this MCL are summarised and compared against an actual heart and the results from other MCLs in Table 5-2. The comparison shows that this MCL could closely replicate the cardiac output at 60 bpm and 5 L/min of a normal heart. The ventricle pressure was affected by the oscillation so the systolic and diastolic pressure is 126.2/-15.2 mmHg, which slightly deviates from the target setting at 120/80 mmHg. Nevertheless, the result is still in a similar range to the MCLs of Pentalos (Pantalos et al., 2004) and Liu (Liu et al., 2006) which have the pressure at 139/-9.3 mmHg and 12.32/-20 mmHg, respectively. The MCL designed by Timms (Daniel L. Timms et al., 2011) has a better result for the ventricle pressure setting compared to other MCLs because the ventricular contractility was controlled by electro-pneumatic regulators which are a more accurate and flexible method than the mechanism of this MCL. This pneumatic control also allows passive diastolic filling to avoid the negative pressure, which could not be done with the displacement pump of this MCL. However, this MCL could closely replicate the aortic pressure as the peak systolic pressure is 119.9 and the diastolic pressure is 80.4 mmHg, while there is also low oscillation in the signal; hence, the MAP calculated from Equation

[4-4] is 93.6 mmHg which is very close to the target setting. The atrial pressure is almost steady at 8.24 mmHg in this MCL as it acted as a reservoir to supply the preload to the ventricle, and this value is within the target setting range of 8-10 mmHg.

According to the output parameters from this MCL, it could closely replicate the circulatory condition of a healthy human. Therefore the CHF condition could be established in this configuration procedure.

Table 5-2: Comparison of output from this MCL, a real heart, and other research under the normal heart condition

	Flow		**Pressure (mmHg)**						
	HR (bpm)	**Q (L/min)**	**VP_{sys}**	**VP_{dias}**	**AOP_{sys}**	**AOP_{dias}**	**PP**	**MAP**	**AP**
Real Heart (Target settings)	60	5.0	120	0-8	120	80	40	93.3	8-10
(Pantalos et al., 2004)	80	5.0	139.5	-9.3 – 2.4	125.5	68	57.7	95.3	10.5
(Liu et al., 2006)	60	5.2	123.2	-20 – 5.1	125	80.1	44.9	95	8.2
(Daniel L. Timms et al., 2011)	60	5.15	120	7	120	80	40	98	10
This MCL	60	4.99	126.2	-15.2 – 1.4	119.9	80.4	39.49	93.6	8.24

5.2.2 CHF Configuration

The result from normal heart simulation has shown that this MCL can simulate the flow condition of the human circulatory system, despite the oscillation in the ventricle pressure from insufficient compliance. The MCL was then set to replicate the cardiovascular condition of a heart failure patient which has a significantly decreased cardiac output and ventricle pressure to ensure that the pump tested in this loop could provide sufficient support for the needs of patients. The target parameters of this configuration are referred to in Table 5-1.

The configuration to archive the target settings was done in the same procedure as described in the previous test. In this systemic CHF condition, the target aortic pressure was reduced to 55/80 mmHg to simulate the degree of loss in ventricular contractibility and the cardiac output is reduced to 2.5 L/min. The target heart rate, however, was increased to 90 bpm to simulate the attempt of a natural heart in maintaining the perfusion and to compensate for the loss of pumping pressure. The compliance reduced to 0.96 as a result of the decrease in the pulse pressure. The target atrial pressure was maintained to approximately 8 mmHg which is sufficient to provide preload to the ventricle simulator.

The output pressures and cardiac output of the CHF configuration are shown in Figures 5-4 and Figure 5-5. According to these Figures, the pulse rate generated from the ventricle is 90 pulse/min and the cardiac output is 2.48 L/min. The lower ventricle pressure leads to lower force applied on the check valves hence lower oscillation is observed on the signal compare to healthy condition. Nevertheless, the signal spike from aortic valve still presented at the end of diastolic phase. The peak systolic pressure measured from the ventricle is 78.89 mmHg and the peak diastolic pressure is -12.09 mmHg. The peak systolic pressure is reduced to 75.72 mmHg in the aorta and the peak diastolic pressure is 52.82 mmHg; the calculated mean aortic pressure is 60.45 mmHg, and the atrial pressure is 7.95 mmHg.

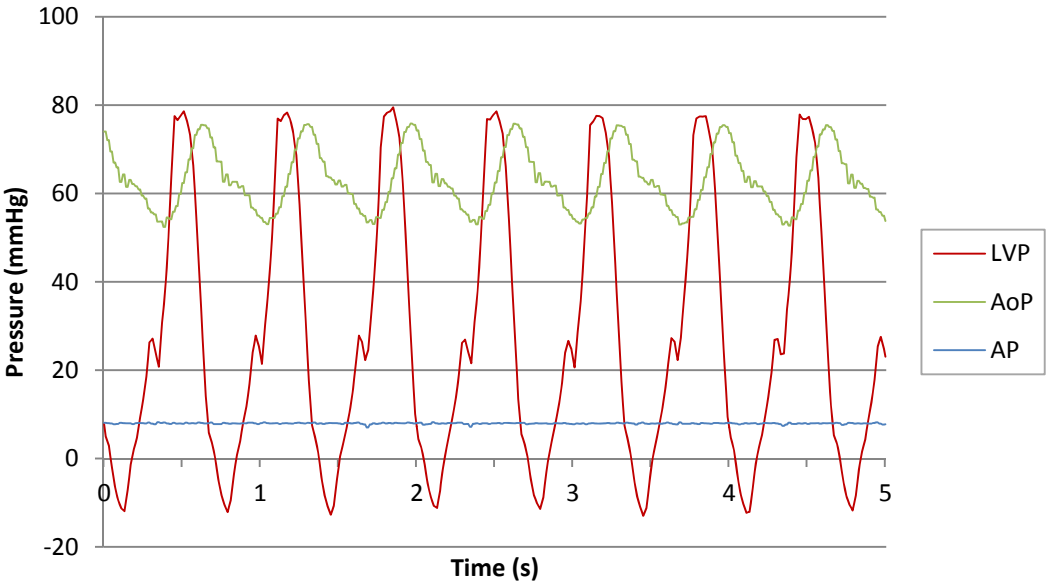

Figure 5-4: The output parameters from the normal heart configuration. : LVP, Left ventrical pressure; AoP, Aortic pressure

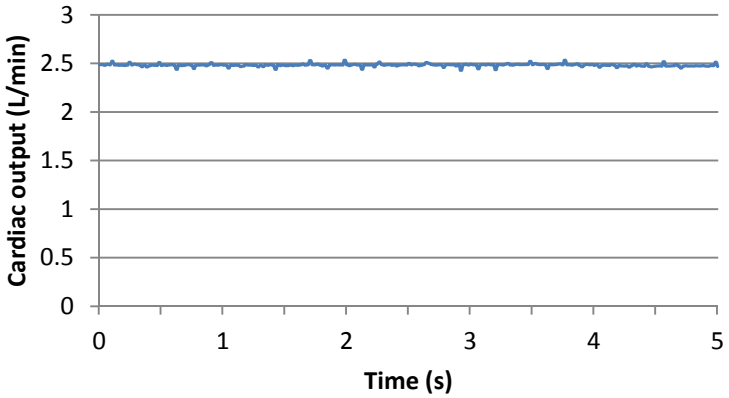

Figure 5-5: Cardiac output from CHF configuration

The results from this MCL configuration can be compared with the target settings and the results from other MCLs, as shown in Table 5-3. According to the large variation in the degree of heart failure, some parameters from each MCL may differ from others depending on the required application in each research and the structure of the MCL. In general, the output pressures of this MCL are close to the configuration of Liu et al. (Liu et al., 2006) which also mainly focuses on the systemic circulation, and has similar negative pressure ventricle filling mechanism; but this MCL has higher level of systolic pressures which is closer to the configuration of Timms et al. (Daniel L. Timms et al., 2011). The ventricle pressure

from this experiment is 78.89/-12.09 mmHg while the configuration of Liu et al. is 72.2/-10 mmHg and Timms et al. is 80/16 mmHg. The peak systolic pressure is drop for approximately 4% due to the pipe loss so the aortic pressure is measured 75.72/52.82 mmHg. This loss is slightly higher than Liu's MCL that has aortic pressure 70.4/46.4 mmHg (2.5% loss) but less than Timms' configuration at 75/60 mmHg (6.25% loss). The MAP calculated from aortic pressure is 52.82 mmHg which is slightly lower than the target setting at 55 mmHg. The atrium pressure of this MCL is 7.95 mmHg, close to the target setting at 8.0 mmHg and slightly higher than 7.2 mmHg in Liu's MCL; while Timms' MCL has much higher pressure at 20 mmHg as it is the full circulation loop that also simulate the Frank-starling response.

Another adjustment for the CHF condition is the heart rate. The output heart rate is measured 90 bpm which is the same value as the target setting. This heart rate is the same as Timms' configuration but this MCL has slightly higher cardiac output at 2.48 l/min, where the flow rate is 2.7L/min in Timms' MCL. This heart rate compensation function was not included in the MCL of Liu et al. which the heart rate was maintained at 60 bpm, but the cardiac output was reduced to 2.0 L/min from the stroke volume adjustment.

Table 5-3: Comparison of heart failure condition

	Flow		**Pressure (mmHg)**						
	HR (bpm)	**Q (L/min)**	**LVP_{sys}**	**LVP_{dias}**	**AOP_{sys}**	**AOP_{dias}**	**PP**	**MAP**	**VP/LAP**
Target setting	90	2.5	80	0-8	80	55	25	63.3	8
(Pantalos et al., 2004)	80	3.0	93	-0.9 - 13.7	84	43	41	60	16.3
(Liu et al., 2006)	60	2.0	72.2	-10 - 24.6	70.4	46.4	24	54.4	7.2
(Daniel L. Timms et al., 2011)	90	2.7	80	16	75	60	15	67	20
This MCL	90	2.48	78.89	-12.09 – 20.76	75.72	52.82	22.9	60.45	7.95

The pulse characteristic and pressure parameters simulated from this MCL are close to the target setting for the CHF condition and similar to the output from other literature; hence, this configuration can be used for the experimental evaluation of the VAD prototype in this study.

5.3 EXPERIMENTAL RESULT OF VAD ON THE MCL

The VAD is connected to the MCL via a ½in tube that connects from the ventricle simulator to the compliance tank. In the VAD experiment the valves at the inlet and outlet of this connecting tube were opened to create the secondary flow through the VAD. This setting is similar to an actual VAD transplantation that has a heart pump connected from a ventricle to either the aorta or the pulmonary artery and generates a parallel flow path to a natural circulation.

Steady flow experimentation

In the first experiment, the VAD was tested in the steady condition without the flow from the ventricle simulator to identify the pressure head - flow rate characteristic of the pump. The pump speed was varied between 2,500 – 4,500 rpm which covered the designed speed for an LVAD at 4,020 rpm and an RVAD at 3,070 rpm. The ball valve at the VAD outlet was tuned to vary the flow rate through the pump. The head pressure was recorded and plotted against the flow rate, as shown in Figure 5-6.

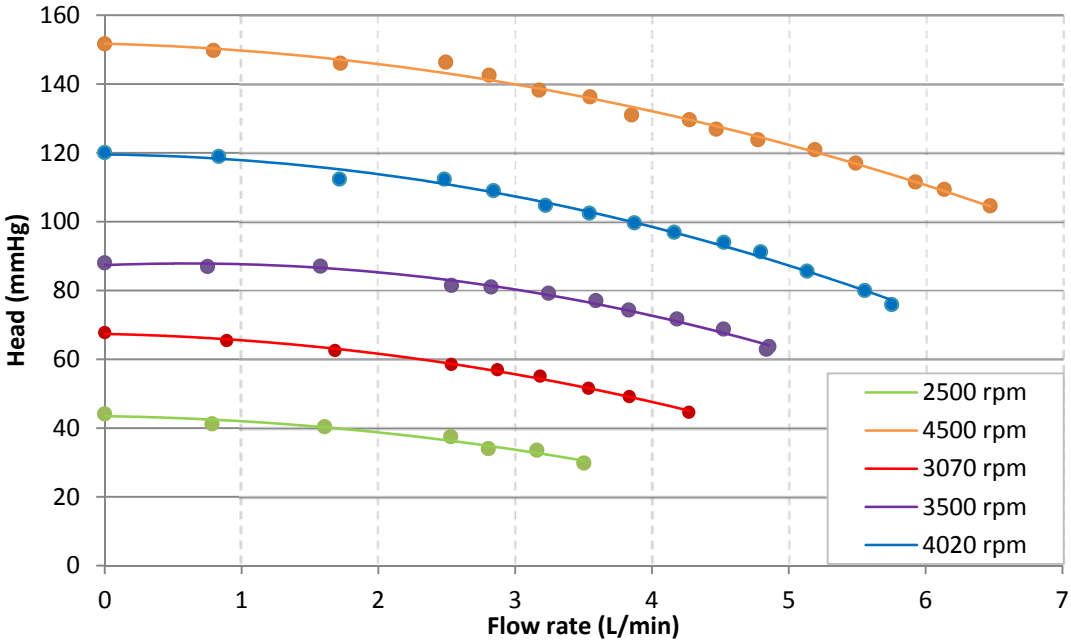

Figure 5-6 : Head pressure - flow rate curve of VAD at different pump speeds

According to Figure 5-6, the head pressure from the VAD is the maximum at a zero flow rate or when the valve is closed. The head pressure is reduced as a larger volumetric flow rate is pumped through this VAD. The graph also shows that a higher pump speed increases the pump head and maximum flow rate through the pump while it also increases the maximum flow capacity that the pump could achieve. Under the pump speed range of this evaluation, this VAD could generate the maximum head pressure of 151.66 mmHg at the pump speed of 4,500 rpm, while the maximum flow capacity is 6.47 L/min. The lowest speed in the evaluation (2,500 rpm) could generate a maximum flow rate of 3.5 L/min at the head pressure of 26.0 mmHg.

At the LVAD design speed (4,020 rpm), the maximum head pressure that the pump could generate is 120.06 mmHg under a zero flow rate. The maximum flow capacity that the pump can deliver at this flow speed is 5.75 L/min where the head pressure is reduced to 75.87 mmHg. The pump performance at this speed can be compared to the previous CFD simulated results from Chapter 3, as shown in Figure 5-7. The plot shows the same trend between the simulated and the experimental results in which the head pressure drops as the flow rate is increased. However, there is some difference between the simulated and experimental values in that the maximum error is 22% at the flow rate of 5.75 L/min. This large percentage of error

is attributed to the lack of an efficient suspension mechanism. The current magnetic motor can drive the pump but it was not designed to provide the suspension force to the impeller, so it was not possible for the impeller to maintain its position on the centre of the rotating axis. This situation causes a big impact to the pump's performance because it affects the gap between the impeller blades and the chamber so that the performance is reduced from the designed value. Therefore, the pump performance should be evaluated again on the prototype with a shaft-driven rotor to confirm the performance when the position of the impeller is fully controlled.

Another plot in this Figure (Figure 5-7) is the RVAD design speed condition at 3,070 rpm. In this condition the head pressure between the experimentation and simulation also has a similar pattern. The experimentation displays a maximum head pressure of 67.74 mmHg at a zero flow rate and a reduced pressure to 44.59 mmHg at the maximum flow rate of 4.27 L/min. The maximum error of the head pressure in this condition is approximately 27%. This error also is caused by the impeller suspension, as described in the LVAD condition above, but the loss of the pump's performance in this condition also leads to insufficient pump capacity, as the pump could only deliver a maximum flow of 4.27 L/min, while the requirement is 5.0 L/min.

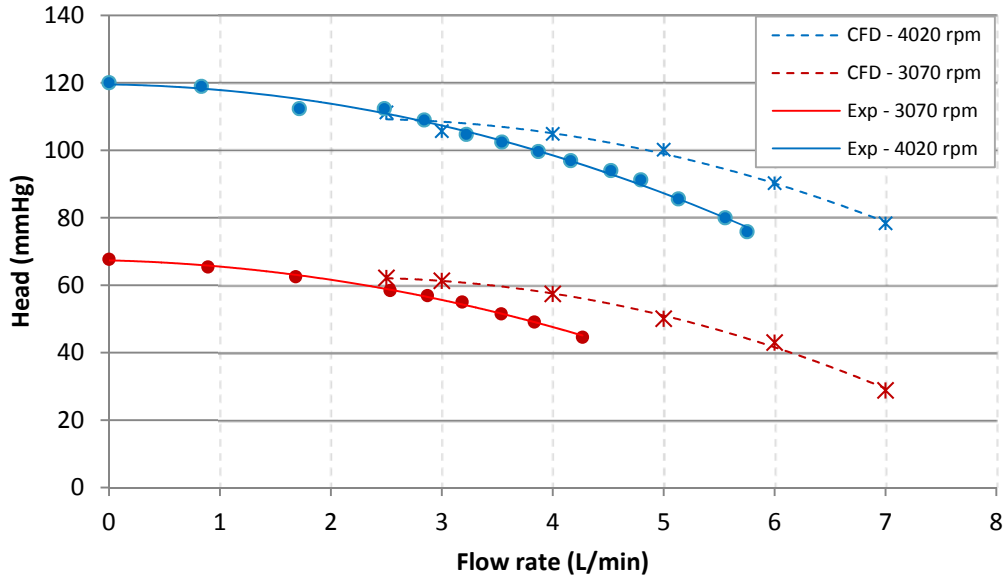

Figure 5-7: Comparison of head – flow rate from the CFD and experiment on the mock circulation loop (Exp) under the designed speed

Unsteady flow experimentation

This second test was conducted to observe the pump response under the pulsatile flow, which is closest to the actual pump operation environment. The ventricle simulator was turned on and set to the CHF condition, as described in Section 5.2.2. The pump speed was then varied in the same range as the previous test (2,500-4,500 rpm), and the flow rate through the VAD was adjusted by the valve at the pump outlet.

The average head was plotted against the average flow rate and compared with the steady flow result from previous test, as shown in Figure 5-8. From the plot, it can be observed that that the pump still operates under the same trend as the characteristic curve of the steady flow that has been examined previously in Figure 5-6. However, the maximum flow rate in the pulse flow condition was reduced from the previous test. This was because the flow rate read from the flow meter was the average value; hence, the maximum flow rate shown in the plot is lower than the actual flow.

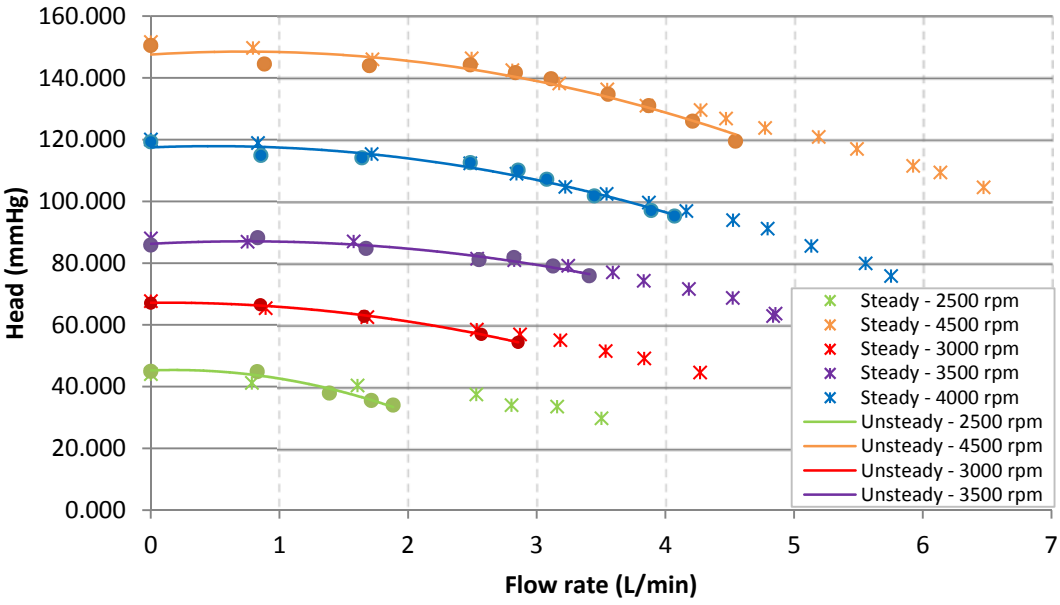

Figure 5-8 : Head pressure – flow rate curve of VAD under the pulse flow compared with steady flow conditions.

To simulate the VAD function in supporting heart failure, the pump speed was adjusted to 4,020 rpm which is the speed that could raise the MAP to the normal

level, as shown in Figure 5-9. The comparison of the pressure signal of the CHF with and without the VAD support in Figure 5-10 shows that the peak systolic pressure is increased from 75.72 mmHg to 105.95 mmHg. It can be seen that the ventricle pressure signal is less affected by the oscillation, and the continuous flow from the pump reduces the variation of arterial pressure in the pulsatile flow. The continuous flow from VAD reduces the pulse pressure in the aorta (PP = P_{sys}-P_{dias}) from 22.9 mmHg to 13.8 mmHg, while the MAP is raised from 60.45 mmHg to 96.75 mmHg which is close to the level of a normal heart. The atrial pressure reduced slightly from 7.95 mmHg to 7.49 mmHg. However, the cardiac flow with the VAD support in this condition is 4.13 L/min which is 17% lower than the normal level (5 L/min) because of the performance loss from the lack or rotor suspension, as described earlier. More evaluation results at different flow rate and pump speed can be found in the Appendix 5-1.

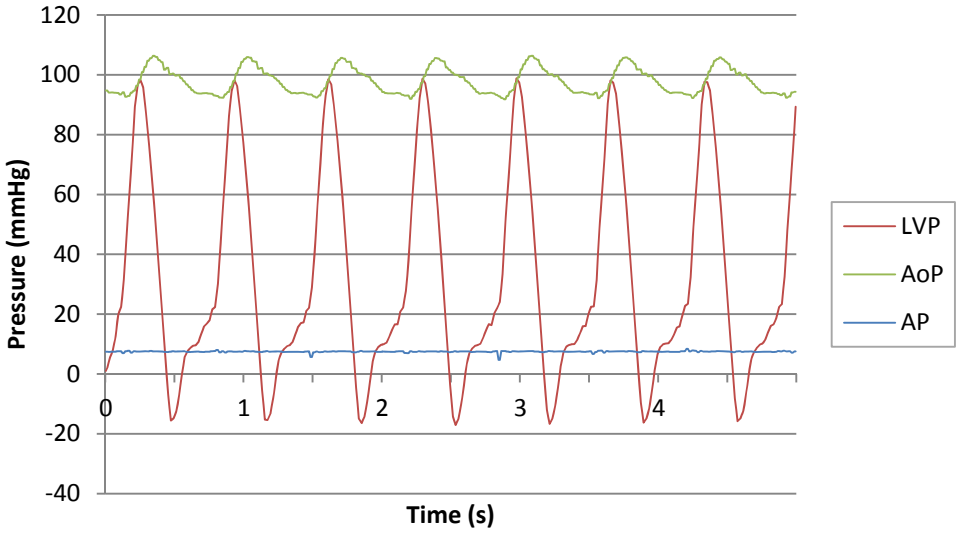

Figure 5-9: The output parameters from CHF systemic circulation with VAD support

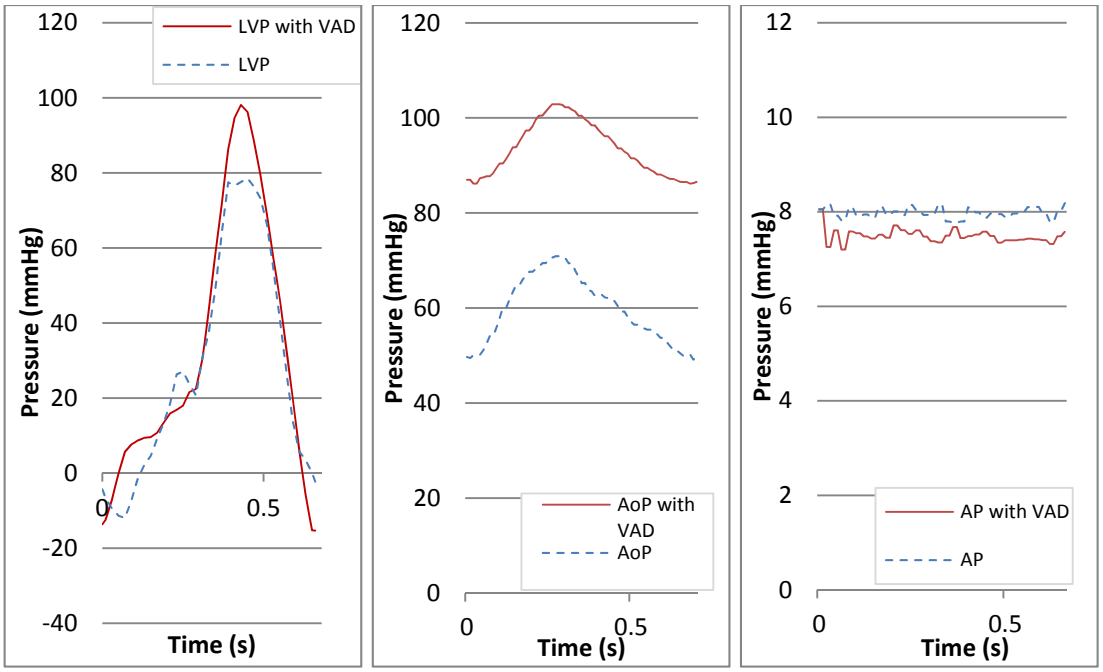

(a) (b) (c)

Figure 5-10: Comparison of pressure output between CHF condition and CHF with VAD support: (a) Ventricle pressure (b) Aortic pressure (c) Atrial pressure

The results of the VAD test in both a steady and unsteady flow condition demonstrate that this pump could generate sufficient head pressure to provide support for the failing heart simulated from this MCL. However the pump capacity should be optimised by increasing it further to provide sufficient flow rate under the pulse flow condition.

Nevertheless, in the current state, the capacity is also affected by the pump's performance issue as it is lower than the prediction from the CFD analysis. This poor performance is mainly attributed to the magnetic drive motor that is not specifically designed for this pump; hence, the impeller is not suspended properly and this leads to excessive loss from friction between the rotor and the housing. Moreover, the pump is also susceptible to slipping between the driving magnet and the rotor at high load, because the magnetic drive in this motor was designed for pumping water which has a lower density than the glycerol mixture in this experiment. Therefore, at this load level, the magnetic coupling between the motor and the rotor may not be strong enough to prevent the slipping that could reduce the output hydraulic power from this pump.

Another issue for this experiment is the efficiency calculation. Normally, the pump's efficiency could be calculated by the ratio between the output hydraulic power and the input electrical power of the pump motor. However, the results are not presented here due to a large loss of friction in the motor and the inaccurate power consumption measurement. The loss from the motor is caused by a large clearance in the motor design that allows the rotor to rub against its housing. In a normal pump with a shaft-driven impeller, this loss could be calculated by running the pump dry and calculating the excessive power to overcome the friction by comparing with the motor's efficiency (Daniel Timms, 2005). However, this method could not be applied to this magnetic drive pump as the dry impeller would have much more friction and also there would be a risk of damaging the pump. Therefore, it would require another pump prototype in which the power is directly transferred from the motor by a shaft, not the magnetic force, to properly evaluate the pump's performance.

5.4 CONCLUSION

The mock circulation loop in this experiment could successfully reproduce the human circulation in both a normal heart and a failing heart condition, although it does not include the pulmonary system. It was sufficient for the initial experiment of the pump's performance to provide the design verification and performance information for the prototype's optimization until the pump is ready for an in-vitro trial in an animal.

The VAD prototype was tested in the MCL under the steady flow condition to identify the pump's characteristics before testing in the pulse flow condition which fully simulates the CHF environment. The results of the pressure head – flow rate characteristics test followed the same trend as the CFD prediction but there was a relatively large error at a higher flow rate as the pump suffered from the lack of proper suspension for the rotor. However, the pump could provide enough support for the simulated CHF condition and also provided information for further experimentation and optimization.

Chapter 6: : Conclusions

This chapter summarises the conclusion of each section in this study that leads to the completion of achieving the aim of this research. The results and problems encountered in each stage are summarised, and suggestions for their improvements are provided for future research.

6.1 CONCLUSION

This thesis is primarily aimed at developing a new VAD that can be used for long-term support for a heart failure patient. CFD analysis was implemented to evaluate the designs in different aspects in order to reduce the development costs and time that otherwise were needed during the design process. The literature review in this thesis provides both identification of the research gap and information about the design consideration items of the VAD development, including simulation techniques that can be applied to the heart pump analysis. The CFD analysis process in this study provides a performance comparison between the impeller designs and allows the design optimization to be done before producing a working prototype. The human mock circulation loop was developed as a testing facility for this newly designed pump to simulate the pulse flow environment of a heart failure patient. The pump's hydraulic performance was then investigated to verify the simulation results and address other critical issues that were not identified during the CFD simulations. The conclusion of each stage of the research leads to the outcomes of this thesis.

6.1.1 Literature review

In the beginning of this thesis, a literature review was conducted. It covered the current development of CHF and the shortage of hearts for transplantation. The review identified the VAD as one of the promising alternative treatments; however, many patients in long-term clinical trials still suffer from device complications due to hemolysis, thrombosis and mechanism failure. Moreover, another major problem of the VAD is the complication of the device during transplantation and management for bi-ventricular failure, where two devices are needed for each ventricle. These

issues point to the need for an effective and durable BiVAD that can be used in long-term support as a bridge to transplantation or destination therapy.

In order to effectively develop a new device, CFD analysis was reviewed and adopted as a primary development tool for its capability in providing critical information in both the hydrodynamic and hemodynamic aspects of the VAD development. The review highlighted the techniques that are used for the estimation of hydrodynamic performance and the predication of blood damage and coagulation which can be applied to the simulation of this blood pump.

6.1.2 Design and development of VAD

The development of this heart pump was established on the preliminary design of the BiVAD. The fluid models were successfully created on the solid design of the pump for the simulation. A total of five different designs of impeller were evaluated using these models to find the operating speed that could deliver the required head pressure and sufficient perfusion to the failing ventricles. The results were then analysed for the hydraulic efficiency and the impeller force which provide important information for the design of the suspension and driving mechanism. The hemodynamic properties were also analysed in terms of shear- induced blood damage and thrombosis. With these analysis data, the best design of impeller was successfully selected for the heart pump, and the design issues were identified for further optimization.

The pump design in this stage lacks the driving mechanism which needs to be developed separately and is out of the scope of this study. Therefore, the pump was split into the individual LVAD and RVAD which can be operated on the magnetic drive motor of a general application pump. The necessary modifications were done to compensate for the loss of the washout and suspension mechanism due to the separation of the pump module. CFD simulation conducted on this optimized design confirmed its performance and availability to be used as a single-sided module, which can later be combined to a BiVAD once the motor design is ready.

The pump prototype was successfully designed and created based on the analysis information from this section. This prototype allowed the pump's performance to be verified in the human mock circulation loop.

6.1.3 Mock circulation loop

A mock circulation loop designed and constructed in this study complements the aim of establishing a pump testing facility that could recreate the circulation of a CHF patient. The pulsatile pressure and flow rate are controlled by a ventricle simulator and the pressure is damped by the compliance effect which is configured by the ratio of air and fluid in the air trapped in the compliance tank. The resistance valve is used to simulate the vascular resistance before the fluid returns to the reservoir that provides the preload to the ventricle simulator. This MCL can be used to evaluate the efficiency of the pump prototype created in this study.

6.1.4 Experimentation evaluation of VAD on human mock circulation loop

The MCL test was to reproduce the flow condition of both the normal heart and failing heart conditions. In both conditions the MCL could closely produce the pressure range, flow rate, and pressure waves of a natural heart, although large oscillations were observed from the ventricle pressure signal at the end of the systolic and diastolic phases. The oscillations were found to be an effect of the bouncing of the non-return valves that were forced to close suddenly at high pressure. This could be later improved by introducing additional compliance to provide a better damping to the flow.

The pump pressure head – flow rate performance was successfully identified under the steady condition and the pump was also tested to verify its performance under the pulsatile flow CHF condition. The pump could generate the head pressure that raises the mean arterial pressure to the normal level; however, the overall pump performance was affected by the unsuitable driving motor so the results are lower than the expectation from the CFD prediction. Nevertheless, the tests provide sufficient information for the current pump performance under each flow condition which could be used for further design refinement.

With all the design, analysis and experimentation processes, this thesis could achieve its aims in providing insight analysis of the BiVAD heart pump by individual analysis using CFD simulation. The pump performance was verified in the experimentation evaluation that successfully provided the vital information for further development in the combination of pump modules for a complete BiVAD.

6.2 FUTURE RESEARCH

The remaining items from this research and suggestions for improvement that may lead to expansion of future research are described as follows:

6.2.1 Pump design

- According to the simulation results, the pump has a risk of forming thrombosis at low pump speed and low flow rate in the RVAD function. The design of the right side of the VAD should be further optimized for better performance.
- The pump should be optimised further to increase the flow capacity to ensure that the pump can supply enough blood perfusion at a low pump speed.
- The prototype of this pump with a transplant housing can be made for particle image velocimetry (PIV) experimentation to verify the flow path and possible stagnation in the pump.
- The current pump results still lack the impeller force evaluation because the current magnetic driving mechanism does not allow the installation of the sensors. In order to measure the force, another pump prototype driven by a shaft must be produced, so that force sensors can be attached directly onto the shaft. In addition, it will also allow the pump performance to be measured more accurately.
- With the predicted force from the CFD analysis in this thesis and the measured force suggested above, the suspension system can then be designed for the pump so that the impeller will be able to levitate within the chamber by magnetic/hydraulic force.
- The pump developed from this research could be used for further study with some minor optimization to increase the flow capacity. A more durable prototype can be made with bio-compatibile materials like PEEK and titanium using the suggested design in Appendix 3-2 for further hemolysis study.

- With the pump prototype that is produced with the proper hemocompatible material, the pump could be tested with real blood to verify the blood damage result obtained from CFD analysis.

6.2.2 Mock circulation loop

- The oscillation of ventricle pressure can be reduced by introducing additional venous compliance or by including the pulmonary system to the MCL with a pulmonary compliance tank.
- This mock circulation loop can be upgraded to the full circulation loop with an additional venous and pulmonary compliance tank, right atrium, and right ventricle simulator. This will allow the full version of the BiVAD prototype to be tested under the bi-ventricular failure condition.
- The motor of the ventricle simulator can be redesigned and replaced with a servo motor which will allow a higher degree of control over the stroke volume and ejection fraction.
- The flow meters should be replaced with a meter type that has a high enough sampling rate to capture the flow rate change in the pulse system and that should be able to measure the reversed flow. A medical clamp-on ultrasonic flow meter with a high sampling rate is recommended because it has lower resistance to the system and will be able to capture the pulsatile flow at high frequency.

Bibliography

Andrade, A., Nicolosi, D., Lucchi, J., Biscegli, J., Arruda, A. F., Ohashi, Y., . . . Nosé, Y. (1999). Auxiliary Total Artificial Heart: A Compact Electromechanical Artificial Heart Working Simultaneously with the NaturalHeart. *Artificial Organs, 23*(9), 876-880. doi: 10.1046/j.1525-1594.1999.06273.x

ANSYS, I. (2009). *ANSYS 12 CFX User's Manual*

Apel, J., Neudel, F., & Reul, H. (2001). Computational fluid dynamics and experimental validation of a microaxial blood pump. *ASAIO journal, 47*(5), 552-558.

ASTM. (1998). Standard practice for assessment of hemolysis in continuous flow blood pumps *Annual Book of ASTM Standards, F1844-97* (Vol. 13, pp. 1-5): American Society for Testing and Materials.

Athanassiou, L., Hancock, S., & Mahajan, R. (2005). Doppler estimation of zero flow pressure during changes in downstream pressure in a bench model of a circulation using pulsatile flow*. *Anaesthesia, 60*(2), 133-138.

Attisani, M., Centofanti, P., Torre, M. L., Boffini, M., Ricci, D., Ribezzo, M., . . . Rinaldi, M. (2012). Advanced heart failure in critical patients (INTERMACS 1 and 2 levels): ventricular assist devices or emergency transplantation? *Interactive CardioVascular and Thoracic Surgery, 15*(4), 678-684. doi: 10.1093/icvts/ivs256

Avrahami, I., Rosenfeld, M., Raz, S., & Einav, S. (2006). Numerical Model of Flow in a Sac-Type Ventricular Assist Device. *Artificial Organs, 30*(7), 529-538. doi: 10.1111/j.1525-1594.2006.00255.x

Ayre, P. J., Lovell, N. H., & Woodard, J. C. (2003). Non-invasive flow estimation in an implantable rotary blood pump: a study considering non-pulsatile and pulsatile flows. *Physiological Measurement, 24*(1), 179-189. doi: 10.1088/0967-3334/24/1/313

Baldwin, J. T., Borovetz, H. S., Duncan, B. W., Gartner, M. J., Jarvik, R. K., Weiss, W. J., & Hoke, T. R. (2006). The national heart, lung, and blood institute pediatric circulatory support program. *Circulation, 113*(1), 147-155.

Baldwin, J. T., Robbins, R. C., & National Heart, L. a. B. I. W. G. (2005). Executive Summary for the National Heart, Lung, and Blood Institute Working Group on Next Generation Ventricular Assist Devices for Destination Therapy. *Seminars in thoracic and cardiovascular surgery, 17*(4), 369-371. doi: 10.1053/j.semtcvs.2005.10.005

Baloa, L. A., Boston, J. R., & Antaki, J. F. (2001). Elastance-Based Control of a Mock Circulatory System. *Annals of Biomedical Engineering, 29*(3), 244-251. doi: 10.1114/1.1355275

Barrett, K. E. (2010). *Ganong's review of medical physiology*: McGraw-Hill Medical Asia.

Bates, P. D., Lane, S. N., Ferguson, R. I., John, W., & Sons. (2005). *Computational fluid dynamics: applications in environmental hydraulics*. Hoboken, NJ: J. Wiley.

Behbahani, M., Behr, M., Hormes, M., Steinseifer, U., Arora, D., Coronado, O., & Pasquali, M. (2009). A review of computational fluid dynamics analysis of

blood pumps. *European Journal of Applied Mathematics, 20*(04), 363-397. doi: doi:10.1017/S0956792509007839
Berne, R. M., Levy, M. N., Koeppen, B. M., & Stanton, B. A. (1998). Physiology. Mosby. *Inc., St. Louis, Missouri*.
Birks, E. J. M. P., Tansley, P. D. F., Hardy, J. M. B. B. S. B., George, R. S. M. B., Bowles, C. T. P., Burke, M. F., . . . Yacoub, M. H. F. R. S. (2006). Left Ventricular Assist Device and Drug Therapy for the Reversal of Heart Failure. *The New England Journal of Medicine, 355*(18), 1873-1884.
Bock, E. G., Antunes, P. I., da Silva, G. G. P., Leme, J., Legendre, D. F., Fonseca, J. W., . . . Arruda, A. C. F. (2007). Normalized Index of Hemolysis Evaluation of an Implantable Centrifugal Blood Pump For Long Term Ventricular Assistance.
Bottrell, S., Bennett, M., Augustin, S., Thuys, C., Schultz, B., Horton, A., & Horton, S. (2014). A comparison study of haemolysis production in three contemporary centrifugal pumps. *Perfusion, 29*(5), 411-416. doi: http://dx.doi.org/10.1177/0267659113509000
Bowles, C. T., Shah, S. S., Nishimura, K., Clark, C., Cumming, D. V., Pattison, C. W., . . . Yacoub, M. H. (1991). Development of mock circulation models for the assessment of counterpulsation systems. *Cardiovascular research, 25*(11), 901-908. doi: 10.1093/cvr/25.11.901
Braunwald, E. (2013). Heart Failure. *JACC: Heart Failure, 1*(1), 1-20. doi: 10.1016/j.jchf.2012.10.002
Braunwald, E. (2015). The war against heart failure: the Lancet lecture. *Lancet (London, England), 385*(9970), 812-824. doi: 10.1016/S0140-6736(14)61889-4
Brazier, M. A. B. (1988). *A History of Neurophysiology in the 19th Century*: Raven Pr.
Burgreen, G. W., Loree, H. M., Bourque, K., Dague, C., Poirier, V. L., Farrar, D., . . . Schob, R. (2004). Computational Fluid Dynamics Analysis of a Maglev Centrifugal Left Ventricular Assist Device. *Artificial Organs, 28*(10), 874-880. doi: 10.1111/j.1525-1594.2004.07384.x
Burke, D. J., Burke, E., Parsaie, F., Poirier, V., Butler, K., Thomas, D., . . . Maher, T. (2001). The HeartMate II: Design and Development of a Fully Sealed Axial Flow Left Ventricular Assist System. *Artificial Organs, 25*(5), 380-385. doi: 10.1046/j.1525-1594.2001.06770.x
Capdeville, M., & Smedira, N. G. (2013). Advances and future directions for mechanical circulatory support. *Anesthesiology clinics, 31*(2), 321-353.
Carswell, D., Hilton, A., Chan, C., McBride, D., Croft, N., Slone, A., . . . Foster, G. (2013). Development of a radial ventricular assist device using numerical predictions and experimental haemolysis. *Medical engineering & physics, 35*(8), 1197.
Cassot, F., Morvan, D., Issartier, P., & Pelissier, R. (1985). New versatile physical model fitting the systemic circulation accurately. *Medical & biological engineering & computing, 23*(6), 511-516. doi: 10.1007/BF02455304
Chan, C. H. H., Pieper, I. L., Hambly, R., Radley, G., Jones, A., Friedmann, Y., . . . Thornton, C. A. (2015). The CentriMag Centrifugal Blood Pump as a Benchmark for In Vitro Testing of Hemocompatibility in Implantable Ventricular Assist Devices. *Artificial Organs, 39*(2), 93-101. doi: 10.1111/aor.12351

Chan, W. K., Wong, Y. W., Ding, Y., Chua, L. P., & Yu, S. C. M. (2002). Numerical Investigation of the Effect of Blade Geometry on Blood Trauma in a Centrifugal Blood Pump. *Artificial Organs, 26*(9), 785-793. doi: 10.1046/j.1525-1594.2002.06954.x

Chemla, D., Hebert, J.-L., Coirault, C., Zamani, K., Suard, I., Colin, P., & Lecarpentier, Y. (1998). Total arterial compliance estimated by stroke volume-to-aortic pulse pressure ratio in humans. *AJP - Heart and Circulatory Physiology, 274*(2), H500.

Chua, L. P., Song, G., Lim, T. M., & Zhou, T. (2006). Numerical Analysis of the Inner Flow Field of a Biocentrifugal Blood Pump. *Artificial Organs, 30*(6), 467-477. doi: 10.1111/j.1525-1594.2006.00243.x

Colacino, F. M., Moscato, F., Piedimonte, F., Danieli, G., Nicosia, S., & Arabia, M. (2008). A Modified Elastance Model to Control Mock Ventricles in Real-Time: Numerical and Experimental Validation. *ASAIO journal, 54*(6), 563-573. doi: 10.1097/MAT.0b013e31818a5c93

Cowger, J. A., Romano, M. A., Shah, P., Shah, N., Mehta, V., Haft, J. W., . . . Pagani, F. D. (2014). Hemolysis: a harbinger of adverse outcome after left ventricular assist device implant. *The Journal of Heart and Lung Transplantation, 33*(1), 35-43.

Curtas, A. R., Wood, H. G., Allaire, P. E., McDaniel, J. C., Day, S. W., & Olsen, D. B. (2002). Computational Fluid Dynamics Modeling of Impeller Designs for the HeartQuest Left Ventricular Assist Device. *ASAIO journal, 48*(5), 552-561. doi: 10.1097/00002480-200209000-00019

Davidson, L. (2003). An introduction to turbulence models. *Department of Thermo and Fluid Dynamics, Chalmers University of Technology, Gothenburg, Sweden*.

Davis, P., Rinehimer, A., & Uddin, M. (2012). *A comparison of RANS-based turbulence modeling for flow over a wall-mounted square cylinder.* Paper presented at the 20th Annual Conference of the CFD Society of Canada.

Day, S. W., McDaniel, J. C., Wood, H. G., Allaire, P. E., Landrot, N., & Curtas, A. (2001). Particle Image Velocimetry Measurements of Blood Velocity in a Continuous Flow Ventricular Assist Device. *ASAIO journal, 47*(4), 406-411. doi: 10.1097/00002480-200107000-00021

Day, S. W., McDaniel, J. C., Wood, H. G., Allaire, P. E., Song, X., Lemire, P. P., & Miles, S. D. (2002). A prototype HeartQuest ventricular assist device for particle image velocimetry measurements. *Artificial Organs, 26*(11), 1002-1005.

DeBakey, M. E. (1997). Development of a Ventricular Assist Device. *Artificial Organs, 21*(11), 1149-1153. doi: 10.1111/j.1525-1594.1997.tb00464.x

DeBakey, M. E. (2000). The odyssey of the artificial heart. *Artificial Organs, 24*(6), 405-411.

Dembitsky, W. P. (2006). REMATCH and Beyond: The Cost of Treating Heart Failure Using an Implantable Left Ventricular Assist Device. *Seminars in Cardiothoracic and Vascular Anesthesia, 10*(3), 253-255. doi: 10.1177/1089253206291148

Donovan, J. F. M. (1975). Design of a hydraulic analog of the circulatory system for evaluating artificial hearts. *Biomaterials, medical devices, and artificial organs, 3*(4), 439.

Farinas, M.-I., Garon, A., Lacasse, D., & N'Dri, D. (2006). Asymptotically consistent numerical approximation of hemolysis. *Journal of biomechanical engineering, 128*(5), 688. doi: 10.1115/1.2241663

Ferrari, G., De Lazzari, C., Kozarski, M., Clemente, F., Górczynska, K., Mimmo, R., . . . Guaragno, M. (2002). A hybrid mock circulatory system: testing a prototype under physiologic and pathological conditions. *ASAIO journal, 48*(5), 487-494.

Ferrari, M., Kruzliak, P., & Spiliopoulos, K. (2015). An insight into short- and long-term mechanical circulatory support systems. *Clinical Research in Cardiology, 104*(2), 95-111. doi: 10.1007/s00392-014-0771-6

Ferziger, J. H., & Peric, M. (1996). *Computational methods for fluid dynamics*. New York: Springer-Verlag.

Flint, K. M., Matlock, D. D., Lindenfeld, J., & Allen, L. A. (2012). Frailty and the selection of patients for destination therapy left ventricular assist device. *Circulation: Heart Failure, 5*(2), 286-293.

Fraser, K. H., Taskin, M. E., Griffith, B. P., & Wu, Z. J. (2011). The use of computational fluid dynamics in the development of ventricular assist devices. *Medical Engineering & Physics, 33*(3), 263-280. doi: 10.1016/j.medengphy.2010.10.014

Fraser, K. H., Taskin, M. E., Zhang, T., Griffith, B. P., & Wu, Z. J. (2010). Comparison of Shear Stress, Residence Time and Lagrangian Estimates of Hemolysis in Different Ventricular Assist Devices (Vol. 32, pp. 548-551). Berlin, Heidelberg: Springer Berlin Heidelberg.

Fraser, K. H., Zhang, T., Taskin, M. E., Griffith, B. P., & Wu, Z. J. (2012). A quantitative comparison of mechanical blood damage parameters in rotary ventricular assist devices: shear stress, exposure time and hemolysis index. *Journal of biomechanical engineering, 134*(8), 081002.

Frazier, O., Rose, E. A., Macmanus, Q., Burton, N. A., Lefrak, E. A., Poirier, V. L., & Dasse, K. A. (1992). Multicenter clinical evaluation of the HeartMate 1000 IP left ventricular assist device. *The Annals of Thoracic Surgery, 53*(6), 1080-1090.

Fuhrman, B. P., & Zimmerman, J. J. (2011). *Pediatric Critical Care : Expert Consult Premium*. London: Mosby.

Gagnon, D., Petty, M., & Lahpor, J. R. (2000). HeartMate® family of left ventricular assist systems. *Perfusion, 15*(4), 345-354.

Garcia, M. A. Z., Enriquez, L. A., Dembitsky, W., & May-Newman, K. (2008). The Effect of Aortic Valve Incompetence on the Hemodynamics of a Continuous Flow Ventricular Assist Device in a Mock Circulation. *ASAIO journal, 54*(3), 237-244. doi: 10.1097/MAT.0b013e31816a309b

Garon, A., & Farinas, M.-I. (2004). Fast Three-dimensional Numerical Hemolysis Approximation. *Artificial Organs, 28*(11), 1016-1025. doi: 10.1111/j.1525-1594.2004.00026.x

Gaudino, M., Farina, P., Bernazzali, S., Bruno, P., Colizzi, C., Sani, G., & Massetti, M. (2014). Ventricular Assistance Devices as Bridge to Transplantation. *Heart failure clinics, 10*(1), S39-S45.

Gelman, S. (2008). Venous function and central venous pressure: a physiologic story. *ANESTHESIOLOGY-PHILADELPHIA THEN HAGERSTOWN-, 108*(4), 735.

George, W. K. (20013). Lectures in Turbulence for the 21st Century. Retrieved 4 June, 2015, from www.turbulence-online.com

Giersiepen, M., Wurzinger, L. J., Opitz, R., & Reul, H. (1990). Estimation of shear stress-related blood damage in heart valve prostheses--in vitro comparison of 25 aortic valves. *The International journal of artificial organs, 13*(5), 300-306.

Goldstein, D. J. M. D., Oz, M. C. M. D., & Rose, E. A. M. D. (1998). Implantable left ventricular assist devices. *The New England Journal of Medicine, 339*(21), 1522-1533.

Goubergrits, L., & Affeld, K. (2004). Numerical Estimation of Blood Damage in Artificial Organs. *Artificial Organs, 28*(5), 499-507. doi: 10.1111/j.1525-1594.2004.07265.x

Gräf, F., Finocchiaro, T., Laumen, M., Mager, I., & Steinseifer, U. (2015). Mock Circulation Loop to Investigate Hemolysis in a Pulsatile Total Artificial Heart. *Artificial Organs*.

Greenwood, J. C., & Herr, D. L. (2014). Mechanical circulatory support. *Emergency medicine clinics of North America, 32*(4), 851-869. doi: 10.1016/j.emc.2014.07.009

Gregory, S. D., Timms, D., Gaddum, N., Mason, D. G., & Fraser, J. F. (2011). Biventricular assist devices: a technical review. *Annals of Biomedical Engineering*, 1-16.

Grigioni, M., Daniele, C., Morbiducci, U., D'Avenio, G., Benedetto, G. D., & Barbaro, V. (2004). The Power-law Mathematical Model for Blood Damage Prediction: Analytical Developments and Physical Inconsistencies. *Artificial Organs, 28*(5), 467-475. doi: 10.1111/j.1525-1594.2004.00015.x

Grigioni, M., Morbiducci, U., D'Avenio, G., Benedetto, G. D., & Gaudio, C. D. (2005). A novel formulation for blood trauma prediction by a modified power-law mathematical model. *Biomechanics and Modeling in Mechanobiology, 4*(4), 249-260. doi: 10.1007/s10237-005-0005-y

Gu, L., & Smith, W. A. (2005). Evaluation of Computational Models for Hemolysis Estimation. *ASAIO journal, 51*(3), 202-207. doi: 10.1097/01.MAT.0000161939.29905.93

Haft, J. W., Bull, J. L., Rose, R., Katsra, J., Grotberg, J. B., Bartlett, R. H., & Hirschl, R. B. (2003). Design of an Artificial Lung Compliance Chamber for Pulmonary Replacement. *ASAIO journal, 49*(1), 35-40. doi: 10.1097/00002480-200301000-00006

Hall, J. E., & Guyton, A. C. (2011). *Textbook of medical physiology*: Saunders.

Hall, M. J., Levant, S., & DeFrances, C. J. (2015). Hospitalization for congestive heart failure: United States, 2000–2010. *age, 65*(23), 29.

Harris, K. R., & Thompson, M. K. (2012). Heart failure. *InnovAiT, 5*(11), 687-695. doi: 10.1093/innovait/ins181

HeartWare. (2015). HeartWare Image Library. 2015, from http://www.heartware.com/image-library

. HeartWare Ventricular System: Instruction for use. (2012): HeartWare Inc.

Heuser, G., & Opitz, R. (1979). A Couette viscometer for short time shearing of blood. *Biorheology, 17*(1-2), 17-24.

Holman, W. L. (2012). Interagency Registry for Mechanically Assisted Circulatory Support (INTERMACS): What Have We Learned and What Will We Learn? *Circulation, 126*(11), 1401-1406. doi: 10.1161/circulationaha.112.097816

Inoguchi, H., Tanaka, T., Maehara, Y., & Matsuda, T. (2006). Mock Circulatory Systems for Vascular Tissue Engineering. *Inflammation and Regeneration, 26*(3), 175-180.

. INTERMACS Quarterly Statistical Report 2014 Q4. (2015): The Data Collection and Analysis Center, University of Alabama.

James, N. L., Wilkinson, C. M., Lingard, N. L., Meer, A. L. v. d., & Woodard, J. C. (2003). Evaluation of Hemolysis in the VentrAssist Implantable Rotary Blood Pump. *Artificial Organs, 27*(1), 108-113. doi: 10.1046/j.1525-1594.2003.07188.x

Jikuya, T., Tsutsui, T., Shigeta, O., Sankai, Y., & Mitsui, T. (1998). Species differences in erythrocyte mechanical fragility: comparison of human, bovine, and ovine cells. *ASAIO journal, 44*(5), M452-M455.

Johnson Jr, C. A., Vandenberghe, S., Daly, A. R., Woolley, J. R., Snyder, S. T., Verkaik, J. E., . . . Wagner, W. R. (2011). Biocompatibility Assessment of the First Generation PediaFlow Pediatric Ventricular Assist Device. *Artificial Organs, 35*(1), 9-21. doi: 10.1111/j.1525-1594.2010.01023.x

Jorde, U. P., Kushwaha, S. S., Tatooles, A. J., Naka, Y., Bhat, G., Long, J. W., . . . Park, S. J. (2014). Results of the Destination Therapy Post-Food and Drug Administration Approval Study With a Continuous Flow Left Ventricular Assist Device. *Journal of the American College of Cardiology, 63*(17), 1751-1757. doi: 10.1016/j.jacc.2014.01.053

Kafagy, D., & Gitano-Briggs, H. (2013a). Axial flow artificial heart blood pumps: a brief review. *Trends in Biomaterials and Artificial Organs, 27*, 124+.

Kafagy, D., & Gitano-Briggs, H. (2013b). Axial flow artificial heart blood pumps: a brief review. *Trends in Biomaterials and Artificial Organs, 27*(3), 124.

Katz, J. N., Jensen, B. C., Chang, P. P., Myers, S. L., Pagani, F. D., & Kirklin, J. K. (2015). A multicenter analysis of clinical hemolysis in patients supported with durable, long-term left ventricular assist device therapy. *The Journal of heart and lung transplantation : the official publication of the International Society for Heart Transplantation, 34*(5), 701. doi: 10.1016/j.healun.2014.10.002

Kido, K., Hoshi, H., Watanabe, N., Kataoka, H., Ohuchi, K., Asama, J., . . . Takatani, S. (2006). Computational Fluid Dynamics Analysis of the Pediatric Tiny Centrifugal Blood Pump (TinyPump). *Artificial Organs, 30*(5), 392-399. doi: 10.1111/j.1525-1594.2006.00231.x

Kirklin, J. K., & Naftel, D. C. (2008). Mechanical circulatory support: registering a therapy in evolution. *Circulation.Heart failure, 1*(3), 200-205. doi: 10.1161/CIRCHEARTFAILURE.108.782599

Kirklin, J. K., Naftel, D. C., Kormos, R. L., Stevenson, L. W., Pagani, F. D., Miller, M. A., . . . Young, J. B. (2013). Fifth INTERMACS annual report: Risk factor analysis from more than 6,000 mechanical circulatory support patients. *The Journal of Heart and Lung Transplantation, 32*(2), 141-156. doi: 10.1016/j.healun.2012.12.004

Kirklin, J. K., Naftel, D. C., Pagani, F. D., Kormos, R. L., Stevenson, L. W., Blume, E. D., . . . Young, J. B. (2014). Sixth INTERMACS annual report: a 10,000-patient database. *The Journal of heart and lung transplantation : the official publication of the International Society for Heart Transplantation, 33*(6), 555-564. doi: 10.1016/j.healun.2014.04.010

Kirklin, J. K., Naftel, D. C., Stevenson, L. W., Kormos, R. L., Pagani, F. D., Miller, M. A., . . . Young, J. B. (2008). INTERMACS Database for Durable Devices for Circulatory Support: First Annual Report. *The Journal of Heart and Lung Transplantation, 27*(10), 1065-1072. doi: 10.1016/j.healun.2008.07.021

Koenig, S. C., Pantalos, G. M., Gillars, K. J., Ewert, D. L., Litwak, K. N., & Etoch, S. W. (2004). Hemodynamic and Pressure–Volume Responses to Continuous and Pulsatile Ventricular Assist in an Adult Mock Circulation. *ASAIO journal, 50*(1), 15-24. doi: 10.1097/01.MAT.0000104816.50277.EB

König, C. S., Clark, C., & Mokhtarzadeh-Dehghan, M. R. (1999). Comparison of flow in numerical and physical models of a ventricular assist device using low- and high-viscosity fluids. *Proceedings of the Institution of Mechanical Engineers.Part H, Journal of engineering in medicine, 213*(5), 423-432. doi: 10.1243/0954411991535031

Legendre, D., Antunes, P., Bock, E., Andrade, A., Biscegli, J. F., & Ortiz, J. P. (2008). Computational Fluid Dynamics Investigation of a Centrifugal Blood Pump. *Artificial Organs, 32*(4), 342-348. doi: 10.1111/j.1525-1594.2008.00552.x

Lin, C. Y., Wu, G. H., Hou, X. T., Li, H. Y., Liu, X. J., Xu, C. Y., . . . Chen, C. (2013). *In vitro and vivo evaluation of Tongxin LVAD*.

Liu, Y., Allaire, P., Wu, Y., Wood, H., & Olsen, D. (2006). Construction of an Artificial Heart Pump Performance Test System. *Cardiovascular Engineering, 6*(4), 153-158. doi: http://dx.doi.org/10.1007/s10558-006-9019-z

Lobanoff, V. S., & Ross, R. R. (2013). *Centrifugal Pumps: Design and Application*. Burlington: Gulf Professional Publishing.

Mancini, D., & Colombo, P. C. (2015). Left Ventricular Assist Devicee: A Rapidly Evolving Alternative to Transplant. *Journal of the American College of Cardiology, 65*(23), 2542-2555. doi: 10.1016/j.jacc.2015.04.039

Maniar, S., Kondareddy, S., & Topkara, V. K. (2011). Left ventricular assist device-related infections: past, present and future. *Expert Review of Medical Devices, 8*(5), 627-634.

Mann, D. L., Zipes, D. P., Libby, P., & Bonow, R. O. (2014). *Braunwald's heart disease: a textbook of cardiovascular medicine*: Elsevier Health Sciences.

Manolis, A. S., & Manolis, T. A. (2014). Totally Implantable Artificial Heart: Still a Major Challenge. *Hospital Chronicles, 9*(1 Sup), 60-62.

Marieb, E. N., & Hoehn, K. (2007). *Human anatomy & physiology*: Pearson Education.

Masuzawa, T., Ohta, A., Tanaka, N., Qian, Y., & Tsukiya, T. (2009). Estimation of changes in dynamic hydraulic force in a magnetically suspended centrifugal blood pump with transient computational fluid dynamics analysis. *Journal of Artificial Organs, 12*(3), 150-159. doi: 10.1007/s10047-009-0459-2

May-Newman, K. (2010). Computational Fluid Dynamics Models of Ventricular Assist Devices. In J. M. Guccione, G. S. Kassab, & M. B. Ratcliffe (Eds.), *Computational Cardiovascular Mechanics* (pp. 297-316): Springer US.

McNeil, K., Dunning, J., & Morrell, N. W. (2003). The pulmonary physician in critical care. 13: the pulmonary circulation and right ventricular failure in the ITU. *Thorax, 58*(2), 157-162. doi: 10.1136/thorax.58.2.157

Medvitz, R. B., Boger, D. A., Izraelev, V., Rosenberg, G., & Paterson, E. G. (2011). Computational Fluid Dynamics Design and Analysis of a Passively Suspended Tesla Pump Left Ventricular Assist Device. *Artificial Organs, 35*(5), 522-533. doi: 10.1111/j.1525-1594.2010.01087.x

Medvitz, R. B., Kreider, J. W., Manning, K. B., Fontaine, A. A., Deutsch, S., & Paterson, E. G. (2007). Development and Validation of a Computational Fluid Dynamics Methodology for Simulation of Pulsatile Left Ventricular

Assist Devices. *ASAIO journal, 53*(2), 122-131. doi: 10.1097/MAT.0b013e31802f37dd
Mendis, S., Puska, P., & Norrving, B. (2011). *Global atlas on cardiovascular disease prevention and control*: World Health Organization.
Menter, F. R. (1993). Zonal two equation k-turbulence models for aerodynamic flows. *AIAA paper, 2906*, 1993.
Menter, F. R. (1994). Two-equation eddy-viscosity turbulence models for engineering applications. *AIAA Journal, 32*(8), 1598-1605. doi: 10.2514/3.12149
Miller, L. W. M. D., Pagani, F. D. M. D. P., Russell, S. D. M. D., John, R. M. D., Boyle, A. J. M. D., Aaronson, K. D. M. D., . . . Frazier, O. M. (2007). Use of a Continuous-Flow Device in Patients Awaiting Heart Transplantation. *The New England Journal of Medicine, 357*(9), 885-896. doi: http://dx.doi.org/10.1056/NEJMoa067758
Mitoh, A., Yano, T., Sekine, K., Mitamura, Y., Okamoto, E., Kim, D.-W., . . . Kawada, S. (2003). Computational Fluid Dynamics Analysis of an Intra-Cardiac Axial Flow Pump. *Artificial Organs, 27*(1), 34-40. doi: 10.1046/j.1525-1594.2003.07190.x
Moosavi, M.-H., Fatouraee, N., & Katoozian, H. (2009). Finite element analysis of blood flow characteristics in a Ventricular Assist Device (VAD). *Simulation Modelling Practice and Theory, 17*(4), 654-663. doi: 10.1016/j.simpat.2008.11.002
Morsi, Y., Yang, W., Witt, P., Ahmed, A., & Umezu, M. (2001). Numerical analysis of the flow characteristics of rotary blood pump. *Journal of Artificial Organs, 4*(1), 54-60. doi: 10.1007/bf01235837
Mozaffarian, D., Benjamin, E. J., Go, A. S., Arnett, D. K., Blaha, M. J., Cushman, M., . . . Turner, M. B. (2015). Heart Disease and Stroke Statistics—2015 Update: A Report From the American Heart Association. *Circulation, 131*(4), e29-e322. doi: 10.1161/cir.0000000000000152
Najjar, S. S., Slaughter, M. S., Pagani, F. D., Starling, R. C., McGee, E. C., Eckman, P., . . . Boyce, S. W. (2014). An analysis of pump thrombus events in patients in the HeartWare ADVANCE bridge to transplant and continued access protocol trial. *The Journal of Heart and Lung Transplantation, 33*(1), 23-34. doi: 10.1016/j.healun.2013.12.001
Nakata, K., Yoshikawa, M., Takano, T., Maeda, T., Nonaka, K., Linneweber, J., . . . Nose, Y. (2000). Antithrombogenicity Evaluation of a Centrifugal BloodPump. *Artificial Organs, 24*(8), 667-670. doi: 10.1046/j.1525-1594.2000.06610.x
Naughton, P., & Bashour, C. A. (2002). Mechanical Support After Cardiac Surgery. *Seminars in Cardiothoracic and Vascular Anesthesia, 6*(3), 237-257. doi: 10.1177/108925320200600307
NIH. (2012). What Is a Total Artificial Heart? Retrieved 30 June, 2015, from http://www.nhlbi.nih.gov/health/health-topics/topics/tah
Nishimura, T. (2014). Current status of extracorporeal ventricular assist devices in Japan. *Journal of Artificial Organs, 17*(3), 211-219. doi: 10.1007/s10047-014-0779-8
Nordqvist, C. (2014). What is endocarditis? What causes endocarditis? Retrieved 26 September, 2015, from http://www.medicalnewstoday.com/articles/151016.php

Nosé, Y. (1998). Design and Development Strategy for the Rotary Blood Pump. *Artificial Organs, 22*(6), 438-446. doi: 10.1046/j.1525-1594.1998.06098.x

Nosé, Y., & Motomura, T. (2005). Is It a Mistake to Develop a Totally Implantable Blood Pump for Destination Therapy? *Artificial Organs, 29*(2), 93-94. doi: 10.1111/j.1525-1594.2005.29031.x

Nosé, Y., Nakata, K.-i., Yoshikawa, M., Letsou, G. V., Fujisawa, A., Wolner, E., & Schima, H. (1999). Development of a totally implantable biventricular bypass centrifugal blood pump system. *The Annals of Thoracic Surgery, 68*(2), 775-779. doi: 10.1016/s0003-4975(99)00528-7

Nosé, Y., Yoshikawa, M., Murabayashi, S., & Takano, T. (2000). Development of Rotary Blood Pump Technology: Past, Present, and Future. *Artificial Organs, 24*(6), 412-420. doi: 10.1046/j.1525-1594.2000.06634.x

Ohuchi, K., & Takatani, S. (2006). Currently available ventricular-assist devices: capabilities, limitations and future perspectives. *Expert Review of Medical Devices, 3*(2), 195-205. doi: http://dx.doi.org/10.1586/17434440.3.2.195

Okamoto, E., Hashimoto, T., Inoue, T., & Mitamura, Y. (2003). Blood Compatible Design of a Pulsatile Blood Pump Using Computational Fluid Dynamics and Computer-Aided Design and Manufacturing Technology. *Artificial Organs, 27*(1), 61-67. doi: 10.1046/j.1525-1594.2003.07183.x

Olsen, D. B. (1999). Rotary Blood Pumps: A New Horizon. *Artificial Organs, 23*(8), 695-696. doi: 10.1046/j.1525-1594.1999.00778.x

Olsen, D. B. (2000). The History of Continuous-Flow Blood Pumps. *Artificial Organs, 24*(6), 401-404. doi: 10.1046/j.1525-1594.2000.06652.x

Oz, M. C., Gelijns, A. C., Miller, L., Wang, C., Nickens, P., Arons, R., . . . Moskowitz, A. J. (2003). Left ventricular assist devices as permanent heart failure therapy: the price of progress. *Annals of Surgery, 238*(4), 577-278. doi: 10.1097/01.sla.0000090447.73384.ad

Özalp, F., Bhagra, S., Bhagra, C., Butt, T., Ramesh, B., Robinson-Smith, N., . . . MacGowan, G. A. (2014). Four-year outcomes with third-generation centrifugal left ventricular assist devices in an era of restricted transplantation. *European Journal of Cardio-Thoracic Surgery, 46*(3), e35-e40. doi: 10.1093/ejcts/ezu258

Pagani, F. D. (2008). Continuous-Flow Rotary Left Ventricular Assist Devices with "3rd Generation" Design. *Seminars in thoracic and cardiovascular surgery, 20*(3), 255-263. doi: 10.1053/j.semtcvs.2008.08.002

Palgrave, R. (2005). Centrifugal pump basics. *World Pumps, 2005*(460), 37-39. doi: http://dx.doi.org/10.1016/S0262-1762(05)00457-8

Pantalos, G. M., Koenig, S. C., Gillars, K. J., Giridharan, G. A., & Ewert, D. L. (2004). Characterization of an adult mock circulation for testing cardiac support devices. *ASAIO journal, 50*(1), 37-46.

Park, S. J., Milano, C. A., Tatooles, A. J., Rogers, J. G., Adamson, R. M., Steidley, D. E., . . . Slaughter, M. S. (2012). Outcomes in advanced heart failure patients with left ventricular assist devices for destination therapy. *Circulation: Heart Failure, 5*(2), 241-248.

Paul, R., Apel, J., Klaus, S., Schügner, F., Schwindke, P., & Reul, H. (2003). Shear Stress Related Blood Damage in Laminar Couette Flow. *Artificial Organs, 27*(6), 517-529. doi: 10.1046/j.1525-1594.2003.07103.x

Perin, E. C., Dohmann, H. F. R., Borojevic, R., Silva, S. A., Sousa, A. L. S., Silva, G. V., . . . Willerson, J. T. (2004). Improved Exercise Capacity and Ischemia 6 and 12 Months After Transendocardial Injection of Autologous Bone

Marrow Mononuclear Cells for Ischemic Cardiomyopathy. *Circulation, 110*(11 suppl 1), II-213-II-218. doi: 10.1161/01.cir.0000138398.77550.62
Pinotti, M., & Rosa, E. S. (1995). Computational Prediction of Hemolysis in a Centrifugal Ventricular Assist Device. *Artificial Organs, 19*(3), 267-273. doi: 10.1111/j.1525-1594.1995.tb02326.x
Porepa, L. F., & Starling, R. C. (2014). Destination Therapy With Left Ventricular Assist Devices: For Whom and When? *Canadian Journal of Cardiology, 30*(3), 296-303. doi: http://dx.doi.org/10.1016/j.cjca.2013.12.017
Prandtl, L., & Wieghardt, K. (1947). *Über ein neues Formelsystem für die ausgebildete Turbulenz*: Vandenhoeck & Ruprecht.
Raman, J., & Jeevanadam, V. (2004). Destination Therapy with Ventricular Assist Devices. *Cardiology, 101*(1-3), 104-110. doi: 10.1159/000075990
Rose, E. A., Gelijns, A. C., & Moskowitz, A. J. (2001). Long-term use of a left ventricular assist device for end-stage heart failure. *The New England Journal of Medicine [H.W.Wilson - GS], 345*(20), 1435.
Rose, E. A., Gelijns, A. C., Moskowitz, A. J., Heitjan, D. F., Stevenson, L. W., Dembitsky, W., . . . Levitan, R. G. (2001). Long-term use of a left ventricular assist device for end-stage heart failure. *New England Journal of Medicine, 345*(20), 1435-1443.
Rose, E. A., Moskowitz, A. J., Packer, M., Sollano, J. A., Williams, D. L., Tierney, A. R., . . . Gelijns, A. C. (1999). The REMATCH trial: rationale, design, and end points. *The Annals of Thoracic Surgery, 67*(3), 723-730. doi: 10.1016/S0003-4975(99)00042-9
Rosenberg, G., Phillips, W. M., Landis, D. L., & Pierce, W. (1981). Design and evaluation of the Pennsylvania State University mock circulatory system. *ASAIO J, 4*(2), 41-49.
Saad, T. (2011). Turbulence modeling for beginners. *University of Tennessee Space Institute*.
Sciolino, M. (2012). Development, Optimization, and Twisted Adjustment of an Axial Flow Blood Pump for Fontan Patients.
Scotten, L. N., Walker, D. K., & Brownlee, R. T. (1979). Construction and evaluation of a hydromechanical simulation facility for the assessment of mitral valve prostheses. *Journal of Medical Engineering & Technology, 3*(1), 11-18. doi: doi:10.3109/03091907909161597
Selgrade, B. P. (2010). *Fluid dynamics of a centrifugal left ventricular assist device.*
Selgrade, B. P., & Truskey, G. A. (2012). Computational Fluid Dynamics Analysis to Determine Shear Stresses and Rates in a Centrifugal Left Ventricular Assist Device. *Artificial Organs, 36*(4), E89-E96. doi: 10.1111/j.1525-1594.2011.01416.x
Silverthorn, D. U. (2014). *Human physiology: an integrated approach*. Harlow: Pearson Education.
Smart, F. W., & Palanichamy, N. (2005). Left ventricular assist device therapy for end-stage congestive heart failure: from REMATCH to the future. *Congestive heart failure (Greenwich, Conn.), 11*(4), 188-193. doi: 10.1111/j.1527-5299.2005.04406.x
Song, X., Throckmorton, A. L., Untaroiu, A., Patel, S., Allaire, P. E., Wood, H. G., & Olsen, D. B. (2003). Axial flow blood pumps. *ASAIO journal, 49*, 355-364.
Song, X., Throckmorton, A. L., Wood, H. G., Allaire, P. E., & Olsen, D. B. (2004). Transient and Quasi-Steady Computational Fluid Dynamics Study of a Left Ventricular Assist Device. *ASAIO journal, 50*(5), 410-417.

Song, X., Throckmorton, A. L., Wood, H. G., Antaki, J. F., & Olsen, D. B. (2003). Computational fluid dynamics prediction of blood damage in a centrifugal pump. *Artificial Organs, 27*(10), 938-941.

Song, X., Throckmorton, A. L., Wood, H. G., Antaki, J. F., & Olsen, D. B. (2004). Quantitative Evaluation of Blood Damage in a Centrifugal VAD by Computational Fluid Dynamics. *Journal of Fluids Engineering, 126*(3), 410-418.

Song, X., Wood, H. G., Day, S. W., & Olsen, D. B. (2003). Studies of Turbulence Models in a Computational Fluid Dynamics Model of a Blood Pump. *Artificial Organs, 27*(10), 935-937. doi: 10.1046/j.1525-1594.2003.00025.x

Song, X., Wood, H. G., & Olsen, D. (2004). Computational Fluid Dynamics (CFD) study of the 4th generation prototype of a continuous flow Ventricular Assist Device (VAD). *Journal of biomechanical engineering, 126*(2), 180. doi: 10.1115/1.1688776

Sorensen, E. (2007). Ventricular-Assist Devices and Total Artificial Hearts. *Biomedical Instrumentation & Technology, 41*(5), 385-389.

Stephenson, L. W., Arbulu, A., Bassett, J. S., Silbergleit, A., & Hughes, C. H. (2002). The Michigan Heart: The World's First Successful Open Heart Operation? Part I. *Journal of cardiac surgery, 17*(3), 238-246. doi: 10.1111/j.1540-8191.2002.tb01209.x

Stergiopulos, N., Meister, J. J., & Westerhof, N. (1994). Simple and accurate way for estimating total and segmental arterial compliance: The pulse pressure method. *Annals of Biomedical Engineering, 22*(4), 392-397. doi: 10.1007/BF02368245

Stone, M. E. (2007). *Current status of mechanical circulatory assistance.* Paper presented at the Seminars in Cardiothoracic and Vascular Anesthesia.

Stoney, W. S. (2009). Evolution of cardiopulmonary bypass. *Circulation, 119*(21), 2844-2853.

T, Y., K, S., A, M., Y, M., E, O., D-W, K., . . . R, Y. (2003). An Estimation Method of Hemolysis within an Axial Flow Blood Pump by Computational Fluid Dynamics Analysis. *Artificial Organs, 27*(10), 920-925. doi: 10.1046/j.1525-1594.2003.00034.x

Tang, D. G., Oyer, P. E., & Mallidi, H. R. (2009). Ventricular assist devices: history, patient selection, and timing of therapy. *Journal of cardiovascular translational research, 2*(2), 159-167.

Taskin, M. E., Fraser, K. H., Zhang, T., Gellman, B., Fleischli, A., Dasse, K. A., . . . Wu, Z. J. (2010a). Computational Characterization of Flow and Hemolytic Performance of the UltraMag Blood Pump for Circulatory Support. *Artificial Organs, 34*(12), 1099-1113. doi: 10.1111/j.1525-1594.2010.01017.x

Taskin, M. E., Fraser, K. H., Zhang, T., Gellman, B., Fleischli, A., Dasse, K. A., . . . Wu, Z. J. (2010b). Computational characterization of flow and hemolytic performance of the UltraMag blood pump for circulatory support. *Artificial Organs, 34*(12), 1099. doi: 10.1111/j.1525-1594.2010.01017.x

Taskin, M. E., Fraser, K. H., Zhang, T., Wu, C., Griffith, B. P., & Wu, Z. J. (2012). Evaluation of Eulerian and Lagrangian Models for Hemolysis Estimation. *ASAIO journal, 58*(4), 363-372. doi: 10.1097/MAT.0b013e318254833b

Teh, A. (2015). BiVACOR. Retrieved 30 June, 2015, from http://bivacor.com/

Teuteberg, J. J., & Chou, J. C. (2014). Mechanical Circulatory Devices in Acute Heart Failure. *Critical care clinics, 30*(3), 585-606.

ThoratecCorporation. (2006). *HeartMate® XVE LVAS Operating Manual*. CA: Thoratec Corporation.
Throckmorton, A. L., & Kishore, R. A. (2009). Design of a Protective Cage for an Intravascular Axial Flow Blood Pump to Mechanically Assist the Failing Fontan. *Artificial Organs, 33*(8), 611-621. doi: 10.1111/j.1525-1594.2009.00779.x
Throckmorton, A. L., & Untaroiu, A. (2008). CFD Analysis of a Mag-Lev Ventricular Assist Device for Infants and Children: Fourth Generation Design. *ASAIO journal, 54*(4), 423-431. doi: 10.1097/MAT.0b013e31817efaa8
Throckmorton, A. L., Untaroiu, A., Allaire, P. E., Wood, H. G., Matherne, G. P., Lim, D. S., . . . Olsen, D. B. (2004). Computational Analysis of an Axial Flow Pediatric Ventricular Assist Device. *Artificial Organs, 28*(10), 881-891. doi: 10.1111/j.1525-1594.2004.00009_1.x
Timms, D. (2005). *Design, development and evaluation of centrifugal ventricular assist devices.* Queensland University of Technology.
Timms, D., Fraser, J., Hayne, M., Dunning, J., McNeil, K., & Pearcy, M. (2008). The BiVACOR Rotary Biventricular Assist Device: Concept and In Vitro Investigation. *Artificial Organs, 32*(10), 816-819. doi: 10.1111/j.1525-1594.2008.00633.x
Timms, D., Fraser, J., Thompson, B., McNeil, K., & Steinseifer, U. (2009). *In-vitro and In-vivo testing of the BiVACOR Rotary BiVAD/TAH.* Paper presented at the World Congress on Medical Physics and Biomedical Engineering, September 7-12, 2009, Munich, Germany.
Timms, D., Hayne, M., McNeil, K., & Galbraith, A. (2005). A Complete Mock Circulation Loop for the Evaluation of Left, Right, and Biventricular Assist Devices. *Artificial Organs, 29*(7), 564-572. doi: 10.1111/j.1525-1594.2005.29094.x
Timms, D. L., Gregory, S. D., Greatrex, N. A., Pearcy, M. J., Fraser, J. F., & Steinseifer, U. (2011). A Compact Mock Circulation Loop for the In Vitro Testing of Cardiovascular Devices. *Artificial Organs, 35*(4), 384-391. doi: 10.1111/j.1525-1594.2010.01088.x
Timms, D. L., & Queensland University of Technology. School of Engineering, S. (2005). *Design, development and evaluation of centrifugal ventricular assist devices.* (Dissertation/Thesis).
Tsukamoto, Y., Ito, K., Sawairi, T., Konishi, Y., Yamane, T., Nishida, M., . . . Taenaka, Y. (2000). Computational Fluid Dynamics Analysis of a Centrifugal Blood Pump with WashoutHoles. *Artificial Organs, 24*(8), 648-652. doi: 10.1046/j.1525-1594.2000.06604.x
Tu, J. (2007). *Computational Fluid Dynamics: A Practical Approach*: Butterworth-Heinemann.
Tu, J., Yeoh, G.-H., & Liu, C. (2013). *Computational Fluid Dynamics: A Practical Approach*. GB: Butterworth Heinemann.
Untaroiu, A., Wood, H. G., Allaire, P. E., Throckmorton, A. L., Day, S., Patel, S. M., . . . Olsen, D. B. (2005). Computational Design and Experimental Testing of a Novel Axial Flow LVAD. *ASAIO journal, 51*(6), 702-710. doi: 10.1097/01.mat.0000186126.21106.27
Verdonck, P., Kleven, A., Verhoeven, R., Angelsen, B., & Vandenbogaerde, J. (1992). Computer-controlledin vitro model of the human left heart. *Medical*

& biological engineering & computing, 30(6), 656-659. doi: 10.1007/BF02446800

Vogel, E. (2013). The Importance Of Best Efficiency Point (BEP). Retrieved 30 June, 2015, from http://www.maintenancetechnology.com/2013/05/the-importance-of-best-efficiency-point-bep/

Vosse, v. d. F. N., Tuzun, E., Dat, M., Rutten, M. C. M., Kadipasaoglu, C., & Mol, d. B. (2011). Continuous-flow cardiac assistance : effects on aortic valve function in a mock loop. *Journal of Surgical Research, 171*(2), 443. doi: 10.1016/j.jss.2010.05.040

Watanabe, K., Ichikawa, S., Asai, T., Motomura, T., Hata, A., Ito, S., . . . Nosé, Y. (2004). Centrifugal Blood Pump with a Hydraulically-levitated Impeller for a Permanently Implantable Biventricular Assist Device. *Artificial Organs, 28*(6), 556-563. doi: 10.1111/j.1525-1594.2004.07311.x

Wells, R. E., & Merrill, E. W. (1961). The variability of blood viscosity. *The American Journal of Medicine, 31*(4), 505-509. doi: 10.1016/0002-9343(61)90134-6

Wells, R. E., & Merrill, E. W. (1962). Influence of flow properties of blood upon viscosity-hematocrit relationships. *The Journal of clinical investigation, 41*(8), 1591-1598. doi: 10.1172/JCI104617

Wilcox, D. C. (1988). Reassessment of the scale-determining equation for advanced turbulence models. *AIAA Journal, 26*(11), 1299-1310.

Wilcox, D. C. (1998). *Turbulence modeling for CFD*. La Cãnada, Calif: DCW Industries.

Wilcox, D. C. (2008). Formulation of thek-ωTurbulence Model Revisited. *AIAA Journal, 46*(11), 2823-2838. doi: 10.2514/1.36541

Wilson, K. C., Addie, G. R., & Sellgren, A. (2006). *Slurry Transport Using Centrifugal Pumps* Retrieved from http://QUT.eblib.com.au/patron/FullRecord.aspx?p=302643

Wilson, S. R., Givertz, M. M., Stewart, G. C., & Mudge Jr, G. H. (2009). Ventricular Assist Devices:: The Challenges of Outpatient Management. *Journal of the American College of Cardiology, 54*(18), 1647-1659.

Woodcock, J. P. (1976). Physical properties of blood and their influence on blood-flow measurement. *Reports on Progress in Physics, 39*, 65. doi: 10.1088/0034-4885/39/1/002

Woodruff, S. J., Sharp, M. K., & Pantalos, G. M. (1997). Compact Compliance Chamber Design for the Study of Cardiac Performance in Microgravity. *ASAIO journal, 43*(4), 316-320. doi: 10.1097/00002480-199707000-00010

Wu, H., Wang, Z., & Lv, X. (2011). Design and Simulation of Axial Flow Maglev Blood Pump. *International Journal of Information Engineering and Electronic Business, 3*(2), 42-48. doi: 10.5815/ijieeb.2011.02.06

Wu, J., Antaki, J. F., Verkaik, J., Snyder, S., & Ricci, M. (2012). Computational Fluid Dynamics-Based Design Optimization for an Implantable Miniature Maglev Pediatric Ventricular Assist Device. *Journal of Fluids Engineering, 134*(4), 41101. doi: 10.1115/1.4005765

Wu, J., Paden, B. E., Borovetz, H. S., & Antaki, J. F. (2010). Computational Fluid Dynamics Analysis of Blade Tip Clearances on Hemodynamic Performance and Blood Damage in a Centrifugal Ventricular Assist Device. *Artificial Organs, 34*(5), 402-411. doi: 10.1111/j.1525-1594.2009.00875.x

Wurzinger, L., Opitz, R., & Eckstein, H. (1986). Mechanical blood trauma: An overview. *Angeiologie, 38*, 81–97.

Wysoczynski, M., Hong, K. U., & Moore, J. B. (2014). Bone marrow cell therapies in ischemic cardiomyopathy. *Expert Opinion on Biological Therapy, 14*(9), 1229-1232. doi: doi:10.1517/14712598.2014.925873

Yamane, T., Kyo, S., Matsuda, H., Abe, Y., Imachi, K., Masuzawa, T., . . . Tsuchiya, T. (2010). Japanese Guidance for Ventricular Assist Devices/Total Artificial Hearts. *Artificial Organs, 34*(9), 699-702. doi: 10.1111/j.1525-1594.2010.01091.x

Yamane, T., Miyamoto, Y., Tajima, K., & Yamazaki, K. (2004). A Comparative Study Between Flow Visualization and Computational Fluid Dynamic Analysis for the Sun Medical Centrifugal Blood Pump. *Artificial Organs, 28*(5), 458-466. doi: 10.1111/j.1525-1594.2004.07161.x

Yoshino, M., Uemura, M., Takahashi, K., Watanabe, N., Hoshi, H., Ohuchi, K., . . . Takatani, S. (2001). Design and Evaluation of a Single-Pivot Supported Centrifugal Blood Pump. *Artificial Organs, 25*(9), 683-687. doi: 10.1046/j.1525-1594.2001.06856.x

Zannoli, R., Corazza, I., & Branzi, A. (2009). Mechanical simulator of the cardiovascular system. *Physica Medica, 25*(2), 94-100. doi: 10.1016/j.ejmp.2008.02.007

Zareba, K. M. (2002). The artificial heart--past, present, and future. *Medical Science Monitor, 8*(3), RA72-RA77.

Zhang, J., Gellman, B., Koert, A., Dasse, K. A., Gilbert, R. J., Griffith, B. P., & Wu, Z. J. (2006). Computational and experimental evaluation of the fluid dynamics and hemocompatibility of the CentriMag blood pump. *Artificial Organs, 30*(3), 168-177.

Zhang, T., Taskin, M. E., Fang, H.-B., Pampori, A., Jarvik, R., Griffith, B. P., & Wu, Z. J. (2011). Study of flow-induced hemolysis using novel Couette-type blood-shearing devices. *Artificial Organs, 35*(12), 1180. doi: 10.1111/j.1525-1594.2011.01243.x

Zhang, Y., Zhan, Z., Gui, X.-M., Sun, H.-S., Zhang, H., Zheng, Z., . . . Jin, D.-H. (2008). Design Optimization of an Axial Blood Pump With Computational Fluid Dynamics. *ASAIO journal, 54*(2), 150-155. doi: 10.1097/MAT.0b013e318164137f

Zhou, W., Zhao, Z., Lee, T. S., & Winoto, S. H. (2003). Investigation of Flow Through Centrifugal Pump Impellers Using Computational Fluid Dynamics. *International Journal of Rotating Machinery, 9*(1), 49-61. doi: 10.1155/S1023621X0300006X

Appendices

Appendix 3-1

BiVAD Simulation results at the design condition

Turbulence Kinetic Energy

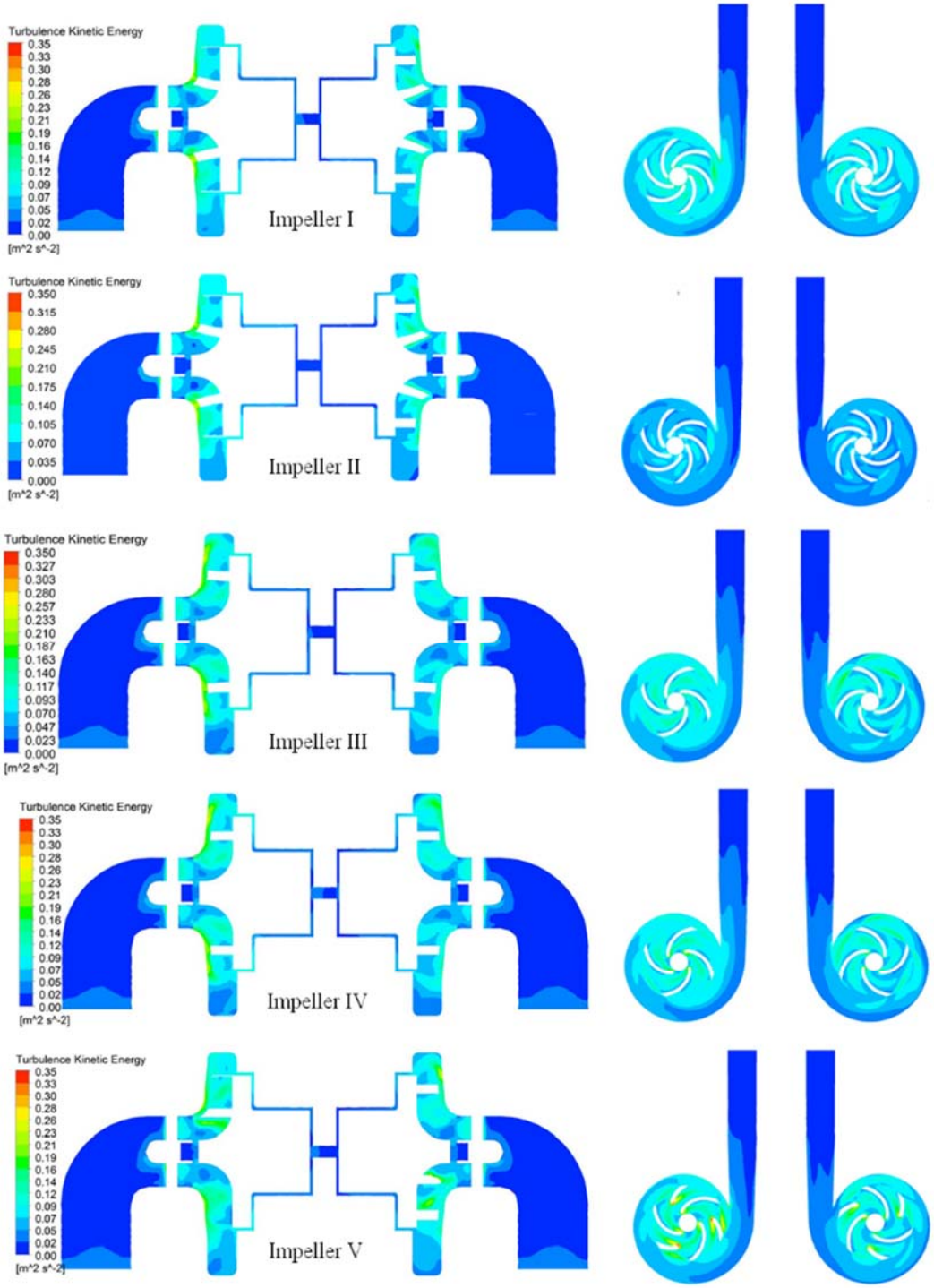

Turbulence kinetic energy distribution found to be highest at the leading edge of all the impeller designs. The overall kinetic energy in Impeller II is lowest among the designs, however the magnitude is still in the same range and does not have significant difference compare to other designs.

Velocity

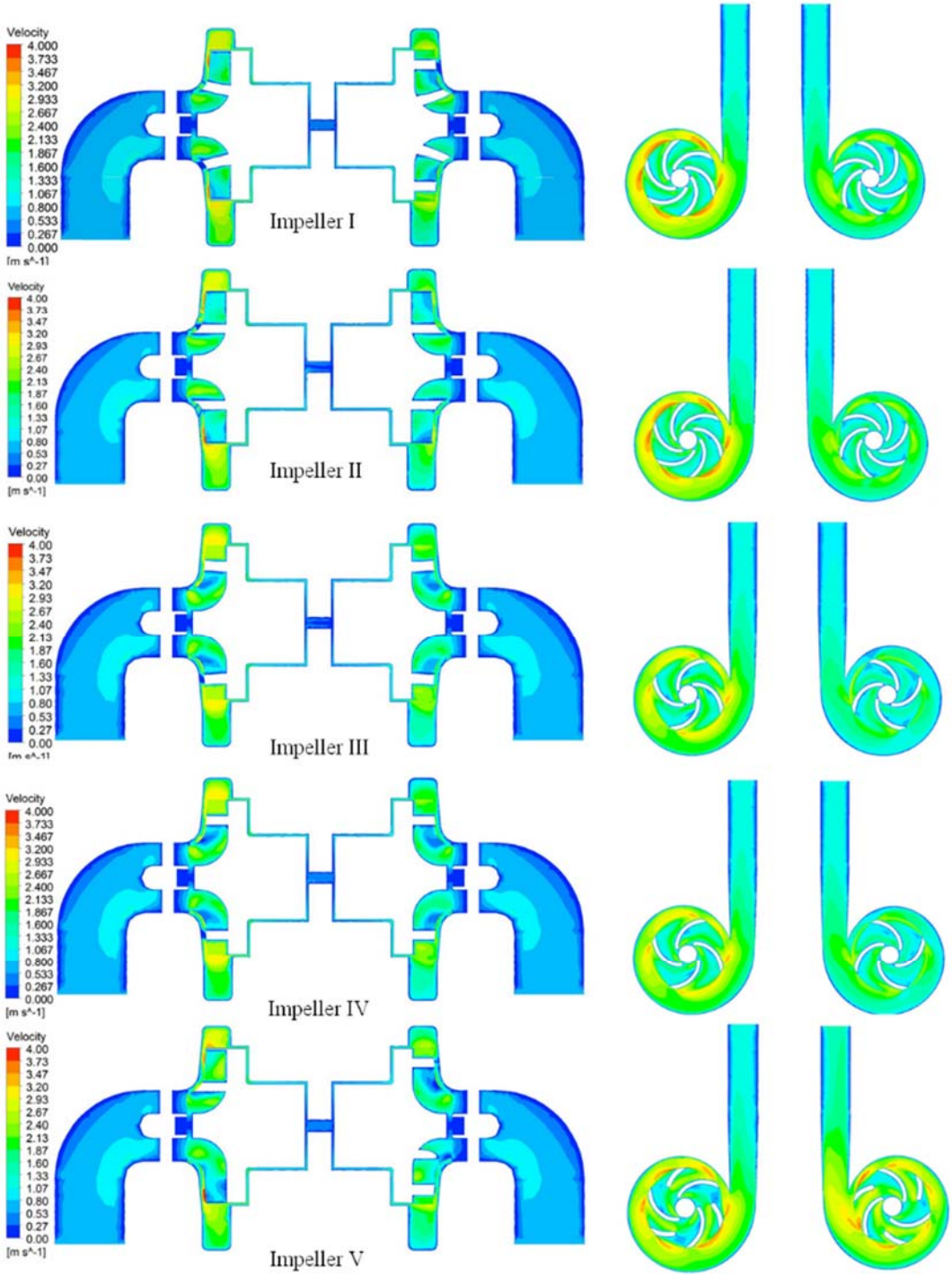

The low velocity regions observed at the inlet elbow and near wall of the outlet port in all the designs. The overall velocity in the volute of the LVAD side is higher than

the RVAD due to higher impeller speed. The velocity is found to be high at the region around the impeller and reduced as the fluid flow toward the expansion of the outlet port.

Pressure

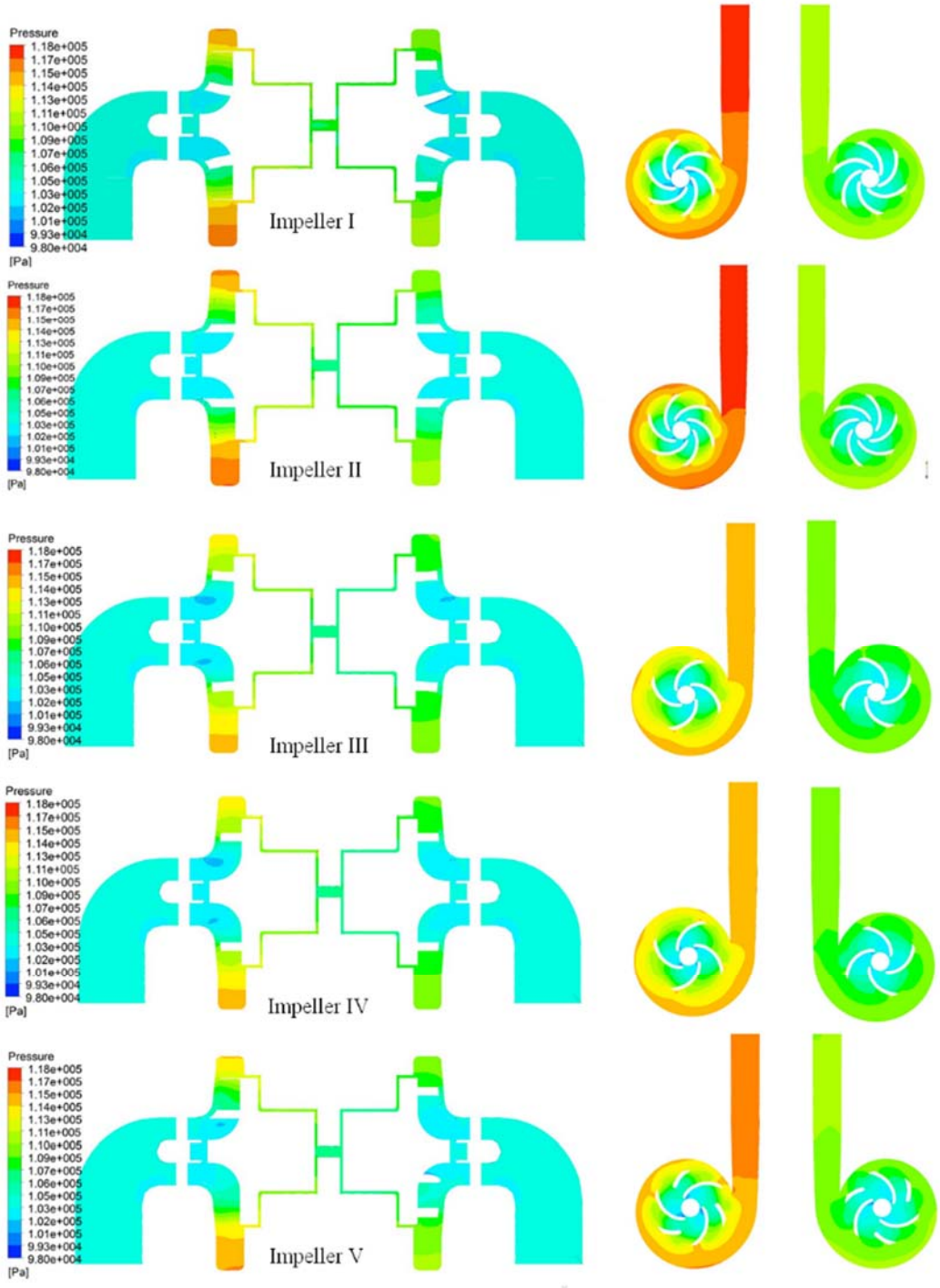

The pressure is higher on LVAD than RVAD side in all the design due to the higher impeller speed. It can clearly see from the figure that the Impeller I & II has highest pressure at the pump outlet follows by Impeller V, while the Impellers III and IV

which have lowest number of blade has lowest outlet pressure. This pressure plot shows an agreement with the head pressure results in shown in section 3.5.4 of this thesis.

Shear Stress

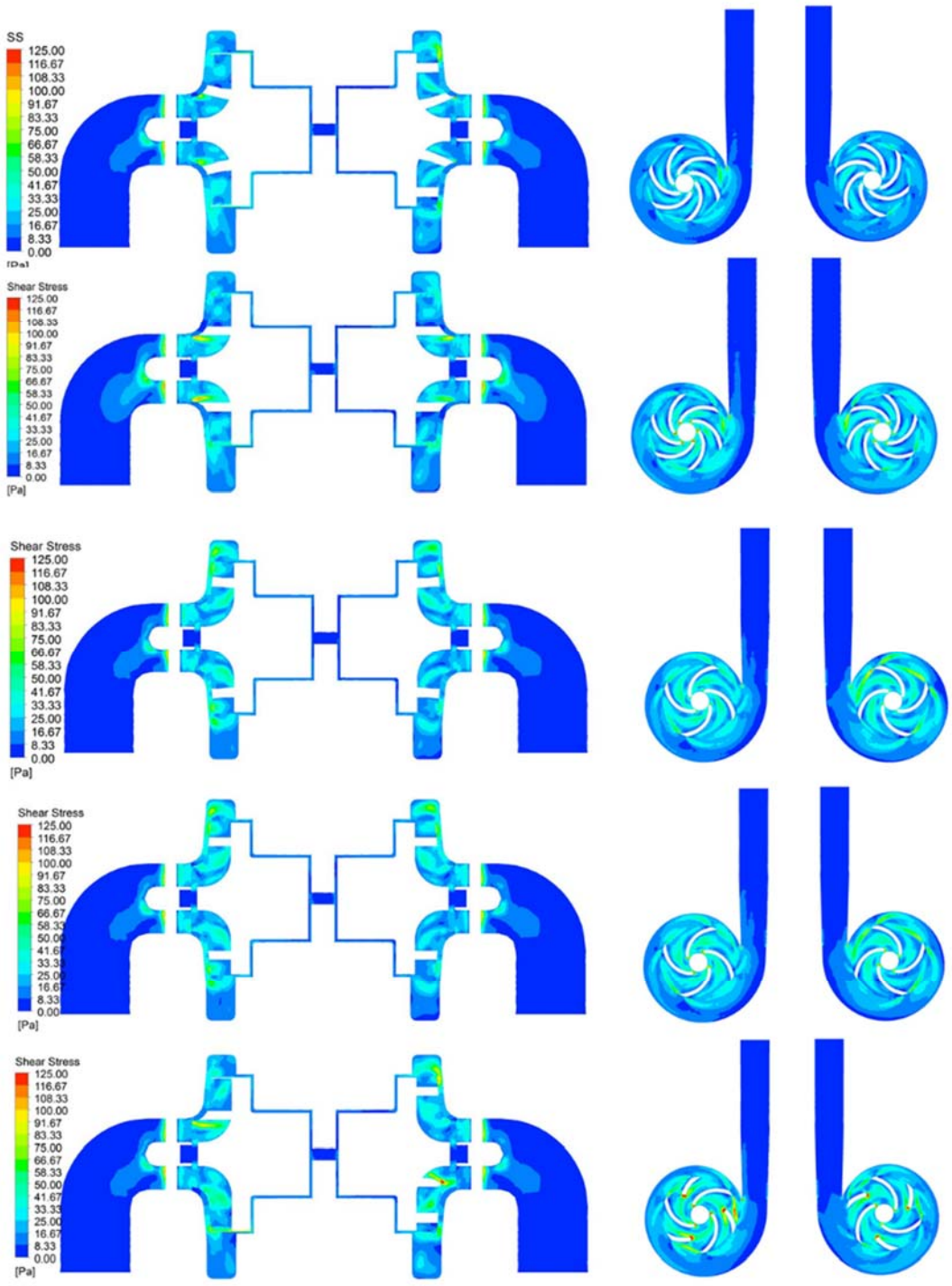

Shear stress found to be highest at the leading edge of all the impeller designs. According to this figure, Design V has the largest region of high shear stress above 125 Pa which can be related to the highest blood damage as shown in Figure 3-27.

Appendix 3-2

Proposed design of hemocompatible prototype.

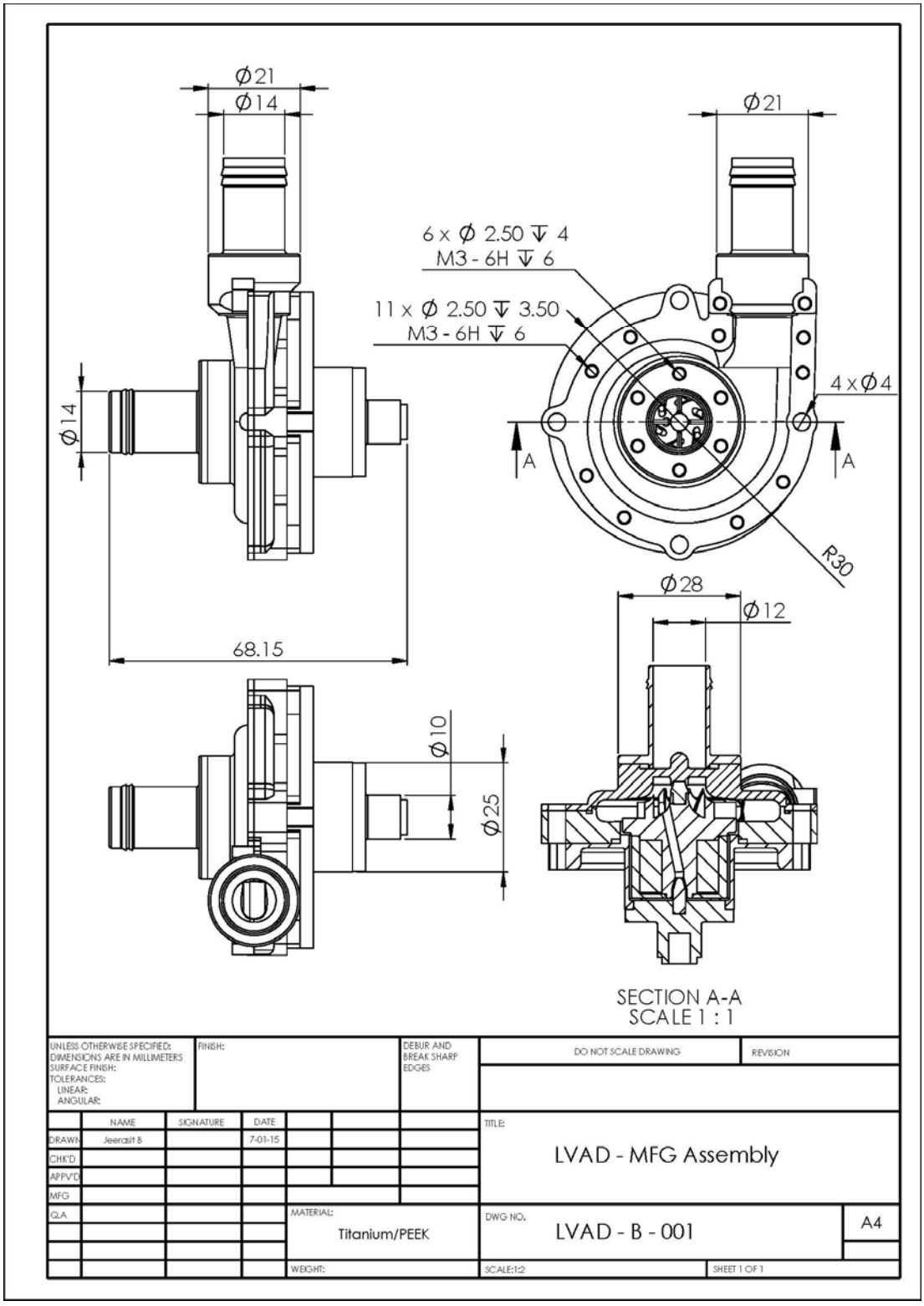

The modified drawing of VAD for future prototype which will be suitable for the experiment with real blood for hemolysis evaluation. This design mainly aim for the ease of machining on hard material like Titanium and reducing the manufacturing

cost. The chamber was designed to incorporate additional O-rings instead of sealant that use on the current prototype to prevent hemo-compatibility issue.

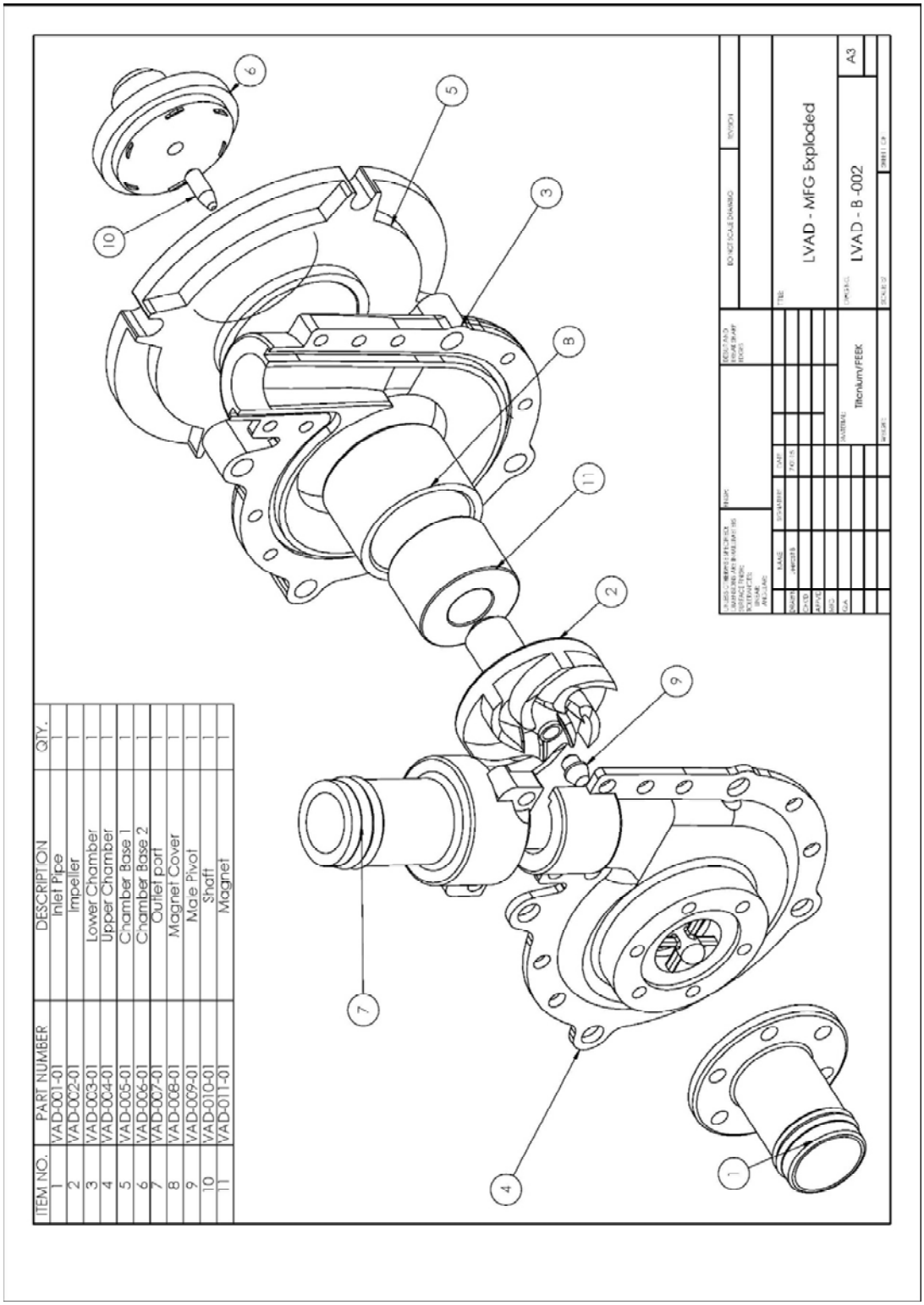

Appendix 4-1

Specification of the equipment:

Pressure Transducer: GE UNIK5000	
Power supply	7-32 V
Output	4-20 mA
Current consumption	4-20 mA
Frequency response	5 kHz
Operating Pressure range - guage	70 mbar to 70 bar
Operating Pressure range - absolute	350 mbar to 700 bar
Accuracy	±0.5%
Pressure connector	¼ NPT female
Flow meter: Measuring sensor Krohne Optiflux 1000 / Signal converter Krohne IFC050C	
Power supply	100-230 VAC
Power consumption	5.6W
Output	4-20 mA
Pulse rate	0.01 – 10000 pulse/s
Measuring accuracy	±0.5% above 0.5 m/s, ±2.5% below 0.5m/s
Operating Range	0.03 – 12 m/s
DAQ I/O module: NI9207	
Number of channels	16 analog input channels: 8 voltage and 8 current
ADC resolution	24 bits
Input range	Voltage channels: Min ±10.2 V, Typical ±10.4V Current channels: Min ±21.5 mA, Typical ±22.0mA
Conversion time (per channel)	2ms /52 ms
Power consumption	295 mW max
Compact DAQ Chassis: cDAQ9172	
Input voltage range	11 – 30 V
Maximum required input power	15 W
Input FIFO size	2,047 samples
Maximum sample rate	3.2 MS/s (multi-channel, aggregate)

Number of channels supported	16
Maximum output update rate	1.6 MS/s (multi-channel, aggregate)
Output FIFO size	8,191 samples shared among channels used
Variable speed controller: Invertek Optidrive E2	
Supply voltage	110-115V ± 10% 200-240V ± 10%
Supply frequency	48-62 Hz
Output power	110V 1 Phase Input: 0.5-0.75HP 230V 1 Phase Input: 1-1.5HP
Overload Capacity	150% for 60 s, 175% for 2s
Output Frequency	0-120Hz, 0.1 Hz resolution
Control Method	Single Phase V/F with starting boost

Appendix 5-1

The plots in this section shows the pressure signals of CHF heart with VAD support under different flow rates in the pulsatile flow environment. The pump speed was varied from 2500 to 4500 rpm to investigate the pump characteristic as discussed in Chapter 5.

Pump speed = 2500 rpm

Q = 0.00 L/min

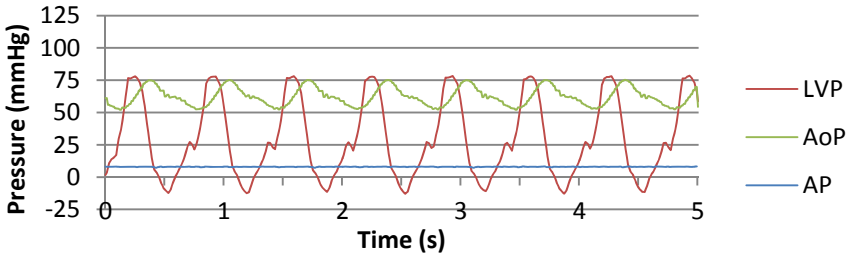

Q = 0.83 L/min

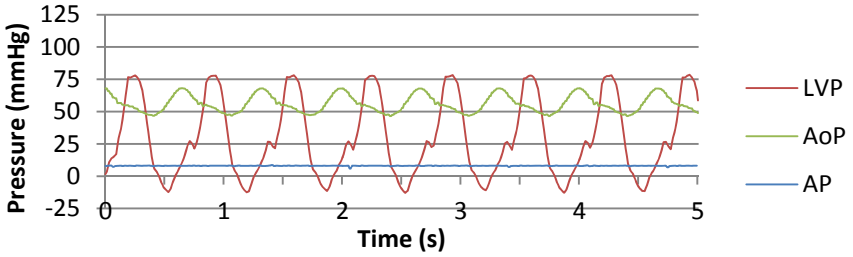

Q = 1.39 L/min

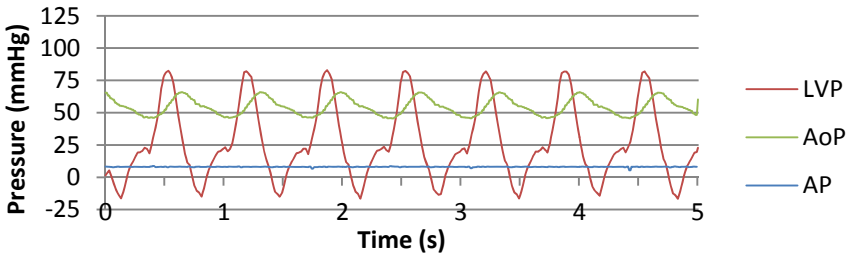

Q = 1.72 L/min

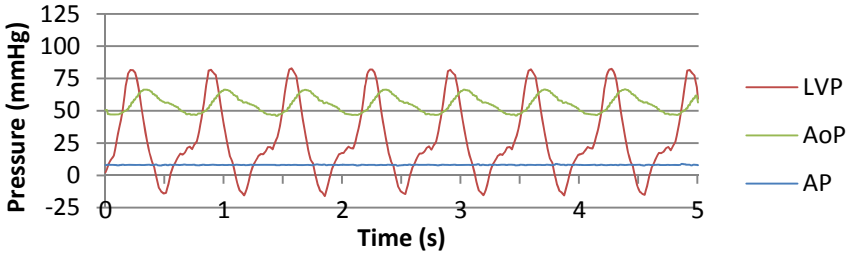

Q = 1.88 L/min

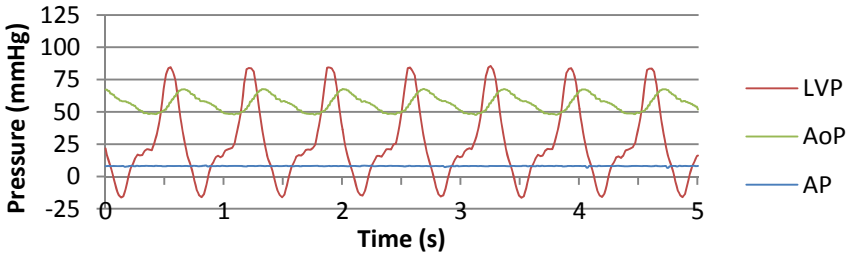

Pump speed = 3070 rpm

Q = 0.00 L/min

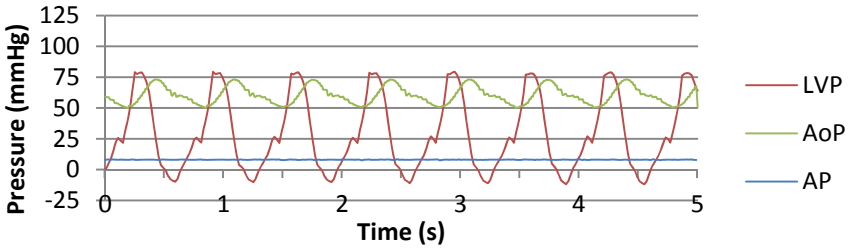

Q = 0.86 L/min

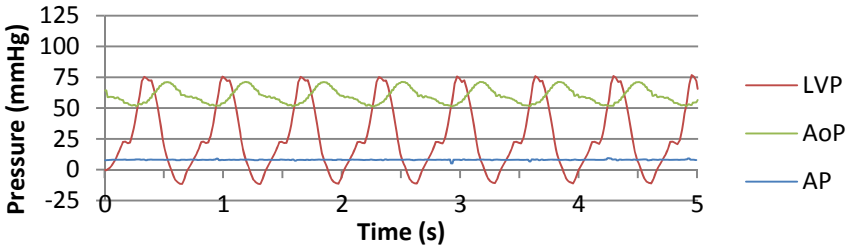

Q = 1.66 L/min

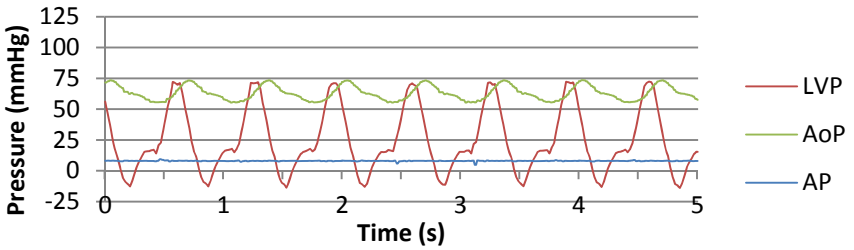

Q = 2.57 L/min

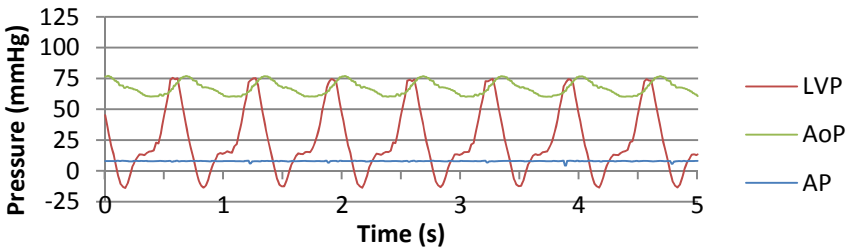

Q = 2.86 L/min

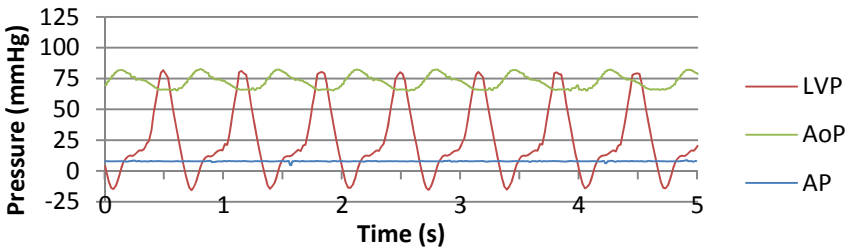

Pump speed = 3500 rpm

Q = 0.00 L/min

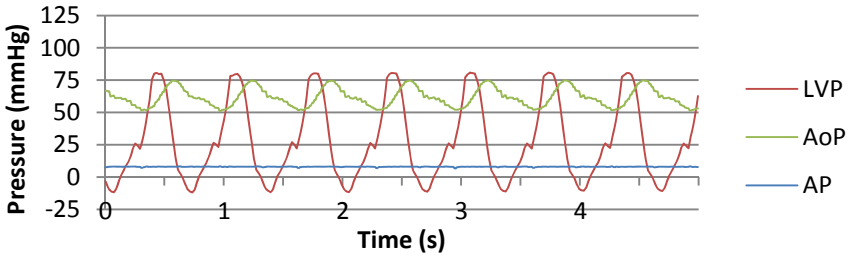

Q = 0.83 L/min

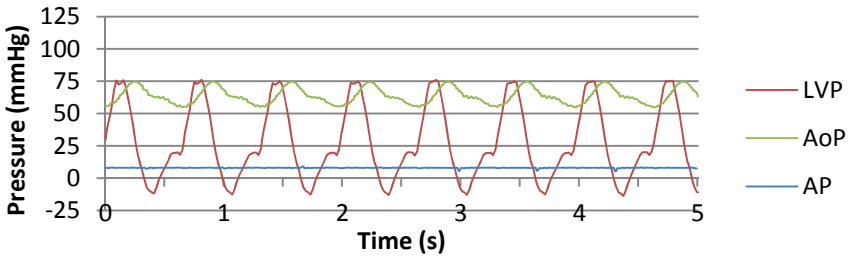

Q = 1.67 L/min

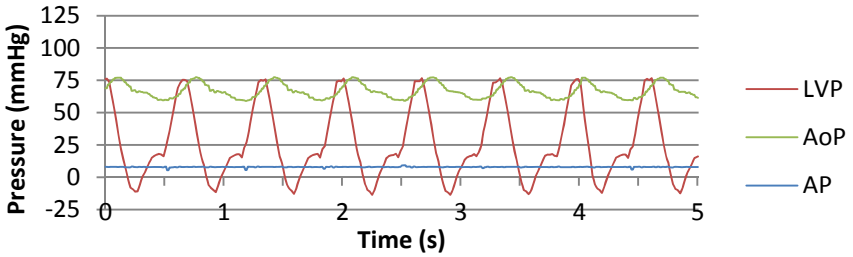

Q = 2.55 L/min

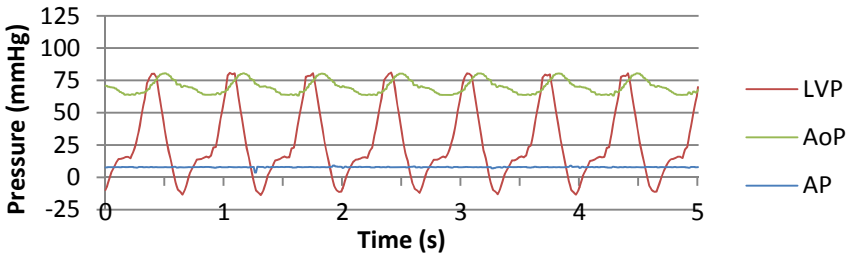

Q = 2.82 L/min

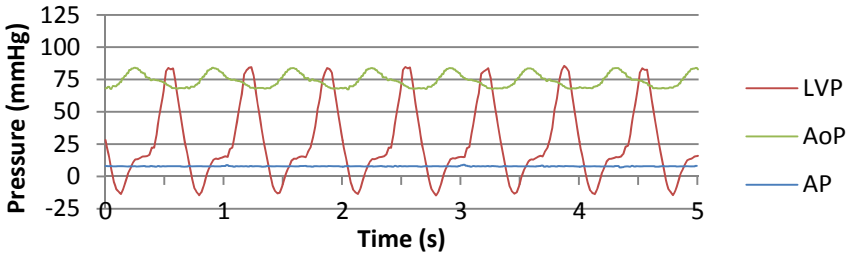

Q = 3.13 L/min

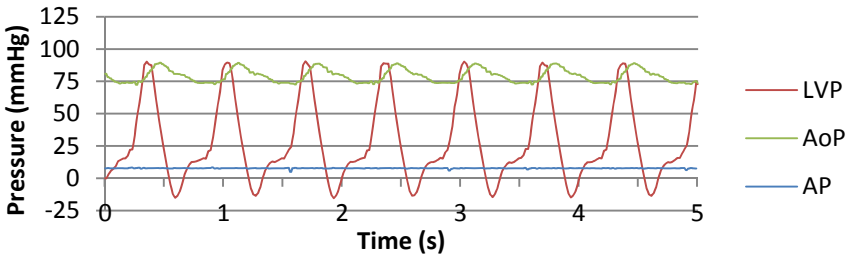

Q = 3.41 L/min

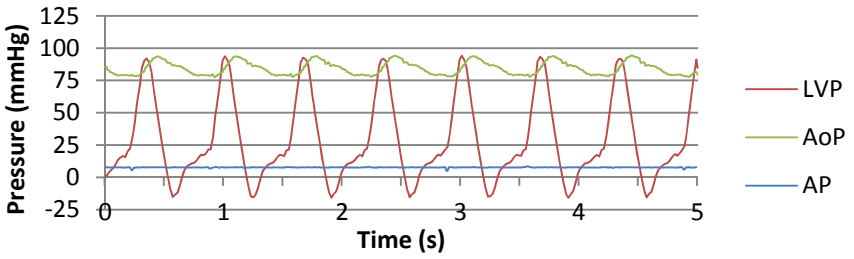

Pump speed = 4020 rpm

Q = 0.00 L/min

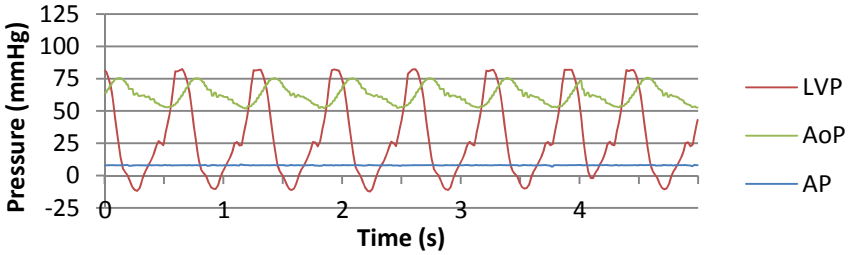

Q = 0.86 L/min

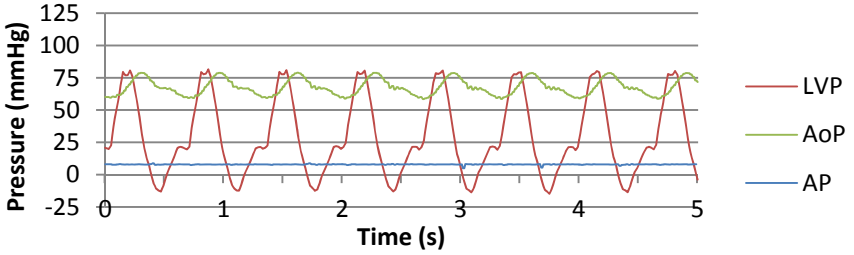

Q = 1.64 L/min

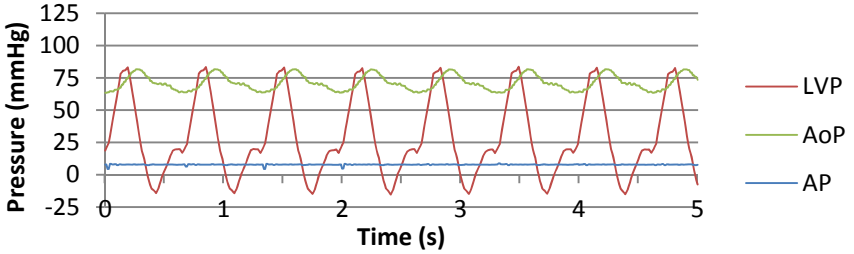

Q = 2.48 L/min

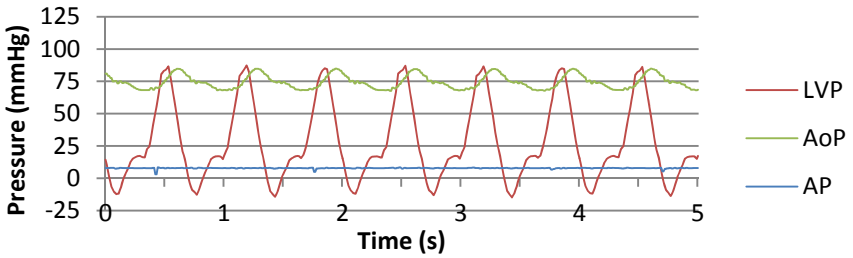

Q = 2.86 L/min

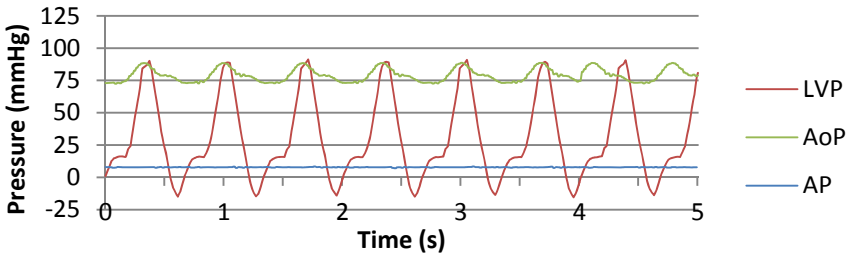

Q = 3.08 L/min

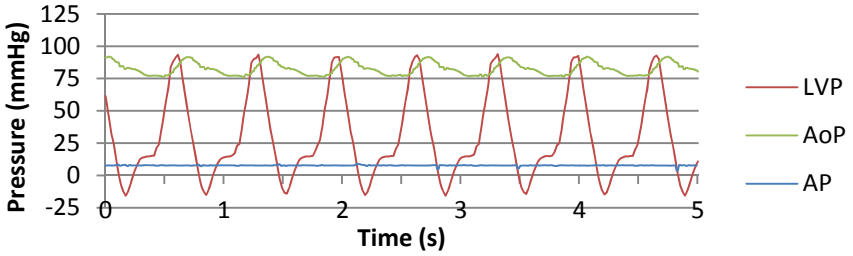

Q = 3.45 L/min

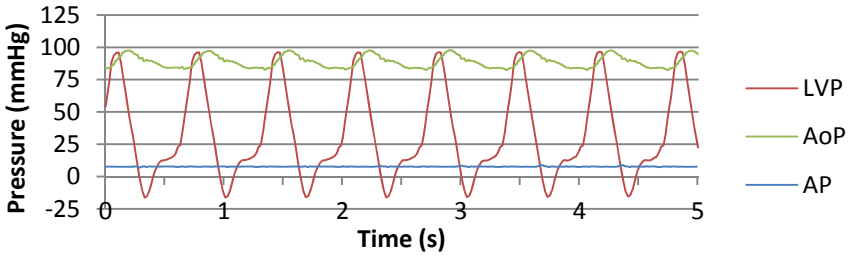

Q = 3.89 L/min

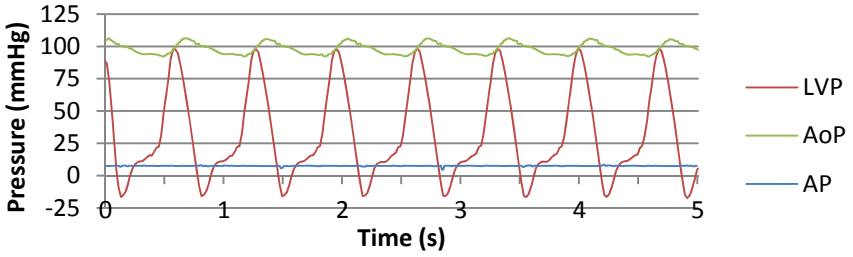

Q = 4.07 L/min

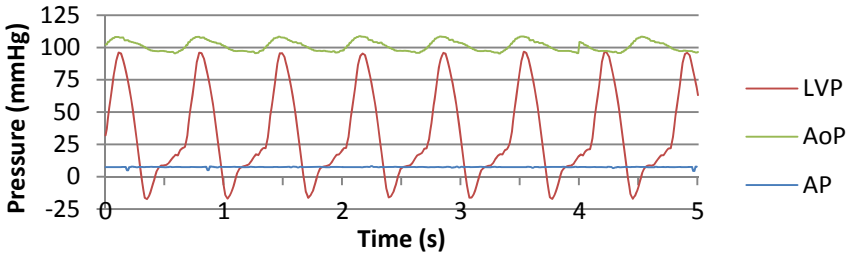

Pump speed = 4500 rpm

Q = 0.00 L/min

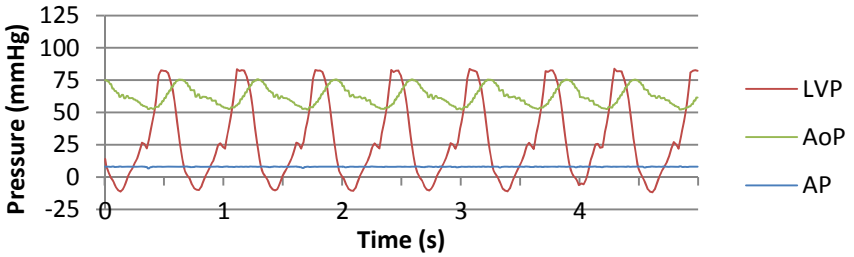

Q = 0.88 L/min

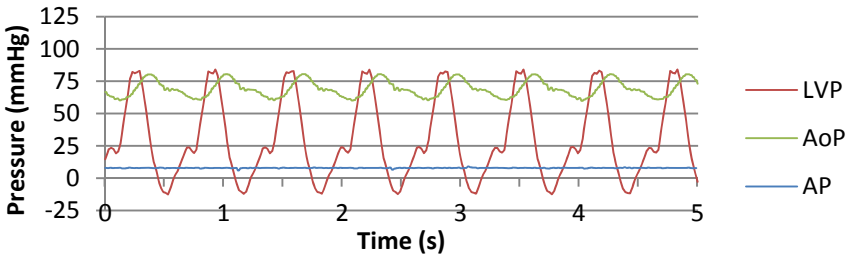

Q = 1.69 L/min

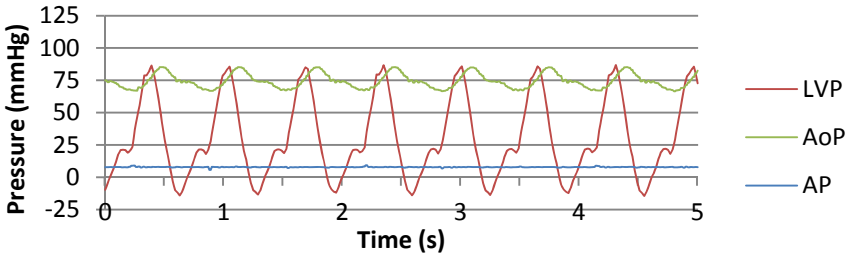

Q = 2.48 L/min

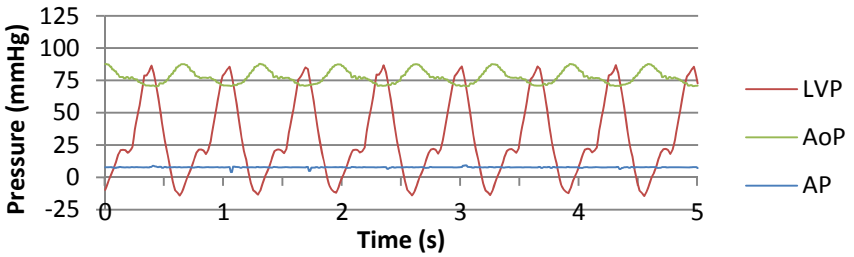

Q = 2.83 L/min

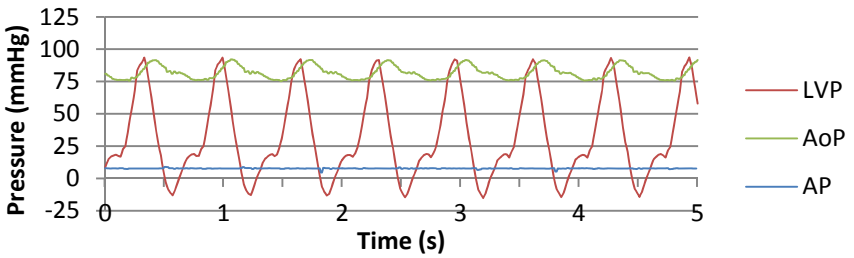

Q = 3.11 L/min

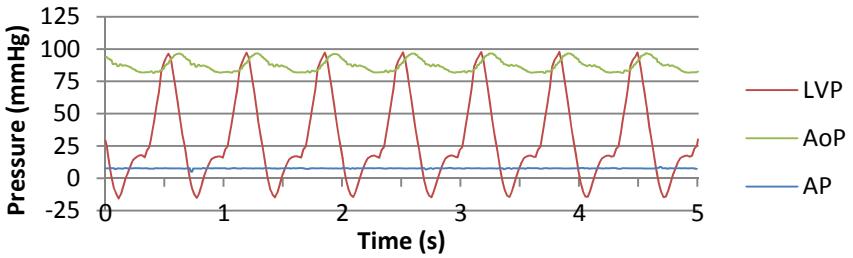

Q = 3.55 L/min

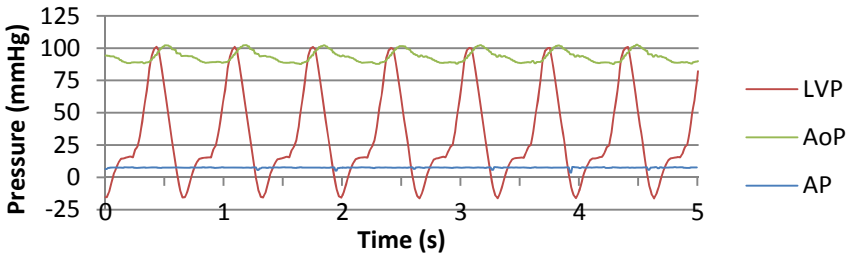

Q = 3.87 L/min

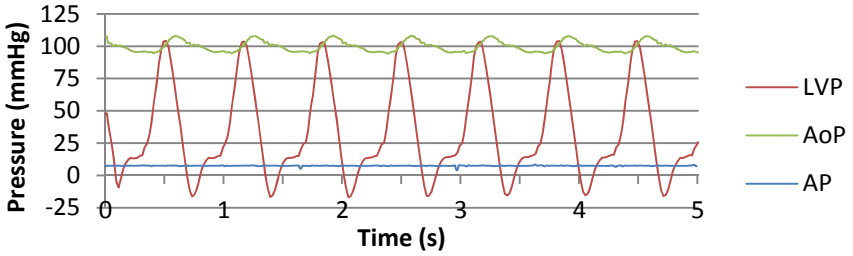

Q = 4.21 L/min

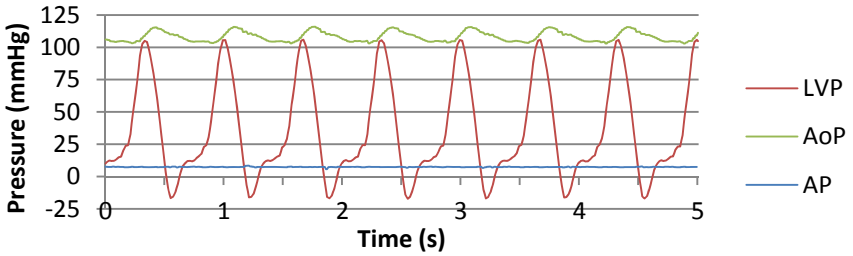

Q = 4.54 L/min